PULSED ELECTRIC FIELDS AND CURRENTS FOR CANCER THERAPY

A thesis submitted in partial fulfilment of the requirements for the

Degree of

Doctor of Philosophy

in Electrical and Electronic Engineering

at the University of Canterbury,

Christchurch, New Zealand,

by Thomas Frederick Cronjé,

in November 2016.

ABSTRACT

Incidence of cancer is growing in modern society, especially in New Zealand and the U.K. where cancer is now the leading cause of death, motivating development and research into new therapies. The ultimate goal of the work in this thesis is to offer novel electrical methods in destroying cancer cells.

Literature suggests that there are certain physical means of producing more consistent electroporation among a variety of different cells in a tumour, such as the use of higher frequency pulsing electric fields, and these means need to be further investigated. The goal of this thesis was to design apparatus that can be used to investigate these new means of improving electroporation, including producing more uniform electroporation among a range of different cell sizes and morphologies as is typically present in malignant tumours, and to validate this apparatus.

A novel electroporator apparatus that uses a dual stage cascaded multilevel inverter topology with high voltage RF MOSFETs has been designed and used successfully for the experiments in this study. The electroporator meets the broad specifications of being adjustable or programmable in terms of voltage (output ranging from 100 V to 1250 V peak), frequency (monopolar pulses of up to 500 μs and bipolar pulses ranging from 10 kHz to 800 kHz), and pulse burst regime (programmable number of pulses, with programmable inter-pulse burst intervals). The electroporator offers a variety of output waveforms and is also capable of producing bipolar or monopolar pulses. It has demonstrated reasonable performance with an output slew rate of up to 2 x 10^{10} V/s for frequencies up to 1 MHz pulses into a load of 80 Ω in parallel with 235 pF from a dual isolated supply of 1600 VDC total, despite substantial coupled noise in the circuit.

A robust cuvette, that produces a uniform electric field between its electrodes, has been developed for the experiments in this study and has withstood the rigors of all the electroporation work done successfully. Cell culture and electroporation protocols have been developed for the experiments undertaken.

A substantial body of work was carried out involving pulsed electric field electroporation of Ishikawa human cancer cells (a commercial human endometrial adenocarcinoma cell line) in suspension. Two methods were employed including fluorescence microscopy and particularly flow cytometry. Microscopic analysis proved less productive than flow cytometric analysis and

also lacked fluorescence resolution. Differences between bipolar and monopolar pulses were examined and characterised in detail. DC (monopolar) pulses appear to have more detrimental effects on cells compared to AC (bipolar) pulses for an equivalent mean fluorescence. Also, monopolar fields do not allow loading of cells with non-permeable small molecules (can only rapidly penetrate cells when they are porated) to the same high concentration as for bipolar fields in the case where high viability is desirable. Thus bipolar fields show a clear advantage over monopolar fields if the aim is not to kill cells directly. No direct evidence could be found whether higher frequency (ranging from 10 kHz to 800 kHz) bipolar fields produce better normalisation of the electroporation effect across a range of cell sizes (6 μm to 43 μm, ±10 %) for isolated cells in suspension. Higher frequencies also tend to demand higher amplitude electric fields to produce the same degree of electroporation than at lower frequencies due to inherent membrane time constant and relative slew rate limitations of the MOSFET switches. If the aim is to kill cells over loading of cells with external molecules (in this case fluorescent dye), monopolar pulses may offer the best result so long as the electric field can be adequately applied to the cells. The added complexity of cells embedded within a tissue structure, which may yield different results regarding comparative electroporation between monopolar and bipolar pulses, has not been investigated here.

Radio frequency ablation is used in cancer therapy treatment motivating development of a radio frequency ablator. The general H-bridge topology was employed for this radio frequency ablator as it allows for flexibility of ablation frequencies. Also, a practical radio frequency ablation probe has been developed and a low power ablation protocol has been established for the low power experimental work on *ex-vivo* animal liver at room temperature. The radio frequency ablator system was used to ablate fresh animal liver successfully and reliably with very similar characteristics to standard commercial radio frequency ablation systems, creating an average lesion of 2.7 cm^3 for a 2 cycle 20 W ramped ablation protocol lasting 5 minutes. The ablator compared well with the literature, where low power protocols were used on healthy animal liver as a convenient model. The system performed less electrically efficiently at high frequencies (excessive heat was produced in the circuit due to the particular topology used). It could not be established whether higher frequencies (above 460 kHz) are capable of producing better ablation performance as could be expected when considering that tissues tend to be more conductive at higher frequencies due to inherent tissue capacitance causing the impedance to drop.

Several novel contributions have been made to the fields of electroporation, electrochemotherapy and radio frequency ablation techniques and technologies, as identified above.

For future work, further investigation of electroporation effects across a wider range of electric field pulse frequencies, burst parameters, cell types, and various tissues is required. Lastly, radio frequency ablation of tumours at higher frequencies (than the normal 450 kHz used for the commercial sinusoidal output radio frequency ablators) of pulsed bipolar electric currents is still required. Higher frequencies may produce more uniform ablation within the highly inhomogeneous tissue of unhealthy liver. A multimodal apparatus has been described and proposed, combining electroporation with radio frequency ablation, as a candidate for non-invasive deep tissue tumour therapy, and for other applications including gene therapy, genome editing and electrofusion.

In conclusion, a general H-bridge topology and its extension using a cascaded multilevel inverter arrangement has been employed to design and implement practical circuits that produce pulsatile output voltages for various uses, including an application in electroporation and an application in radio frequency ablation. A non-conventional method for analysing the effect of variable electroporation electric field pulses across a frequency range of 10 kHz to 800 kHz (bipolar pulses) and for single monopolar pulses, across a range of electric fields from 0.5 x 10^5 V/m to 3.5 x 10^5 V/m, based on flow cytometry, has been studied and presented. This study demonstrates how these various parameters affect Ishikawa cells in suspension, in terms of loading of exogenous molecules, and survival, and may promote the use of specific sets of parameters for specific applications. These applications may include the use of bipolar electric field pulses for biotechnology applications where survival is important, and monopolar or low frequency bipolar electric field pulses used in combination with very high fields for irreversible electroporation and may be used to ablate undesirable tissue such as tumours in the presence of other important surrounding tissues such as blood vessels. It has also been shown that pulsed AC electric currents (as opposed to sinusoidal alternating currents) may be used to ablate liver tissue, similar to commercial radio frequency ablators.

ACKNOWLEDGEMENTS

I wish to express sincere appreciation to Associate Professor Paul Gaynor for his extremely generous assistance in the preparation of this thesis. My supervisory team have been of great assistance and have encouraged me throughout the long period of part-time study. They include Dr Gabriel Lau (a radiologist) and Associate Professor Richard Duke.

A great number of staff at the department of Electrical and Computer Engineering have also assisted and encouraged me. This includes members of the technical staff: Edsel Villa, Nick Smith, Randy Hampton, Mike Cusdin, Jack Woudberg, Paul Agger, Dave Healy, Ken Smart, the late Pieter Kikstra, Philipp Hoff, Florin Predan, Dave van Leeuwen, Mike Shurety, Helen Devereux, and Gary Turner. I would especially like to thank Dr Bill Heffernan for some very insightful advice at a crucial time. Dr Steve Weddell helped me initially with the VHDL programming – thank you! Dr Kim Eccleston also kindly helped me characterise an RF aspect of my design. Professor Phil Bones has also been a great encourager. Professor Richard Jones from the NZ Brain Institute has also been very encouraging.

In the area of biology, where I have spent many months doing experimental work on live human cancer cells, many individuals have assisted and encouraged me along. I would like to mention Dr Kenny Chitcholtan from Otago University for his very generous and helpful advice and help in acquiring cells and some reagents. Postgraduate students from both Otago (especially Tiffany Tan) and Canterbury (especially Izani Othman, now Dr) Universities have been so helpful and encouraging. Associate Professor Steve Gieseg from the School of Biological Sciences, head of the Free Radical Biochemistry group, was very generous in allowing me access to his laboratory facilities for an extended period of time – this has been one of my most productive periods, thanks to you! Also thanks to staff members in that area, including Craig Galilee, Nicole Lauren-Manuera, Jackie Healy, Jan McKenzie and Graeme Bull.

My employer, Ara Institute of Canterbury (previously CPIT), and especially a great number of senior management members, peers and also students there have also greatly contributed by continuous encouragement and always showing interest in my research work. I do appreciate all the support I got!

Peers I would like to thank are you-know-who but especially Lynn Murray (now Dr) for training me in matters biology, without which I would never have developed the skills and confidence to work in a controlled biology laboratory. Dr Volker Nock was always helpful in all ways to help smooth out things for me. Our “international PG office team” of Lynn, Robert Heinhold (now Dr) and Salim Elzwawi (now Dr) have always engaged with deep, interesting and meaningful philosophic discussions. Thanks also to Prateek Benhal (now Dr) for your assistance in using Comsol. Thank you also Prateek Mehrotra (now Dr) for helping me sort out the VHDL programming, and for your ongoing encouragement!

Thanks to all my personal friends and your continual and unwavering encouragement. This includes also Dr Dirk Pons, who has always shown a strong belief in my ability to succeed, although I never did myself.

Last, but probably most importantly, I would like to thank my dearest wife Alexandra, my children Jean, Michelle and Louise, and my broader family, for enduring my pressurised behaviour for too many years.

Without you I would not have been able to tackle this project.

PREFACE

This project of developing and validating an apparatus for applying intense pulsed electric fields and currents for applications in cancer therapy and biotechnology has developed slowly but gradually over a period of slightly over 9 years. It started off in February 2007 and culminated at submission of the final draft by the end of July 2016. Part of this long period is attributed to the great earthquakes suffered here in Christchurch, New Zealand, and its ongoing aftershocks, striking on September 4th 2010 (7+ on the Richter scale), followed by the more devastating February 22nd 2011 (6+).

Initially defined as a high-voltage, high-frequency electronic amplifier PhD project, it evolved into the development of a fast and high voltage pulser and how it may be applied especially with a focus on cancer therapy, hence our collaboration with Dr Gabriel Lau, an interventional radiologist from Dunedin Hospital.

The department of Electrical and Computer Engineering at the University of Canterbury in New Zealand has been well placed for doing work in the areas of high-speed, high-voltage power electronics and in the area of electroporation in terms of resources and capabilities. It also offered its own tiny biology laboratory as a government registered physical containment level 2 (PC2) facility for doing work on cells, like culturing and assay work using various tools like microscopes. However, it became apparent that for this work we required a flow cytometer, the only one of which has been located in the School of Biological Sciences, and which had been pursued in order to further investigate operation of the electroporation system which had been built.

TABLE OF CONTENTS

TABLE OF FIGURES

LIST OF TABLES

GLOSSARY OF ACRONYMS AND ABBREVIATIONS

x10^5 V/m	100 000 V/m = 1 kV/cm = Kilovolt per centimetre
ABS	Acrylonitrile butadiene styrene
AC	Alternating current
AM	Amplitude modulation
BJT	Bipolar junction transistor
BNC	Bayonet Neill–Concelman connector
C	Capacitance
CHO	Chinese hamster ovary
CISPR	Comité International Spécial des Perturbations Radioélectriques
CMC	Common mode choke
CPLD	Complex programmable logic device
DC	Direct current
di/dt	Rate of change in current
DMEM	Dulbecco's modified Eagle medium
DNA	Deoxyribonucleic acid
DSP	Digital Signal Processor
dv/dt	Rate of change in volts
E or C	Experiment or Control
ECT	Electrochemotherapy
ELISA	Enzyme-linked immune assay
EM	Electromagnetic
EMC	Electromagnetic compatibility
EMI	Electromagnetic interference
EPB	Electroporation buffer
FACS	Fluorescence-activated cell sorting
FDA	U. S. Food and Drug Administration
FEA	Finite element analysis
FM	Frequency modulation
FOFS	Fluorescence over forward scatter units
FPGA	Field programmable gate array
HV	High voltage
i/o	Inputs and outputs
IC	Integrated circuit
IF	Intermediate frequency
IGBT	Insulated-gate bipolar transistor
IRE	Irreversible electroporation

kHz	Kilohertz
L	Inductance
LC	Inductance-capacitance
LED	Light-emitting diode
LFH	Laminar flow hood
LV	Low voltage
LVDS	Low-voltage differential signalling
MHz	Megahertz
MLI	Multilevel inverter
MOS	Metal-oxide-semiconductor
MOSFET	Metal-oxide-semiconductor field-effect transistor
NTIRE	Non-thermal irreversible electroporation
OEM	Original equipment manufacturer
PBS	Phosphate-buffered saline
PCB	Printed circuit board
PI	Propidium iodide
PWM	Pulse width modulation
R	Resistance
RCD	Resistor-capacitor-diode
RF	Radio frequency
RFA	Radio frequency ablation
RLC	Resistance-inductance-capacitance
RMS	Root mean square
ROM	Read-only memory
RPM	Revolutions per minute
RT	Room temperature
SCR	Silicon controlled rectifier
SHF	Super high frequency
SPICE	Simulation programme with integrated circuit emphasis
TB	Trypan blue
VHF	Very high frequency
VHDL	Very high speed integrated circuit hardware description language

CHAPTER 1
INTRODUCTION

1.0 Introduction

This chapter presents the motivation for this study, states the aims, and gives an overview of the structure of the thesis.

1.1 Motivation

Life expectancy around the world has increased dramatically from an average of 64 years to 70 years in just a generation (from 1990 to 2011), according to the World Health Organisation [1]. This figure was for all people at birth. At 60 years of age, life expectancy had increased from an additional 18 to 20 years, so such a person could expect to live to 80. These increases have been attributed mainly to a large drop in child mortality and general health improvements in China and India. It is expected that this trend will continue for the vast majority of countries.

We are more likely to become a victim of cancer as we get older. Statistics from the U.K. and New Zealand show that cancer has become the single largest cause of death in the developed world [2, 3], with the exception, among others, of the United States and also Australia where it is number two [4, 5]. It may be argued that the growing population of older people might account for this trend. But industrialisation is also to blame for polluting the environment, owing to inappropriate disposal and thus dispersal of environmental contaminants due to large scale manufacturing, automation and consumerism. This includes especially carcinogenic substances like those synthesised for agriculture, such as insecticides, which can be ultimately concentrated in the food chain. Living longer and being exposed to more carcinogens (and mutagens) means we are more likely to develop cancer [6].

Cancer is a group of about 200 diseases that is characterised by affected cells having the ability to aggressively grow and divide and therefore to displace and damage healthy tissues and organs, and even to spread to other areas in the body via the circulatory or lymphatic systems [7]. For instance, several mutations are required before a common colon cancer can start metastasising,

and this likelihood is increased by carcinogens [8]. Chromosomal aberrations are common in mature tumours and are a consequence of faulty repair of DNA damage and rearrangements of chromosomes (loss or gain) [9]. These unstable changes can make cancers more invasive and more resistant to chemotherapy. It can be argued that this is the main reason why cancer is so complex and therefore highly effective cures remain elusive.

Despite these factors, cancer has generally become more curable over time. However, the global burden to society associated with cancer has grown, especially in developing countries. This is due to population growth, population ageing, and lifestyle choices including smoking, reduced physical activity and diets associated with highly processed foods [10]. Finding a universal cure for cancer would be ideal but is unlikely.

A promising new biophysical process known as electroporation has been researched and applied since the late 1960's [11], but has not yet reached maturity as applied to cancer therapy. Studies by leading groups of researchers investigating this process and its application to cancer therapy (to be discussed in chapter 2) suggest that by changing ways of implementing electroporation we may achieve better results in affecting cancer cells and bring about other more patient-tolerated treatment regimes. The study detailed in this thesis has been proposed and pursued to improve cancer therapy involving application of electric fields.

Cancer therapies often include surgery, and often other modalities are also employed in the hope to improve the total effect of therapy. Standard non-surgical therapies include radiation therapy, chemotherapy, and radiofrequency ablation [12-14]. Multimodal cancer therapy, where 2 or 3 different therapies are combined sequentially or concurrently, is widely accepted as better than a single modality as it provides overlap but also produces reduced side-effects [15]. This latter study demonstrated a clear advantage in using three modalities over any two or single modality strategy. It is therefore one of the general aims in this project to develop a system or apparatus that is capable of multimodal cancer therapy.

The challenge for this project was to develop a new apparatus using modern electronics technology to extend medical research further into the use of electroporation and other electric field based treatment as a tool for treating cancer, and to validate it as proof of principle. As an added feature, use of the basic layout and design of this new tool for other purposes like biotechnology and other associated biomedical applications has been specifically considered. Applications may include microorganism genetic modification [16], gene therapy [17], genome editing [18], hybridoma production [19], cloning [20], membrane modification [21], and sterilisation of liquids and some foods [22-24].

1.2 Aims

The general aim was to research, design and test electronic apparatus which can be used for several high voltage biomedical applications, including electroporation, radio frequency ablation, dielectrophoresis, and others, with the ability to provide high voltage and high frequency bipolar and monopolar signals.

The primary aim of this thesis project was to develop a suitable experimental apparatus for clinical trials in electroporation. This apparatus had to deliver high-voltage of up to around 2 kV, and high-frequency of up to about 2 MHz, bipolar pulses for application. A secondary aim was to produce continuous bipolar voltages of up to around 200 V for other applications such as radio frequency ablation and dielectrophoresis.

A more specific aim was to design an apparatus to improve cancer therapy through use of higher frequencies and higher intensity bipolar electric fields than is commercially available, to electroporate cancer cells, and also to improve on the standard radio frequency ablation technique commonly used for organ tumours (e.g. liver), with both ultimately integrated into a dual-modality cancer therapy system.

1.3 Thesis Structure

This thesis is organised as follows:

Chapter 1 is the introduction and provides the motivation for this study, the aims and hypothesis, and how the thesis is organised.

Chapter 2 states the background for this thesis and provides insight into subject areas of electroporation and radio frequency ablation, setting the context for later chapters in this thesis.

Chapter 3 presents the electroporator circuit design and electrical results. This chapter provides detailed design considerations, modelling, and electrical testing results for the electroporator including induced noise and thermal effects.

Chapter 4 investigates electroporation of human cancer cells. This chapter provides a set of experimental electroporation results on human cancer cells in suspension and draws conclusions based on these findings.

Chapter 5 presents the radio frequency ablator hardware design and electrical testing. This chapter provides the detailed design process for the radio frequency ablator followed by its thermal and electrical results.

Chapter 6 applies the designed radio frequency ablator to liver. This chapter provides the probe design followed by 3 sets of thermal ablation experiments of animal liver at various power and frequency settings.

Chapter 7 reflects on the work carried out in this thesis, provides recommendations for future work, identifies the contributions made, and lists publications to date arising from the research.

1.4 References

[1] World Health Organisation, 2013, *World Health Statistics 2013*, [Online]. Available: http://www.who.int/gho/publications/world_health_statistics/EN_WHS2013_Full.pdf

[2] New Zealand Ministry of Health, 2011, *New Zealand mortality statistics: 1950 to 2010 (provisional)*, [Online]. Available: http://www.health.govt.nz/system/files/documents/publications/nz-mortality-statistics-1950-2009-provisional.pdf

[3] UK National Statistics, 2011, *Life expectancy, all-age-all-cause mortality, and mortality from selected causes, overall and inequalities*, Update to include data for 2010, Mortality Monitoring Bulletin, [Online]. Available: https://www.gov.uk/government/uploads/system/uploads/attachment_data/file/215417/dh_130738.pdf

[4] Australian Bureau of Statistics, 2013, *Causes of Death, Australia, 2011*, Table 1.1 Underlying cause of death, All causes, Australia, 2011, [Online]. Available: http://www.abs.gov.au/AUSSTATS/abs@.nsf/DetailsPage/3303.02011?OpenDocument

[5] S. L. Murphy, J. Xu and K. D. Kochanek, "Deaths: Final Data for 2010", Division of Vital Statistics, *National Vital Statistics Reports*, Vol. 61, No. 4, 2013.

[6] J. Vapnek, et, al. (ed), *Law for water management: a guide to concepts and effective approaches*, Food and Agriculture Organisation of the United Nations, 2009, [Online]. Available: http://www.fao.org/docrep/012/i1284e/i1284e.pdf

[7] O. K. Dzivenu and J. O'Donnell-Tormey, Cancer Research Institute, 2003, Cancer and the Immune System: The Vital Connection, [Online]. Available: http://www.cancerresearch.org/CRI/media/Content/Cancer%20Immunotherapy/Cancer-and-the-Immune-System-The-Vital-Connection.pdf

[8] D. Weatherall, et al., "Science and Technology for Disease Control: Past, Present, and Future", Chapter 5, Disease Control Priorities in Developing Countries, 2nd Ed., *Disease Control Priorities Project*, D. T Jamison, J. G. Breman, A. R. Measham, et al., Eds, Washington, World Bank, 2006.

[9] S. L. Thompson and D. A. Compton, "Chromosomes and cancer cells", *Chromosome Res*, Vol. 19, No. 3, pp. 433-444, 2011.

[10] A. Jemal, et al., "Global Cancer Statistics", *CA-Cancer J Clin*, 2011; Vol. 61, No. 2, pp. 69-90, 2011.

[11] A.J.H. Sale and W.A. Hamilton, "Effects of high electric fields on microorganisms: I. Killing of bacteria and yeasts", *BBA Gen Subjects*, Vol. 148, No. 3, pp. 781-788, 1967.

[12] W. Lawrence, "Does "Multimodal" Therapy for Cancer Really Work?", *CA-Cancer J Clin,* Vol. 35, No. 1, pp. 57-60, 1985.

[13] W. G. Payne, et al., "Wound Healing in Patients with Cancer", *Eplasty*, Vol. 8, No. e9, pp. 69-90, 2008.

[14] Y. Ni, S. Mulier, et al., "A review of the general aspects of radiofrequency ablation", *Abdom Imaging*, Vol. 30, No. 4, pp. 381-400, 2005.

[15] P. E. Huber, et al., "Trimodal Cancer Treatment: Beneficial Effects of Combined Antiangiogenesis, Radiation, and Chemotherapy", *Cancer Res*, Vol. 65, No. 9, pp. 3643-3655, 2005.

[16] J. Puchalka, et al., "Genome-Scale Reconstruction and Analysis of the Pseudomonas putida KT2440 Metabolic Network Facilitates Applications in Biotechnology", *PLoS Comput Biol*, Vol. 4, No. 10, pp. 1-18, 2008.

[17] T. Y. Tsong, "Electroporation of cell membranes", *Biophys J*, Vol. 60, No. 2, pp. 297-306, 1991.

[18] M. Hashimoto and T. Takemoto, "Electroporation enables the efficient mRNA delivery into the mouse zygotes and facilitates CRISPR/Cas9-based genome editing", *Scientific Reports*, Vol. 5, No. 11315, pp. 1-7, 2015.

[19] R. Bos and W. Nieuwenhuizen, "Enhanced Transfection of a Bacterial Plasmid into Hybridoma Cells by Electroporation: Application for the Selection of Hybrid Hybridoma (Quadroma) Cell Lines", *Hybridoma*, Vol. 11, No. 1, pp. 41-51, 1992.

[20] K. Munger, et al., "The E6 and E7 genes of the human papillomavirus type 16 together are necessary and sufficient for transformation of primary human keratinocytes", *J Virol*, Vol. 63, No. 10, pp. 4417-4421, 1989.

[21] E. P. Spugnini, et al., "Ultrastructural modifications of cell membranes induced by "electroporation" on melanoma xenografts", *Microsc Res Tech*, Vol. 70, No. 12, pp. 1041-1050, 2007.

[22] K. Smith, G.S. Mittal and M.W. Griffiths, "Pasteurization of Milk Using Pulsed Electrical Field and Antimicrobials", *J Food Sci*, Vol. 67, No. 6, pp. 2304-2308, 2002.

[23] M. Bazhal and E. Vorobiev, "Electrical treatment of apple cossettes for intensifying juice pressing", *J Sci Food Agric*, Vol. 80, No. 11, pp. 1668-1674, 2000.

[24] B. H. Lado and A. E. Yousef, "Alternative food-preservation technologies: efficacy and mechanisms", *Microbes Infect*, Vol. 4, No. 4, pp. 433-440, 2002.

CHAPTER 2
BACKGROUND

2.0 Introduction

This chapter presents background information about electroporation and radio frequency ablation in the context of this project. It is intended to inform the reader about the basics of these areas, in order to aid understanding especially with respect to experimental findings.

2.1 Electroporation

The term electroporation has been derived from the use of electric fields to produce pore-like structures in the membrane of a cell. More specifically, electroporation is a popular technique in biotechnology that makes the membrane of living cells more permeable to larger molecules, enabling dosing with drugs or genetic material in laboratory and clinical applications. Other uses include electrofusion, where two cells in contact are fused using electroporation [1], and also sterilisation and food preservation. Another term, electropermeabilisation, has also been used in the literature [2, 3], and is synonymous with the term electroporation, but the term electroporation will be used extensively in this thesis.

Electroporation has been studied now for about 40 years, although practical applications of this effect have only been utilised for the last few decades [4]. In this latter study it is reported that one of the newest clinical applications has been non-thermal irreversible electroporation (NTIRE), a very intense type of electroporation with the goal of directly ablating[1] cancerous tissue without the need for drugs.

[1] NTIRE ablation is not to be confused with radio frequency ablation, where the latter is a process that creates Joule heating as opposed to NTIRE. Radio frequency ablation is discussed later in this chapter, in section 2.2.

2.1.1 Basics of Electroporation

Cells are fundamental units of all known living organisms. Animal cells consist of a high density of organelles and a nucleus suspended in a medium called the cytoplasm, the bulk of which is contained within a surrounding membrane, the cell membrane. To maintain internal structural integrity and relative location of organelles inside the cell, it also has a cytoskeleton – a network of fibres reaching across its entire internal volume [5]. The cell membrane, in turn, is surrounded by an extracellular medium, and is generally in close proximity to other cells (within a large multicellular organism). Both the cytoplasm and extracellular medium possess relatively high electric conductivities since they are richly supplied with electrolytes. The cell membrane, illustrated in figure 2.1, however, has a conductivity of many orders of magnitude lower than surrounding media, due to the electrical properties of its primary structure of two layers of tightly packed phospholipid molecules. Other secondary components of the membrane include proteins and other molecules such as carbohydrates and cholesterols that either completely or partially penetrate it.

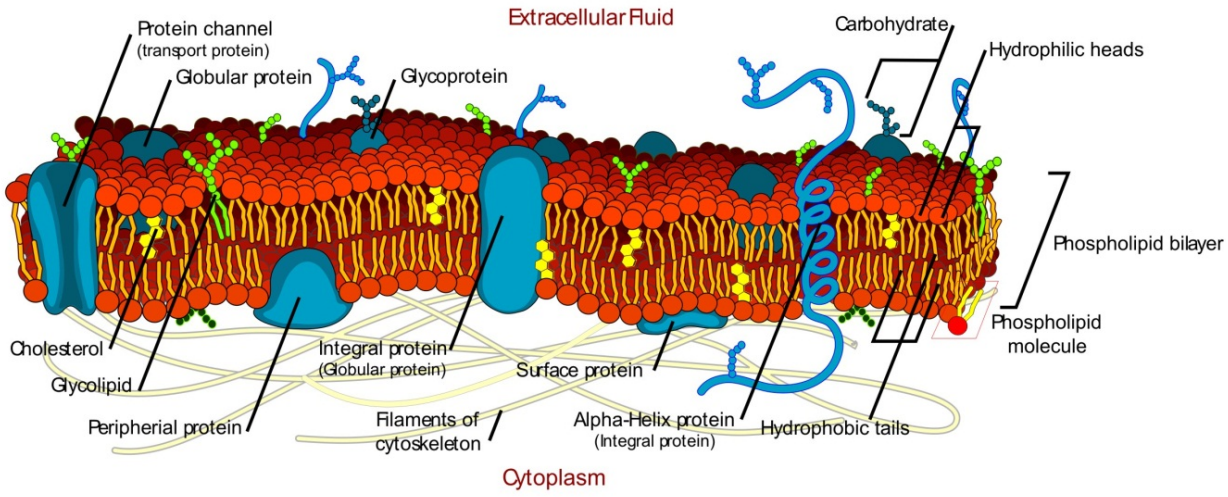

Figure 2.1. Basic structure of a typical cell membrane, comprising mainly the bilayer lipid membrane with other molecules entwined (Ruiz [6]).

For the purpose of examining the basic concepts of the biophysical phenomenon of electroporation, a (suspended) cell can be simplified to a spherical entity of salty aqueous solution surrounded by a thin closed spherical surface of insulating material suspended inside a body of salty aqueous solution. Figure 2.2 is a diagrammatic representation of such a simplified cell, with two parallel electrodes on either side of the cell.

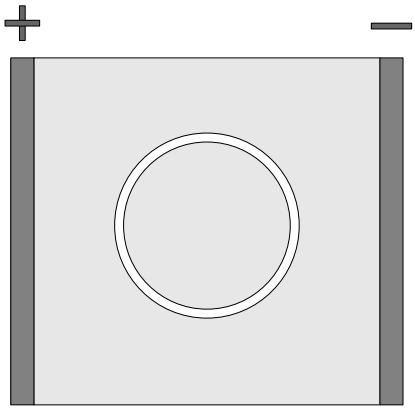

Figure 2.2. Two-dimensional electrostatic system of a highly simplified cell suspended in a conductive liquid medium (light grey), between two highly conductive electrodes (dark grey) between which the electric field is generated. The contents of the cell are also a conductive liquid. Note that this illustration is not to scale, but merely shows the basic arrangement.

When applying a static potential difference across the electrodes, the electric field can be depicted as in figure 2.3.

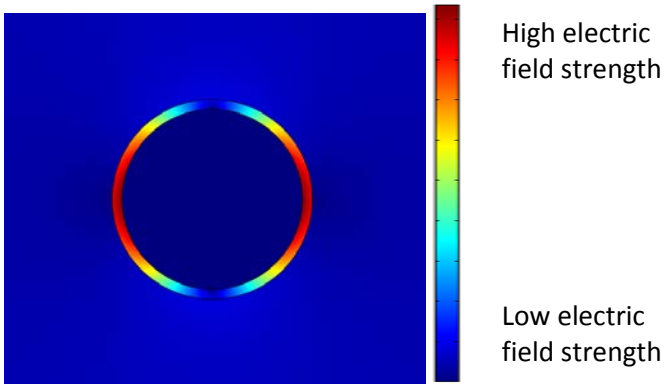

Figure 2.3. A plot of a simulated two-dimensional illustrative cell model of a similar system as shown in figure 2.2. This shows the electric field strength represented as a colour spectrum, with dark blue representing a low magnitude and dark red a high magnitude, with the remaining colours following the normal spectral sequence of colours. Proportions shown here are not to scale for a typical cell, as the membrane thickness is typically of the order 10^{-3} of the cell radius. This model is detailed further in Appendix A.

Figure 2.3 shows clearly that the electric field is intensely concentrated inside the insulating membrane, with the balance distributed over a large area with far lower values. Of further interest is that the field magnitude is highest on the poles (left and right) facing the electrodes, and near

zero on the perpendicular poles (top and bottom). This demonstrates that the electric field is spatially variable around the circumference of the cell.

For a spherical cell (modelled by a sphere with conductive interior and a concentric layer of insulation at its outer boundary) suspended within a static and homogeneous electric field, Laplace's equation yields a simple relationship (by Schwan [7]) of a transmembrane potential difference of

$$\Delta \Psi_{\mathrm{m}} = 1.5\, ER \cos\theta, \qquad (2.1)$$

with E the electrical field strength, R the radius of the cell, and θ the angle measured from the cell centre between the direction of the applied field and the point of interest on the membrane, as illustrated in figure 2.4.

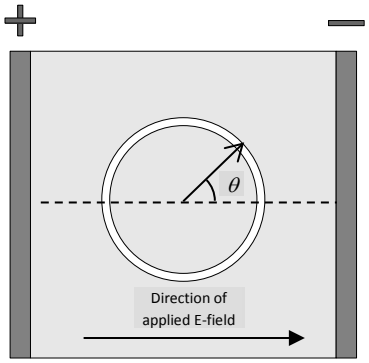

Figure 2.4. Metrics for the cell model.

Applying the relationship given by equation 2.1 shows that the potential difference across the membrane at the top and bottom (where $\theta \approx \pm 90^{\circ}$) will tend to be zero and a maximum at the poles facing the electrodes, thus follows a cosine characteristic. This is intuitive as the conductive (light-grey) areas produce a relatively insignificant voltage drop across their bulk distances, leaving the majority of voltage drop to be distributed and thus concentrated over the insulating membrane. When considering this horizontally, it produces the majority of the voltage drop across the smallest distance at the electrode facing poles. Hence the field is greatly concentrated across these regions, and diminishes as θ increases from zero to 90°, then again develops to a maximum at the opposite pole. Finally, the membrane potential difference is also proportional to the applied field, and also to the radius of the cell. The latter means that larger cells will experience a greater membrane potential difference across their electrode facing poles than smaller cells will at any particular applied electric field strength. What this also means is that for cells with different sizes within a population there will be differing electric field-induced effects on their membranes.

When applying slow changing electric fields – slow in comparison with the relaxation time constant of the membrane (detailed later in this chapter) – there are two thresholds of note. The first threshold is the onset or minimum point of electroporation, and the second is the "point-of-no-return" or maximum point of electroporation. These thresholds are popularly believed to be obtained at applied electrical field strengths of about 0.5×10^5 V/m and 1.5×10^5 V/m, respectively[2], for slowly varying applied electric fields [8]. Ideally for the process of electroporation the applied electric field strength should remain between these limits, but also only for a short period of time. Normally, this will allow the cell membranes to recover to a relatively normal level of permeability.

In the literature there are no images showing actual electropores[3]. This is probably due to the minute size expected in the nm range – to view such small dimensions requires the use of a transmission electron microscope, for which samples require special pre-treatment likely to destroy or distort the highly unstable state of the cell membrane. The only way to know that pores are formed (and close up again) is by using molecules that have an effect on the target cells only when effective electroporation has been applied. These molecules range between quick response small molecules such as fluorescent markers/dyes, or slower response macro-molecules such as DNA or proteins that will have a desired slow response effect on the target cells. These molecules or materials are normally not permeable through the membrane, and will then ultimately prove that electropores must have existed, allowing these materials through and subsequently remaining inside the cell after membrane permeability has returned to normal.

Another factor is time duration. Generally, for an equivalent electroporation effect, time duration of applied electric fields can be varied in opposition to field strength. Thus when increasing the applied field strength, the duration should be decreased, or *vice versa*. This will be discussed later in more detail.

When considering shorter pulses, the transient nature of the behaviour of cell membranes will start to play a role. Transient behaviour may initially be approximated by the following equation (also by Schwan [7]), as long as it is for a pulse longer than about 1 μs (or for a pulse frequency below 1 MHz),

---

[2] These thresholds are applicable to normal mammalian cells. For bacterial cells or other pathogens, much higher levels are required for the same effect [9].

[3] However, images are presented in a paper [10] of pores (or "craters") on the surface of red blood cells, but the accuracy of the pores have subsequently been disputed as they were considered a lot larger than normal, possibly due to Maxwell stress (tensors) causing pores to be severely enlarged by osmotic or hydrostatic pressure. A published experiment in 1999 [11] showed that pores were typically substantially smaller. This dispute is supported by [12].

$$\Delta \Psi_m = 1.5\, ER\, (\cos\theta)(1 - e^{-t/\tau}), \quad (2.2)$$

where $\Delta \Psi_m$ is the transmembrane potential, E is the field strength, R is the cell radius, and τ is the time constant of the membrane. This is similar to the previous relationship but with a natural decay.

The membrane time constant is the product of its equivalent resistance and capacitance, representing a delay from application of an electric field to the final potential difference developed across the membrane. For time variant electric fields the time constant is also dependent on other factors including the conductivities of the material inside and outside the cell. The membrane time constant can be described by the relationship [13]

$$\tau = RC\,(1/\sigma_i + 1/2\sigma_o), \quad (2.3)$$

where C is membrane capacitance (in the order of 10^{-2} F/m^2), σ_i is the material conductivity inside the cell and σ_o is the conductivity outside the cell. This means the time constant is very dependent on the external medium conductivity, especially when the conductivity is lowered as for biotechnology applications, resulting in an increased time constant. For instance, τ is scaled by a factor of 5 when using conductivities of 0.3 S/m for both inside and outside the cell (0.3 S/m is based on a modelling study by [14]). That is, $\tau = 5RC$. The membrane time constant is increased with a scaling factor of 7.2 when reducing the external medium conductivity to 0.13 S/m, representing an increase of 44 % in τ. This relationship can be further refined to include the effect of cell membrane thickness and also the conductivity of the membrane, although the latter factor is usually quite constant [15],

$$\tau = RC / \{[\, 2\sigma_i\, \sigma_e / (\sigma_i + 2\sigma_e)] + [R\, \sigma_m / h]\}, \quad (2.4)$$

where σ_m is the membrane conductivity and h is the membrane thickness.

Membrane or pore dynamics are much more complex. The above simplifications assume static or passive conditions and ignore the non-linear behaviour of a membrane once pores start developing. The lipids making up the bilayer membrane have viscoelastic properties which rapidly change in time with an applied electric field pulse [16]. Also, once a pore is created and develops, the conductivity in its vicinity tends to increase causing a form of “regulation” of the transmembrane potential [17]. A study [18] modelled molecular dynamics of an artificial bilayer membrane with added peptide channels. It found that in the presence of an electric field, protrusions of water molecules appeared to rapidly form and penetrate the membrane from both sides and to join up to form irregular water channels, followed by a rapid rearrangement of the

lipid molecules to form channels surrounded by lipid polar heads. It also demonstrated how pores were less likely to form in the close proximity of the peptide channels. This modelling has been considered quite appropriate and useful for better understanding of the dynamics and it was suggested that more molecular dynamic modelling be performed [15]. Two very recent molecular dynamic modelling studies have demonstrated that a) water bridges are formed in bilayer phospholipid membranes in nanoseconds, and that external electric fields enhance this process [19] and b) that low intensity millisecond pulses compared to high intensity nanosecond pulses produced different hydrophilic pore morphologies, and also that addition of cholesterol molecules raised the threshold potential for electroporation [20].

Cells of different shapes (morphologies) than purely spherical experience differences from the relationships mentioned. Typical morphologies include cylindrical (for skeletal muscle), flat hexagonal (for endothelia), prolate spheroids and also more irregular shapes as is more typical for tumour cells. Modelling these, especially irregular shaped cells, is a challenge. Modelling and actual cell electroporation was performed on Chinese hamster ovary (CHO) cells [21], yielding an interesting result – any protrusions facing electrodes are more likely to amplify the electroporation effect within these protrusions with pronounced transmembrane potentials. This is also consistent with the equations where the potential difference is amplified at the poles and also for larger radii.

When considering cells in close proximity, or when more densely packed such as in tissue, or in tumours, the factors influencing electroporation become more complicated and need to be investigated further [22]. This is complicated further by several factors, including a population of different cell types, different cell sizes, cells at different stages of development (e.g. some cells dividing, and some not), difference in concentrations of gases, nutrients and waste products (depending on the level of vascularisation of capillaries in the area) and presence of gap junctions (highly specialised protein channels interconnecting cells). Appendix A shows a further illustrative example of simple 2-dimensional modelling of multiple cells in close proximity. The distortion of the electric field distribution in and around cells, statically and for a time variant applied field, is shown. This modelling helps to visualise and understand how complex electric field distributions are in and around cells, even for very simplified and approximate models.

2.1.2 Application of a Very Intense Electric Field

A more severe type of electroporation, known as irreversible electroporation (IRE), has also been studied and published [23-25]. This involves using electrical field pulses in excess of 1.5×10^5 V/m applied for a relatively long time of up to 10 seconds and using multiple pulses of around 100 μs.

The purpose here is to deliberately and directly kill the cells, such as tumour cells or pathogens. A prominent study [23] on an animal model demonstrated that IRE had several advantages over thermal ablation, including killing tumour cells via apoptosis and causing minimal or no damage to peri-ablative structures like vessels and ducts.

Another type of electroporation is where ultra-short, ultra-high intensity electrical field pulses [26-28] are used. These invariably include pulses of duration less than or equal to 300 ns, but also extreme fields up to 300 x 10^5 V/m [29]. The latter study has indicated that membranes of subcellular structures are affected rather than the cytoplasmic membrane. This is likely the result of better penetration of higher frequency signals that couple directly into deeper structures such as organelles and the nucleus [30]. The first mentioned study [26] has shown that effects include cell death via apoptosis and generally cause tumour inhibition.

2.1.3 Influencing Factors

Factors that affect electroporation can be categorised as internal and external. Internal factors may include variables such as temperature, medium composition such as conductivity and pH, cytosol composition, cell proximity, inter-cell communication such as gap-junctions, cell size and shape (morphology), cell inhomogeneity (different cell types together) [31], and membrane resting potential. External factors include applied electric field strength, time spent above the minimum threshold for inducing electroporation, field pulse waveforms and time variable electric field strengths, orientation with respect to the prevailing field, field distribution as would be produced by the electrodes, and the tissue/cells arrangement surrounding the target tissue [31].

Resting cell potential follows on from the Nernst equation that relates an electrical gradient (potential difference) to a maintained ion concentration gradient (difference) between the potassium, sodium and chloride ion concentrations across a selectively permeable cell membrane at rest [32]. A living cell at rest typically exhibits a transmembrane potential of -70 mV measured from the inside with respect to the outside of the cell. This will favour the side facing the positive electrode, as it enhances the potential by that amount. The opposite is true for the membrane facing the negative electrode – effectively reducing that potential by 70 mV.

2.1.4 Applications

Current applications of electroporation include the areas of clinical therapy [33], biotechnology [34] and food technology [35].

One major clinical therapy application is electrochemotherapy (ECT), where cancerous tumours are preloaded with chemotherapeutic agents then bulk electroporated to enhance cell penetration

mainly for superficial cancers such as melanoma, basal cell carcinoma and deep skin sarcoma [36]. Another interesting study [37] investigated applying ECT to cancer stem cells as a new potential technique in cancer therapy. ECT has become a well-used and very successful strategy offered in more than 130 cancer centres in Europe [4]. ECT is also used in immunotherapy applications [38]. Another clinical therapy application is gene therapy where tissue or suspensions of cells are externally loaded with DNA and electroporation is used instead of viral vectors [27, 28, 39]. Recently, a new technique known as "genome editing", has been achieved successfully on mouse zygotes [40], using electroporation as the vector. Other noteworthy clinical applications for electroporation are transdermal drug delivery [4], and electroporation for wound healing [38].

Biotechnology applications include cell fusion (electrofusion) where two cells are brought into contact with each other and electroporated, which then initiates a process whereby the membranes merge, forming a single cell. Electrofusion is used to produce cloned microorganisms [41], immortalised cell lines, and genetically modified organisms [42]. Other applications include treatment of microorganisms to produce desirable chemicals or to eliminate harmful waste [43].

Food technology applications include disinfection of fluids like water [44] or milk (pasteurisation) for human or animal consumption [45], of fruit for juice extraction [46], and disinfection of fresh produce for export and increased shelf life [47].

2.1.5 Evolution

A favourably cited paper [48] has been published on the possibility of electroporation from lightning as being a driver of early rapid evolution of simple organisms. This concept, which may account for accelerating early evolution of animals and plants, is a worthy hypothesis for further reading and study.

2.1.6 Studies Related to the Aims of this Thesis

Studies indicate that electroporation may be more effective by using applied electric pulses that contain higher frequency elements (that is, short pulses). Studies also suggest use of bipolar (alternating or fluctuating around zero) electric fields over monopolar fields (typically rectangular and not fluctuating around zero). These studies [2, 49-55] cover the two themes that were of greatest interest to this thesis project and have been pursued at the experimental stage, and are reported on in chapter 4. All these prior studies considered a single spherical cell in suspension.

An early study [2] demonstrated that cell membranes were exclusively electroporated symmetrically when using bipolar AC pulses, compared to monopolar DC or monopolar AC pulses.

However, a limitation of this study is the limited electric field strength that was used at the high frequency of 1 MHz. Another early study [49] applied a DC shifted radio frequency electric field at 40 kHz, compared to normal DC pulses, and found evidence that the bipolar AC pulses produced better gene transfection results than monopolar DC pulses and also was less selective for a variety of cell sizes. Limitations of this study are the use of 40 kHz, being low frequency in comparison with the study in this thesis, and the net electric field was of single polarity, considering it was DC shifted AC sinusoidal pulses. The square wave nature of the study in this thesis is quite different.

Another study [50] compared cells being exposed to monopolar against symmetrical bipolar electrical field pulses and found that a) a symmetrical bipolar (similar shaped pulses alternating either side of zero) 1 kHz electric field amplitude of 20 % less was required to produce the same electroporation effect than for monopolar fields, b) more than 20 % increased uptake of introduced molecules resulted from using the bipolar over the same amplitude monopolar fields, and c) there was a theoretical link between the use of bipolar (AC) symmetrical field pulses and a symmetry in poration areas over a non-symmetry, with respect to the 2 poles facing the applied electrodes, when using monopolar (DC) field pulses. A second study from the same group [51] compared contamination of metal ions liberated from the electrodes between using bipolar over monopolar electric fields and found that there was an order of magnitude less contamination for bipolar over monopolar fields. They also reported that the aluminium ions (from the aluminium electrodes) were much less toxic than the iron ions from the stainless steel electrodes. These two studies utilised electric field pulses that were limited in frequency to a maximum of 1 kHz and also only used either monopolar or simple positive-negative pulses (not alternating more than once), per burst.

A further study [52] performed analytical modelling comparing dynamic transmembrane potential and pore density for various electrical field pulses. They found that short monopolar pulses produced an asymmetrical pore density while bipolar pulses produced a symmetrical pore density, and also that bipolar pulses did not produce a higher electroporation yield than monopolar pulses at the same pulse amplitudes. The latter finding has been attributed to the membrane time constant during transitions causing shorter total periods of the membrane being over the threshold needed for electroporation. A second study by the same group [53] investigated electroporation efficiency by varying the electrical field intensity and extracellular conductivity, with an emphasis on normalisation of effect on cells of different radii. The term normalisation, used in this context, refers to the partial equalisation of electroporation effect on smaller cell radii, which are naturally not affected as much as their larger counterparts. They found that: a) good normalisation occurred at over 100 kHz when the external medium

conductivity was 0.05 S/m and at over 1 MHz when the external conductivity was 0.2 S/m, both of which are lower than physiological conductivities, as may be used in biotechnology applications, and b) a sinusoidal bipolar field produced better normalisation than a square wave bipolar pulse field, although the sinusoidal field was less efficient at the same peak levels. A third study by the same general group [54, 55] compared sinusoidal fields of 100 kHz and 1 MHz (and DC) pulses and found that the higher frequency produced a better normalisation of poration effect across different cell radii, and also that bipolar pulses performed better in this aspect than monopolar pulses. They suggested a need for further experimental investigation to validate this theory.

The resting potential of a cell is a clear influencing factor for creating non-symmetrical electroporation behaviour of the membrane when exposing it to a monopolar field [2]. It is unclear whether a greater net permeabilisation effect occurs when a monopolar electric field is applied for the same duration and of the same magnitude (presuming low frequency pulsing), but what is known is that a bipolar field creates a population of nano-pores that have a smaller variation in size, as reported in a theoretical study [55]. This is likely the result of the disparity in transmembrane potentials for monopolar fields, effectively generating two types of sub-population – one with larger pores on the side facing the negative electrode and one with smaller pores on the side facing the positive electrode; also these larger pores are less likely to exist with bipolar fields, as shown in the latter study.

A review [56] has identified a relatively unexplored region of electroporation pulse duration publications in the region of 1 μs to 100 μs, with the hypothesis that intracellular membrane intervention effects are likely and may cause the desirable effect of cellular apoptosis.

In summary, bipolar fields (over monopolar fields) and higher frequencies warrant further study as they have been shown in modelling and limited physical experiments to produce better all-round electroporation with more symmetrical electroporation, improved normalisation between different cell sizes, and less metal ion contamination from the electrodes due to electrolysis.

2.1.7 Measuring Electroporation

There are several methods (assays) to measure the effect or degree of electroporation on cells, including the degree of electroporation that has been achieved for individual cells or the percentage of cells affected. These include assays such as fluorescence-type measurements, electrical measurements, DNA expression of proteins, and ELISAs (see references below).

Fluorescence assays typically include fluorescence microscopy, and flow cytometry [57]. These assays offer a method for showing ingress into a cell of molecules of fluorescent dye, which can be easily and rapidly detected using optics and electronics technologies. Fluorescence microscopy allows the study of optical imaging and thus morphological analysis on individual cells, while flow cytometry allows the study of finely resolved ingress of fluorescence dye on a large population of cells, with data generated for each cell or particle. For these convenient reasons fluorescence assays were chosen in this study.

Electrical measurement assaying of electroporated tissues is a useful method for determining bulk electroporation, since the conductivity of the tissue responds rapidly to electroporation treatment, by increasing substantially [58]. This method is useful in clinical practice as a form of feedback to the clinician as it reflects the outcome and is easy to measure.

When transfecting cells with DNA fragments to modify them genetically, transfection can be performed using a viral vector or electroporation. The success of the method can be determined by detecting the presence and measuring concentration of specific proteins expressed by the new DNA [59].

The enzyme-linked immunosorbent assay (ELISA) can be used together with electroporation to immunise organisms against dangerous virus infections such as avian influenza [60]. This assay measures the presence of antibodies by an indicator colour change of the liquid medium and the quantity of antibody is assessed by the density of this colour change compared with a positive and a negative sample [61].

2.2 Radio frequency ablation

The term radio frequency ablation derives its name from two concepts, radio frequency, and ablation. It literally means using radio frequency energy to take away or erode material. A definition [62] is:

"A minimally invasive treatment called radiofrequency ablation (RFA), one of several types of ablation therapy, may be an alternative when surgery for certain types of cancer is not a good option. Guided by imaging techniques, the doctor inserts a thin needle through the skin and into the tumor. High-frequency electrical energy delivered through this needle heats and destroys the tumor. Months after the procedure, dead cells turn into a harmless scar."

Figure 2.5 shows a typical application of RFA applied to the liver.

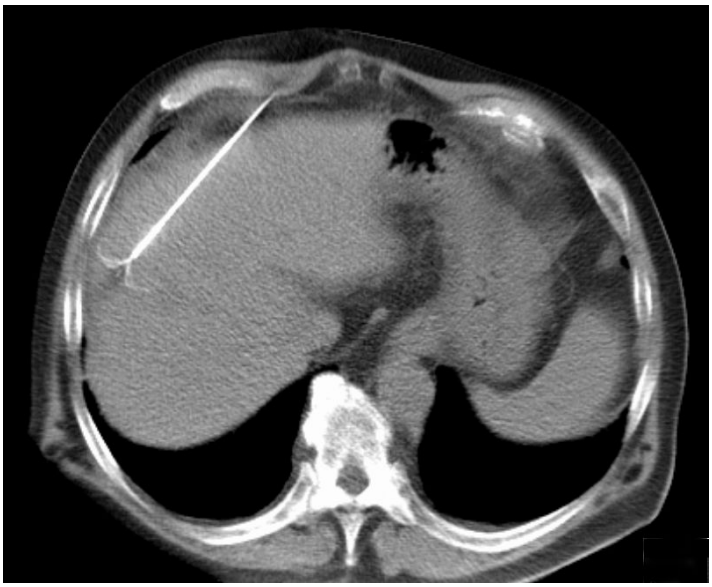

Figure 2.5. A computed tomography (CT) scan image showing a patient cross section through the liver during an RFA procedure of a liver lesion. Note the white electrode inserted into the liver of the patient. Its lower tip has several tines to increase the ablation volume (Hellerhoff [63]).

Radio frequency ablation (RFA) is a form of surgical energy deposition used for destroying undesirable tissue such as a tumour, somewhat like cauterisation but not for the primary purpose of sealing off bleeding arteries or veins. It is a form of Joule heating that relies on the electrical resistance of tissue between two electrodes, to which an alternating electrical potential is applied for a relatively long time in the order of minutes. Where the current density is sufficient, Joule heating will denature the proteins. Mammalian cells start dying at temperatures above about 45 ^{0}C, and even hyperthermia (slightly raised body temperature below about 43 ^{0}C) renders

cancer cells more sensitive to thermal cytotoxicity [64] and also to radiation treatment and to certain drugs [65]. Successful tumour ablation occurs at a temperature above approximately 60 ^{0}C [66]. A later study [67] performed by the latter group reported that a temperature above 110 ^{0}C is undesirable as it reduces coagulation necrosis due to cavitation and charring. The general aim is thus to achieve heating of tissue to lie between 60 ^{0}C and 100 ^{0}C, or just below 100 ^{0}C to avoid formation of steam that may cause damage to other tissue and structures in the vicinity. The active electrode can reach a higher temperature, but modern electrodes employ water cooling systems to restrict electrode temperature.

RFA is regarded as minimally invasive as it only needs insertion of a single needle electrode into the target area, and no tissue removal is necessary [68]. The return electrode is often a large area metal pad placed under the buttocks, or two thigh pads [69]. This would be classified as a "monopolar"[4] electrode system in a clinical context. "Bipolar" electrodes are also used (a pair of electrodes spaced reasonably close together).

Joule heating occurs where the current density is of sufficient magnitude to cause heating above 60 ^{0}C, which will be directly around a monopolar electrode and radiate around it. Design of the active electrode is quite critical to guarantee sufficient current density around it, balancing this with the available applied voltage and the typical tissue resistance as a load. Blood perfusion in the surrounding tissues must be taken into consideration as it may restrict heating, as it will carry heat away in the blood. Also, relative water content in the tissue must be considered, as this directly affects the relative resistance of the tissue.

Radio frequency energy can be readily generated with standard electronics technology, especially in the medium-wave band of 300 kHz to 3 MHz. A purely symmetrical alternating current sinusoidal waveform is used. Generating a fixed single frequency is easy as it requires a simple inductive-capacitive (LC) resonant circuit. As there is no mention in the literature why 450 kHz to 460 kHz is typically used in RFA technology, it is likely that it is used since 455 kHz is commonly employed as an intermediate frequency (IF) for frequency modulation (FM) and amplitude modulation (AM) systems in radio communication systems. There are benefits in using different frequencies over a fixed frequency. Higher frequency pulses may cause more evenly distributed heating for various tissue types, based on electroporation modelling (see section 2.1.6 above), and

[4] The terms monopolar and bipolar have different meanings in medicine and in electrical engineering. In medical terms a monopolar electrode means a single electrode at the target site, while in electrical engineering the terms monopolar or bipolar are normally associated with polarity of a potential or a current – here, monopolar means an average DC value, and bipolar means that the physical quantity alternates between positive and negative values.

lower frequencies could improve ablation volume of cancerous liver tissue for a given power due to a higher conductivity than healthy liver tissue [70].

RFA is very successfully used mainly for treatment of primary or metastatic tumours located within the liver and also for the kidney and the lung [68]. It also is used in cardiac surgery to ablate faulty cardiac tissue that causes atrial fibrillation [71].

2.3 Conclusion

Electroporation has been defined and described. Literature has been cited that develops and supports considerations regarding the basics and major factors that have an effect on this non-thermal and indirect technique of destroying undesirable tumorous tissue.

The key to electroporation is the electric potential induced across the outer cell membrane. It is widely accepted as a threshold effect, occurring reversibly between a lower and upper limit of transmembrane potentials within a limited applied electric field time range. These potentials are expressed in Schwan's equation where it is proportional to overall cell dimension, angle, and other factors, for static and quasi-static situations. Dynamic situations have been discussed briefly.

The use of overly intense electric field pulses which kill cells directly without the use of heating have recently become a new option in electroporation, including IRE and ultra-short, ultra-high intensity electric field pulses. The former has been reported to be selective to tumour tissue, while the latter causes cell apoptosis. However, this thesis has focused on normal electroporation, limited to electric field pulses below 4×10^5 V/m and above 0.5×10^5 V/m.

Electroporation can be detected or measured readily using fluorescence microscopy and flow cytometry, and have been pursued as the main methods for determining electroporation effect in this thesis. Other methods also exist such as electric impedance measurement, protein expression and ELISA.

Applications in electroporation include oncologic and cardiac therapy, biotechnology and food technology.

Electroporation studies related to the aims of this thesis have been discussed. Bipolar electric fields (over monopolar fields) and higher frequencies warrant further study as they have been shown in modelling and limited physical experiments to produce better all-round electroporation with more symmetrical electroporation, improved normalisation between different cell sizes, and less metal ion contamination from the electrodes due to electrolysis.

Radio frequency ablation has been defined and a brief outline has been provided on this mainly oncologic therapeutic technique. Essentially it exploits the phenomenon of Joule heating where the patient is part of the instrument, in order to achieve severe denaturation of the undesirable (tumorous) tissue to destroy it. It is primarily used for ablating tumours in the liver, kidney and lung, but also for ablating faulty cardiac tissue, in a less invasive fashion than in reductive surgery.

2.4 References

[1] M. K. Kanduser and D. Miklavcic, "Electroporation in Biological Cell and Tissue: An Overview", in *Electrotechnologies for Extraction from Food Plants and Biomaterials*, Food Engineering Series, E. Vorobiev, N. Lebovka, Eds., Springer, pp. 1-37, 2008.

[2] E. Tekle, R. D. Astumian and P. B. Chock, "Electro-permeabilization of cell membranes: effect of the resting membrane potential", *Biochem Bioph Res Co*, Vol. 172, No. 1, pp. 282-287, 1990.

[3] J. Teissié, et al., "Electropermeabilization of cell membranes", *Adv Drug Deliver Rev*, Vol. 35, No. 1, pp. 3-19, 1999.

[4] M. L. Yarmush, et al., "Electroporation-based technologies for medicine: principles, applications, and challenges", *Annu Rev Biomed Eng*, Vol. 16, pp. 295-320, 2014.

[5] N. A. Campbell, et al., *Biology*, 8th ed., Chapter 6, The Cell, San Francisco, CA, Pearson Benjamin Cummings, 2008, pp. 94-141.

[6] M. Ruiz, *Cell Membrane Image*, [Online]. Available: https://upload.wikimedia.org/wikipedia/commons/d/da/Cell_membrane_detailed_diagram_en.svg

[7] H. P. Schwan, "Electrical properties of tissue and cell suspensions", *Adv Biol Med Phys*, Vol. 5, pp. 147-209, 1957.

[8] J. Gehl, et al., "In vivo electroporation of skeletal muscle: threshold, efficacy and relation to electric field distribution", *BBA Gen Subjects*, Vol. 1428, pp. 233-240, 1999.

[9] J. F. Miller, W. J. Dower and L. S. Tompkins, "High-voltage electroporation of bacteria: genetic transformation of Campylobacter jejuni with plasmid DNA", *P Natl Acad Sci USA*, Vol. 85, No. 3, pp. 856–860, 1988.

[10] D. C. Chang, T. S. Reese, “Changes in membrane structure induced by electroporation as revealed by rapid-freezing electron microscopy”, *Biophys J*, Vol. 58, pp. 1-12, 1990.

[11] E. Neumann, S. Kakorin and K. Toensing, “Fundamentals of electroporative delivery of drugs and genes”, *Bioelectrochem Bioenerg*, Vol. 48, No. 1, pp. 3-16, 1999.

[12] Z. Fei, “Membrane Sandwich Electroporation for In Vitro Gene Delivery”, PhD dissertation, Ohio State University, 2009.

[13] C. Grosse and H. P. Schwan, “Cellular membrane potentials induced by alternating fields”, *Biophys J*, Vol. 63, No. 6, pp. 1632-1642, 1992.

[14] T. Kotnik, D. Miklavcic and T. Slivnik, “Time course of transmembrane voltage induced by time-varying electric fields: a method for theoretical analysis and its application”, *Bioelectroch Bioener*, Vol. 45, No. 1, pp. 3-16, 1998.

[15] C. Chen, et al., “Membrane electroporation theories: a review”, *Med Biol Eng Comput,* Vol. 44, No. 1-2, pp. 5–14, 2006.

[16] W. Sung and P. J. Park, “Dynamics of Pore Growth in Membranes and Membrane Stability”, *Biophys J*, Vol. 73, No. 4, pp. 1797-1804, 1997.

[17] J. C. Weaver, “Electroporation of biological membranes from multicellular to nano scales”, *IEEE T Dielect El In*, Volume 10, Issue 5, pp. 754 – 768, 2003.

[18] M. Tarek, “Membrane electroporation: a molecular dynamics simulation”, *Biophys J*, Vol. 86, No. 6, pp. 4045-4053, 2005.

[19] P. T. Vernier, Z. A. Levine and M. A. Gundersen, “Water Bridges in Electropermeabilized Phospholipid Bilayers”, *P IEEE*, Vol. 101, No. 2, pp. 494-504, 2013.

[20] M. Casciola, et al., “A molecular dynamic study of cholesterol rich lipid membranes: comparison of electroporation protocols”, *Bioelectroch*, Vol. 100, pp. 11-17, 2014.

[21] T. Kotnik, G. Pucihar and D. Miklavcic, “The Cell in the Electric Field”, Chapter 3 in *Clinical aspects of electroporation*, S. T. Kee, J. Gehl and E. Lee, Eds, Springer, 2011, pp. 19-29.

[22] T. R. Gowrishankar and J. C. Weaver, “An approach to electrical modeling of single and multiple cells”, *P Natl Acad Sci USA*, Vol. 100, No. 6, pp. 3203-3208, 2002.

[23] E. W. Lee, et al., “Advanced Hepatic Ablation Technique for Creating Complete Cell Death: Irreversible Electroporation”, *Radiology*, Vol. 255, No. 2, p. 426-433, 2010.

[24] E. Maor, et al., "The Effect of Irreversible Electroporation on Blood Vessels", *Technology in Cancer Research and Treatment*, Vol. 6, No. 4, pp. 307-312, 2007.

[25] B. Al-Sakere, et al., "A Study of the Immunological Response to Tumor Ablation with Irreversible Electroporation", *Technology in Cancer Research and Treatment*, Vol. 6, No. 4, pp. 301-305, 2007.

[26] S. J. Beebe, et al., "Nanosecond pulsed electric field (nsPEF) effects on cells and tissues: apoptosis induction and tumor growth inhibition", *IEEE T Plasma Sci*, Vol. 30, No. 1, p 286-292, 2002.

[27] R. Sundararajan, "Nanoelectroporation: a first look". *Methods Mol Biol*, Vol. 423, pp. 109-28, 2008.

[28] R. Sundararajan, "Nanosecond electroporation: another look", *Mol Biotechnol*, Vol. 41, No. 1, pp. 69-82, 2009.

[29] N. Chen, et al., "Nanosecond electric pulses penetrate the nucleus and enhance speckle formation", *Biochem Bioph Res Co*, Vol. 364, No. 2, pp. 220-225, 2007.

[30] W. Frey, et al., "Plasma Membrane Voltage Changes during Nanosecond Pulsed Electric Field Exposure", *Biophys J*, Vol. 90, No. 10, pp. 3608-3615, 2006.

[31] S. Y. Ho and G. S. Mittal, "Electroporation of Cell Membranes: A Review", *Crit Rev Biotechnol*, Vol. 16, No. 4, pp. 349-362, 1996.

[32] D. Junge, *Nerve and Muscle Excitation*, 3rd Ed., Sinauer Associates, Sunderland, MA, 1992.

[33] Electroporation-Based Therapies for Cancer: From Basic to Clinical Applications, R. Sundararajan, Ed., Woodhead Publishing Series in Biomedicine, Number 49, Elsevier, 2014.

[34] T. Kotnik, et al., "Electroporation-based applications in biotechnology", *Trends Biotechnol*, Vol. 33, No. 8, pp. 480-488, 2015.

[35] S. Mahnic-Kalamiza, E. Vorobiev and D. Miklavcic, "Electroporation in food processing and biorefinery", J Membrane Biol, Vol. 247, No. 12, pp. 1279-1304, 2014.

[36] C. R. Rossi and L. G. Campana, "Clinical Electrochemotherapy: The Italian Experience", in Chapter 20 from *Advanced Electroporation Techniques in Biology and Medicine*, Biological

Effects of Electromagnetics Series, A. G. Pakhomov, D. Miklavcic and M. S. Markov, Eds., CRC Press, Taylor & Francis Group, Boca Raton, 2010.

[37] K. Sankaranarayanan, et al., "Effective electro-chemo-therapy for proliferation control of adult human mesenchymal stem cells", *J Electrostat*, Vol. 69, No. 4, pp. 267-274, 2011.

[38] J. Gehl, "Electrochemotherapy as Part of an Immunotherapy Strategy in the Treatment of Cancer", in Chapter 22 from *Advanced Electroporation Techniques in Biology and Medicine*, Biological Effects of Electromagnetics Series, A. G. Pakhomov, D. Miklavcic and M. S. Markov, Eds., CRC Press, Taylor & Francis Group, Boca Raton, 2010.

[39] J. Escoffre, et al., "Gene Electrotransfer: From Basic Processes to Preclinical Applications", in Chapter 14 from *Advanced Electroporation Techniques in Biology and Medicine*, Biological Effects of Electromagnetics Series, A. G. Pakhomov, D. Miklavcic and M. S. Markov, Eds., CRC Press, Taylor & Francis Group, Boca Raton, 2010.

[40] M. Hashimoto, and T. Takemoto, "Electroporation enables the efficient mRNA delivery into the mouse zygotes and facilitates CRISPR/Cas9-based genome editing", *Scientific Reports*, Vol. 5, No. 11315, pp. 1-7, 2015.

[41] T. Y. Tsong, "Electroporation of cell membranes", *Biophys J*, Vol. 60, No. 2, pp. 297-306, 1991.

[42] K. Munger, et al., "The E6 and E7 genes of the human papillomavirus type 16 together are necessary and sufficient for transformation of primary human keratinocytes", *J Virol*, Vol. 63, No. 10, pp. 4417-4421, 1989.

[43] J. Puchalka, et al., "Genome-Scale Reconstruction and Analysis of the Pseudomonas putida KT2440 Metabolic Network Facilitates Applications in Biotechnology", *PLoS Comput Biol*, Vol. 4, No. 10, pp. 1-18, 2008.

[44] M. A. Malik, A. Ghaffar and S. A. Malik, "Water purification by electrical discharges", *Plasma Sources Sci Technol*, Vol. 10, No. 1, pp. 82-91, 2001.

[45] K. Smith, G.S. Mittal and M.W. Griffiths, "Pasteurization of Milk Using Pulsed Electrical Field and Antimicrobials", *J Food Sci*, Vol. 67, No. 6, pp. 2304-2308, 2002.

[46] M. Bazhal and E. Vorobiev, "Electrical treatment of apple cossettes for intensifying juice pressing", *J Sci Food Agric*, Vol. 80, No. 11, pp. 1668-1674, 2000.

[47] B. H. Lado and A. E. Yousef, "Alternative food-preservation technologies: efficacy and mechanisms", *Microbes Infect*, Vol. 4, No. 4, pp. 433–440, 2002.

[48] T. Kotnik, "Lightning-triggered electroporation and electrofusion as possible contributors to natural horizontal gene transfer", *Physics of Life Reviews*, Vol. 10, No. 3, pp. 351-370, 2013.

[49] D. C. Chang, P. Gao and B. L. Maxwell, "High efficiency gene transfection by electroporation using a radio-frequency electric field", *BBA-Mol Cell Res*, Vol. 1092, No. 2, pp. 153-160, 1991.

[50] T. Kotnik, et al., "Cell membrane electropermeabilization by symmetrical bipolar rectangular pulses: Part I. Increased efficiency of permeabilisation", *Bioelectroch*, Vol. 54, No. 1, pp. 83-90, 2001.

[51] T. Kotnik, D. Miklavcic and L. M. Mir, "Cell membrane electropermeabilization by symmetrical bipolar rectangular pulses: Part II. Reduced electrolytic contamination", *Bioelectroch*, Vol. 54, No. 1, pp. 91-95, 2001.

[52] S. Talele and P. Gaynor, "Non-linear time domain model of electropermeabilization: Response of a single cell to an arbitrary applied electric field", *J Electrostat*, Vol. 65, No. 12, pp. 775-784, 2007.

[53] S. Talele and P. Gaynor, "Non-linear time domain model of electropermeabilization: Effect of extracellular conductivity and applied electric field parameters", *J Electrostat*, Vol. 66, No. 5-6, pp. 328-334, 2008.

[54] S. Talele, et al., "Modelling single cell electroporation with bipolar pulse parameters and dynamic pore radii", *J Electrostat*, Vol. 68, No. 3, pp. 261-274, 2010.

[55] Talele, et al., "Modelling Single Cell Electroporation with Bipolar Pulse: Simulating Dependance of Electroporated Fractional Pore Area on the Bipolar Field Frequency", *Technological Developments in Education and Automation*, pp. 355-359, 2010.

[56] J. C. Weaver, et al., "A brief overview of electroporation pulse strength-duration space: A region where additional intracellular effects are expected", *Bioelectroch*, Vol. 87, pp. 236-243, 2012.

[57] P. J. Canatella, et al., "Quantitative Study of Electroporation-Mediated Molecular Uptake and Cell Viability", *Bioph J*, Vol. 80, No. 2, pp. 755-764, 2001.

[58] A. Ivorra, et al., "In vivo electrical conductivity measurements during and after tumor electroporation: conductivity changes reflect the treatment outcome", *Phys Med Biol*, Vol. 54, No. 19, pp. 5949-5963, 2009.

[59] H. Potter and R. Heller, "Transfection by Electroporation", *Current Protocols in Molecular Biology*, pp. 9.3: 9.3.1–9.3.6, 2003.

[60] O. Ogunremi, et al., "A single electroporation delivery of a DNA vaccine containing the hemagglutinin gene of Asian H5N1 avian influenza virus generated a protective antibody response in chickens against a North American virus strain", *Clin Vaccine Immunol*, Vol. 20, No. 4, pp. 491-500, 2013.

[61] S. D. Gan and K. R. Patel, "Enzyme Immunoassay and Enzyme-Linked Immunosorbent Assay", *J Invest Dermatol*, Vol. 133, pp. 1-3, 2013.

[62] Mayo Clinic, Definition of "Radiofrequency ablation for cancer", [Online]. Available: http://www.mayoclinic.org/tests-procedures/radiofrequency-ablation/basics/definition/prc-20013951

[63] Karin Hellerhoff, *CT scan of liver during RFA procedure*, [Online]. Available: http://commons.wikimedia.org/wiki/File:RFA_CT_Leber_001.jpg#mediaviewer/File:RFA_CT_Leber_001.jpg

[64] K. J. Henle and L. A. Dethlefsen, "Time-temperature relationships for heat-induced killing of mammalian cells", *Annals of the New York Academy of Sciences*, Vol. 335, No. 1, pp. 234-253, 1980.

[65] U.S. National Cancer Institute, *Definition of "hyperthermia therapy"*, NCI Dictionary of Cancer Terms, [Online]. Available: http://www.cancer.gov/dictionary?CdrID=46263

[66] G. S. Gazelle, et al., "Tumor ablation with radio-frequency energy", *Radiology*, Vol. 217, No. 3, pp. 633-646, 2000.

[67] D. Haemmerich, et al., "Hepatic radiofrequency ablation with internally cooled probes: effect of coolant temperature on lesion size". *IEEE Trans Biomed Eng*, Vol. 50, No. 4, pp. 493-500, 2003.

[68] S. Tatli S, et al., "Radiofrequency ablation: technique and clinical applications", *Diagn Interv Radiol*, Vol. 18, No. 5, pp. 508-516, 2012.

[69] S. A. Curley SA, “Radiofrequency Ablation of Malignant Liver Tumors”, *Annals of Surgical Oncology*, Vol. 10, No.4, pp. 338-347, 2003.

[70] D. Haemmerich and B. J. Wood, “Hepatic radiofrequency ablation at low frequencies preferentially heats tumour tissue”, *Int J Hyperthermia*, Vol. 22, No. 7, pp. 563-574, 2006.

[71] P. Jais, et al., “A Focal Source of Atrial Fibrillation Treated by Discrete Radiofrequency Ablation”, *Circulation*, Vol. 95, No. 3, pp. 572-576, 1997.

CHAPTER 3
ELECTROPORATOR CIRCUIT DESIGN AND ELECTRICAL RESULTS

3.0 Introduction

This chapter presents the design of the electroporator and results showing its electrical performance and capabilities. Much of the information here appears in a full conference paper [1]. Specifications are initially identified. The topology, the design approach, the design considerations and modelling then follow. The chapter finishes off by presenting results with discussion and conclusions.

3.1 Design Specifications

One of the primary aims of this project was to develop a suitable experimental apparatus for clinical trials in electroporation. This apparatus should be able to deliver high-voltage (up to several thousand volts), high-frequency (up to several million hertz) bipolar AC pulses to a biological load. Upper limits of the specifications are not well defined as there is no evidence to the author's knowledge that clearly defines what upper voltage and frequency limits are required for the various applications. The intent is to maximise these capabilities within practical limits. A secondary aim was that this apparatus should be capable of delivering continuous bipolar AC voltages of up to several hundred volts for other applications such as radio frequency ablation and dielectrophoresis. The secondary aim is pursued in chapter 5.

This primary aim has been developed into broad specifications for the electroporation apparatus, namely:

- High frequency – several MHz (up to 2 MHz)
- High voltage pulsing – several kV peak (up to 2 kV)

and, although not mentioned above, there should be provision for:

- Capability of monopolar and bipolar pulses – this was an important aspect, since the majority of commercial electroporation equipment only produce monopolar pulses and are incapable of producing bipolar waves, and studies need to be able to compare bipolar over monopolar pulses [2, 3], as applied to biological cells.

- Adjustability or selectivity of above parameters, including frequency, peak voltage, monopolar or bipolar, and also a pulse regime including number of bursts of pulses, number of pulses per burst, and interval between bursts.

- A way to shape the pulses – a simple method is to superimpose pulses of varying widths upon each other, narrower pulses above broader ones, and in this way being able to generate arbitrary step-shaped waves.

3.2 Topology

A class D amplifier design had been considered as a good candidate as it is a highly efficient topology, especially in terms of the output devices. It is also clearly identified in the literature [4] that there is no specific need to produce sinusoidal pulses which are complex to generate using a pulse type design and suffer from poor efficiency when employing output devices in the linear region. Electroporation is dependent mainly on exceeding a threshold electric field amplitude value for an amount of time that produces the desired level of effect.

For the intended switching frequencies, the best devices would be metal oxide semiconductor field effect transistors (MOSFETs), due to their low inherent capacitances. MOSFETs have another advantage over bipolar junction transistors (BJTs) in that they do not require a constant supply of current into their controlling terminals. A newer technology, aimed more at larger power applications, namely the IGBT, still suffers from an unacceptably long delay before turn-on, so was eliminated as a practical candidate.

The next consideration was the high peak voltages in excess of the highest voltage rated MOSFETs, which was 1200 V at the time this design was developed. To overcome this problem, several MOSFETs may be switched in cascade to share the peak voltage between them.

The full bridge (or H-bridge) is considered most suitable to control bipolar pulses of alternating polarity as it offers excellent controllability, and is a well-used and understood topology.

Finally, the arrangement chosen for combining the MOSFETs (and the H-bridges), was the cascaded multilevel inverter (MLI). Briefly, the cascaded multilevel inverter cascades several H-

bridges together to form the main switching circuit, as is depicted in figure 3.1. For a more detailed description and analysis of the MLI, and for a classification of different types including the cascaded type, appendix B may be consulted. Advantages of this topology include modular design, and lowest number of switching devices per voltage level. Appendix D also gives a short account of the proliferation of MLI topologies during the first several years of the 2000s.

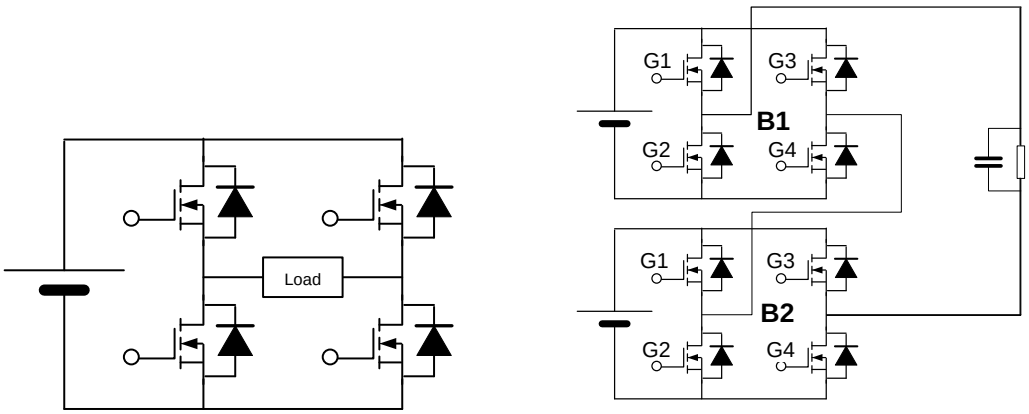

Figure 3.1. On the left is a typical H-bridge using MOSFETs as the primary switches (diodes shown are the intrinsic body diodes for each MOSFET). On the right is a basic two-stage cascaded multilevel inverter, showing the isolated DC voltage sources on the left, two stacked H-bridge stages connected in series, and the modelled biological load on the right. Labels are included for reference in figure 3.2.

The switching protocol was chosen as defined in [5]. This protocol uses a pulse width of 180^0 (π radians) of the full cycle, as illustrated in figure 3.2. This protocol offers the possibility of equal average loading of each switching device, and also a mechanism for zeroing the output at its intended zero values, since a pair of switches (bottom or top) are turned on together to help with discharging the load capacitance rapidly during the off-time. Appendix B explains operation in detail. A simplified single-cycle version of a MOSFET control algorithm has been used in this design, not allowing for completely equal loading of each MOSFET. Equal loading can only be achieved when a multi-cycle control algorithm approach is taken, where the active bridges are alternated or swapped during consecutive switching cycles. However, switch utilisation or average loading in the design was close to balanced (power difference identified in Appendix B), especially for a square wave output, as was the case for the electroporation studies presented in chapter 4.

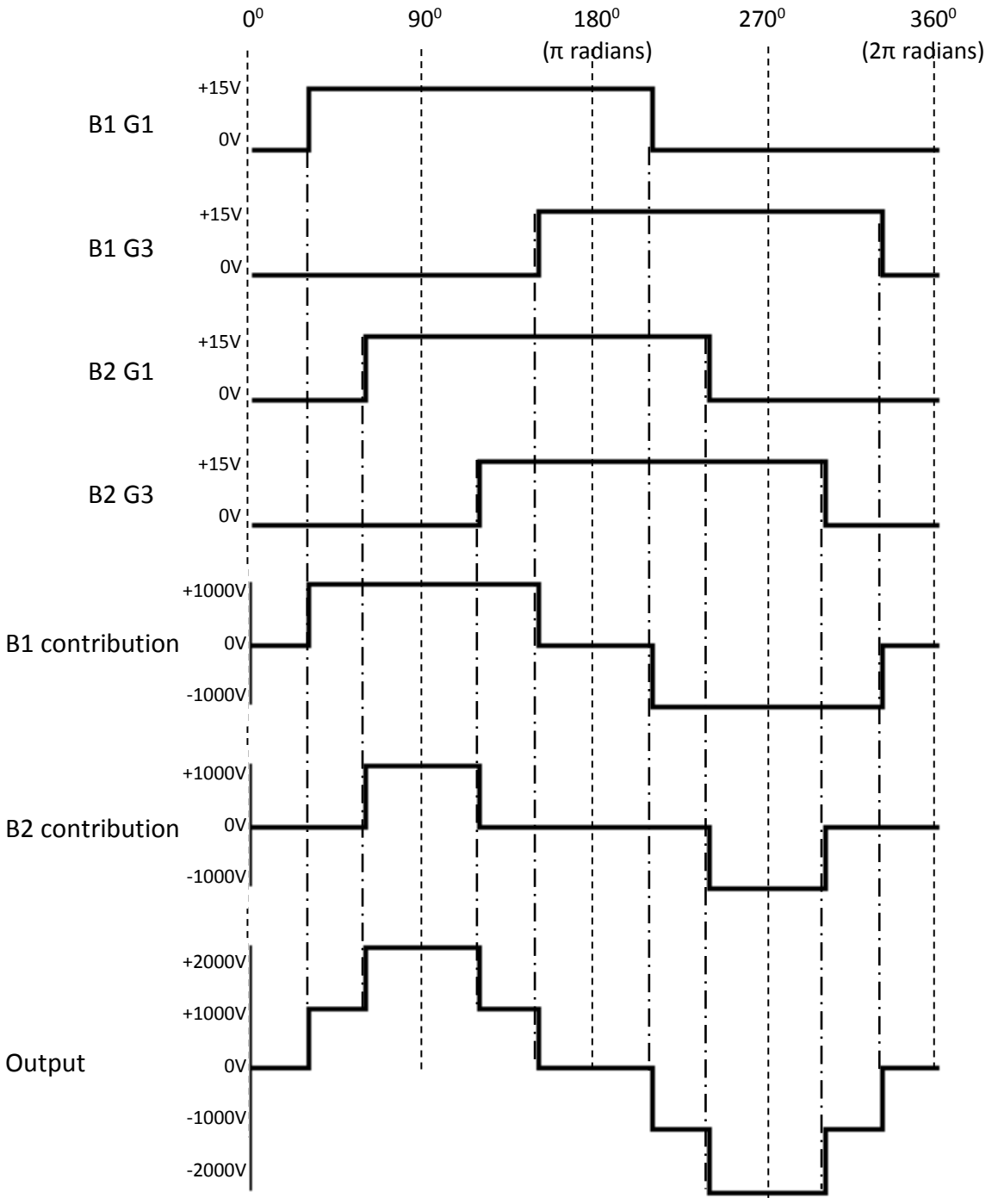

Figure 3.2. Diagram illustrating the timing of gating signals for a double cascaded multilevel inverter using H-bridges, and the resultant output. Each stage is supplied by an independent fully-floating DC source of 1000 V. B1 refers to the upper bridge and B2 the lower bridge shown in figure 3.1, right diagram. The gate numbers G1 and G3 refer to the left and right upper MOSFET gates, respectively. The gates of the remaining (lower) MOSFETs, G2 and G4, are controlled by using the logic inverse signals for their upper

counterparts, G1 and G3, respectively. For more details on operation, refer to appendix B, figure B.1.

From an overall perspective, the system is illustrated in figure 3.3. It shows the controller (an FPGA board) with its control signals feeding the two pulser boards via a breakout board and cables. Each pulser board contains an H-bridge, and series connection between the bridges is made. There is also a load (patient) lead. This system comprises two pulser boards, but can be extended easily to several such boards, making it a modular, scalable design.

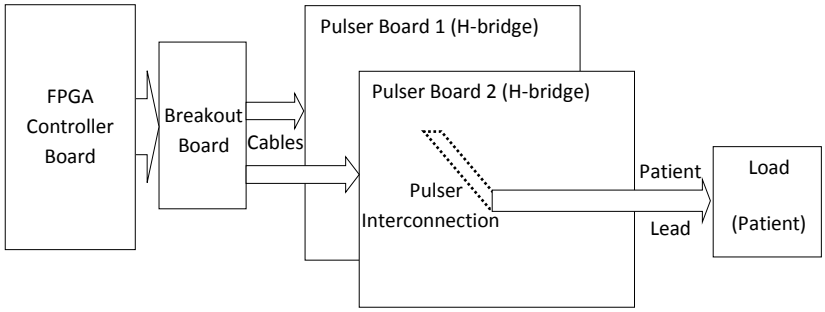

Figure 3.3. Block diagram of the general hardware scheme of the electroporation system. It shows an FPGA pulse controller board with breakout board and cables for connecting to the 2 pulser boards, with their interconnection and output (patient) lead.

Figure 3.4 shows the control signal path for each MOSFET gate. An optocoupler was used to offer the required isolation for electrical safety of medical equipment, in the order of 4 kV (see footnote 1). To ensure proper gate drive, a gate driver IC was selected and used. The gate driver circuit was supplied by a separately isolated AC to DC source with its own medical grade[1] isolation, to directly power the low-side of the H-bridge gate circuits, while the high-side power was derived from the same supply via bootstrap circuits.

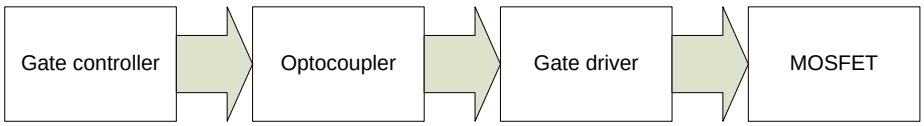

Figure 3.4. Block diagram for the control signal path of each MOSFET.

[1] Medical grade (double or reinforced) isolation for electrical medical equipment connected to mains voltage is 4 kV, in accordance with IEC60101-1: Medical electrical equipment – Part 1: General requirements for basic safety and essential performance.

3.3 Design Approach

From the outset it was decided to approach the design and development incrementally and systematically. This cautious approach allowed for a good understanding of the principles and challenges faced, and the subsequent solution of the problems over time. Numerous prototypes were built and studied, starting with a single MOSFET switch. Initially, low voltages, currents and frequencies were used, and these variables were gradually increased until the prototype reached its limits. Then the next prototype would be designed and tackled using the same approach. Seven prototypes were designed and tested, culminating in an adequately performing final prototype.

3.4 Design Considerations

This section has been broken down into the digital controller, switching devices (MOSFETs), gate drivers, gate driver external resistors, power supplies, output circuitry, optocouplers, input signal conditioning, and EMC considerations.

3.4.1 Digital Controller

The digital controller selected was a field programmable gate array (FPGA). An embedded controller system was needed, and the choices considered were a microcontroller, a field programmable gate array (FPGA), a complex programmable logic device (CPLD), or a digital signal processor (DSP). An FPGA was selected for several reasons including high clock speed ability, very high input-output pin-count, and the author's familiarity with programmable logic devices. A Spartan 3E Starter Board from Digilent [6], that uses the Spartan 3E FPGA from Xilinx, was selected for several reasons, but particularly because it provides differential outputs. Differential signal lines are highly desirable as they are superior in rejecting externally induced noise (very EMC robust) to which the signalling interface could be susceptible – especially at the signal leads between the FPGA board and the pulser board. Also, the FPGA offered reliable operation, and substantial capacity for future development – for instance it offered a very scalable solution, allowing for easy addition of multiple extra H-bridge pulser modules, and very rapid controller design iteration. Finally, the FPGA also offered space for substantial design changes and added complexity if desired.

Embedded software was developed by the author for the FPGA using the hardware description language VHDL. Several algorithms were created, including the main gate switching sequence, a user interface, and a debouncing algorithm. The switching sequence used a simple nested conditional statement determining the timing of each output (gate), and is easily scalable to 3 or

4 H-bridges. The on-board clock frequency of the FPGA was 50 MHz, thus the smallest increments in time were 20 ns, which was used to create the dead time (described in appendix B), and was the time resolution for the switching protocol. The user interface algorithm offered the user a set of predetermined protocols, each of which could be selected using a different switch combination. Since a push button was used to activate the pulsing (firing) sequence and was designed to be manually pressed down until completion of the pulsing as a safety feature, a debounce algorithm was required, and was designed to provide a 20 ms delay after the first logic high was detected. This delay was based on experimentally probing the push button switch with an oscilloscope, trying numerous ways to press the button, and setting the delay to twice the longest bounce interval that was observed.

3.4.2 Switching Devices

As stated in section 3.2, high frequency switching above approximately 100 kHz requires MOSFET devices. Radio frequency capable (RF) MOSFETs are ideal for this application since they possess very short switching durations and delays in the order of ns. These fast MOSFETs reduce losses attributed to switching and allow very fast switching of high voltages. Two of the major original equipment manufacturers (OEMs) that produce these devices are Microsemi Corporation and Ixys Corporation.

At the time of the design, Microsemi offered devices suitable for high voltages, notably 500 V, 1000 V and 1200 V. This company appeared to specialise in super high frequency (SHF – 3 GHz to 30 GHz) RF MOSFETs (but at a lower voltage than was required for this design) and also in very high frequency (VHF – 30 MHz to 300 MHz) high voltage RF MOSFETs, which were suitable candidates for this application.

Ixys offered a good range of MOSFETs, especially in their DE-package range, which they classified as (RF) Power MOSFETs (switch-mode). They offered suitable MOSFET drivers including using the DE package [7]. A full range of MOSFETs from a 100 V up to 1200 V rating with current ratings from 8 to 55 A were available, so they offered a much wider range. Also, they offered Spice-models for all their discrete components, which Microsemi did not have at the time of purchase.

The optimal choice for this application was the Ixys DE375-102N12A [8]. Ratings for this device are 1000 V maximum drain-source voltage, 12 A maximum drain current, 1.05 Ω channel resistance, 3 ns rise time, 8 ns fall time, and 2500 pF gate capacitance. This device uses the DE375 package with thermal resistance of 0.16 ^{0}C/W (junction to case), and device average power dissipation capability of 4.5 W for continuous operation at 25 ^{0}C, without the need for a heatsink. With such superior thermal properties, an estimate (using the TINA circuit simulator – see Section

3.5) of MOSFET average power dissipation of 353 mW each at a switching frequency of 2 MHz for a duty cycle of 0.05 % showed that heatsinking is not required. This was due to the very low duty cycle and also for an operating period of only several seconds, despite an instantaneous peak load power of approximately 20 kW (using 1250 V across 80 Ω). Typical pulse bursts required in the final prototype have been produced and the system performed successfully without using heatsinks.

3.4.3 Gate Drivers

A special gate driver was required. It had to provide high current peaks (order of several amps) for rapid charge and discharge of the gate capacitance of the MOSFET. For the very low duty cycle it was unlikely to need a heat sink, thus packaging requirements favoured a surface mount package to minimise circuit parasitic parameters. The device selected was the UCC37321 [9]. This device offered specifications of 9 A peak, a continuous power rating of 650 mW at an ambient temperature of 25 ^{0}C, and a typical value of $R_{S(OL)}$ of 1.1 Ω (output-low resistance). The selected MOSFET had a gate lead resistance of 0.3 Ω, which may need to be considered in the design of an external series resistance R_G for guaranteeing 20 ns switching times at the output. A value of 20 ns had been chosen since it conveniently represented one clock cycle of the FPGA controller.

Average MOSFET gate switching power P_{gate} can be estimated by using a conservative estimate of gate charge Q_g = 115 nC for the MOSFET [8], thus

$$P_{gate} = \text{Energy stored / Time interval for one cycle} \quad (3.1)$$

$$= E / T$$

$$= Ef$$

$$= \tfrac{1}{2} C V^2 f$$

$$= \tfrac{1}{2} Q V f$$

$$= \tfrac{1}{2} Q_g V_{drv} f_{sw} \quad (3.2)$$

$$= 1.73 \text{ W},$$

for V_{drv} = 15 V as the gate drive voltage, and f_{sw} = 2 MHz as the bipolar pulsing frequency. A target maximum frequency of 2 MHz was chosen to provide worst case conditions.

The biasing power requirement for this driver IC, in contrast, is negligible with a supply current of approximately 5 mA or less, thus equalling 75 mW or less, taking the total up to 1.8 W.

Power consumed in the gate drive IC depends on switching frequency, drive voltage, total gate charge for the MOSFET and also MOSFET gate resistance. To calculate this power a similar equation to equation 3.2 was used, but was broken down into its ratiometric fractions, for both switch-on and switch-off. This was because they were slightly different – see $R_{s(OH)}$ (output-high resistance) and $R_{s(OL)}$ (output-low resistance) from the Spice model. During both these switching events the gate driver consumes power, so should include both $P_{drv(off)}$ and $P_{drv(on)}$, representing the gate drive power when the MOSFET is turned on, and turned off, respectively. Total gate drive IC power consumption $P_{drv(tot)}$ was estimated as follows (using worst case values for $R_{s(OH)}$ and $R_{s(OL)}$ of 2 Ω),

$$P_{drv(tot)} = P_{drv(off)} + P_{drv(on)} \quad (3.3)$$

$$= [R_{s(OH)}/(R_{s(OH)} + R_{G\_MOSFET})]\, P_{gate} + [R_{s(OL)}/(R_{s(OL)} + R_{G\_MOSFET})]\, P_{gate} \quad (3.4)$$

$$= 2\ [2/(2+0.3)]\ 1.73]$$

$$= 3.0\ \text{W}.$$

At the low duty ratio of 0.1 %, $P_{drv(tot)}$ is negligible, thus no additional heat sinking was required.

3.4.4 Gate Driver External Resistors

Gate driver external resistors, connected in series between the gate driver output and the MOSFET gate terminal, need careful consideration. The resistance value depends on the needs of the MOSFET for optimal fast switching. Total gate circuit resistance includes lead resistances of both the MOSFET gate and the gate driver output, total printed circuit track resistances and gate drive power supply resistance. When this total resistance is too small, turn-on of the MOSFET might be too fast generating excessive overshoot and electromagnetic compatibility (EMC) problems and more importantly, susceptibility to high MOSFET output dv/dt when the MOSFET is switched off. The latter may ultimately cause catastrophic failure of the MOSFET due to back coupling via the Miller capacitance (c_{dg}) raising the gate voltage just beyond the threshold and inadvertently turning on the MOSFET when it was supposed to remain turned off. Such an event may lead to destruction of the gate driver IC and other upstream low voltage circuitry if the MOSFET fails as a short between drain and gate. Another consequence of this situation is that it is also likely to produce shoot-through, which is where both upper and lower MOSFETs in a half bridge are conducting simultaneously (also known as cross conduction). When this potentially destructive failure occurs it poses a safety risk during experimental work. At the other extreme, when the overall resistance is too large, several problems may arise, including slow switching (on) of the MOSFET that may cause excessive power dissipation in the MOSFET. For these reasons external

gate resistors were omitted, since gate drive circuit resistance was already in the order of 2 Ω which was large enough to avoid the dv/dt problem during switch off yet small enough to avoid excessively slow switch on for required operation.

3.4.5 Independent Gate Drive Power Supplies

The gate drive ICs required an isolated power source. A medical grade direct PCB-mount encased power supply module was selected [10]. It was decided to use 15 VDC as this voltage allows for maximally fast switching of the high voltage power MOSFETs, and also allows capacity for voltage drop. This was the simplest solution, although another solution using combined signal isolation and power transfer (inductive transfer), was also available. This option was eliminated as it offered only 5 VDC and not sufficient power (50 mW), and also only at an isolation voltage of less than medical grade (4 kV). Since the gate drive of each MOSFET itself demands around 3 W while pulsing, this totals 12 W for the four MOSFETs in a single H-bridge. The optocouplers consume, worst case, 26 mA, and with a 1 kΩ load (pull down or up resistor for safety), another 5 mA. This gives a total of 31 mA, yielding 0.47 W for each optocoupler on the output side. The required minimum total isolated gate drive DC supply for the H-bridge is then 14 W.

To drive the two high-side H-bridge MOSFETs, two independent floating or fully isolated power supplies of 15 VDC were required. These high-side power supplies have to be floating with respect to the low side gate drive power supply, which in turn was referenced to the H-bridge supply common node. A bootstrap charge pump, under very low duty cycle and 180^0 firing angle conditions, is an elegant solution in providing cheap and reliable power to a high-side gate driver circuit of a bridge [11]. The major limitation of this technique is that if the charging path contains too much resistance (see below for added damping resistance), this will slow down charging of the bootstrap capacitor. The very low duty cycle used here eliminated this problem. The bootstrap capacitor is charged by keeping the low-side MOSFETs fully turned on (effectively shorting them) while the high-side MOSFETs are turned off. Bootstrap diode requirements dictated small reverse recovery charge, sufficient reverse blocking voltage, and a high peak current. The US1M, an ultrafast recovery surface mount silicon diode [12], was thus selected, rated at 1000 V and 1 A.

3.4.6 Output Circuitry

The output of the pulser is essentially an *RLC* circuit due to its physical construction. This resonant circuit, with relatively low losses, naturally causes undesirable ringing and overshoot when pulsed. Simulation of the circuit was performed and a solution was found by using resistive

damping. This naturally resulted in a loss in efficiency, however this loss was considered acceptable for this application owing to the very low duty cycle. Substantial resistance was added (in the order of 20 % of load resistance) with load resistance of 50 Ω. This amount of resistance was determined empirically, with the aim of limiting the overshoot to 10 % of the plateau voltage. To enable maximal functionality, the damping resistors were inserted into each of the four H-bridge legs between the switches (MOSFETs) and the H-junctions, as shown in figure 3.5. This also offered shoot through current limiting, thus limiting over current should both upper and lower switches be unexpectedly turned on at the same time. Using 5 Ω damping resistors results in total damping resistance of 20 Ω, considering that there are two connected in diagonal in each bridge and that there are two bridges.

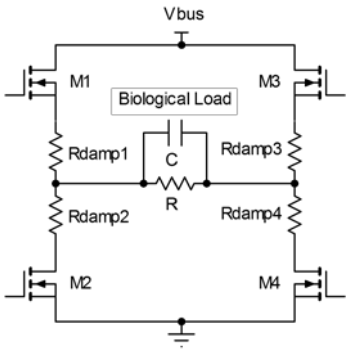

Figure 3.5. Schematic diagram of the H-bridge showing placement of damping resistors.

Pulsed damping power loss P_{damp} can be estimated as follows:

$$P_{\text{damp}} = \{ R_{\text{damp}} / [\, 2\, (R_{\text{load}} + R_{\text{damp}} + R_{\text{DS(on)}}\,)] \}\, P_{\text{load}} \tag{3.6}$$

$$= \{ R_{\text{damp}} / [\, 2\, (R_{\text{load}} + R_{\text{damp}} + R_{\text{DS(on)}}\,) \,] \} \cdot [\, (V_{\text{Lpeak}}/\sqrt{2})^2 / R_{\text{L}} \,] \tag{3.7}$$

$$= \{ 20 / [\, 2\, (50 + 20 + 4) \,] \}\, [\, (1600^2/2)/\, 50 \,]\ \text{W}$$

$$= 3.5\ \text{kW}.$$

Each of the 8 resistors would consume 440 W continuously, but at 0.1 % duty cycle this drops to a more tolerable 0.44 W each, for several seconds only. Using two resistors for each resistance this drops to 0.22 W. As such the damping resistors needed to be rated at 0.5 W at least, plus required a very substantial pulse withstanding capability – that is, able to tolerate very high energy short pulses. Pulse withstanding resistors rated at 2 W were used [13].

External anti-parallel diodes were added to protect the MOSFETs due to their poorly performing internal body diodes which are susceptible to high output dv/dt. These diodes shunt rapid reverse

current away from the body diode and are required to be high speed with a low forward voltage drop. These diodes were rated at 1 A due to very low expected average currents. Selection of low current diodes was prudent as it meant that other parameters of the diodes were more ideal such as junction capacitance, reverse recovery time and avalanche energy that are lower making them more desirable. Again, ultra-fast recovery silicon rectifier diodes (US1M) were selected. They were soldered directly across the pins of the MOSFETs to minimise unwanted parasitics such as inductance.

For additional protection of the MOSFETs, thus reducing ringing and overshoot, resistor-capacitor-diode (RCD) snubbers were used, as demonstrated in figure 3.6. Once again, the same diodes (US1M) were used. A simple approach was followed in designing the values for R and C. Resistance R was set to load resistance divided by 10 (4.7 Ω) and C was chosen to be double the MOSFET output capacitance (1 nF). This worked out close to the suggested design guidelines for calculating turn-off resistor-capacitor (RC) snubber values [14]. The design guideline suggests first estimating inductance, then capacitance, then adding additional capacitance, followed by estimating a resistance value for critical or near-critical damping. D2 only allows dissipative damping for reverse resonant currents from circuit parasitic inductance. D1 is the external body diode protection diode. Components D2, R and C form the RCD snubber. The snubber resistors produce heat and have been selected on a similar basis to the damping resistors as they need to withstand pulse currents. These resistors were rated at 2 W and pulse withstanding. All RCD snubber components are rated for 1 kV.

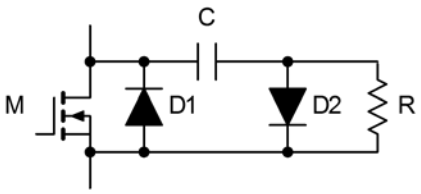

Figure 3.6. MOSFET with external components, showing an external anti-parallel diode, D1, and an RCD snubber that comprises the rest of the components.

3.4.7 Optocouplers and Input Signal Conditioning

The interface between the digital controller and the gate driver ICs have the following requirements [1]:

1. Medical grade safety isolation between system and mains supply (order of 4 kV).
2. Ample data rate capability for adequate slew rate of pulses (order of 20 MBd).
3. Small range of propagation delays for minimal skew between channels (order of 30 ns).
4. Ability to connect several standard cables to the controller board (CAT 5E patch cords convenient, cheap and optimal for 110 Ω balanced transmission lines required for quasi-LVDS[2] signals from the FPGA).
5. High common-mode transient immunity for EMC robustness (order of 1 x 10^{10} V/s at high common mode voltage)
6. EMC-robust pulsing to the gates created by charging voltages and currents in the signal (capable of withstanding excessive transient electric and magnetic near fields, order of 1 x 10^{10} V/s and 2.7 x 10^{9} A/s, respectively, separated by several cm).

To electrically isolate but link the pulser PCB from the controller, the Avago HCPL-2400 optocoupler [15] was selected. This optocoupler offered a speed of up to 40 Mbps, isolation of 3.75 kV and common mode noise suppression of 1 x 10^{11} V/s. Since the H-bridge needs four independent signals, four single optocouplers were used. The optocoupler needs a 5 VDC supply which required voltage regulation from the existing 15 VDC supplies for each gate drive circuit. Common mode chokes were inserted between the controller and the optocoupler LEDs to improve noise suppression performance. High impedance cylindrical ferrite cores were used around which 6 well-spaced windings of a tightly twisted pair of thin single conductors were wound – more practical details follow in the EMC guidelines below.

[2] Although Xilinx used the term *LVDS* in their datasheet for the Spartan 3E FPGA, the actual signal values were not true to this technology, which is actually 3.5 mA in either direction into 100 Ω, implying only a differential 0.35 V [16]. Instead, theirs was simply a differential 3.3 V (high logic) or -3.3 V (low logic). This required the design to be modified as the LVDS receivers originally designed for the system were greatly overdriven resulting in errors. Finally, a pair of 110 Ω series connected resistors was used (to maintain balance and limit current) on either side of the differential line. A clamping anti-parallel diode was placed in parallel at the input of the optocoupler (to avoid damaging its sensitive LED with excessive reverse voltage). This late modification has worked satisfactorily, but may have increased its sensitivity to noise pickup at the cables. One slight advantage of these modifications was the proper and fast turning off of the optocoupler LED with a slight negative drive voltage (about –0.7V) in the logic zero condition.

3.4.8 EMC Considerations

Success of high voltage and current pulsing systems is heavily reliant on good EMC practice. Due to the 1 kV rating, large clearances of at least 5 mm were required and this may give rise to undesirable parasitic inductance in turn causing ringing. Another design constraint was the use of simple double-sided standard one-ounce copper PCB. Use of more layers in the PCB would have improved certain PCB parameters and aided in shielding, but the objective was to keep things as simple as possible allowing for easy manual fabrication of the circuit. A lot of relevant practical constructional information was gained from two reference designs [17, 18].

The following EMC guidelines were applied as effectively as possible for successful operation [1]:

1. Minimise separation between components.
2. Maximise quality of grounding/planes.
3. Minimise track lengths.
4. Minimise current loop areas.
5. Use broader tracks where permitted.
6. Minimise return paths.
7. Extensively use power supply decoupling capacitors.
8. Use only RF quality capacitors.
9. Where large value capacitance is required, use several decade values in parallel with smallest value closest to the chip power pin.
10. Minimise coupling between PCB tracks.
11. Use series resistors before power supply decoupling capacitors in an attempt to further reduce/filter power supply noise at the expense of voltage drop.
12. Use hand-wound common mode chokes at the input of the optocouplers to reduce common mode noise on the cables. Six or seven turns of tightly twisted thin solderable enamel wire with windings maximally separated but tightly wound on a toroidal ferrite core with an impedance of 100 Ω per winding at 100 MHz has been shown to work well with the electroporation system.

13. Maximise separation between signals to minimise cross-talk. This guideline has been added for the sake of completeness.

3.5 Modelling

Modelling has been performed using TINA to provide preliminary validation of the proposed design. TINA [19] is a simulation programme with integrated circuit emphasis (SPICE)-based software package, and is fully capable of solving node defined electric circuits in the time and frequency domains. Manufacturers often produce SPICE models for their devices, which can be included in circuit designs for predictive analysis prior to physical implementation. Figure 3.7 presents the modelled circuit, and figure 3.8 presents some representative simulated results, using TINA.

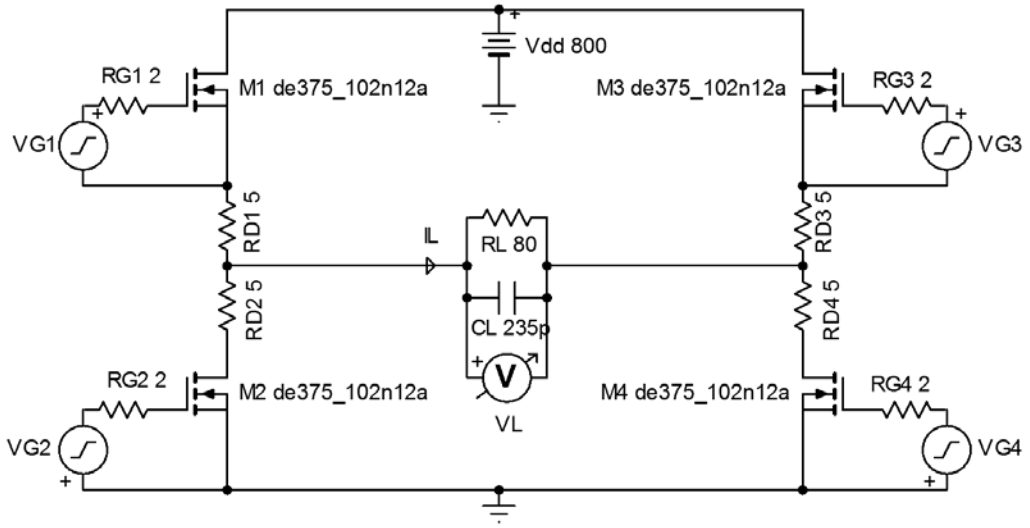

Figure 3.7. Schematic diagram for the proposed design showing only a single H-bridge. It operates at 2 MHz with a 50 % duty cycle.

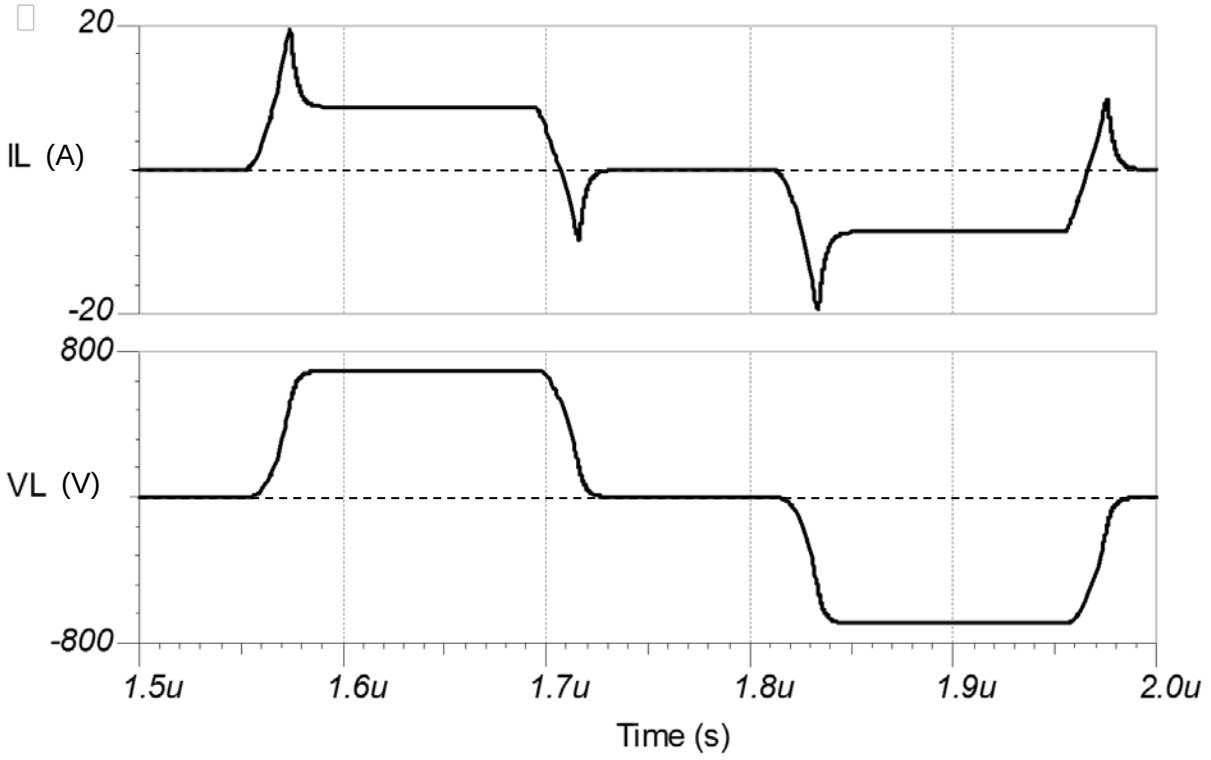

Figure 3.8. Plot for output current and output voltage of the single bridge pulsing circuit shown in figure 3.7.

The circuit in figure 3.7 represents the proposed design showing the specific MOSFET devices incorporating the manufacturer's SPICE model, representative gate resistances of 2 Ω, damping resistors of 5 Ω, and a resistive-capacitive load of 80 Ω in parallel with 235 pF. The resultant output plot in figure 3.8 shows a load pulse voltage plateau of 694 V and a load current plateau of 8.7 A. The pulse voltage slew rate is 6.2 x 10^{10} V/m. Pulse current overshoot is substantial at ΔI = 10.5 A (121 %), due to the capacitance of 235 pF demanding a peak charging current.

However, performance at this pulsing frequency of 2 MHz is affected by parasitic circuit board components such as track inductances. These parasitic values are estimated at 1 nH per mm of track as a guide, and are modelled as 20 nH inductances in the printed circuit layout in the main branches of the bridge, and are thus included in the next simulation, shown as figure 3.9 and figure 3.10.

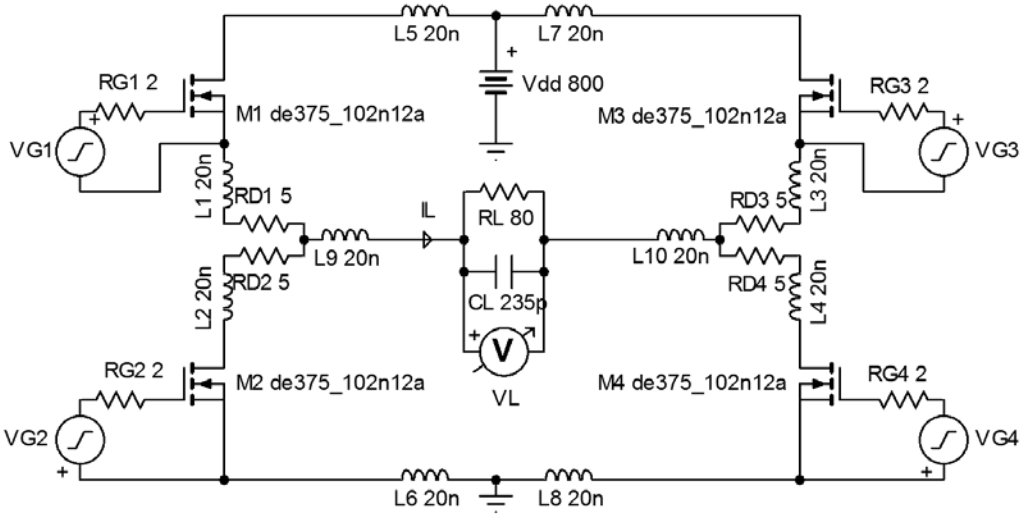

Figure 3.9. Schematic diagram of the single bridge model with estimated parasitic components included.

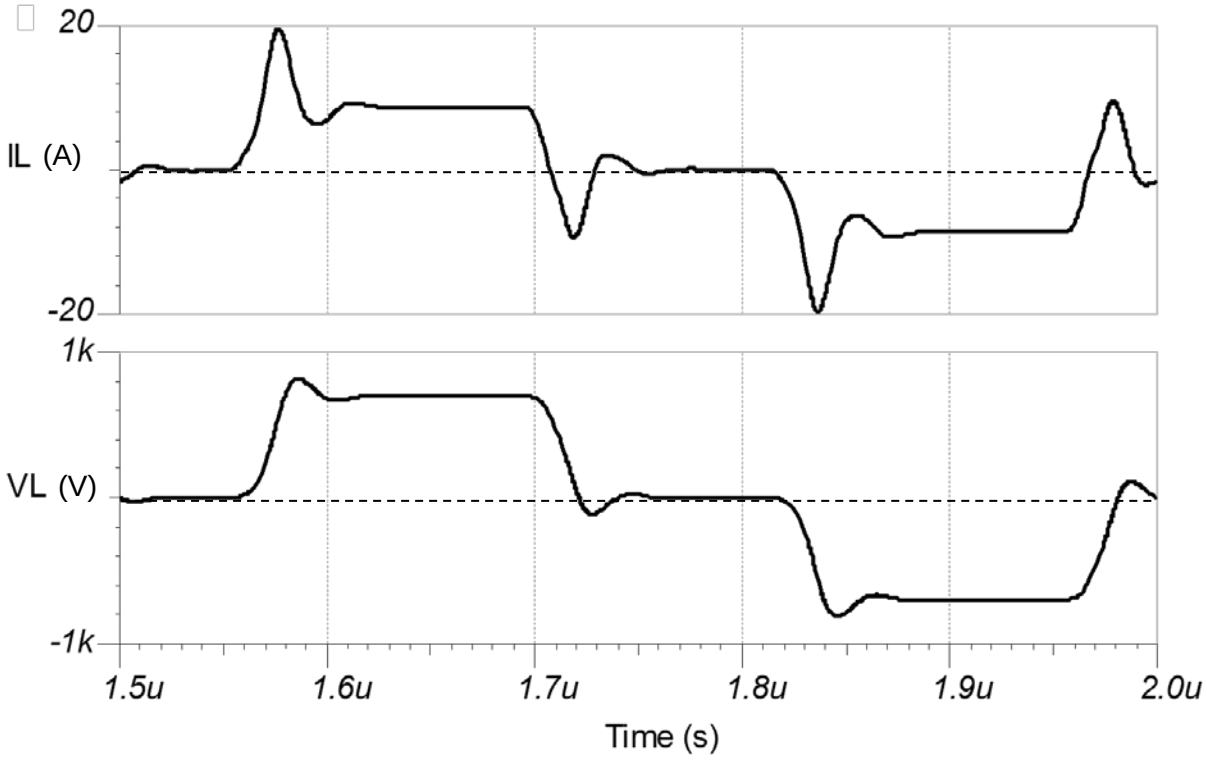

Figure 3.10. Plot for output current and output voltage of the single bridge pulsing circuit shown in figure 3.9.

Observed in the plot of figure 3.10 is the more resonant nature of the waveforms due to the presence of inductances. Load current overshoot is increased to ΔI = 10.9 A (125 %), while load voltage overshoot is now present at ΔV = 118 V (17 %).

The effect of R-C-D snubbers and anti-parallel diodes across each MOSFET are now presented in figures 3.11 and figure 3.12.

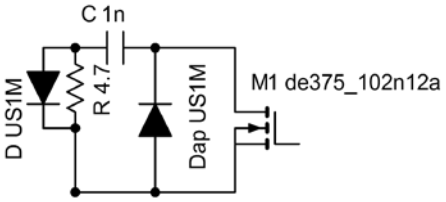

Figure 3.11. Abbreviated schematic diagram showing a MOSFET and its R-C-D snubber and anti-parallel diode.

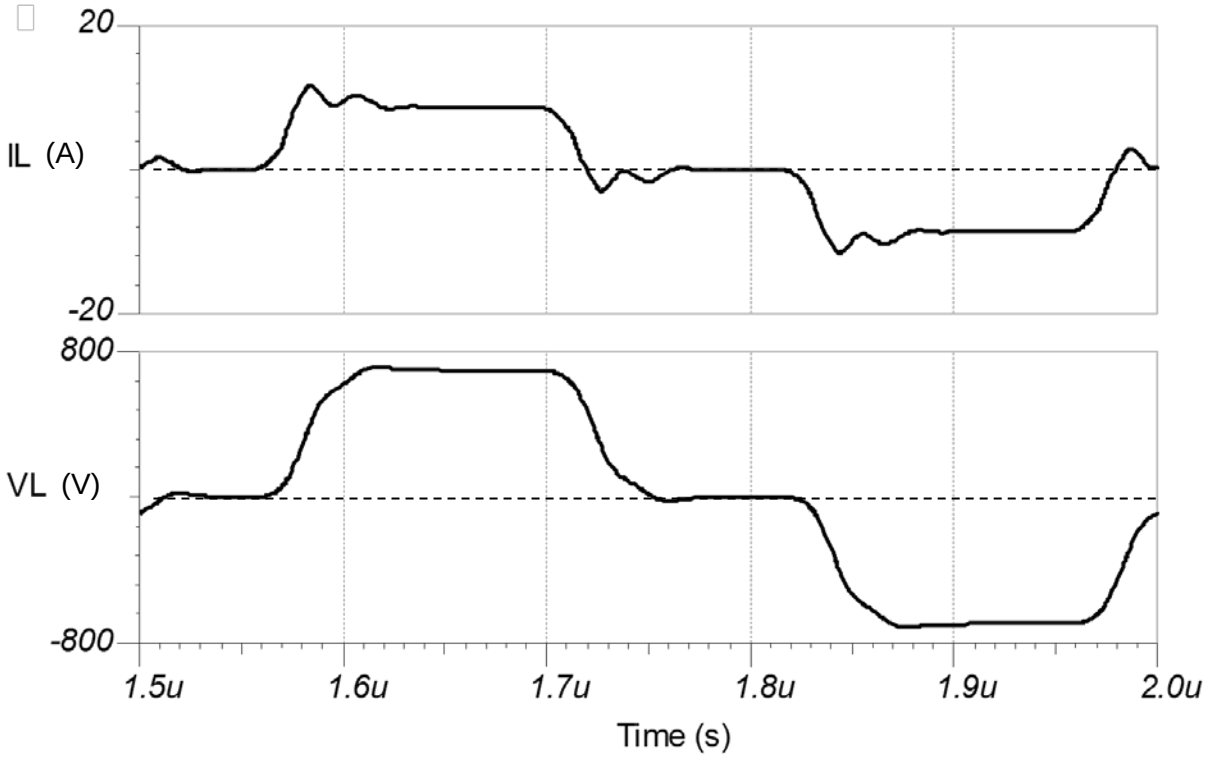

Figure 3.12. Plot for output current and output voltage of the single bridge pulsing circuit shown in figure 3.11.

Figure 3.12 shows the lack of overshoot in the output voltage and also less overshoot (ΔI =31 %) in the current waveform but some additional ringing of approximately 40 MHz. The voltage slew rate here is 2.8 x 10^{10} V/s, which is half the value without parasitic parameters and snubbing.

Figure 3.13 illustrates the output voltage and current of a full dual bridge multilevel inverter.

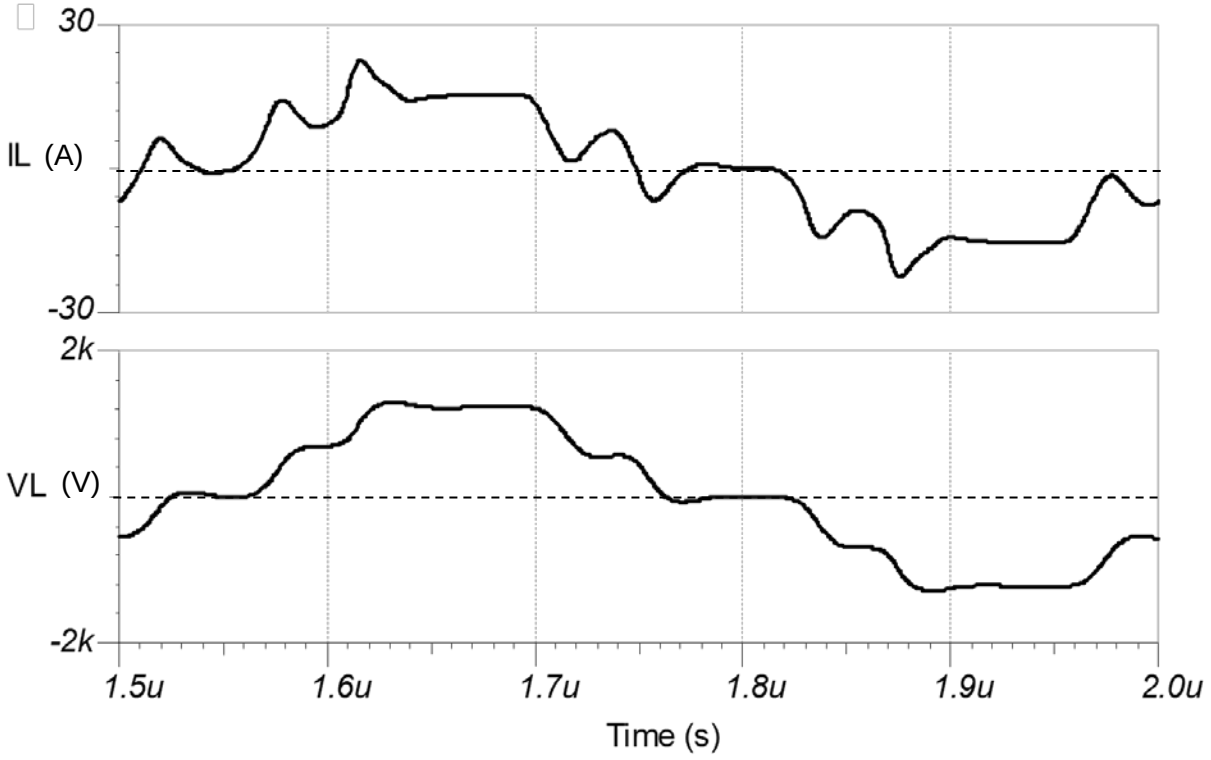

Figure 3.13. Plot for output current and output voltage of the dual bridge multilevel inverter pulsing circuit when combining two identical circuits in series, using identical components and isolated supplies of 800 VDC. Snubbers and anti-parallel diodes were omitted due to simulator limitations.

Observed in figure 3.13 is the full dual bridge multilevel inverter output, which shows the characteristic stepped multilevel voltage. The voltage plateaus are at magnitudes of 686 V and 1230 V, and the maximum current plateau is at a magnitude of 15.3 A.

The simulations demonstrate that the proposed circuit design operates with expected characteristics and therefore has reasonable potential to operate when physically implemented.

3.6 Results and Discussion

The final prototype circuit results are now presented, as well as a photograph of the circuit board. A schematic diagram is included in appendix C. Oscilloscope trace images are shown for an output load of 80 Ω in parallel with 235 pF in figure 3.15. An impedance of 70 Ω to 80 Ω is regarded as average for a human adult for transthoracic defibrillation [20] but this can vary widely. Impedances of 50 Ω and 80 Ω are used in the specifications of a commercial radio frequency ablator [21]. Patient impedance depends on electrode geometry, on the conductivity and morphologies of the tissues between the electrodes, and is also affected by the process of electroporation, since this tends to reduce impedance during poration due to an increase in tissue conductivity [22]. Capacitance is added in parallel to account for prospective work on cell suspensions which exhibit higher impedances but with capacitance, as naturally exists in cell membranes due to their low conductivity. An impedance model for such a situation of a cell in a suspension is provided in [23]. Estimating a practical capacitance is difficult. To derive capacitance for the load model, a simple parallel plate model of $C = \varepsilon_0 \varepsilon_r A/d$ was used. Using an area of 1 cm^2, with the plates separated by 1 cm and a dielectric of $\varepsilon_r = 5000$, yields a capacitance of approximately 442 pF. The actual value is substantially less due to fringing electrostatic field effects, but a conservative approach was taken erring on the high side to ensure reliable operation of the switching circuit. Greater capacitance is more challenging due to a reduction in impedance. Also, at higher frequencies the permittivity of liver drops, resulting in lower capacitance. The relative permittivity for cancerous human liver has been derived from [24-26] at a frequency of around 200 kHz. Using a capacitance of 442 pF in parallel with a resistance of 50 Ω produces a time constant (RC) of approximately 22 ns. Shifting the plates further apart in the same model to produce a higher impedance will result in 80 Ω in parallel with 276 pF. Thus 80 Ω in parallel with 235 pF was used as a slightly lighter but otherwise equivalent load. The high-voltage supplies were both 800 VDC (isolated from each other). A TDS2022B Tektronix oscilloscope (200 MHz) with a high-voltage probe from Tektronix (P5100, 2.5 kV, 250 MHz) was used to measure the outputs at various frequencies. DC vertical accuracy of this oscilloscope is specified as ±3 % of full scale and has a resolution of 8 bits [27]. Figure 3.14 shows the physical circuit.

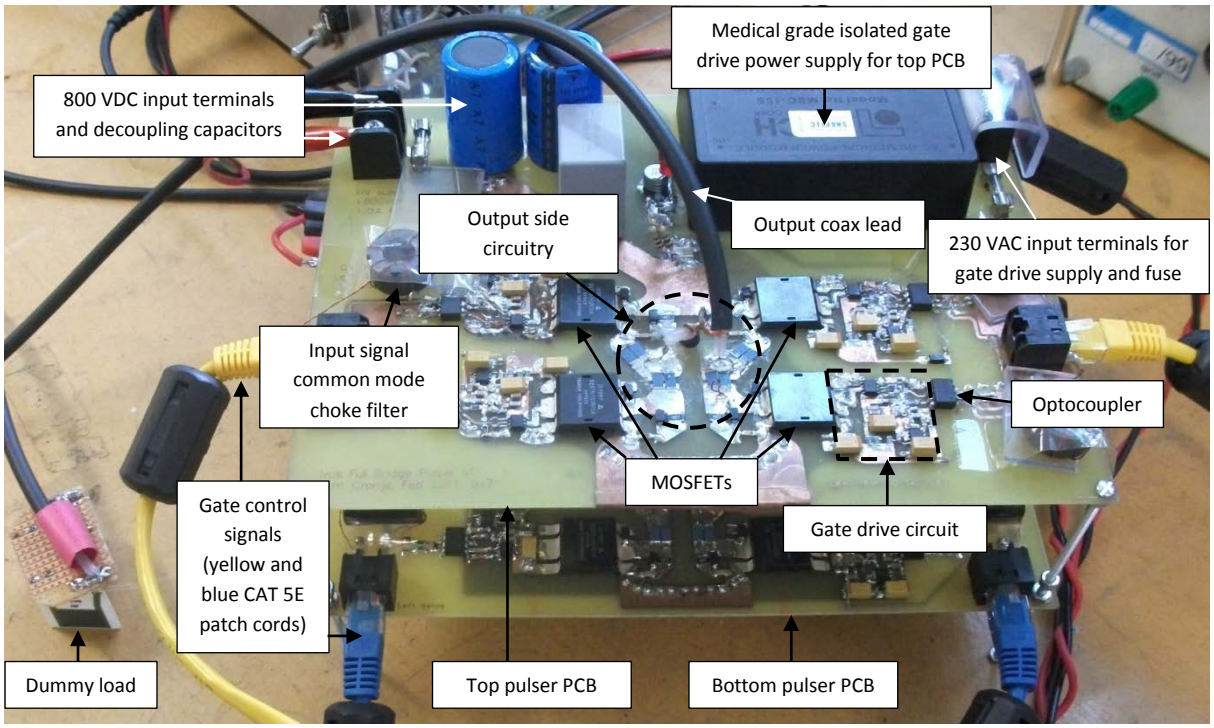

Figure 3.14. Photograph of the electroporator pulser boards with the dummy load (shown on the bottom left corner) fed via the black coaxial lead connected roughly to the centre between the four MOSFETs (black squares). Two H-bridge PCBs are stacked – the interconnection is not visible. Gate control signals enter through the yellow and blue CAT 5E patch cords and power supply leads are connected to the top left and right connectors of each PCB. Note all signal and power leads have black ferrite sleeves close to the PCB entry point. A medical grade 15 VDC power supply is visible on the top right (black rectangular box).

As seen in figure 3.15, outputs up to 500 kHz showed good voltage waveform performance, with a predominantly "staircase" shape. A voltage drop of 22 % is observed when comparing the output to the 1600 V applied (2 x 800 VDC). This was due to the damping resistors of 5 Ω each and MOSFET channel resistances of 1 Ω each. The 1 MHz and 2 MHz switching frequencies however were not able to provide very good waveforms. Slew rate limiting visibly distorted the waveforms, and at 2 MHz the full peak values could not be achieved. Waveforms were also not exactly symmetrical (although very close to being symmetrical) with respect to zero volts, as could be expected. However, careful visual inspection of the circuit confirmed non-symmetric layout. The gate driver circuits could not be physically mirrored (between the high-side and the low-side) as the gate driver chips were not mirrored, although the MOSFETs were.

Power spectral densities throughout this circuit were not examined as literature identifies that time spent above a threshold value [4] and also how far the value is above this threshold [28] are

of importance to the phenomenon of electroporation rather than the relative power distribution versus frequency. This implies that slew rate is an important parameter as a lower slew rate will reduce time above a threshold value for a given pulse width, which becomes particularly significant at the upper frequency range.

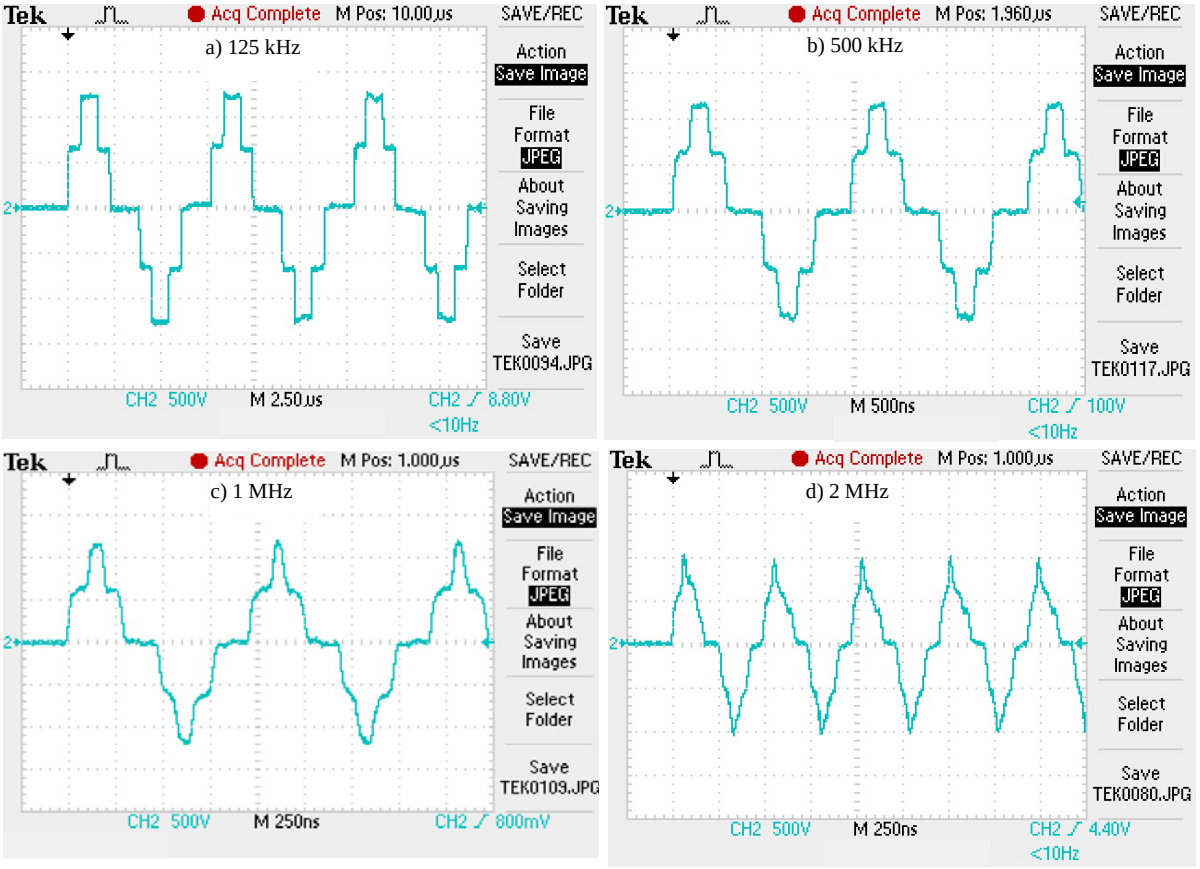

Figure 3.15. Oscilloscope trace images of the output at a) 125 kHz, b) 500 kHz, c) 1 MHz and d) 2 MHz, for the final dual stage electroporator circuit into a load of 80 Ω in parallel with 235 pF, while applying two independent high voltage power supplies of 800 VDC, producing peaks of ±1250 V.

At another time of the year, during summer, the system was again tested at a higher ambient temperature. Previously unobserved waveform distortions were observed. As such these distortions had a link to temperature and a heat gun was used to gently warm the circuit in order to controllably recreate the distortions. This experiment was repeated several times with repeatable results as shown in figure 3.16.

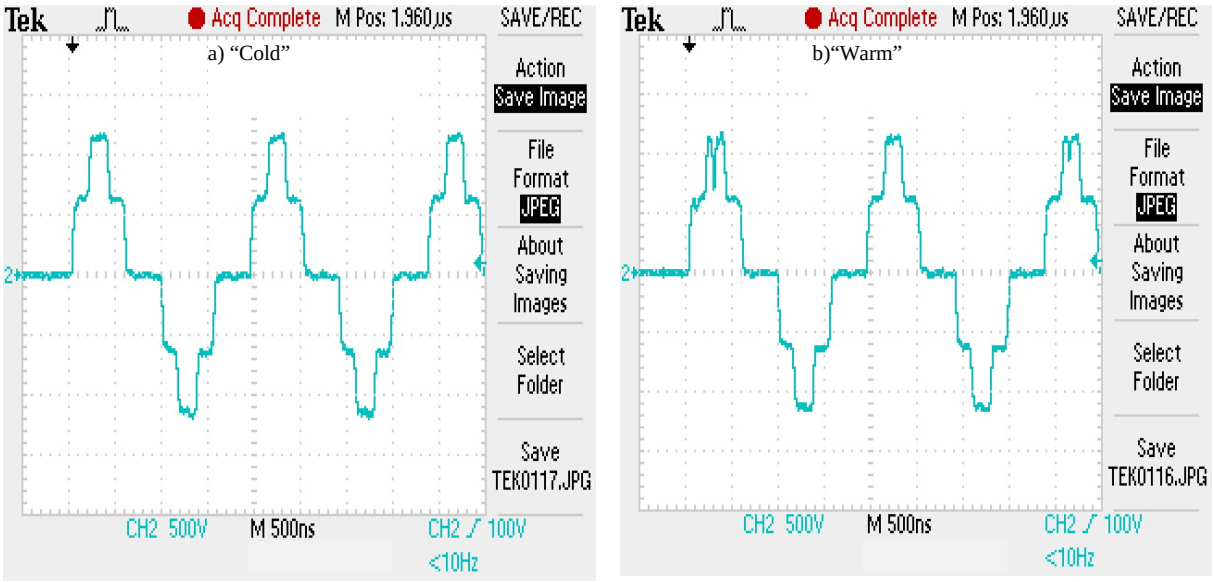

Figure 3.16. Oscilloscope trace images of output waveforms at 500 kHz during a) cool and b) warm ambient conditions. Similar conditions were applied to those prevalent during the testing that produced the results presented in figure 3.15.

Distortion of the output was measured in the gate drive circuit on the left high-side of the H-bridge, corresponding with the positive peaks of the output waveform. An unintended turn-off event was timed at 60 ns after the leading edge of the gate pulse intended to turn on the upper right MOSFET. This corresponds with the output waveform distortion in time and accounts for the MOSFET behaviour during that time. When switching the MOSFET-based H-bridge to produce a pulsed current in the load, an electromagnetic (EM) wave is generated due to high dv/dt and high di/dt in the output, in the order of 2×10^{10} V/s and 3×10^{8} A/s, respectively. Although this EM wave causing the interference had only travelled a fraction of a metre, thus accounting for a delay of 0.33 ns over a distance of 0.1 m (at the speed of light in space), component delays of approximately 30 ns each (optocoupler and gate driver) fully account for this delay.

The temperature problem, where the circuit is affected differently by different ambient temperature, is a well-known effect [29]. It can be ascribed to a change in MOSFET threshold gate voltage as a function of temperature. This threshold voltage drops as the temperature is raised, making the MOSFET more susceptible to noise thus reducing its noise margin. Induced feedback noise at the output of the optocoupler renders the largely MOS-based gate driver more likely to accidentally turn on with its temperature raised. The gate driver inverts its signal thus it passes on the inverse effect, thus turning the MOSFET off, hence the unintended turn-off event.

Further investigation revealed that the distortions could be related to poor gate drive, as can be seen in figure 3.17.

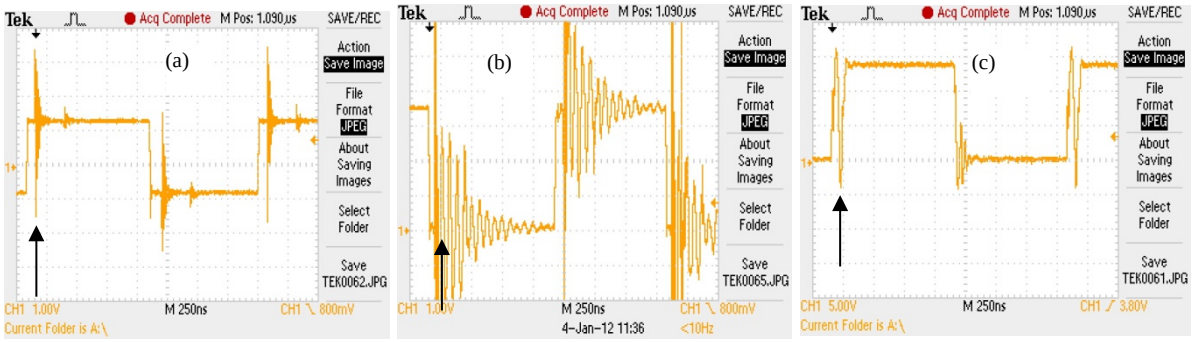

Figure 3.17. Oscilloscope trace images of the left high-side gate driving signal sequence: (a) Optocoupler input voltage; (b) optocoupler output voltage; (c) gate driver output voltage. These results were generated at a frequency of 500 kHz with a 300 VDC MOSFET supply for the sake of safety. All other conditions are as before. These waveforms were created under warm ambient conditions. Arrows indicate the events associated with the unintended distortion.

From figures 3.17 (a) and (b) it is observed that there is a great deal of noise, which is ultimately responsible for the compromised gate drive signal, and ultimately the distorted output signal shown in figure 3.17 (c). Switching noise is induced into the optocoupler input signal shown in figure 3.10 (a) causing very fast ringing of approximately 100 MHz with overshoot of approximately 2.1 V (100 %). The optocoupler input is a diode clamped version of the FPGA differential output. The optocoupler output, with larger magnitude overshoot of approximately 6 V (182 %) at the nominal pulse voltage of 3.3 V, but slower ringing at approximately 17 MHz, then drives the gate driver which nearly filters out all of the noise, with the exception of the worst spike. This is clearly the cause of the unintended distortion. Even so, the gate driver and MOSFET both demonstrated substantial rejection of the original noise, due to gate driver hysteresis and MOSFET slew rate properties. No particular solution has been adopted since subsequent work involved a higher impedance load thus reducing the di/dt (see chapter 4), although a simple fan based cooling system is likely to overcome this problem for higher ambient temperatures.

Slew rates were derived from oscilloscope traces. Gate drive output slew rate was 1×10^9 V/s (10 V in 10 ns), and MOSFET output slew rate ranged from 1×10^{10} V/s to 2×10^{10} V/s (500 V in 50 ns down to 25 ns), in both instances for an output load of 80 Ω parallel with 235 pF. Error for this metric is estimated at 10 %. This explains the shortcomings of the waveforms of the 1 MHz and 2 MHz pulsing waveforms shown in figure 3.8. This measured voltage slew rate is slightly lower than the simulated value of 2.8×10^{10} V/s – this difference is likely due to a slight underestimation of the parasitic PCB parameters, especially the inductances. As stated before, two isolated supplies of 800 VDC were used.

Bipolar square wave and rectangular monopolar pulse output waveforms are also presented in chapter 4, where different waveforms were used for electroporation work on human cancer cells. Figure 3.18 shows a number of different waveforms that can readily be created with the pulsing algorithm used.

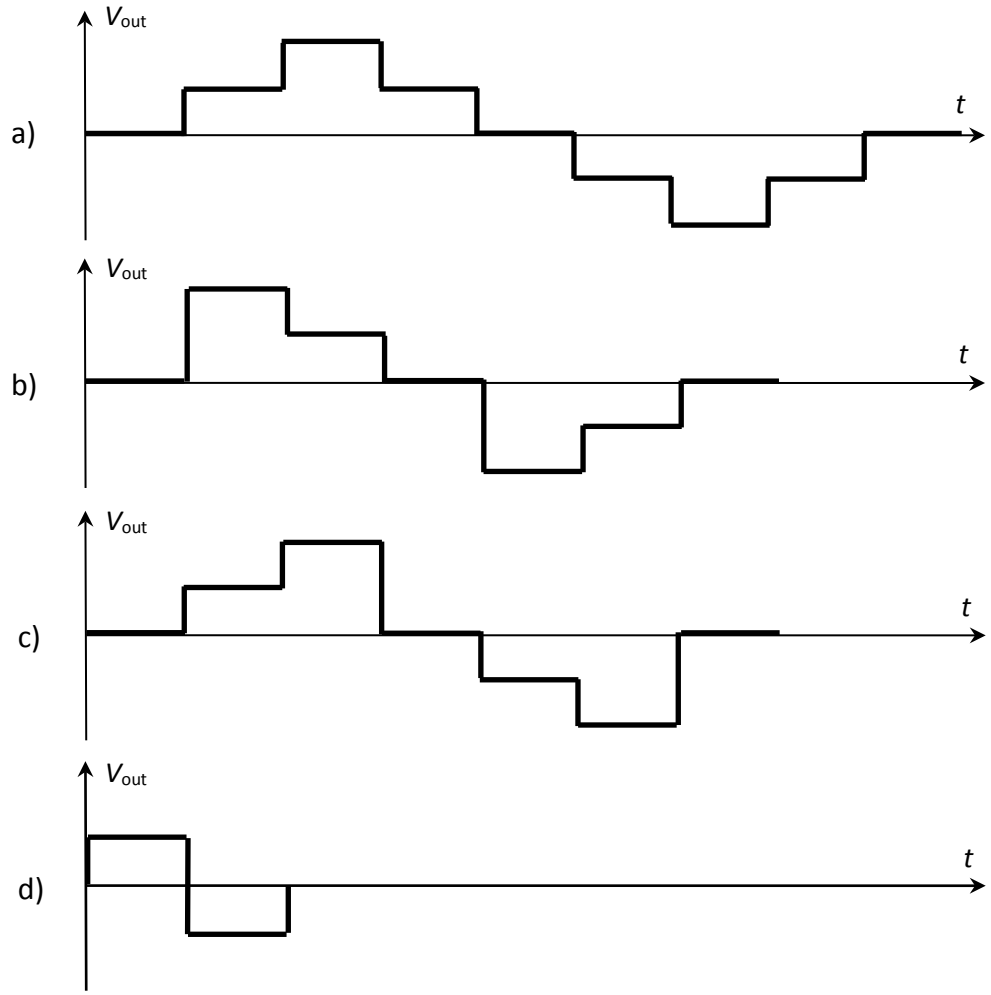

Figure 3.18. Several examples of a variety of bipolar pulsing output waveforms that can be readily generated with this design. a) Typical 5-level cascaded multilevel inverter bipolar waveform using 2 x H-bridge stages (all step widths and null widths are individually programmable, all step heights can be changed, more stages can be added to increase number of levels, and it can also be programmed to generate only positive or negative levels for monopolar operation); b) and c) Ramped 5-level cascaded multilevel inverter bipolar waveforms using 2 x H-bridge stages (variations of a)); d) Simple square wave.

Shown in figure 3.18 is a variety of waveforms (all periodic) that can be produced by the developed pulser. They can be repeated any number of times, and any number of inter-burst

pulses can be created with any desirable intervals, and for any desired number of bursts and inter-burst intervals. They can also be programmed to be monopolar – of single polarity. The smallest programmable step in time is 20 ns, but due consideration of dead time, typically also 20 ns, is essential for reliable operation. Slew rate limitations however restrict pulsing frequencies to a maximum of 2 MHz. The minimum frequency or longest pulse duration is limited by the on board charge storage capacitance, and thus the amount of charge required by the load. For example, as an estimate, the pulse amplitude droops by 5 % for a single pulse width of 350 μs, using a load resistance of 80 Ω and a capacitance of 76 μF.

Further regular tests have confirmed that this circuit has operated reliably. No heating of components above specified maximum temperatures has been observed anywhere around this circuit.

3.7 Conclusions

A novel electroporator apparatus that used a cascaded multilevel topology with high voltage RF MOSFETs has been presented. It meets the broad specifications set out at the beginning of this chapter, being adjustable or programmable in terms of voltage, frequency, and pulse burst regime. It offers a variety of output waveforms and it is also capable of producing bipolar or monopolar pulses. To the author's knowledge, there are no other examples identified in the literature of such a fast high voltage pulser with all these capabilities, which in itself is a contributing factor why comprehensive combined high frequency high voltage electroporation studies have not been carried out yet. The development approach has been discussed, critical design considerations have been stated and implemented, and results have been illustrated. Modelling was performed using realistic estimates of parasitic PCB parameters and demonstrated that the design should operate successfully. The results show successful operation up to approximately 1 MHz at a peak output voltage of 1250 V into a realistic model of a biological tissue load. Conditions used were: a substantial load of 80 Ω in parallel with 235 pF, pulsing frequencies of 125 kHz up to 2 MHz and independent H-bridge supplies of 800 VDC. The circuit achieved a fully loaded output slew rate of up to 2 x 10^{10} V/s. It has been observed that substantial coupled noise was present, however, the circuit was tolerant of this and produced useful output waveforms. Also observed was a prevalent operational dependence on ambient temperature, and an explanation for this was offered. Subsequent operation of this apparatus has proved successful and reliable.

3.8 References

[1] T. F. Cronje and P. T. Gaynor, "High voltage and frequency bipolar pulse generator design for electroporation-based cancer therapy", Hobart, Australia: Australasian Universities Power Engineering Conference (AUPEC 2013).

[2] C. Chen, et al., "Measurement of the efficiency of cell membrane electroporation using pulsed ac fields", *Phys Med Biol*, Vol. 53, No. 17, pp. 4747-4757, 2008.

[3] S. Talele, et al. "Modelling single cell electroporation with bipolar pulse parameters and dynamic pore radii", *J Electrostat*, Vol. 68, No. 3, pp. 261-274, 2010.

[4] T. Kotnik, et al., "Role of pulse shape in cell membrane electropermeabilisation", *BBA*, Vol. 1614, No. 2, pp. 193-200, 2003.

[5] M. H. Rashid, *Power electronics: circuits, devices, and applications*, 3rd ed., Upper Saddle River, NJ, Pearson/Prentice Hall, pp. 417-422, 2004.

[6] Digilent, *Spartan-3E FPGA Starter Kit Board User Guide*, UG230 (v1.2), 2011, [Online]. Available: http://www.xilinx.com/support/documentation/boards_and_kits/ug230.pdf

[7] G. Krausse, *DE-Series Fast Power MOSFET – An Introduction*, Rev. 3, Ixys, 2002, [Online]. Available: http://ixyscolorado.com/index.php/technical-library/ixysrf?task=callelement&format=raw&item_id=241&element=f85c494b-2b32-4109-b8c1-083cca2b7db6&method=download&args[0]=6611513ade03977d533d5fd9a7662c13

[8] Ixys, *DE375-102N12A, RF Power MOSFET Datasheet*, Rev. 6, 2009, [Online]. Available: http://ixapps.ixys.com/DataSheet/de375_102n12a.pdf

[9] Texas Instruments, *UCC37321, Single High-speed Low-side MOSFET Driver with Enable Datasheet*, 2013, [Online]. Available: http://www.ti.com/lit/ds/symlink/ucc37321.pdf

[10] TDK-Lambda, *KM range medical grade power supply datasheet*, 2015, [Online]. Available: http://us.tdk-lambda.com/ftp/Specs/km.pdf

[11] L. Balogh, *Design and Application Guide for High Speed MOSFET Gate Drive Circuits*, [Online]. Available: http://www.radio-sensors.se/download/gate-driver2.pdf

[12] Multicomp, *US1M, Ultra-Fast Recovery Diode Datasheet*, 2011, [Online]. Available: http://www.farnell.com/datasheets/1464448.pdf

[13] TT Electronics, *PWC series pulse withstanding chip resistors datasheet*, 2014, [Online]. Available: http://www.ttelectronicsresistors.com/datasheets/pwc.pdf

[14] Philip C. Todd, *Snubber Circuits: Theory, Design, and Application*, Application Note, Unitrode Corporation, 1993.

[15] Avago, *HCPL-2400, 20 MBd High CMR Logic Gate Optocoupler Datasheet*, 2008, [Online]. Available: http://www.avagotech.com/docs/AV02-0962EN

[16] Fairchild Semiconductor Corporation, *LVDS Fundamentals*, AN-5017, 2006, [Online]. Available: http://www.fairchildsemi.com/an/AN/AN-5017.pdf

[17] G. Choi, *13.56 MHz, Class-E, 1 kW RF Generator using a Microsemi DRF1200 Driver/MOSFET Hybrid*, Application Note 1811, Rev. B, MicroSemi PPG, 2011, [Online]. Available: http://www.microsemi.com/document-portal/doc_download/123873-drf1200-13-56mhz-reference-design-kit

[18] G. Choi, *13.56 MHz, Class-D Half Bridge, RF Generator with DRF1400*, Application Note 1817, Rev. E, MicroSemi PPG, 2012, [Online]. Available: http://www.microsemi.com/document-portal/doc_download/124244-drf1400-13-56-mhz-class-d-half-bridge-rf-generator

[19] DesignSoft, *TINA Pro Circuit Simulator for Analog, RF, Digital, MCU, HDL, Symbolic & Mixed Circuit Simulation with Integrated PCB Design*, 2016, [Online]. Available: http://www.tina.com

[20] R. E. Kerber, et al., "Advance prediction of transthoracic impedance in human defibrillation and cardioversion: importance of impedance in determining the success of low-energy shocks", *Circulation*, Vol. 70, No. 2, pp. 303-308, 1984.

[21] Angiodynamics, *Rita 1500x User's Guide and Service Manual*, Rev. 3, [Online]. Available: http://www.angiodynamics.com/uploads/pdf/102210-114840_Model%201500X%20IFU.pdf

[22] M. Puc, et al., 'Techniques of signal generation required for electropermeabilization. Survey of electropermeabilization devices', *Bioelectrochemistry*, Vol. 64, No. 2, pp. 113-124, 2004.

[23] K. H. Schoenbach, et al., "The effect of pulsed electric fields on biological cells: experiments and applications", *IEEE T Plasma Sci*, Vol. 25, No. 2, pp. 284-292, 1997.

[24] C. Gabriel, S. Gabriel and E. Corthout , "The dielectric properties of biological tissues: I. Literature survey", *Phys Med Biol*, Vol. 41, No. 11, pp. 2231-2249, 1996.

[25] S. R. Smith, et al., "Dielectric Properties of VX-2 Carcinoma Versus Normal Liver Tissue", *IEEE T Biomed Eng*, Vol. 33, No. 5, pp. 522-524, 1986.

[26] S. Laufer, et al., "Electrical impedance characterization of normal and cancerous human hepatic tissue", *Physiol Meas*, Vol. 31, No. 7, pp. 995-1009, 2010.

[27] Tektronix, *Data sheet for Tektronix TDS1000B or TDS2000B Series*, 2010, [Online]. Available: http://www2.tek.com/cmsreplive/psrep/13295/3GM_19558_2_2011.02.10.07.25.34_13295_ES-MX.pdf

[28] J. Gehl, et al., "In vivo electroporation of skeletal muscle: threshold, efficacy and relation to electric field distribution", *Biochim Biophys Acta*, Vol. 1428, No. 2-3, pp. 233-240, 1999.

[29] D. A. Neaman, *Semiconductor Physics and Devices – Basic Principles*, 4th Ed., New York, McGraw-Hill, pp. 388-393, 2012.

CHAPTER 4

ELECTROPORATION OF ISHIKAWA HUMAN CANCER CELLS

4.0 Introduction

The previous chapter detailed the design, development and electrical testing of a novel electroporator pulse generator system. This chapter follows by detailing experimental work carried out on human cancer cells in order to characterise the electroporator in application, and in particular to examine the results obtained utilising the novel properties engendered in its design, namely high frequency and bipolar capabilities. These capabilities contrast with commonly available commercial electroporators that mostly do not offer bipolar pulses and are not capable of producing the high frequencies at high voltage as generated by this new apparatus. The primary goal of these experiments was to gauge the effective degree of electroporation on human cancer cells, particularly Ishikawa cells, under a range of different frequencies, electric field strengths, and durations of pulses, and to compare bipolar with monopolar pulses. Within this context, one of the electroporation results of particular interest is that of a maximal population of viable electroporated cells – that is, to identify a set of pulse parameters that maximises the overall number of viable electroporated cells in the continuum between 0 % electroporated – 100 % viable to 100 % electroporated – 0 % viable. Such a result is of particular importance for applications requiring the maximum number of effectively treated cells to remain viable (such as for gene therapy [1, 2], certain immunology applications [3, 4], and recently also for genome editing [5]). In opposition to the above-mentioned notion of maximal loading with minimal direct killing of cells, irreversible electroporation seeks to achieve maximal direct killing of cells without the need for loading of external molecules and may also benefit from these studies presented in this chapter [6].

This chapter starts off by discussing the design of the cuvette and its modelling – the chamber containing the electrodes into which the cancer cell suspensions are placed and electroporated. This is followed by two sets of experiments, the fluorescence microscope and flow cytometer

experiment sets. Each of these experiment sets is presented with its own experimental method, results and discussions, followed by a conclusion.

4.1 Cuvette Design and Modelling

In biochemistry a cuvette is a straight-sided, optically clear container for holding liquid samples in a spectrophotometer or other instrument [7].

A cuvette to be used in electroporation studies must have an ease of electrical connection. It must also be robust, inert and non-toxic. This is required as the cuvette must hold live cells that are to be stressed severely by application of very high magnitude electric field pulses – and additional stress factors are likely to unduly affect the results of the experiments.

Commercial cuvettes were considered (a number of typical commercial cuvettes are shown in figure 4.1), but these require a large amount of fluid/suspension for proper operation. It was identified that for the intended experiments only a small suspension volume would be practical and would require much less cell culture and electroporation media. This decision had a significant economic advantage over use of commercial cuvettes used in biotechnology.

Figure 4.1. Typical commercial cuvettes from Bio-Rad [8], Eppendorf [9], BTX [10], and USA Scientific [11], respectively, from left to right.

The cuvette required the following set of properties:

1. Inert/non-toxic: Comprise materials that do not interact with cells and are unlikely to be toxic.

2. Robust: Capable of being used for several months' worth of experimental work.

3. Easy to connect to: Have protruding metal tabs for ease of electrical connection.

4. Optically clear: For ease of observation by an optical microscope.

5. Simple design: To be quick and easy to design and fabricate.

6. Small: Should not use more than about 50 μL of cell suspension to fill it.

7. Dimensionally accurate: Provide a uniform electrical field throughout its cell suspension chamber.

Several cuvettes were designed, including two examples shown in figure 4.2.

Figure 4.2. Photographic images of early cuvette designs. The left image shows a set of stainless steel electrodes separated by 10 mm. The right image shows a set of aluminium co-planar electrodes with the cell chamber enclosed by home craft putty (Bostik Blu Tack), which was difficult to seal, allowing the medium and cells to escape.

Early versions of cuvettes shown in figure 4.2 failed for several reasons, including too-large separation of the electrodes (10 mm) requiring very high voltages to maintain fields up to 3.5 x 10^5 V/m, poor fixing of the electrodes onto the container (glass Petri dish), and particularly poor containment of cells in suspension – continual movement of cells or particles due to hydrodynamic motion of the fluid. Other problems included leakage and shifting of electrodes due to insufficient adhesive strength.

With the required properties and prior cuvette designs in mind, glass, silicone rubber, and aluminium were selected as construction materials. Although aluminium is not entirely inert, it was selected due to its low cost, ease of working and reasonably low toxicity, considering that the cell suspension was only going to be in the cuvette for less than a minute and that bipolar electrical fields used would effectively minimise release of the metal ions [12]. Also, media were replaced shortly after electroporation. Commercial cuvettes for electroporation (based on monopolar pulses) also use aluminium electrodes.

Sylgard 184 silicone elastomer, polydimethylsiloxane (PDMS) from Dow Corning [13], was used to form the cuvette chamber, and to cover the rest of the electrode material not forming two of the cuvette chamber walls. Toxicity of the cured PDMS material has been declared by the material safety data sheet (MSDS) [14] as low and it has been successfully used for culturing fibroblast cells in microfluidic chambers [15]. An image of the final cuvette design is shown in figure 4.3.

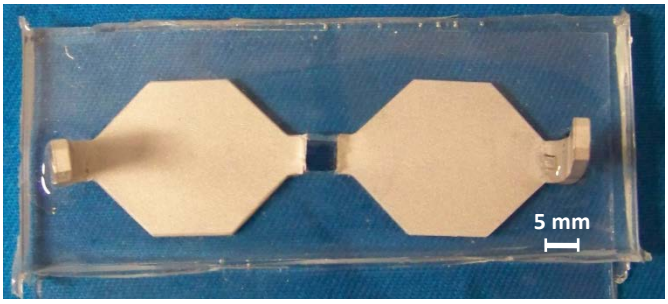

Figure 4.3. Photograph of the cuvette. This plan view shows the two aluminium electrodes located directly above a glass slide and embedded in polydimethylsiloxane (PDMS - a type of silicone rubber) with a 4 mm x 5 mm cut-out to form the chamber.

The glass slide has dimensions of 75 mm x 25 mm x 1 mm and consists of soda-glass (soda lime silica). The aluminium electrodes were fabricated from 2 mm aluminium plate and have a width of 5 mm and are separated by 4 mm to form the chamber into which the cell suspension is pipetted. The protruding tabs of the electrodes allow easy connection of "crocodile" clips from the electroporator leads, and also easy connection of an oscilloscope probe for electric potential monitoring.

Static field modelling was performed on this cuvette design. Table 4.1 presents the parameters used and the finite element analysis (FEA) software tool COMSOL Multiphysics Version 4.2 was used to produce the cross sectional field and potential distribution plots.

The set of parameter values given in table 4.1 provide a starting point, although they are considered constant across frequencies and under constant external applied conditions – this is not true in real cells, but nevertheless assist in providing an understanding of effects.

Table 4.1. Parameters used for the models, based on [16, 17].

PARAMETER DESCRIPTION	PARAMETER
Cell diameter	10 µm
Membrane thickness	5 nm
Intracellular medium conductivity	0.3 S/m
Extracellular medium conductivity	0.3 S/m*
Membrane conductivity	0.3 µS/m
Intracellular relative permittivity	80
Extracellular relative permittivity	80
Membrane relative permittivity	5

** As opposed to physiological mammalian conductivity of around 1.6 S/m*

The electroporator chamber design discussed earlier in this chapter is modelled as shown in figures 4.4 and 4.5.

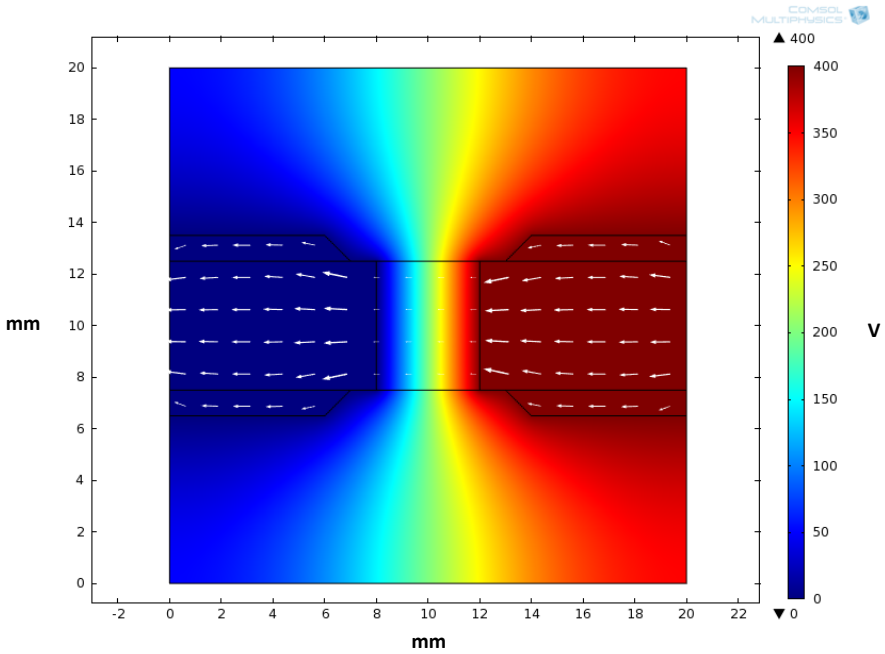

Figure 4.4. Comsol two-dimensional model of the electroporator chamber (plan view) exposed to a field of 1 x 10^5 V/m. Potential distribution and also current density and direction (white arrows) in and around the chamber.

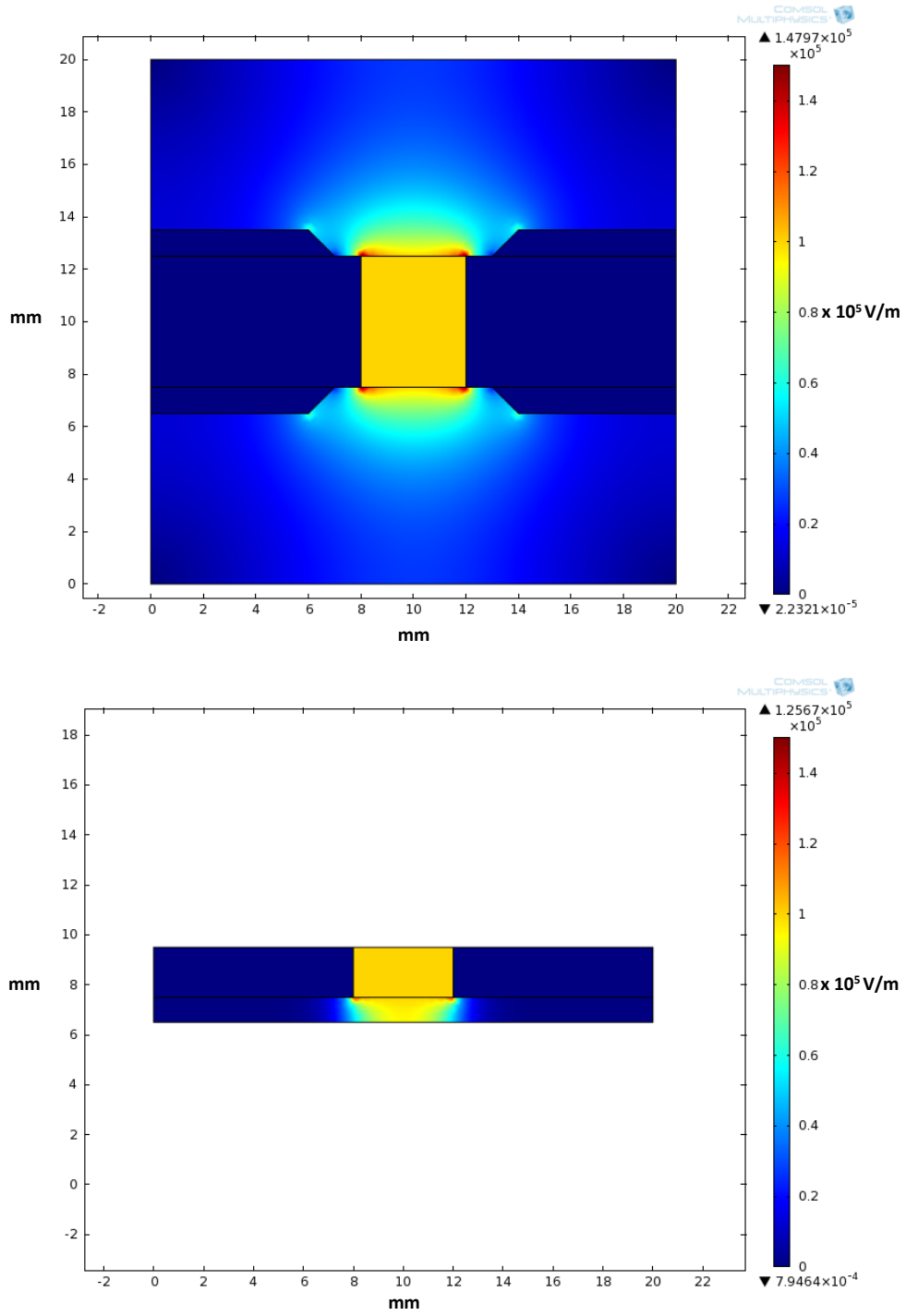

Figure 4.5. Comsol two-dimensional model of the electroporator chamber exposed to a field of 1 x 10^5 V/m showing the electric field distribution through and around the centre cross-sectioned chamber. a) The top image shows the plan view and b) the bottom image shows the lateral view. The upper boundary is air, the bottom material is glass, and the very dark blue material is aluminium (electrodes).

As observed in figure 4.5, the consistent near orange colour of the inside of the electroporator chamber suggests a predominantly constant electric field value of 1 x 10^5 V/m, and most cells

within this region will be exposed to a uniform electric field. When instead applying a rapidly changing potential across the lateral electrodes, it can be argued that the electric field will remain proportional and respond nearly immediately as there is only a very small inter-electrode capacitance, estimated at approximately 10 pF (using a basic parallel plate capacitor model with water as the dielectric). This meets the requirements for the cuvette in this thesis. Experimental work on cells now follows.

4.2 Fluorescence Microscopy Analysis of Electroporation

4.2.1 Materials and Methods

4.2.1.1 Cell line and reagents

Ishikawa cells, a commercially available, commonly used and well-defined human endometrial adenocarcinoma cell line [18, 19], which were gifted by Dr Masato Nishida from Japan [20] to the Otago University School of Medicine in New Zealand, were used for this study. These cells were chosen mainly for availability, ease of culture and prior experience by a colleague at Otago University. Also, they were selected for their property of adherence to surfaces, making them ideal for culture into spheroids – agglomerations of cancer cells that may be used to better emulate 3-D tissue structure [21]. While a non-adherent cell line would have been simpler to culture and assay when using a suspension, since adherent cells need to be regularly agitated to minimise unwanted clumping and adhesion to surfaces (some clumping and adhesion is always present), the intent to carry out spheroid-structure electroporation experiments in the future warranted this manageable amount of extra work. Cells were cultured in a medium of Dulbecco's Modified Eagle's Medium (DME) and Ham's F-12 Nutrient Mixture, DMEM/F12 (Gibco 12400-024, Invitrogen, New Zealand), supplemented with 10% foetal bovine serum, 1 % Glutamax (Gibco 35050-061, Invitrogen) and 1 % Penicillin/Streptomycin (Gibco 15070-063, Invitrogen). Trypan Blue (TB) dye (Gibco 15250-061, Invitrogen) was used, as means of identifying dead cells during culture and also ultimately to detect cells which have not recovered from electroporation. TB is routinely used as a marker for non-viable cells [22]. A non-permeant red fluorescent dye – propidium iodide (PI)(Molecular Probes P3566, Invitrogen) – was also used to penetrate cells whose membranes have been electroporated. Use of this dye was especially useful for counting of electroporation affected over unaffected cells.

A low conductivity electroporation buffer (EPB) was used. It was made up by diluting 100 % chlorine and magnesium-free phosphate-buffered saline (PBS) to 1/16.5 concentrate then adding 1 g sucrose to make up 10.7 mL 1x EPB. The EPB was designed to have a physiological equivalent osmolarity of around 290 mOs (iso-osmolar) [23] – this was to avoid undesirable cell shrinkage or swelling that may lyse/kill cells. Low electrical conductivity was required to avoid unnecessary voltage drooping when using low pulsing frequencies in the order of 10 kHz due to the limited capacitor storage of the electroporation apparatus. Low electrical conductivity was also needed to avoid unnecessary joule heating of the suspension. This buffer medium was based on the buffer used in [24] which had a conductivity of 0.13 S/m.

4.2.1.2 Cell culturing

Cells were cultured and maintained in vented 25 cm^2 flasks (Corning, PS, 430639, Sigma-Aldrich) and were incubated (Contherm Mitre 4000) at 37 ^{0}C in an atmosphere of humidified air with 5 % CO_2. Cells were cultured until they reached 70 % to 80 % confluence, then sub-cultured. The growth medium was replaced every two days until the next sub-culture was performed. Sub-culturing started with removal of used medium, washing of the cell monolayer with PBS (Molecular Probes 00-3002, Invitrogen), and gentle loosening of the cells with trypsin-EDTA ((Ethylenedinitrilo)tetra-acetic acid)(Gibco 15400-054, Invitrogen). After 5 minutes incubation at 37 ^{0}C, addition of fresh medium, centrifugation at 1000 rpm for 5 minutes using the Heraeus Labofuge 300 Centrifuge, aspiration of the supernatant, performance of a cell count using a haemocytometer (improved Neubauer type Bright-Line Haemocytometer, Sigma-Aldrich), then re-seeding at around 0.5 x 10^6 cells/mL into a new sterile vented flask was carried out in that order. Viability of cells was verified using TB dye which ascertained a very high viability was routinely achieved with a very low (negligible) percentage of non-viable cells (5 % or less). This process was repeated several times until experiments were performed. The inverted microscope used was the Nikon Eclipse TS100. An image digitiser from Ximea (XiQ USB3) was also used to view and capture images during cell counting and after electroporation for later visual analysis.

4.2.1.3 Electroporation

Once sufficient cells were cultured, cells in suspension were harvested at a concentration of 3 x 10^6 cells per mL in culture medium. This concentration was used to provide a final concentration of around 1 x 10^6 cells/mL in the cuvette. Several 100 µL samples were made up in Eppendorf tubes and incubated at 37 ^{0}C for at least 5 minutes. A sample was then centrifuged for 1 minute at 1000 RPM, immediately followed by pipette removal of supernatant, and addition of 90 µL EPB (at room temperature) and gentle tapping of the tube to guarantee a homogenous suspension of cells. Immediately following this, 5 µL propidium iodide (PI) was added for a final PI concentration of 10 mg/L (15 µM). The sample was then incubated at room temperature. Aliquots of 45 µL of this solution were pipetted into two identical separate electroporation chambers (Control and Experiment) at room temperature, and electroporated, using a particular pulsing regime. Immediately afterwards the chamber samples were extracted by pipette and placed in fresh Eppendorf tubes. They were both then centrifuged for 1 minute at 1000 RPM and supernatant was discarded and pre-warmed culture media was added. Then they were again incubated at 37 ^{0}C for 5 minutes to ensure adequate binding of the fluorescent dye with nuclear material and recovery of the cells. This was followed by tapping of the tubes and taking 10 µL from each tube (Control and Experiment) and loading of the respective sides of a marked haemocytometer. The

haemocytometer was placed under the microscope and assayed for fluorescence. The assay normally involved viewing both the Control and Experiment samples, looking at 5 random squares (out of the 9) and recording the images for later counting. Each square was viewed using either both bright light and fluorescent light or only fluorescent light (dark view). This assisted with the counting of all cells and only the fluorescing cells. Finally these sets of cells were counted from the images and recorded. These counts represented unaffected cells and electroporated cells in the sample (dead or alive).

PI, a fluorescent dye that fluoresces at an orange-red colour (617 nm), is a commonly used dye to indicate cell non-viability. It is a non-permeant dye which can normally only penetrate a cell membrane when the cell is non-viable and the membrane has become permeable [25]. It is unlike TB in that it can fluoresce and is not as toxic [22]. Because it is non-permeant, PI can be used to indicate both reversible and irreversible electroporation. With the medium containing PI before and during electroporation, PI will penetrate electroporated cells and fluorescence can be observed in the cell cytoplasm as it binds with nucleic acids [26]. This binding with nucleic acids amplifies fluorescence of the dye by a factor of 20 to 30 times [27]. On the other hand, when cells are electroporated in a medium not containing PI, but having PI added afterwards, the dye will then penetrate cells that have been irreversibly electroporated, given that ample time has elapsed for viable cells to recover to a relatively normal membrane permeability. As a major application of electroporation in this thesis is electrochemotherapy, it is the intention to maximally load target cells (tumour cells) with a chemotherapy drug, such as bleomycin or cisplatin. Since these drugs are relatively small molecules (1450 Da and 300 Da, respectively), PI (668 Da)[28] is considered a suitable substitute to indicate penetration into cells via the plasma membrane, and thus uptake into cells. The level of fluorescence can be related directly to the amount of uptake of PI, and thus of other drugs when they are used. So, with PI additionally being easy to detect it is an ideal candidate for electroporation assays for applications like electrochemotherapy.

In this experiment the process identified above was repeated 3 times in short succession using 3 samples, and data were collated. The whole experiment was then repeated 3 times and final data were produced by averaging the repeated results for single points on a graph. For exact details of the electroporation protocol, refer to Appendix E. Appendix F details the sub-culturing protocol used.

4.2.2 Results and Discussion of Fluorescence Microscope Experiments

A typical microscope image where electroporated cells are seen fluorescing post treatment as they are emitting red-orange light is shown in figure 4.6.

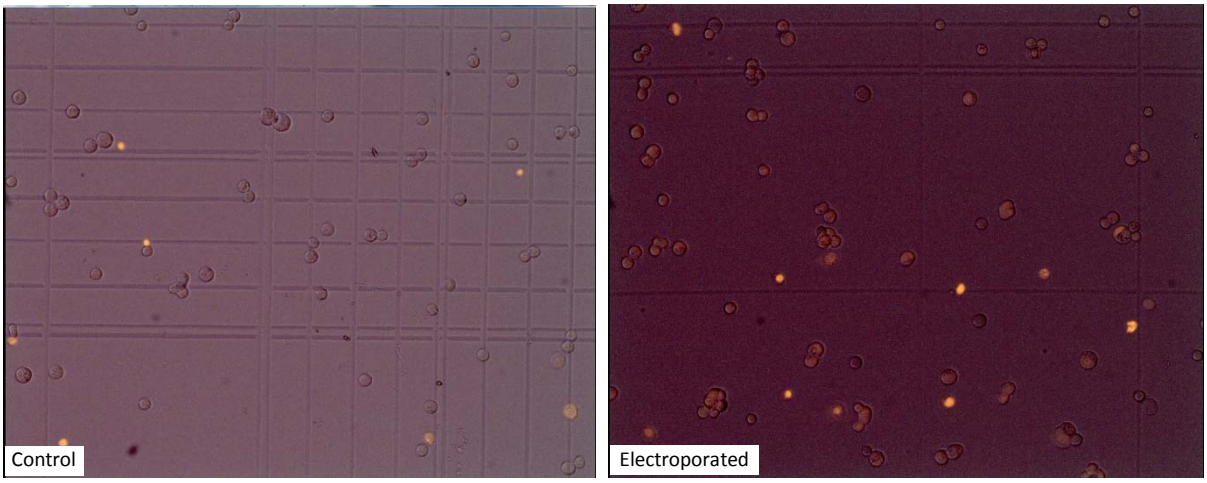

Figure 4.6. Microscope images showing fluorescing Ishikawa cells. This set was produced when two 3.0 x 10^5 V/m, 100 kHz bipolar square wave pulse bursts of 500 µs duration, separated by 1 s, were applied to the electroporated sample of 45 µL.

In the left microscope image of figure 4.6 there is clearly very few cells fluorescing, while in the right image the great majority are fluorescing (some significantly more than others), indicating a very high electroporation rate as expected. The highly fluorescing cells in the Control sample most likely indicate compromised or dead cells, since they were not electroporated and should thus not contain fluorescent dye. In the right image there is a mix of bright and dimly fluorescing cells. The bright cells indicate compromised or dead cells and the dimmer ones indicate electroporated but viable cells. A very small fraction of the cells did not fluoresce – these cells are taken as not electroporated. As can be seen in figure 4.6, the bright non-viable cells are mostly very small. The bright cells had similar counts for both images indicating that for these electroporation settings very few cells were made non-viable as a result of electroporation. When subtracting the bright cell fraction in the Control from the total fluorescing fraction of the electroporated sample, the result is the fraction of cells specifically and successfully electroporated and is defined as the electroporation Yield. Another noteworthy aspect is the large portion of clumped cells, especially in the experiment sample. This was due to the elapsed time during the experimental procedure, during which the cells tend to form clumps as they are very adherent.

For the electrical regime, a range of peak electric field pulse magnitudes of up to 3 x 10^5 V/m was used. Two bursts of 100 kHz bipolar alternating current (or "bipolar" for short) square wave

pulses for a duration of 500 µs each, separated by 1 s. This regime was originally based on another study [29] where 8 pulses of 1 ms square waves were used, each pulse separated by 1 s. This burst length and number of bursts were reduced for electroporation of cell suspensions to the 2 bursts of 500 µs, since this reduces the amount of power delivered to the suspension media yet facilitates observation and study of the full range of electroporation effects, from no discernible electroporation to full effect where essentially all cells appear to have been electroporated. The results are presented in figure 4.7.

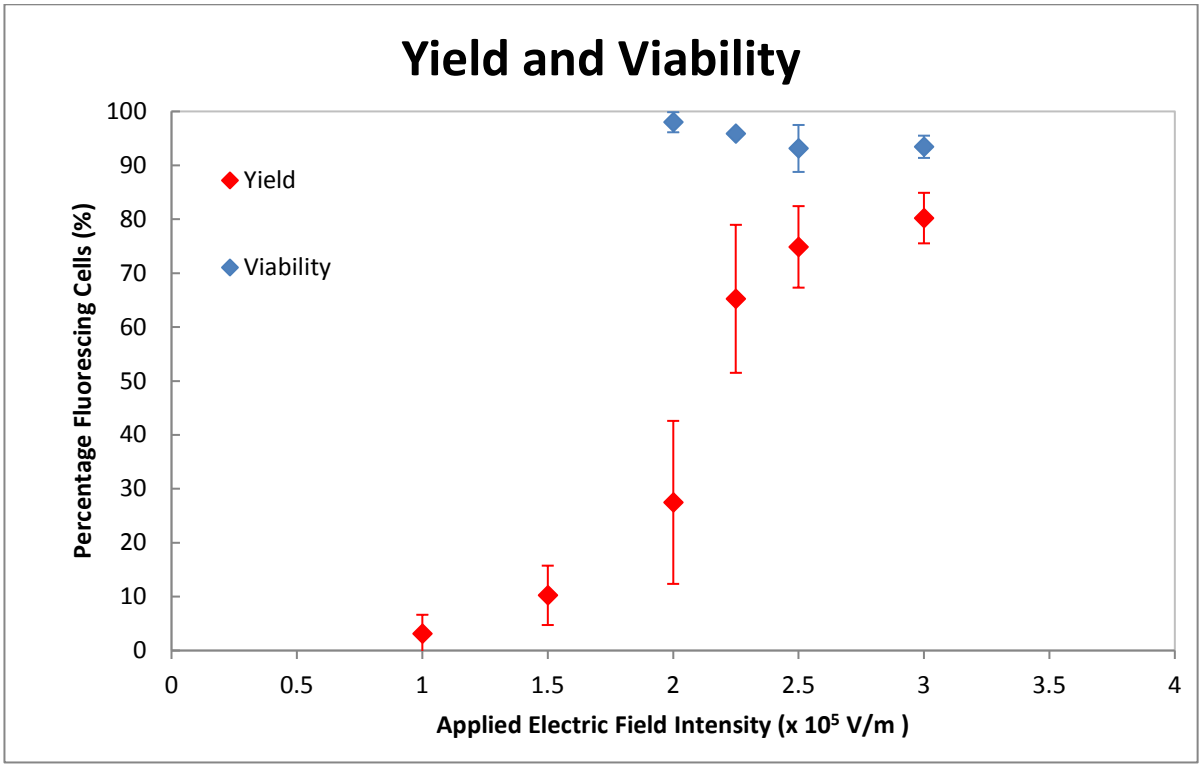

Figure 4.7. Percentage of electroporation-generated fluorescing Ishikawa cells (relative to entire cell population) plotted against electric field strength (2 bipolar square wave pulses of 500 µs duration at 100 kHz) – Yield (red data points). Percentage of viable cells (relative to entire cell population) – Viability (blue data points). Error bars show ± one standard deviation.

The horizontal axis of figure 4.7 represents the peak electric field strength amplitude and the vertical axis represents the percentage of live cells that have been electroporated relative to the entire cell population. The characteristic S-shaped curve is observed [30]. Raw fluorescing cell data post-electroporation include cells that were non-viable before electroporation. The average count of pre-treatment non-viable cells is subtracted from the raw fluorescing cell counts to give the Yield data. Yield is calculated as

$$Yield = \frac{Total\ number\ of\ fluorescing\ cells\ in\ electroporated\ sample}{All\ cells\ in\ electroporated\ sample} - \frac{Total\ number\ of\ fluorescing\ cells\ in\ Control\ sample}{All\ cells\ in\ Control\ sample} \cdot 100\ \% \quad (4.1)$$

Control data show quite a significant fraction of high fluorescing cells, ranging from about 10 % to 12.5 %. The spread of values appeared to range between 3 % and 5.5 % for the Control counts, and between 4.1 % and 16.2 % for Electroporated counts and is most pronounced in the steep region of the plot. This may be due to uncertainty in defining the boundary between the low-fluorescence and no-fluorescence cut-off, as this was determined by eye. Another test value was inserted between 2 x 10^5 V/m and 2.5 x 10^5 V/m (2.25 x 10^5 V/m) to increase the datum points in the vicinity of the steep rise. Data values in this steep rise range were considered adequate at an average of 9 data points each. Interpolation of data points at 50 % fluorescence is at about 2.13 x 10^5 V/m for Yield. Yield also plateaus at around 80 %.

The viability study was brief and based on one experiment with 3 samples for each datum point, so cannot be taken as entirely representative. Viability was calculated as the percentage of manually counted cells that were not coloured blue (viable by TB assay) divided by the sum of blue (non-viable) and non-blue (viable) cells in a TB assay, directly after electroporation.

$$Viability = \frac{Number\ of\ non-blue\ cells}{Number\ of\ blue\ and\ non-blue\ cells} \cdot 100\ \% \quad (4.2)$$

However, a general decay was found, but did not drop rapidly as may have been expected. When using high electrical values it can be expected that a larger percentage of cells would die, and a reverse "S" curve would normally be the result. Figure 4.6 shows the concept of a sigmoid electroporation Yield and an inverse sigmoid for Viability. One study, [25], identified an intersection between the Yield and Viability curves at around 50 %, as is shown in figure 4.8. This aspect is discussed again later in this chapter.

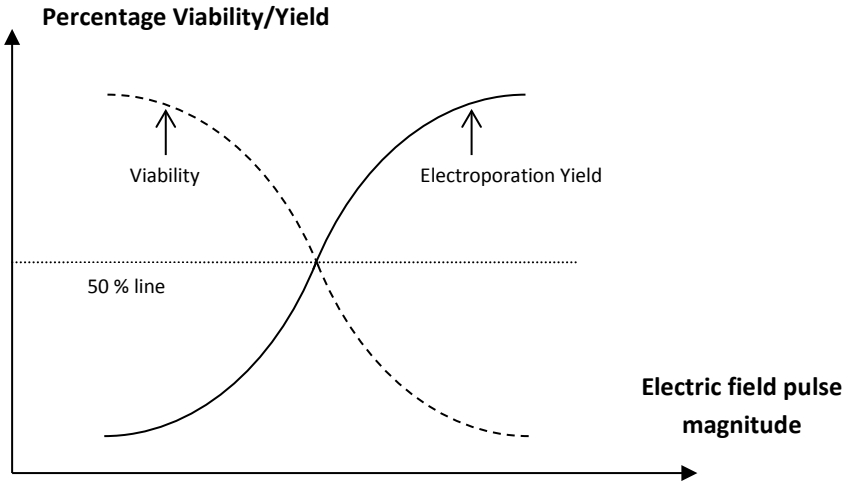

Figure 4.8. Typical electroporation Yield and Viability curves [25].

Not obvious from the data shown in figure 4.7 was the fact that this experimental method was not very productive or efficient. In this instance the experimental work covered a period of approximately 4 months with an estimated 140 hours spent in the laboratory. This experimental protocol was inadequate for the purpose of producing a reasonable body of data for this study within the available time. What also became evident during the counting of fluorescing cells was that some appeared dim, and some appeared bright, and it was impossible to manually rate fluorescence on any useful scale. Video imaging techniques were not employed in this method due to several factors including the large number of samples viewed and especially the lack of a well-controlled bright light setting when determining the counts of both fluorescing and non-fluorescing cells.

Further investigation revealed that a flow cytometer would be a much better candidate for analysis of fluorescence of cells loaded with a fluorescent dye. This modern instrument is capable of counting up to tens of thousands of cells (or particles) per second, and also each cell or particle produces characteristic data such as size, granularity and fluorescence [31, 32]. As such, the experimental data is greatly increased. Flow cytometric fluorescence detection and measurement also has a wide dynamic range of values of several orders of magnitude. This allows fine resolution of fluorescence magnitude that is related to dye uptake and ultimately to cell natural resistance to dye uptake at the one extreme (no electroporation effect) to cell death at the other (including electroporation-induced death). Very little electroporation work has been published with results using flow cytometry techniques, so this technique would produce rare data. For more general information about flow cytometry, consult Appendix G.

4.3 Flow Cytometric Analysis of Electroporation

4.3.1 Materials and Methods

The cell line and reagents were as for the fluorescence microscopy experiments. The protocol used here was very similar to the protocol in the fluorescence microscopy experiments (refer to appendix E for the protocol). The only differences were:

- The concentration of cells used this time for the tube samples was approximately 2 x 10^6 cells/mL (instead of 3 x 10^6 cells/mL).
- The Eppendorf tubes were centrifuged for 2 minutes (instead of 1 minute) to create a higher density pellet that ensures less cell loss during extraction of the supernatant.
- Media added after electroporation was maintained at room temperature (instead of at 37 ^{0}C) to simplify and expedite the process.
- Before and during analysis the tubes were kept in a dark drawer at room temperature close to the flow cytometer until analysed.
- During analysis the tubes were inserted into the flow cytometer one at a time and were assayed using a medium flow rate and 1 x 10^4 particles settings. This process was typically completed within approximately 30 seconds, after which the next tube was started. The choice of 1 x 10^4 cells/particles represented a sizeable percentage (approximately 14 %) of the cells contained in each aliquot. When comparing this to the previous (microscopy) experiment this represents a higher percentage of cells from each aliquot (of about two orders of magnitude).
- The flow cytometer used was a BD Accuri C6 Flow Cytometer from BD Sciences [33] – a modern desktop flow cytometer. Plots presented were extracted from a screen grab of the BD Accuri C6 software interface [34].
- As mentioned earlier, PI has been used to identify electroporated cells (medium containing PI pre-treatment and during electroporation treatment), and to identify cells that were non-viable (PI only added a sufficient time – several minutes – after treatment to detect non-viable cells).

4.3.2 Results and Discussion of the Flow Cytometer Experiments

The range of electrical parameter variations was diverse. Typically, two bursts of a bipolar square wave at various frequencies for a duration of 500 μs each, separated by a duration of 1 second, were used. As stated in Section 4.2.2 this protocol has its origin in another study [29], and was subsequently adopted and adapted for this thesis project. There were several electrical parameters of interest that were manipulated including pulse peak electric field strength, bipolar waveform frequency, pulse type (including bipolar and monopolar pulses), and number of bursts. To ensure appropriate comparison of the effect of pulses across the range of pulse frequencies and between the monopolar and bipolar pulses used, the same peak voltages and thus RMS values have been used.

All experiments included negative controls. Experiments were also performed to produce positive controls. Controls were needed to establish the expected range of fluorescence for all cells, ranging from non-treated cells through to heavily affected cells, including obviously non-viable cells.

Little in-depth electroporation analysis using flow cytometry has been published. A group [35] used a custom-fabricated microfluidic device to study the effect of electric field pulses on mammalian and bacterial cells using a slow monopolar electric pulse regime. They analysed fluorescence intensity against electric field intensity and cell biomechanics such as deformability. The flow cytometry used was simplified in comparison with what modern flow cytometers can produce, hence is of little relevance to this study. Another group [25] studied the effect of electroporation on skin cancer cells in the presence of the cytotoxin bleomycin. Bleomycin is a commonly used chemotherapy drug and it has been used extensively in electrochemotherapy studies [36]. The increase in cell membrane permeability by electroporation increases the transmembrane transfer of the drug in the order of a thousand-fold when used in electrochemotherapy [37]. A single set of overlaid histograms was presented showing the different sub-populations of cells – events against fluorescence intensity. No dot plots were provided. To the best knowledge of the author, no other electroporation studies have focused on flow cytometry in the way presented here.

Figure 4.9 shows typical dot plots for a flow cytometric analysis of an experiment where Ishikawa cancer cells in suspension have been electroporated.

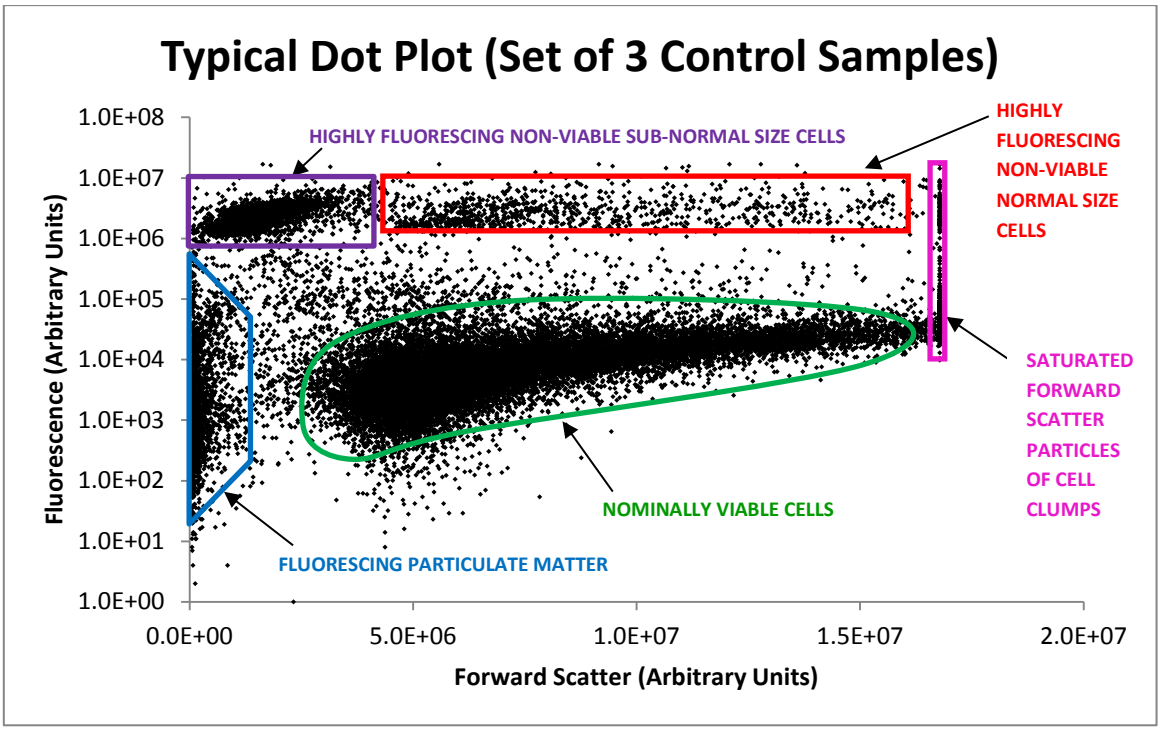

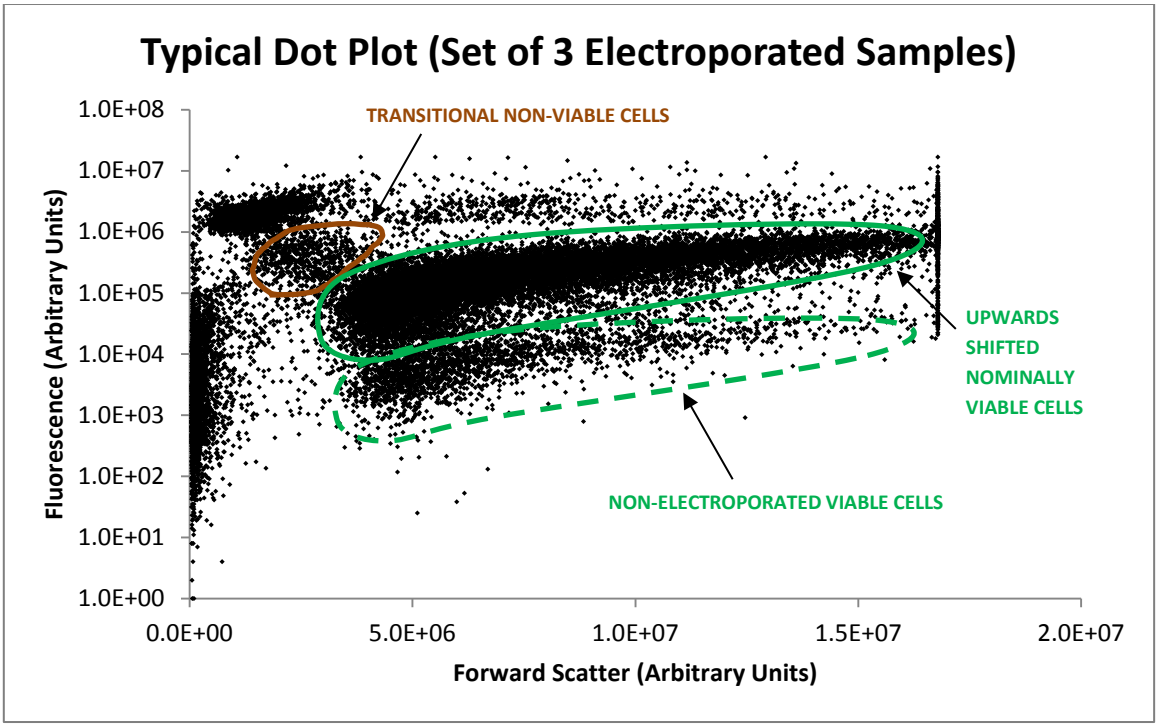

Figure 4.9. Two typical raw log-lin plots from the flow cytometer, plotting fluorescence against forward scatter. The top plot is for a negative control (no electroporation treatment) and the bottom is for samples receiving electroporation treatment of 2.5 x 10^5 V/m peak – 2 bursts of 200 kHz bipolar square waves of a duration of 500 µs, separated by an interval of 1 second. Both samples were chemically and physically treated the same, thus

both received propidium iodide (PI) fluorescent dye. Special features are noted in enclosed regions, representing sub-populations of interest.

The plots shown in figure 4.9 are collections of 3 samples each of 1 x 10^4 particles (a total of 3 x 10^4 particles), collected from the raw data files generated by the flow cytometer software. They were accumulated and processed to form a plot for each electric field setting. One dot represents a detected particle, including cells and any other particulate matter. The vertical axis represents fluorescence (FL3 parameter, arbitrary units) that indicate dye uptake [38, 39] on a log scale while the horizontal axis represents forward scatter (FSC parameter, arbitrary units) that are widely accepted to be proportional to cell size (surface area) [40-42]. Because cell surface area is proportional to the square of the cell radius, this implies that FSC is proportional to the square of the cell radius. Fluorescence is based on an optical emission filter for wavelengths smaller than 670 nm [33], thus passing red emission of PI. Fluorescence is a relative quantity and is measured by a photodetector. A log scale has been used to ease identification of several sub-populations within the entire fluorescence range. For the purposes of flow cytometry experiments it is assumed that the forward scatter and fluorescence units of the flow cytometer have remained stable for the duration of all the reported experiments. Inter-experiment variability in flow cytometry data necessitates the inclusion of a negative control in each experiment, as this is regarded as standard practice [43].

From the plots shown in figure 4.9, the following observations can be made:

- The nominally viable cells (circled in green) represents the sub-population of normal cells (with the enclosed forward scatter range identifying the normal cell size range – the definition of normal cell size range being provided later in this section), showing how that sub-population increases in fluorescence (shifts upwards) as it has been electroporated. Note that the live electroporated cells fluoresce at a much lower intensity than the dead/non-viable cells (highly fluorescing non-viable sub-normal size cells – circled in purple). Also, the dead cells are predominantly much smaller than the live cells. These characteristics are similar to those observed from the optical fluorescence microscopy analysis (see figure 4.7). In the top (Control) plot the nominally viable cells represent the non-electroporated but faintly fluorescing cells. This indicates a very small amount of dye uptake and self-fluorescence that all living cells exhibit, and serves as a negative control or baseline. In the bottom plot (electroporated samples) the nominally viable cells represent the sub-population of live cells that have been electroporated successfully. The Control viable cells lie further to the bottom of the plot than the electroporated cells

showing lower fluorescence by nearly 1.5 orders of magnitude. The shift upwards, indicating increased fluorescence, is the net result of electroporation.

- The electroporation treated nominally viable cells contain a small set of cells which have not substantially increased in fluorescence (circled in dashed green) remaining at a similar fluorescence to the Control nominally viable cells. This is likely to be a sub-population of non-affected (that is not measurably electroporated) and live cells.

- The nominally viable cells sub-population distribution always tends to slope slightly upwards looking along the positive forward scatter axis. This suggests that larger cells fluoresce more than smaller cells. This is a natural consequence of the number of fluorescing dye molecules within a cell, which would be biased towards larger cells as they are likely to trap more fluorescent dye molecules and thus emit more total light. If the nominally viable cells sub-population were to become more horizontal after electroporation (compared to the same population electroporated with a different set of pulse parameters), and/or have a reduced relative distribution of fluorescence within the normal cell size range, this could suggest that the relative degree of electroporation has been made less dependent on cell size [44]. This is potentially an important indicator regarding the effect of electroporation, as a relatively narrower fluorescence and a more horizontal nominally viable cells sub-population distribution would suggest more consistent uptake of the dye over the range of cell sizes in the sample population.

- The small number of highly fluorescing non-viable normal size cells (bounded in red) indicates a sub-population of cells that are in the process of dying or are dead, but still of standard size. The difference in number of cells occupying this area between the Control and treated cell samples is minimal, indicating minimal or no contribution from electroporation to this sub-population for the pulse parameters used.

- The fluorescing particulate matter (enclosed in blue) represents particles mostly of cell fragments and also other small particulate material.

- The transitional non-viable small to sub-normal size cells sub-population (circled in brown) represents heavily compromised cells that are in the process of lysing. These strongly fluorescing cells have clearly shrunk as their size range has dropped, and predominantly no longer fit into the normal range of cell size. While this characteristic is indicative of cells reducing in size due to direct lysis, it is also a characteristic of early apoptosis [45], and as such this possible cell death mechanism could be further investigated.

- The highly fluorescing non-viable sub-normal size cells sub-population (bounded in purple) represents lysed cells. These cells are predominantly below the normal size range.
- The saturated forward scatter particles on the far right (bounded in pink) which represents the sub-population of clumped cells. Due to the Ishikawa cell line being an adherent type, cell clumping commonly occurs, and such cell clumps are excluded in the analyses.
- The majority of the rest of the points in the plot are considered as outliers and represent a very small fraction of all the particles.

Fully linear plots have been used extensively for analysis, as they simplify gating of regions within the dot plot. Most importantly, use of linear plots allowed for extracting simple mathematical relationships between the variables studied. Figure 4.10 shows typical linear dot plots (using the same experimental data set as shown in Figure 4.9).

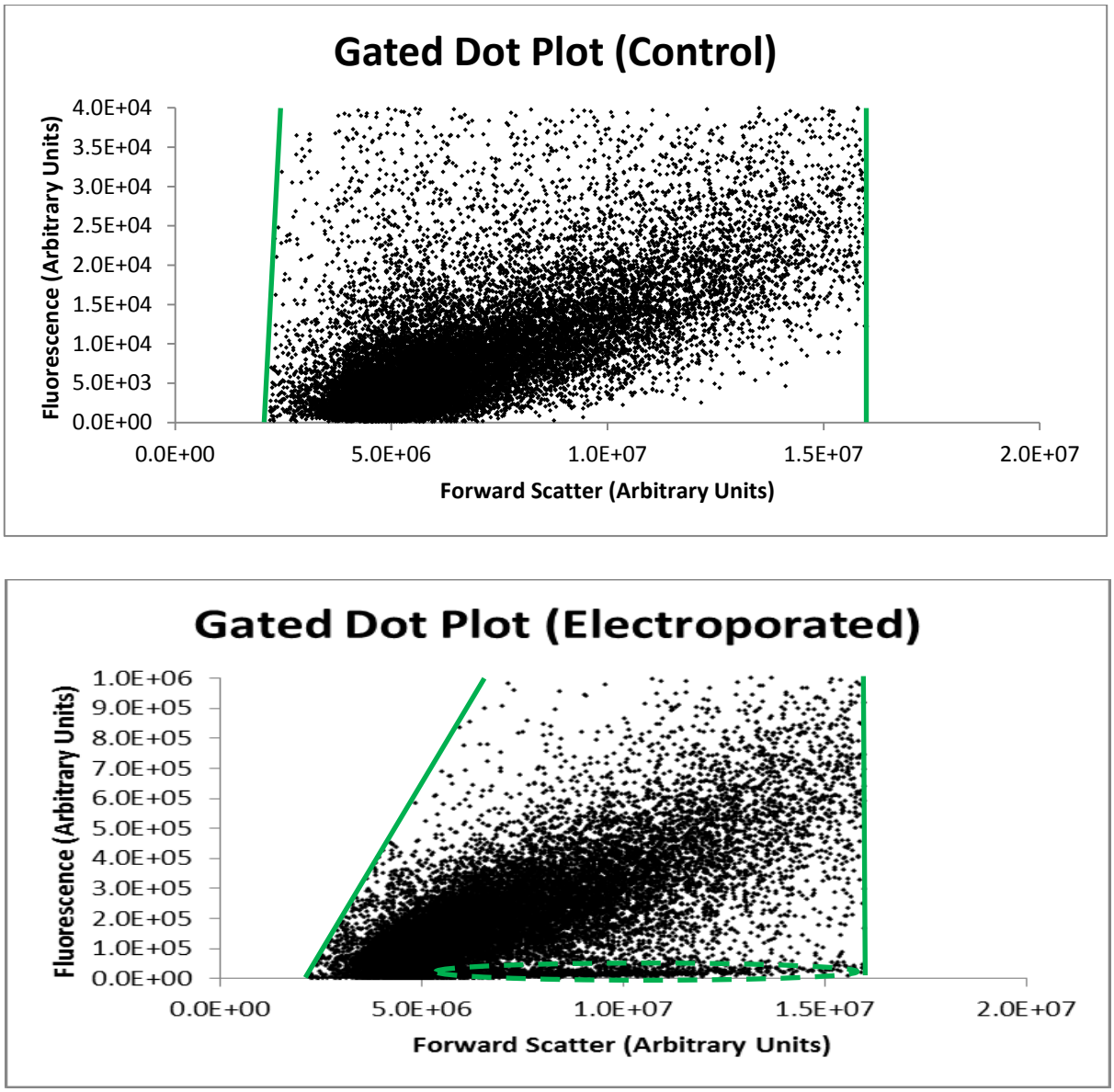

Figure 4.10. Two typical gated plots from the flow cytometer, plotting fluorescence against forward scatter. Green gating lines are included. The top plot is for a negative control (no electroporation treatment) and the bottom is for the electroporated samples (note the vertical scale difference between the two plots). These plots correspond with the data used in the log-lin plots furnished in figure 4.9, gated to show mainly the sub-population of nominally viable normal-sized and electroporated cells. The slim, but distinctive near horizontal grouping in the bottom plot (circled in dashed green) is the immeasurably-electroporated (that is, unaffected or non-electroporated) viable cells sub-population.

From figure 4.10 it can be observed that gating was used. Cells falling in the mainly rectangular region 2.2×10^6 < forward scatter < 16×10^6, and 0.1×10^3 < fluorescence < 2×10^6 were gated to exclude all other cell/particle sub-populations, in order to characterise the viable cells. These criteria are based on smallest viable cell sizes found in the fluorescence microscopy studies of 6.0

(±0.6) µm diameter and largest viable single-cell size of 43 (±4) µm diameter, having observed 40 slides at 250 times magnification using gridlines of an improved Neubauer haemocytometer. Maximum forward scatter was restricted at 16 x 10^6 for practical reasons as there appears to be forward scatter saturation occurring at the flow cytometer's maximum of approximately 16.8 x 10^6, which is likely due to the small number of clumped cells (clumping being an unavoidable feature of an adherent cell line – and can be seen in Figure 4.6). The gate line slope seen on the left side of the plot is due to a need to gate out the transitional non-viable small to sub-normal size cells sub-population from the nominally viable cells. The fluorescence maximum was restricted to 2 x 10^6, as this consistently produced a lower limit for the highly fluorescing non-viable normal size cells sub-population. These gating criteria were consistently applied across all experimental data for analysis.

To investigate whether there was a representative mathematical relationship between the variables, and to examine this across the range of electric field intensities and different frequencies, and between monopolar and bipolar electric field pulses, a maximum cell density (maximum dot density) analysis was performed for each experiment, of which a sample is shown in figure 4.11.

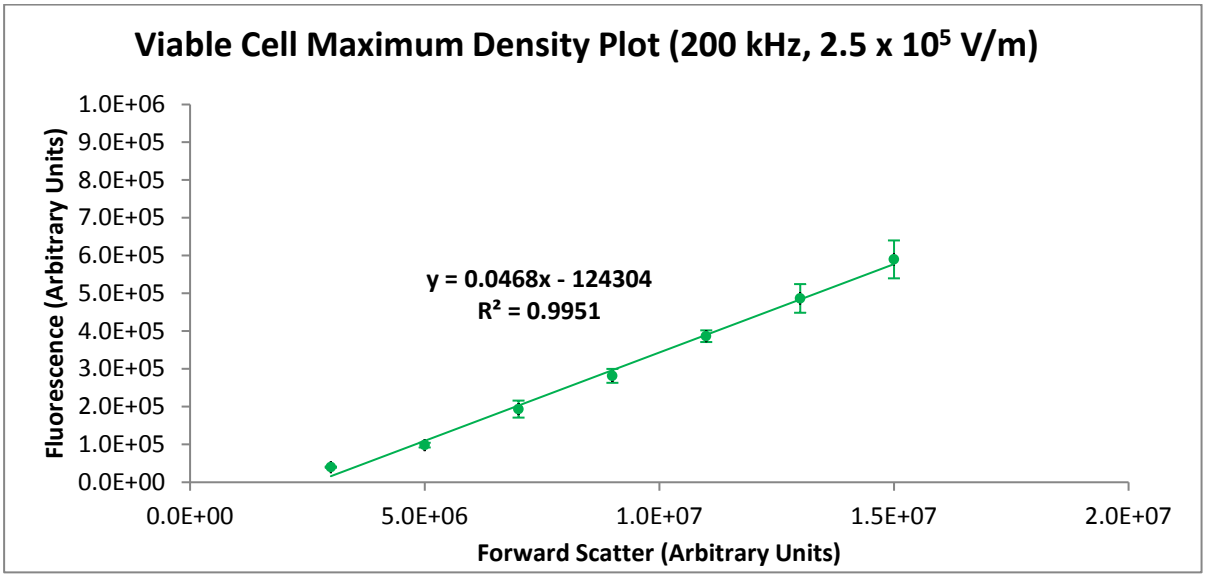

Figure 4.11: A typical maximum cell density plot for 3 electroporated samples at 2.5 x 10^5 V/m using two 200 kHz bipolar square wave pulse bursts for a duration of 500 µs, separated by an interval of 1 s. The green data points represent peak or maximum cell density for the forward scatter bins used. A least mean squares trend line has been added for a linear (green line) best fit, with the accompanying R-squared value as a confidence metric. Error bars are shown for ±1 standard deviation.

The process used to develop the maximum density curve shown in figure 4.11 required several steps. Initial gating of data points was carried out to only include nominally viable cells. Then partitioning of these data points into equal 2 x 10^6 wide forward scatter sections or vertical "bins", ranging from 2 x 10^6 to 16 x 10^6 was performed. A fluorescence histogram for each bin was generated through dividing the fluorescence range into 50 sections (or horizontal bins). The associated fluorescence histogram frequency peak value was then found using a polynomial curve fitting strategy to smooth the histogram curve (see figure 4.12). Finally each of the histogram peak points was plotted (see figure 4.13 for a representative example). To find the histogram peak value, a 5^{th} order polynomial least mean squares best fit algorithm was used to provide consistent high R-squared values of ≥95 % to assure a highly representative smoothed fit. A forward scatter bin width of 2 x 10^6 was selected based on generated data points that show no sudden change from a smooth curve, as there is no expectation of any discontinuity in a biophysical sense. Variation in particle density of viable cells did not appear to occur rapidly in practice. Each vertical forward scatter bin in turn was split up into 50 horizontal fluorescence bins across the occurring range of fluorescence of viable cells for that sample. The 50 fluorescence bins have a width of 2.0 x 10^5 arbitrary fluorescence units in figure 4.12, but have been varied to account for the different fluorescence ranges between separate sets of data (keeping the total number of fluorescence bins at 50). The maximum density plot represents only viable cells, with all other (non-viable) cells and particulates removed. Emerging from this plot are characteristic relationships that relate to the largest number (highest density) of affected cells in the sub-population of the nominally viable cells.

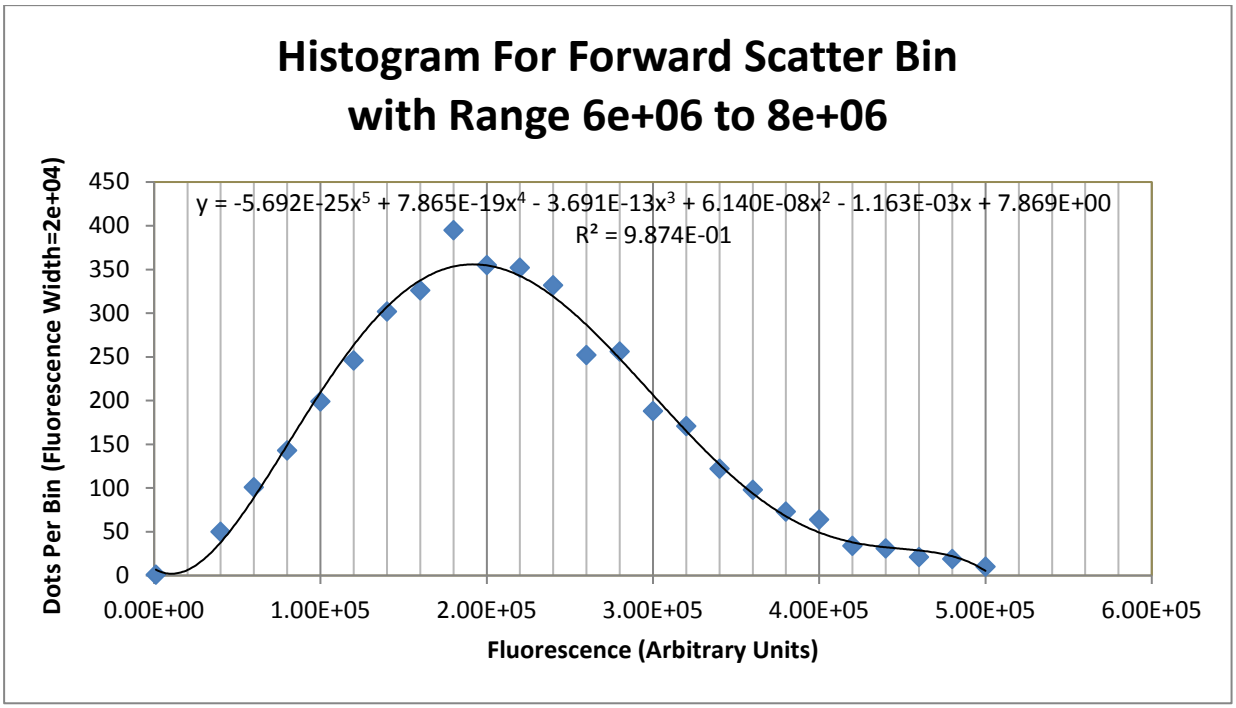

Figure 4.12. Histogram for the forward scatter bin with range 6 x 10^6 to 8 x 10^6 forward scatter units, with fitted 5th order polynomial curve for 1 electroporated sample at 2.5 x 10^5 V/m using two 200 kHz bipolar square wave pulse bursts for a duration of 500 µs, separated by an interval of 1 s. For curve-fitting, a least mean squares best fit algorithm was used to derive the polynomial expression shown on the plot. The R-squared value is also shown, to represent confidence. The result for this fit was a peak at 1.91 x 10^5 Fluorescence Units.

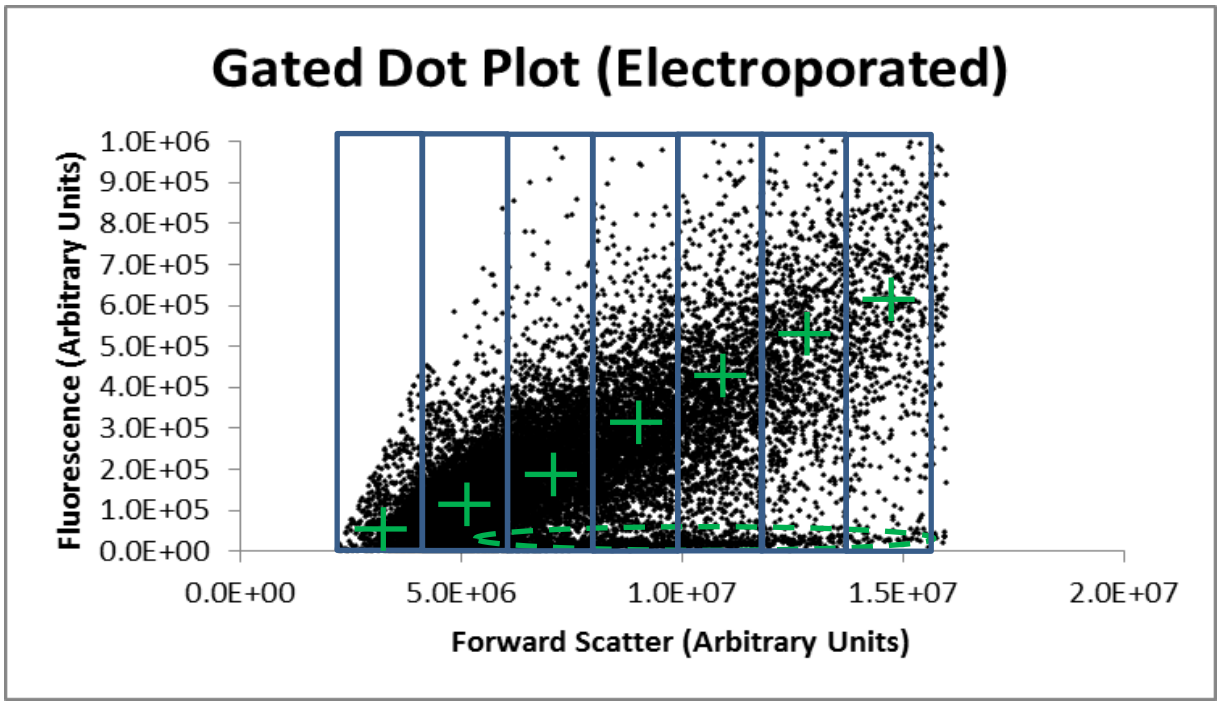

Figure 4.13. A dot plot showing how peak values for fluorescence histograms were produced for the 7 vertical forward scatter bins (blue rectangles) of width 2 x 10^6 forward scatter arbitrary units. The green crosses represent the positions of the peaks of the fitted histogram curves (taken across the 50 horizontal fluorescence axis bins – horizontal bins not shown), and indicate the maximum dot density point for that bin and are located in their geometric centres. Not shown is the effect of the thin horizontal dense region (circled in dashed green), which produce small but sharp peaks in the smoothed histogram curves in that vicinity, but which were ignored as they represent a different sub-population of cells (viable normal-sized cells not measurably electroporated after treatment).

A linear least mean squares approach has been used to determine a best fitting linear trend line for the discrete peak values identified for each set of electrical parameters in the following sections. This has become the standard means of analysis for all density curves in this chapter due to its success with high R-squared values in the order of 0.99, implying high confidence. A second order polynomial fit was considered initially, but was discounted due to the existence of the transitional non-viable cell sub-population, which is located close to the lower cell size peak value but with a slightly higher fluorescence. This transitional non-viable sub population tends to skew the peak density value by increasing its apparent fluorescence value and favouring a slightly curved (second order) fit (see the lowest forward scatter-fluorescence data point in figure 4.11 for an example).

Several studies were conducted and have been grouped into several categories including control studies, bipolar *vs* monopolar studies, and general frequency-magnitude studies. This set of sections is concluded with a list of general observations.

4.3.2.1 Control studies

It was necessary to establish base lines for unaffected cells and dead cells, and also how experimental method time affects results. Control studies included time studies, a PI concentration study, a very high pulse parameter electroporation study and a viability study. These are now presented below.

4.3.2.1.1 Time studies

Two time control studies were conducted including one without electroporation and one with electroporation in order to determine whether typical experimental method durations had an effect on the uptake of dye by the cells and therefore have an effect on the results. Over a period of 40 minutes, an analysis was performed every 10 minutes. Forty minutes was considered enough time as this was equivalent to the maximum time taken to perform the flow cytometric analysis for each experimental session. Two to three samples were analysed at each time point. Figure 4.14 shows results for no electroporation (normal negative control in the electroporation experiments) and figure 4.15 shows results for electroporation.

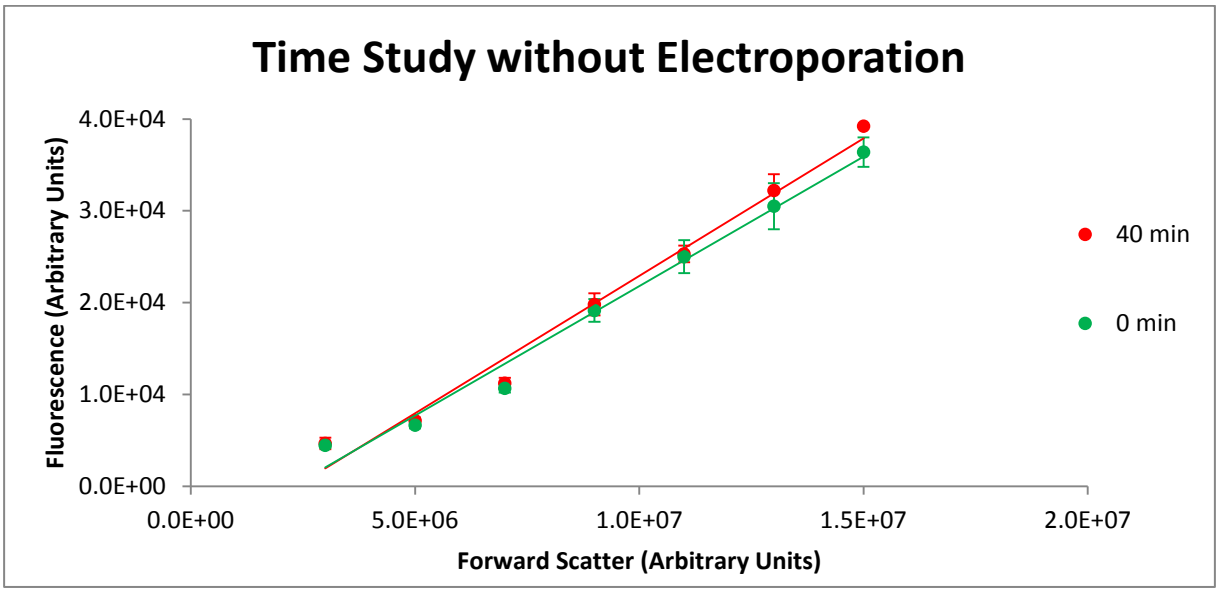

Figure 4.14. Time study maximum viable normal-size cell density plot without electroporation showing a minimum time result (0 minutes) and a maximum time result (40 minutes), to provide a maximum time contrast. Error bars are shown for ±1 standard deviation. Least mean squares linear trend lines have been included.

For the study without electroporation (results shown in figure 4.14), a small observable difference can be seen of a slight increase in fluorescence over time. This difference is easily within the expected range of experimental error (see also section 4.3.2.2) due to the small set of repeat experiments, slight experimental variations, for example when pipetting off slightly different amounts of the supernatant after centrifuging, and natural variation in cell fluorescence levels. Figure 4.15 presents the results of a time study where the cells have been electroporated.

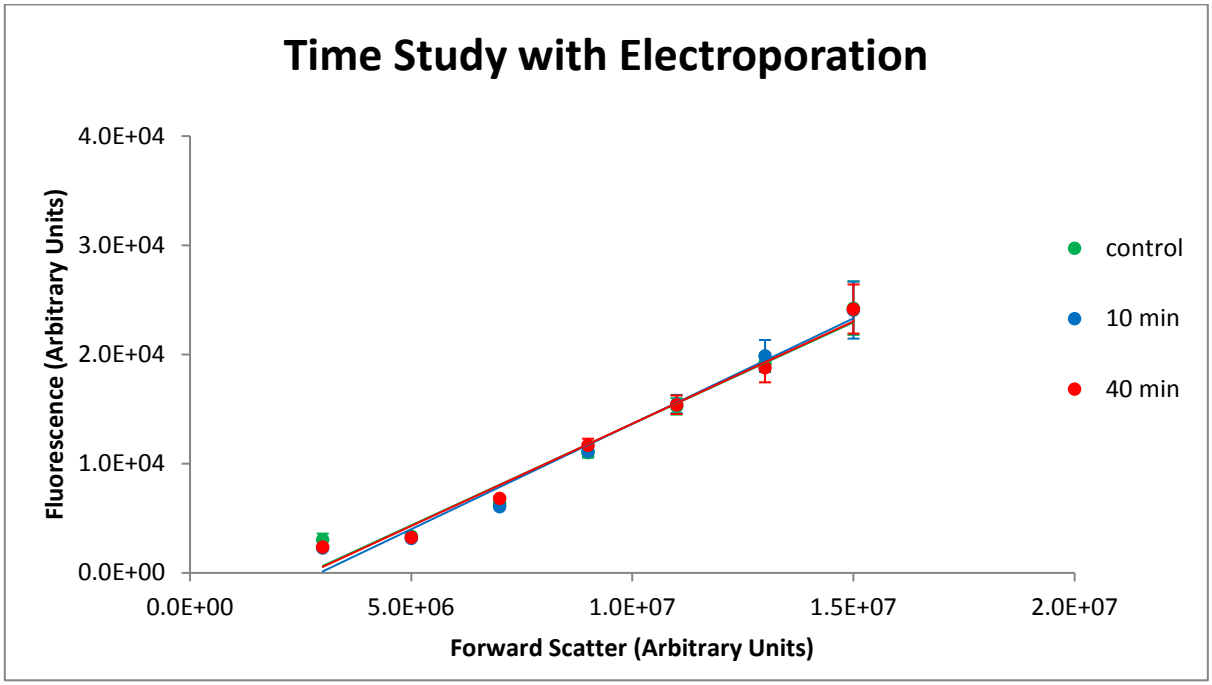

Figure 4.15. Time study maximum viable normal-size cell density plot with electroporation showing a negative control sample (no electroporation at 0 minutes) and two experiment samples, electroporated at 1.0 x 10^5 V/m peak, at 100 kHz, at 10 minutes, then at 40 minutes, to provide a wide time contrast. Error bars are shown for ±1 standard deviation. Least mean squares linear trend lines have been included.

For the study with electroporation in figure 4.15, practically no difference is observed between the Control and Experiment samples as expected due to low level electroporation (using only 2 pulses of 1 x 10^5 V/m at the most prevalently used frequency of 100 kHz, which will later be shown to result in a nearly negligible degree of electroporation), and they remain very consistent over time. The mean fluorescence differences of the two electroporation experiments are minimal and insignificant, suggesting no change in effect over the 30 minute interval between the 10 minutes and 40 minutes electroporated samples.

When comparing figure 4.14 with figure 4.15, it can be seen that the trend line slope of the nominally viable cells sub-population for the negative control has reduced in figure 4.15 (from an average of 2.85 x 10^{-3} to 1.86 x 10^{-3} fluorescence over forward scatter units (FOFS)). This is as a

result of the reduction in PI concentration by one half between these two sample sets. Early experiments used 10 μL of PI (forming a 20 μg/mL or 30 μM final PI concentration), until it was determined that this concentration was generally too high and shown to be saturating the fluorescence level in experiments (see section 4.3.2.1.2). As such, the concentration was halved by using 5 μL of PI per aliquot (forming a 10 μg/mL or 15 μM final PI concentration). This reduced concentration was used for all subsequent experiments identified in this chapter. The reduction in slope is consistent with the reduction of the fluorescent dye concentration.

The findings of these time studies have shown that, within the 40 minutes interval investigated, no observable alteration of samples occurred. As such the effect of time on results over the maximum experimental timeframe was negligible and may be ignored.

4.3.2.1.2 Propidium iodide (PI) concentration studies

Three experiments were conducted to compare monopolar (single pulse) and bipolar (10 kHz square wave) electroporation applications at a peak electric field of 2×10^5 V/m, both using two bursts of 500 μs duration separated by 1 s. The low frequency of 10 kHz was chosen to minimise transitional time loss due to slew rate limitations of the bipolar pulse, thus equalising the duration that the cell membranes are exposed to an electroporation above-threshold electric field for both monopolar and bipolar signals. The three experiments were carried out under almost identical conditions to test for consistency, however the first experiment series used 10 μL of PI forming a 30 μM final PI concentration (presented in figure 4.16) while the latter two used 5 μL of PI forming a 15 μM final PI concentration (presented in figure 4.17).

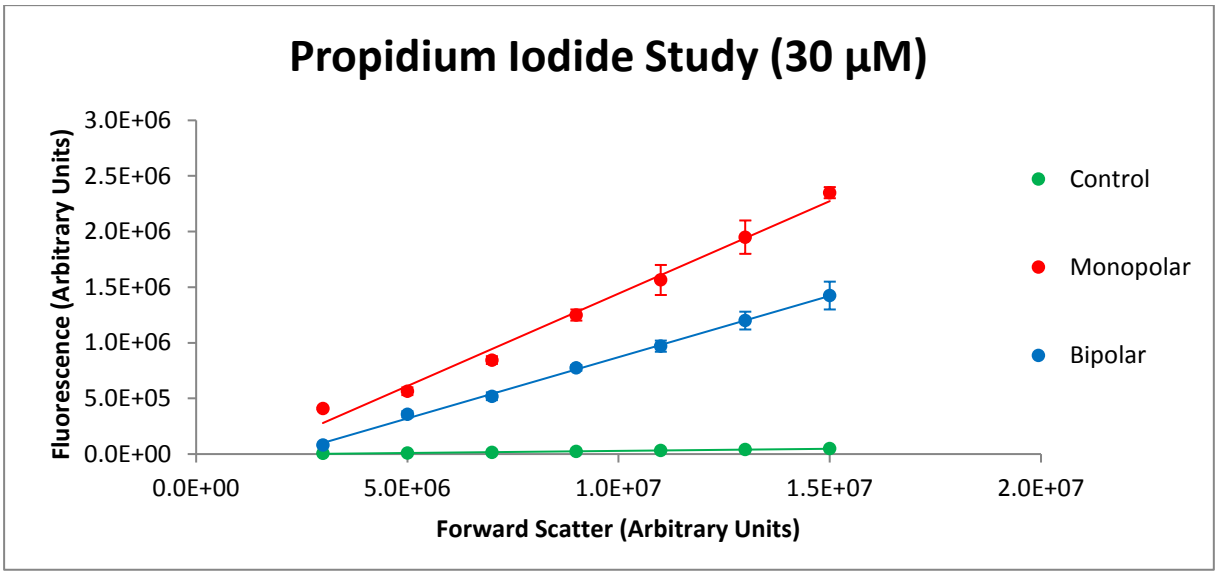

Figure 4.16. A bipolar *vs* monopolar maximum viable normal-sized cell density plot at 2 x 10^5 V/m. All these samples used 30 µM of PI. Error bars are shown for ±1 standard deviation.

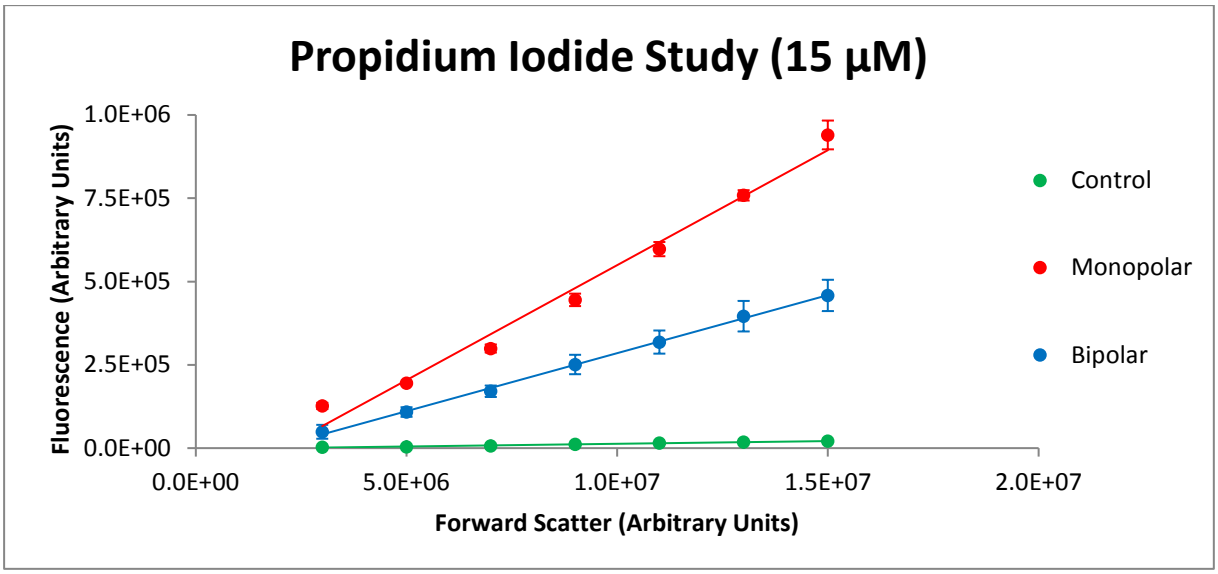

Figure 4.17. A bipolar *vs* monopolar maximum viable normal-sized cell density plot at 2 x 10^5 V/m. All these samples used a PI concentration of 15 µM. Error bars are shown for ±1 standard deviation.

Evident from figures 4.16 and 4.17, the reduction of PI shows a clear, consistent reduction of the trend line slope, where all other characteristics appear quite similar, consistent with previously mentioned observations. From figure 4.16 (30 µM of PI), there is an increase in slope from the Control to the bipolar pulse result, from 3.49 x 10^{-3} FOFS to 1.05 x 10^{-1} FOFS. This slope was further increased to 1.65 x 10^{-1} FOFS for a monopolar pulse regime. From figure 4.17 (15 µM of PI), the increase from the Control to the bipolar result is a slope of 1.63 x 10^{-3} FOFS to 3.64 x 10^{-2} FOFS.

This increase of slope is equivalent to approximately 30 times, or 1.5 orders of magnitude, and is observed for both cases of PI concentration. This was further increased to 6.79 x 10^{-2} FOFS for a monopolar regime. These increases are consistent with a strong electroporation effect at 2 x 10^{5} V/m.

The maximum density plot slopes of the two concentrations of PI for their respective Control samples were 1.63 x 10^{-3} FOFS (15 μM PI) and 3.49 x 10^{-3} FOFS (30 μM PI), suggesting that there is an approximately proportional relationship of fluorescence between dye concentration and maximum density plot slope.

Figure 4.18 shows the raw dot plots of cells for both monopolar and bipolar pulses, including the Control, using 15 μM of PI.

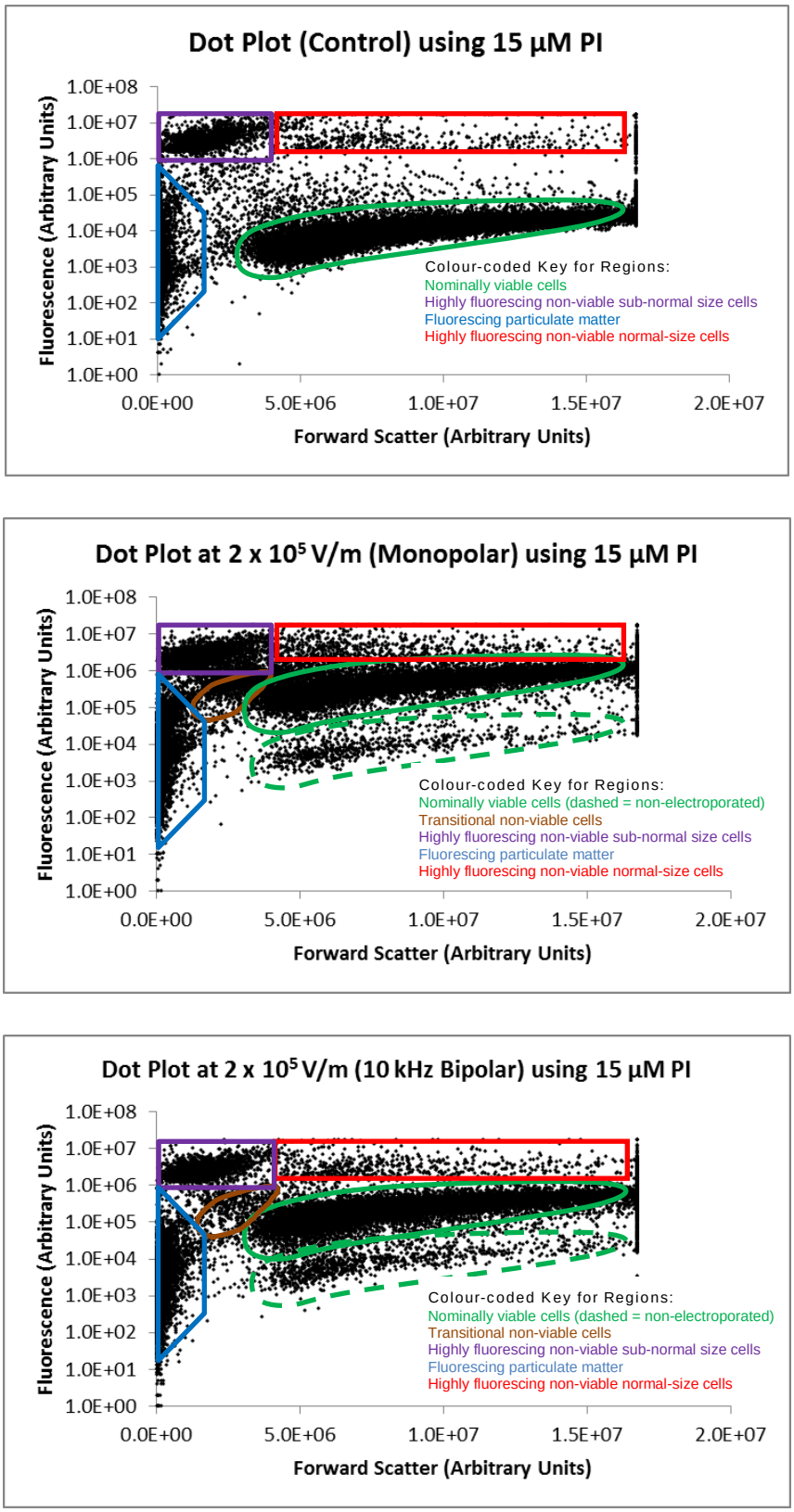

Figure 4.18: Raw dot plots of cells exposed to a field of 2 x 10^5 V/m, all using a PI concentration of 15 µM, corresponding with the maximum cell density plot in figure 4.16. The top plot is for a control, the middle plot for a monopolar field, and the bottom plot for a bipolar field. For clarity, key regions are also identified.

From figure 4.18, the monopolar pulses showed the greatest combination of effects with higher fluorescence of the nominally viable cells, a denser highly fluorescing non-viable sub-normal size cells sub-population, and development of a sub-population of transitional non-viable small cells located between the nominally viable cells and highly fluorescing non-viable sub-normal size cells. The monopolar pulses also produced more fluorescing particulate matter, as compared to bipolar pulses. Thus, this is an early indication that the differences in electroporation characteristics between bipolar and monopolar pulses warrant further investigation.

When comparing the maximum cell density plots in figures 4.16 and 4.17, it should be noted that the 30 µM dye samples show closer value slopes for the monopolar and bipolar results compared to the difference in slope between monopolar and bipolar results for the 15 µM dye samples. This suggests that a level of fluorescence saturation had been reached, which may well affect results in general for higher PI concentrations. Hence, the lower dye concentration using 15 µM of PI was used in all future and presented experiments.

4.3.2.1.3 Very High pulse parameter electroporation study

As another way of establishing a positive control, a study was conducted to probe how especially high electric field strength and/or more pulses would affect cells and how this might appear on the dot plot. Results are shown in figures 4.19 and 4.20.

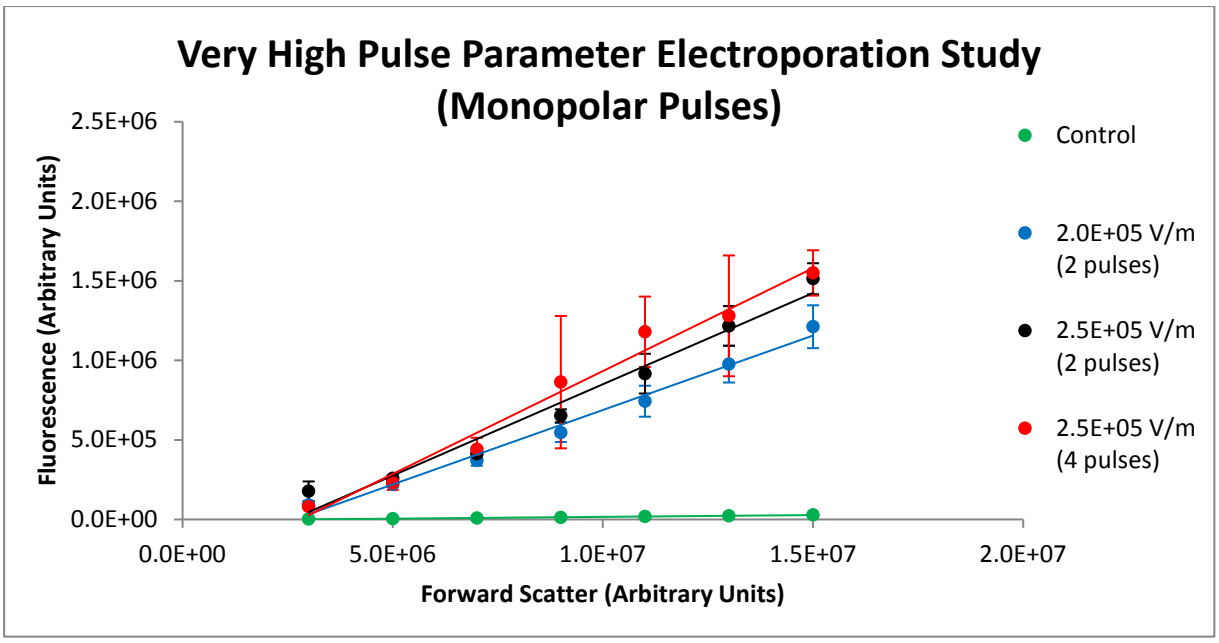

Figure 4.19. Maximum density plot for very high pulse parameter electroporation using monopolar pulses of 2 x 10^5 V/m and 2.5 x 10^5 V/m and also increasing number of pulses from the usual 2 to 4. Error bars represent ±1 standard deviation.

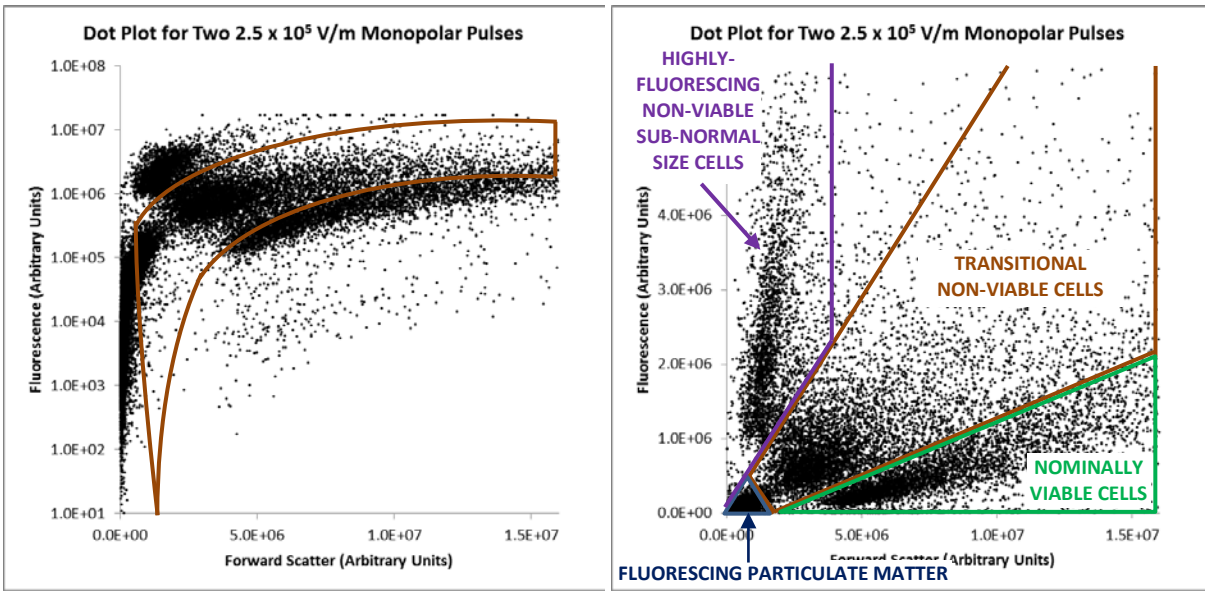

Figure 4.20. Dot plots for the very high pulse parameter electroporation study. The left plot has a log scale for the fluorescence intensity, and the right plot has fully linear axes. The brown gated regions indicate the growing combined sub-populations of transitional non-viable sub-normal size cells and of non-viable normal size cells. For clarity, the other regions have also been identified in the right plot.

Figure 4.19 shows the maximum density plots of viable electroporated cells for this study at the different high electroporation pulse parameters applied. The data points for samples exposed to 6 pulses are not present due to the very low percentage of cells left in the nominally viable cells sub-population, at 2 %, with too few dots to determine a density plot. Observed in figure 4.20 is the existence of 4 sub-populations of cells including the emergence of a relatively large sub-population of transitional non-viable sub-normal size cells and an increase in the non-viable normal size cells, both of which are enclosed in the brown-line bounded region. This brown line bounded region also includes a small amount of particulate matter at its bottom left end (right plot in figure 4.20), which is likely the result of small non-viable cells disintegrating. These larger particles appear to be migrating towards the smaller particulate matter region. This effect is almost not seen at all in the bipolar electrical pulsing regimes, once again identifying a lysing effect on cells that is greater for the monopolar pulse regimes.

Metrics of interest in these electroporation studies are Recovery and Viability of normal cells. Recovery is related to the Control viable cell number as reference, thus calculated as a relative percentage of the Control sample set, where the Control samples naturally show 100 % Recovery (when defined as an electrically treated sample with zero electric field amplitude), and treated samples show a general reduction in this ratio as the treatment regime (pulse parameters) is intensified. Comparing the number of viable cells after electroporation to the number of viable cells in the Control to determine Recovery is justifiable in that the proportion of nominally viable

cells in the experiments (prior to pulsing) will not be significantly different to the Control (as these cells are taken from the same sample stock as the Control at the same time). This metric does not rely on interpretation of a number of sub-populations as viability does. Thus, Recovery is calculated as

$$Recovery\ \% = \frac{Number\ of\ viable\ cells\ of\ electrically\ treated\ sample}{Number\ of\ viable\ cells\ of\ untreated\ (control)\ sample} \cdot 100\ \% \qquad (4.3)$$

Viability is defined here as the ratio of all viable cells divided by the sum of viable and non-viable cells, and is calculated as

$$Viability\ \% = \frac{Number\ of\ viable\ cells}{Number\ of\ viable\ cells\ +\ Number\ of\ non{-}viable\ cells} \cdot 100\ \% \qquad (4.4)$$

Non-viable cells include the sub-populations of highly fluorescing normal size non-viable cells, transitional non-viable cells (both small to sub-normal, and normal size ranges) and highly fluorescing sub-normal size non-viable cells. The number of all non-viable cells are calculated as

$$NVC = HFNSC + HFNNC + TNC \qquad (4.5)$$

with *NVC* = Number of non-viable cells, *HFNSC* = Number of highly fluorescing non-viable sub-normal size cells, *HFNNC* = Number of highly fluorescing non-viable normal size cells, and *TNC* = Number of transitional non-viable cells (both small to sub-normal and normal size ranges).

Shown in figure 4.21 is the growth of compromised cell sub-populations (including highly fluorescing non-viable normal size cell sub-population and highly fluorescing transitional non-viable sub-normal size cell sub-population) as the electric field strength is increased, and also with increased number of pulses. Gating/separation of the 4 sub-populations as fractions of the 1 x 10^4 particles detected in each sample show a marked increase of the fluorescent particulate matter, together with a corresponding reduction in viability. The fluorescing particulate matter count also rose with electric field strength and number of pulses. The nominally viable cells sub-population (not shown) dropped from an initial high fraction (of total particles counted) of 72 % in the Control down to 4 % for the 4 pulses of 2.5 x 10^5 V/m pulse and finally dropped to 2 % for 6 pulses at 2.5 x 10^5 V/m treatment while fluorescing particulate matter (blue bars) increased from 14 % to 56 %. Simultaneously (not shown here), the highly fluorescing non-viable sub-normal sub-population increased from 1.4 % (Control sample) to 14 % (6 pulses) and the highly fluorescing non-viable normal size cell sub-population increased from 1.5 % (Control) to 7.4 % (6 pulses). Viability (green bars) dropped from 86 % (Control) to 5 % (6 pulses of 2.5 x 10^5 V/m) and Recovery (yellow bars) dropped from 100 % (Control) to 9 % (6 pulses of 2.5 x 10^5 V/m). Taken together this appears to indicate that as the electric field amplitude and/or duration is increased

beyond the onset of electroporation, a corresponding migration of particles from the nominally viable cells sub-population to the two transitional non-viable cells sub-populations (the highly fluorescing non-viable sub-normal size cells, and the highly fluorescing non-viable normal size cells), and the fluorescing particulate matter regions, is observed.

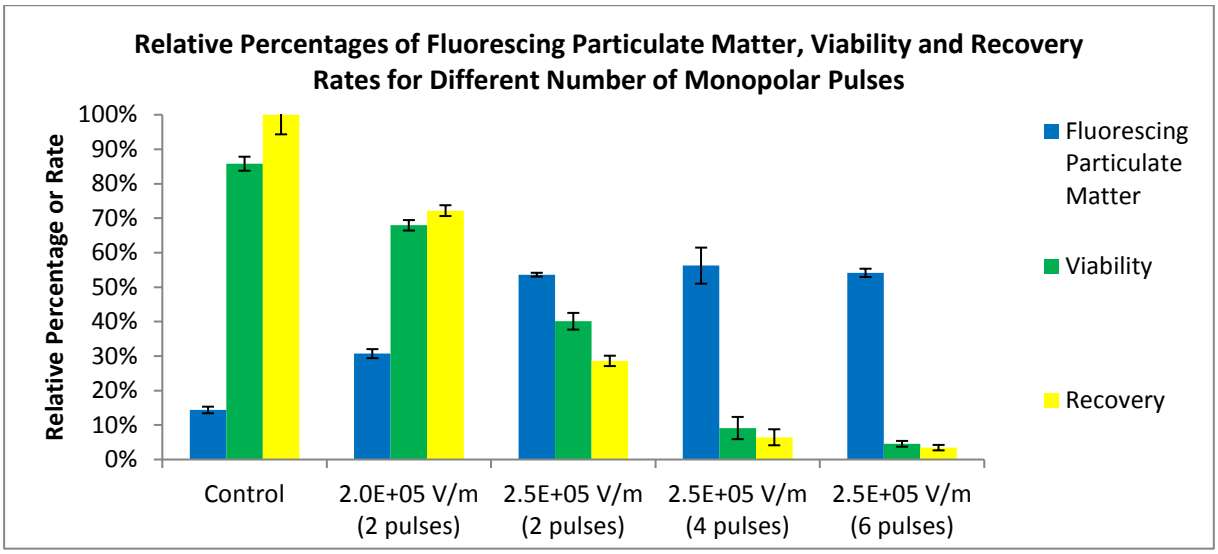

Figure 4.21. Percentages of fluorescent particulate matter, Viability and Recovery for different electric fields and different number of monopolar pulses. Error bars are provided for ±1 standard deviation.

In this study it is observed that the effect of very high pulse parameter electroporation increases as the number of pulses is increased. The nominally viable cells sub-population consistently increased in fluorescence, manifesting as a plot slope increase in the nominally viable cell maximum density curves (in the lin-lin plots), from 0.00226 FOFS (Control) to 0.129 FOFS (4 pulses of 2.5 x 10^5 V/m monopolar pulses), which is suggestive of increased electroporation (see table 4.2 for a summary of the slopes of these maximum density curves). However, cells also appear to be both substantially shrinking and producing small particles in response to very high pulse parameter electroporation, due to the increase of particle counts in the corresponding sub-populations. As demonstrated in figure 4.20 (left plot), the increase of particles in the fluorescing particulate matter field is particularly high at its highest fluorescence and appears to consist of slightly larger particles which tend to merge with the sub-population of transitional sub-normal sized non-viable cells.

Table 4.2. Nominally viable cells maximum density plot slopes showing comparison of the different number of pulses and also different electric field levels, for monopolar pulses, with an interval of 1 s between pulses.

Sample set and its electric field intensity	Number of pulses	Slope (FOFS)
Control (0 V/m)	0	2.26×10^{-3}
2.0×10^{5} V/m	2	9.36×10^{-2}
2.5×10^{5} V/m	2	1.12×10^{-1}
2.5×10^{5} V/m	4	1.29×10^{-1}
2.5×10^{5} V/m	6	*

**Insufficient data due to severity of cell lysis (only 2 % of all particles counted were still present in the viable sub population).*

Thus, cells are very likely dying due to excessive electroporation. These destructively electroporated cells have demonstrated signature characteristics on a flow cytometric dot plot, including the establishment of transitional non-viable small to sub-normal size cells that becomes the majority of cells followed by a reduction in particle size, and with an average fluorescence far above their counterparts in the nominally viable cells sub-population. The destructive nature of these monopolar pulses is also reflected in the substantial rise in the fraction of fluorescing particulate matter, most likely associated with cell fragments.

A link between total duration of pulses and effect has also been established, given an increase of the slope of the nominally viable cells sub-population when the number of pulses were doubled.

4.3.2.1.4 Mid-to-High range pulse parameter electroporation cell Viability and Recovery studies

Two studies were conducted to probe cell Viability and Recovery after mid-to-high range electroporation, thus gauging the fraction of cells that were recovering and also dying due to higher electroporation levels. This was achieved by dividing the samples up into two groups; one receiving its PI dose before electroporation, and the other receiving its dose after electroporation. A selection of maximum density nominally viable cells plots is shown in figure 4.22.

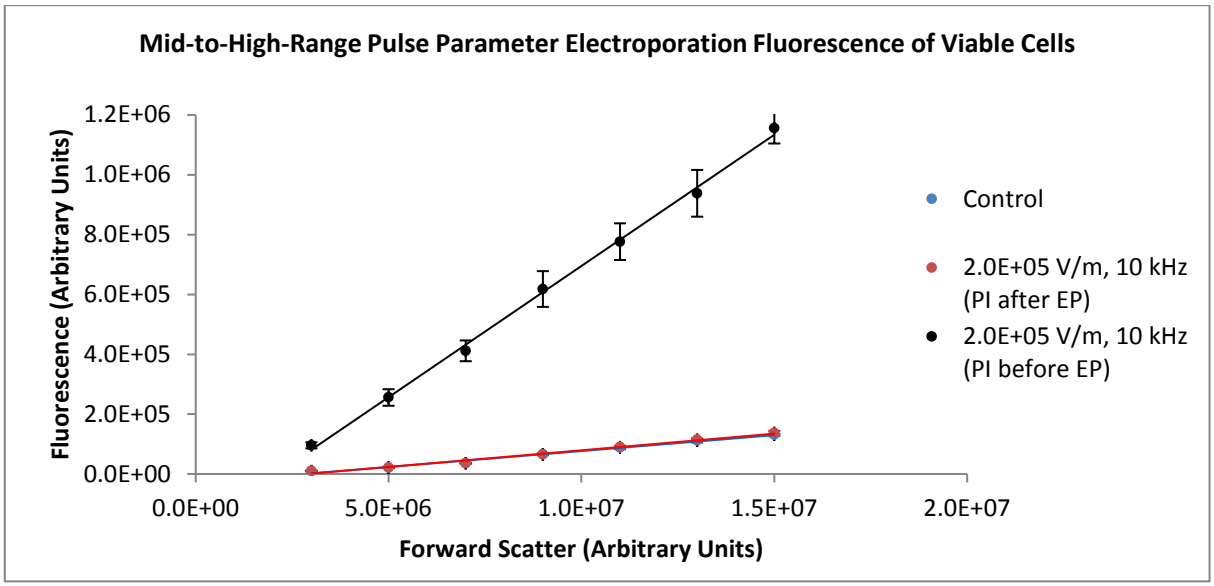

Figure 4.22. Maximum density plots comparing the two groups: PI added *after* electroporation and PI added *before* electroporation. Two bipolar square wave bursts of 500 µs duration at 10 kHz were applied at a peak electric field of 2.0 x 10^5 V/m, separated by 1 s, to the experiment samples. A set of Control samples is also shown. Error bars are shown for ±1 standard deviation.

In figure 4.22 it can be observed, where electroporation was performed before addition of PI, that the change was minimal (blue and red points). This suggests that the cells which recovered after the electroporation process also have a cell membrane that has returned to a non-permeable state as supported by electroporation studies literature [46-48].

The other set of data points in figure 4.22 show the more normal process where PI was added before electroporation, thus showing the substantial increase in the slope, with little other change. This is the marked effect of recoverable electroporation, where in this case there has been a slope increase of 0.0105 FOFS (Control) to 0.0843 FOFS (a factor of 8 increase). Figure 4.23 presents more results from this study.

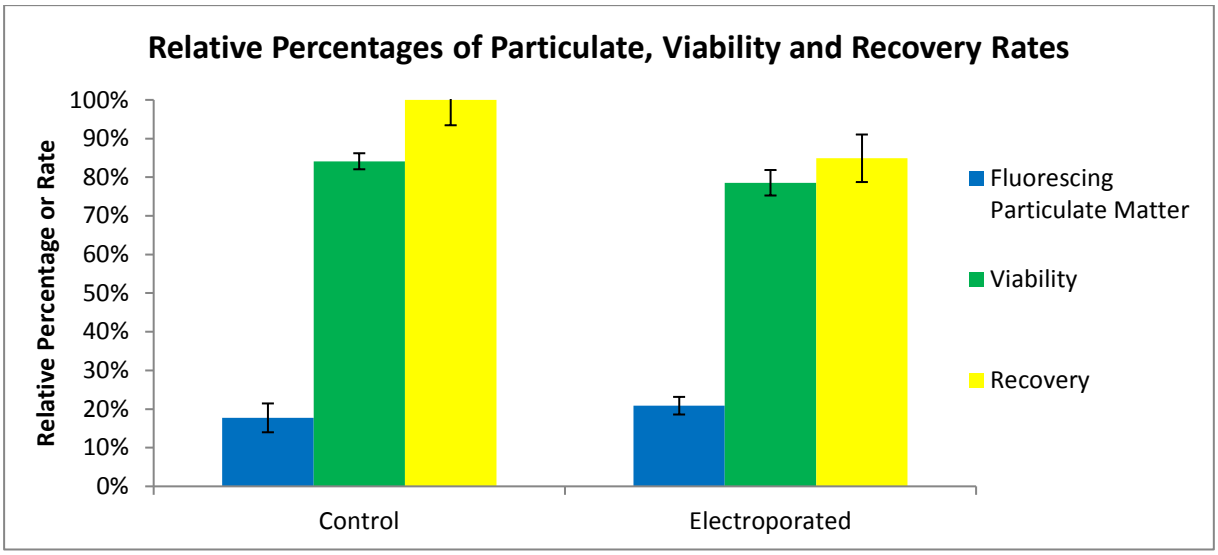

Figure 4.23. Mid-To-High-range pulse parameter electroporation fractions and rates corresponding with results from figure 4.22. The left group represents the Control sample set, and the right group represents the sample set where the cells were dosed with PI before electrical treatment. Error bars are shown for ±1 standard deviation.

Observed in figure 4.23 is the general reduction of Viability of cells (green bars) for the mid-high-range pulse parameter electroporation regime of 2 times 500 µs bipolar pulses of 2 x 10^5 V/m at 10 kHz. Recovery rates are presented by the yellow bars and are consistent with the mentioned behaviour.

The second viability study presented in figure 4.24 was conducted using bipolar *vs* monopolar pulses, and also using slightly higher peak electric fields, notably 2.5 x 10^5 V/m. All the samples were only dosed with PI after electroporation (Control samples were not electroporated).

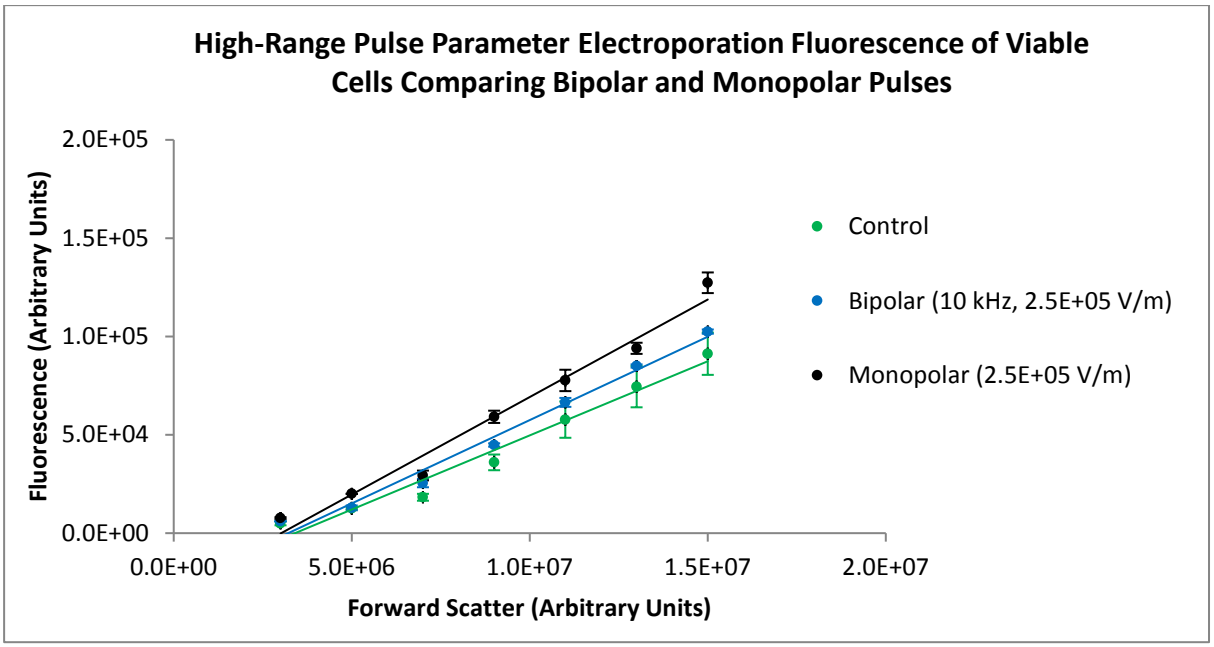

Figure 4.24. Maximum density plots contrasting bipolar and monopolar pulses where both were at peak electric field values of 2.5 x 10^5 V/m. PI was added after electroporation for all cases. Error bars represent ±1 standard deviation.

As observed in figure 4.24, although there is a difference between the Control and the bipolar samples (green and blue, respectively) and again between the bipolar and the monopolar (black) samples, the fluorescence slopes have only slightly increased from 7.54 x 10^{-3} FOFS to 8.48 x 10^{-3} FOFS to 9.92 x 10^{-3} FOFS, respectively. This indicates that the cells that remain viable after electroporation have membranes that return to a relatively normal level of permeability. When considering the sub-populations, as shown in figure 4.25, there is an increase in the fluorescing particulate matter (blue bars) from 14 % (Control) to 24 % (bipolar) then to 52 % (monopolar), signifying an increase in cell death for the monopolar pulses. No significant changes were observed for the highly fluorescing non-viable normal size cells (not shown), remaining at approximately 2 %. The bipolar data shows a slight increase in fluorescence slope compared to the 2.0 x 10^5 V/m case presented in figure 4.22, as expected. Also of note here is that the cell Viability has remained unchanged from 82 % (Control) to 82 % (bipolar) but then dropped to 57 % (monopolar), at a pulsing field of 2.5 x 10^5 V/m. Cell Recovery dropped from 100 % (Control) to 91 % (bipolar) then to 40 % (monopolar). These results suggest that the bipolar pulses had little effect on the overall cell viability while the monopolar pulses caused a reduction of the cell viability at the particular electrical parameter settings used.

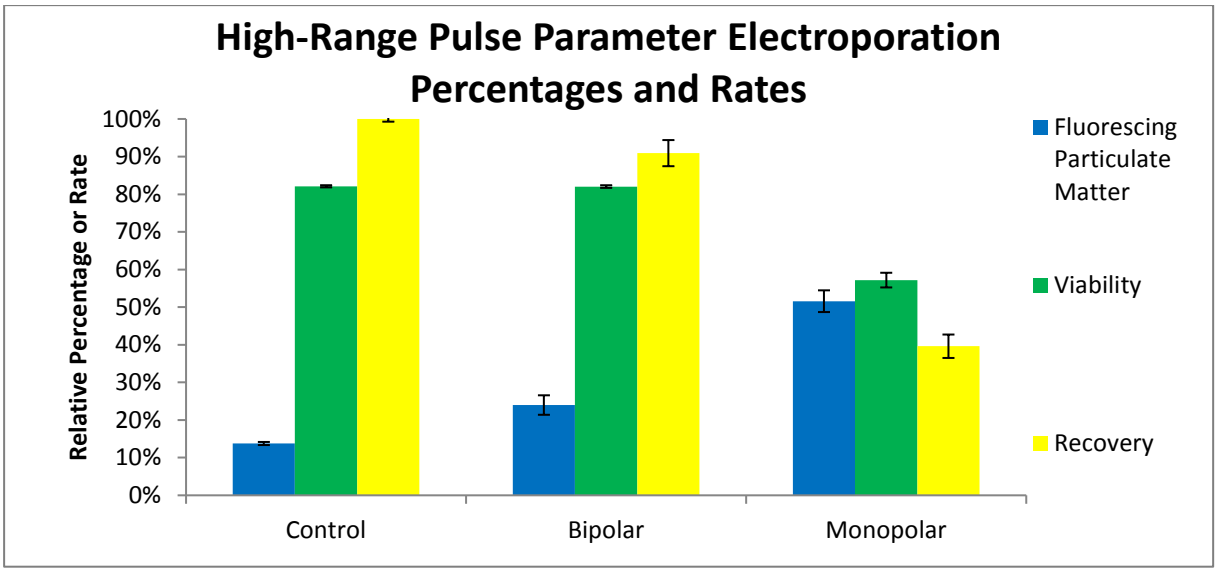

Figure 4.25. High-Range pulse parameter electroporation fractions and rates corresponding with results from figure 4.24. The left group represents the Control sample set, the middle group the sample set where the cells were exposed to bipolar pulses (2.5 x 10^5 V/m, 10 kHz), and the right group represents the were exposed to monopolar pulses (2.5 x 10^5 V/m). Note: PI was added after electroporation in this instance. Error bars are shown for ±1 standard deviation.

In the viability studies, monopolar pulses, above 2 x 10^5 V/m, and particularly at a 2.5 x 10^5 V/m peak electric field, appeared to be relatively destructive to cells compared to bipolar pulses where minimal lysing appeared to occur. Furthermore, the emergence of a large sub-population of small to sub-normal sized transitional non-viable cells and an increase in the highly fluorescing non-viable sub-normal size cells sub-population, signifies a substantially higher total sub-population of dead cells for the monopolar pulses as compared to the bipolar pulses in this instance.

The control studies as a group have established baselines, including a negative control (no effect) and a positive control (substantial lysing effect). It has also been established that the experimental duration had minimal if no effect on the results. It has also been established that the peak cell density slope is approximately proportional to the dye concentration.

When comparing the control studies sub-population results in the sections above with the results presented in section 4.3.2.2 below, it is noted that there are varying inter-experimental values for experiments carried out with the same pulse parameters. This is attributed to normal experimental variation given the small number of experiment replicates.

4.3.2.2 General frequency-magnitude studies

This set of studies dominates the work conducted. Individual studies were carried out generally at a single frequency but at various increasing levels of electric field magnitude. This included frequencies ranging from 0 Hz (monopolar) to 800 kHz, including monopolar, 10 kHz, 20 kHz, 100 kHz, 200 kHz, 400 kHz and 800 kHz, and peak electric field intensity magnitudes ranging from 1 x 10^5 V/m to 3.5 x 10^5 V/m, typically including 0.5, 1.0, 1.5, 2.0, 2.5 and 3.0 (all x 10^5 V/m). Nonetheless, a common pulsing regime was consistently applied of 2 bursts of duration of 500 μs with a pause interval of 1 s. Typical waveforms of these pulses are shown in figure 4.26.

Figure 4.26. Typical electric pulse waveforms used during electroporation. They are all at a peak electric field amplitude of 2 x 10^5 V/m (800 V peak across an electrode separation of 4 mm). a) Monopolar pulse for a duration of 500 µs; b) 10 kHz bipolar burst for a

duration of 500 µs; c) 20 kHz bipolar burst for a duration of 500 µs; d) 100 kHz bipolar burst for a duration of 500 µs; e) 100 kHz bipolar showing waveform detail; f) 200 kHz bipolar burst for a duration of 500 µs; g) 200 kHz bipolar showing waveform detail; h) 400 kHz bipolar burst for a duration of 500 µs; i) 400 kHz bipolar showing waveform detail; j) 800 kHz bipolar burst for a duration of 500 µs; k) 800 kHz bipolar showing waveform detail. All these oscilloscope traces were produced using a typical load in the electroporating chamber (no cells, but exactly the same media, volume and cuvette).

All the left images of the waveforms presented in figure 4.26 demonstrate a single pulse or burst duration of 500 µs. All other images illustrate the difference between a monopolar pulse (top left) and bipolar pulses (all the rest) and also the relative quality of the square waves of the bipolar pulses. Up to 100 kHz the waveforms are reasonably ideal with transitions of 350 ns (over an electric potential transition of 1600 V) yielding a duty cycle of 96.5 %, while relative edge quality deteriorates with frequency from 200 kHz (duty cycle = 93 %), considering the slew rate of the MOSFETs individually were approximately 1 x 10^{10} V/s. Table 4.3 presents the duty cycles for all the different frequency settings.

Table 4.3. Electrical duty cycles for the different pulsing frequencies, using a loaded output of 1.6 x 10^3 V p-p, based on the measured 350 ns transition time.

Pulsing Frequency (kHz)	Duty Cycle (%)
0*	>99
10	>99
20	>99
100	96.5 ±0.5
200	93 ±0.5
400	86 ±1
800	72 ±1

**Monopolar pulses (all others are bipolar pulses)*

This will impact on the effect of electroporation, since cell membranes possess electrical capacitance and thus will take time to charge before they electroporate. A typical time constant for a bilayer lipid membrane is in the order of 100 ns [49, 50], but is increased substantially when the external medium conductivity is lowered as discussed in chapter 2, section 2.1.1. Every time a cell membrane is exposed to a rapid change in electric field intensity, it translates to a delay

before the transmembrane potential needed to initiate electroporation is achieved, hence ultimately delays the electroporation effect. It is not surprising then that the monopolar pulses show more overall effects compared to their bipolar counterparts with similar peak electric field values. Another slight non-ideal property of these waveforms, particularly at the higher frequencies, is the switchover delay when turning on the second supply. This has been designed to share the voltage stress between the two H-bridge stages in the multilevel inverter used. Extra delays are due to obligatory dead times used to avoid shoot-through conditions (where both the top and bottom MOSFET on one side of a bridge are turned on simultaneously) and thus ensure reliability of the MOSFETs and the electrical pulser system.

The studies across a range of frequencies and electric field intensities now follow.

4.3.2.2.1 Monopolar pulse study

Maximum cell density plots for nominally viable cells for the monopolar study are presented in figure 4.27.

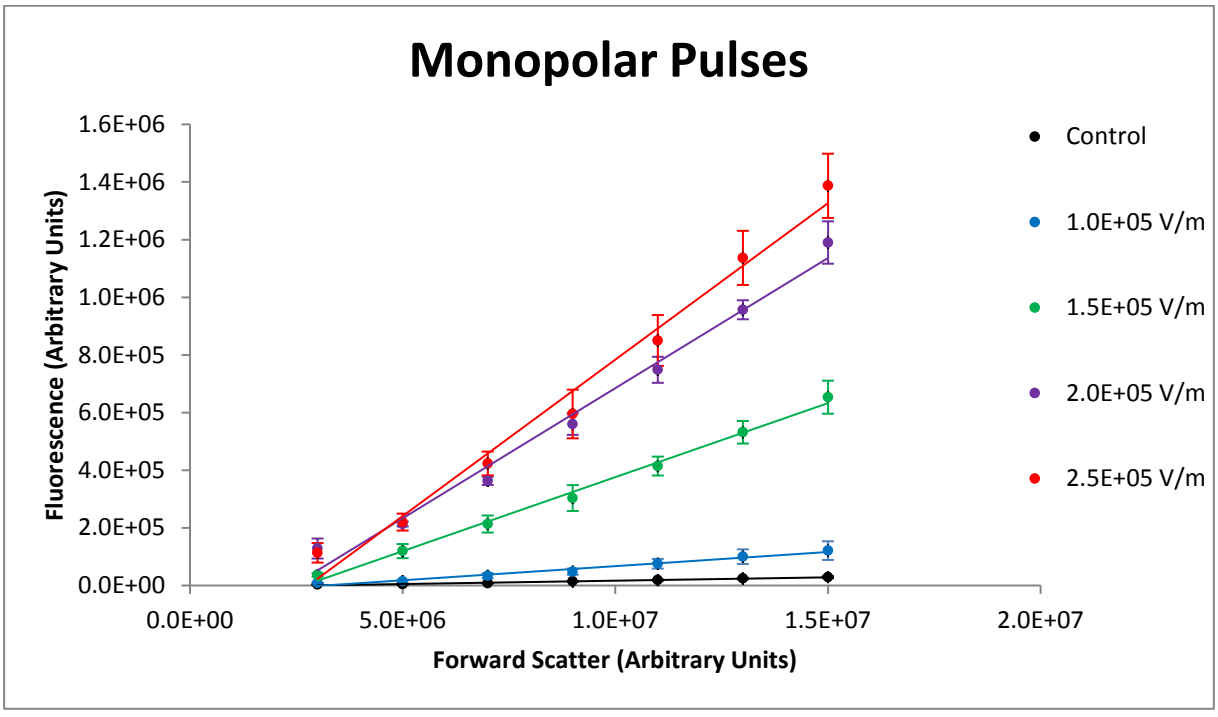

Figure 4.27. Maximum cell density plots using 2 monopolar pulses of 500 µs duration separated by 1 second, exposed to peak electric fields of 1.0 x 10^5 V/m to 2.5 x 10^5 V/m, including a Control. Error bars are shown for ±1 standard deviation.

The maximum cell density plots observed in figure 4.27 show a progressive increase in effect as a function of peak electric field. The slope consistently increased from 0.00233 FOFS (Control), to 0.00982 FOFS (1 x 10^5 V/m), to 0.0514 FOFS (1.5 x 10^5 V/m), to 0.0903 FOFS (2.0 x 10^5 V/m) to

0.109 FOFS (2.5 x 10^5 V/m). This slope increases monotonically and appears to saturate at the highest level of 2.5 x 10^5 V/m. A non-linear trend in the slopes as a function of applied electric field emerges quite clearly and is consistent with a sigmoidal curve where there is a very slight increase (in slope) at low field strength then it increases more rapidly to a maximum (at around 1.5 x 10^5 V/m), followed by a lesser increase of the slope at higher electric field strength.

In figure 4.27 the standard deviation error shown is the deviation within an experiment of 3 samples per parameter setting, each containing 10 x 10^3 particles. The standard deviation is calculated by analysing each sample separately and finding its own maximum density data points, and calculating the mean and standard deviation for n = 3, for each electrical parameter setting. It is observed that the deviation is significant but not overtly substantial, and generally changes proportionally with increasing fluorescence.

Simultaneously, other significant effects were observed. As shown in figure 4.28, the percentage Viability dropped from 73 % (Control) to 34 % (2.5 x 10^5 V/m), while the fluorescing particulate matter rose from 14 % (Control) to 47 % (2.5 x 10^5 V/m). Cell Recovery started at 100 % (Control), and dropped to 97 % (1.5 x 10^5 V/m), 74 % (2.0 x 10^5 V/m), and finally 29 % (2.5 x 10^5 V/m). Above 2.0 x 10^5 V/m there is an apparent significant reduction in the number of viable cells and a clear killing effect is occurring. This is consistent with the earlier positive control experiments. This viable cell reduction is also directly observable in the dot plots (see figure 4.29).

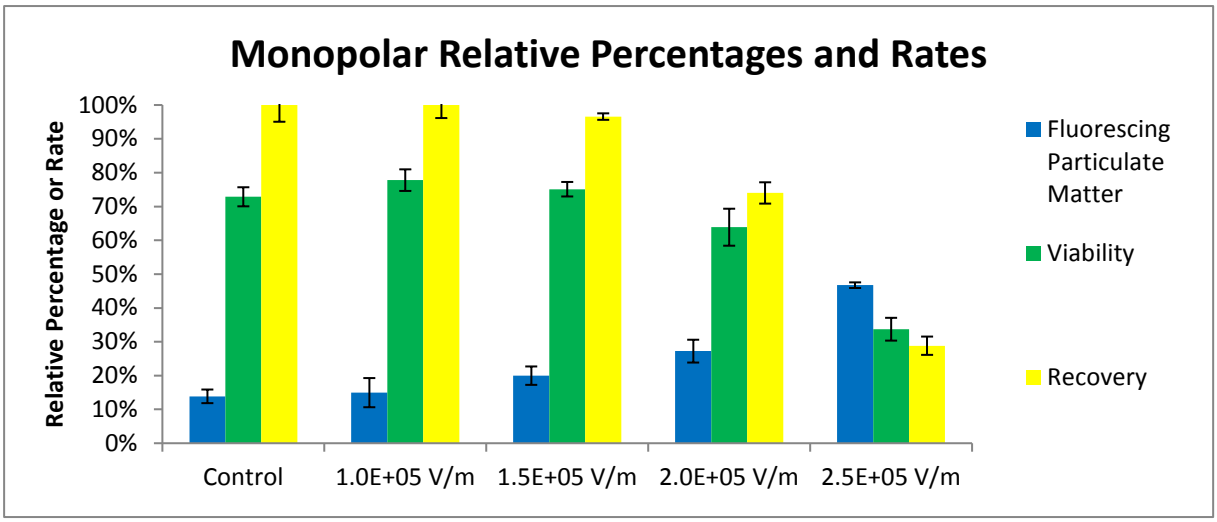

Figure 4.28. Monopolar electric field pulsed electroporation fractions and rates corresponding with results from figure 4.27. The left group represents the Control sample set, and the other groups represent the sample sets where the cells were exposed to monopolar pulses (1.0 x 10^5 V/m to 2.5 x 10^5 V/m). Error bars are shown for ±1 standard deviation.

These plots suggest using an electric field peak of below 2.5 x 10^5 V/m if the goal is not to compromise the viability of the majority of cells. An optimal value of between 1.5 x 10^5 V/m and 2.0 x 10^5 V/m appears to be appropriate, as this level produced the highest fluorescence without adversely affecting the viability of cells, although there are already clear signs of inducing cell lysis (rapid increase of cells in the transitional non-viable small to sub-normal size cells sub-population – see figure 4.28). From the 2.0 x 10^5 V/m sample, the densest point of the viable cells was located at a forward scatter of 5 x 10^6 arbitrary units and a fluorescence of 2.1 x 10^5 arbitrary units.

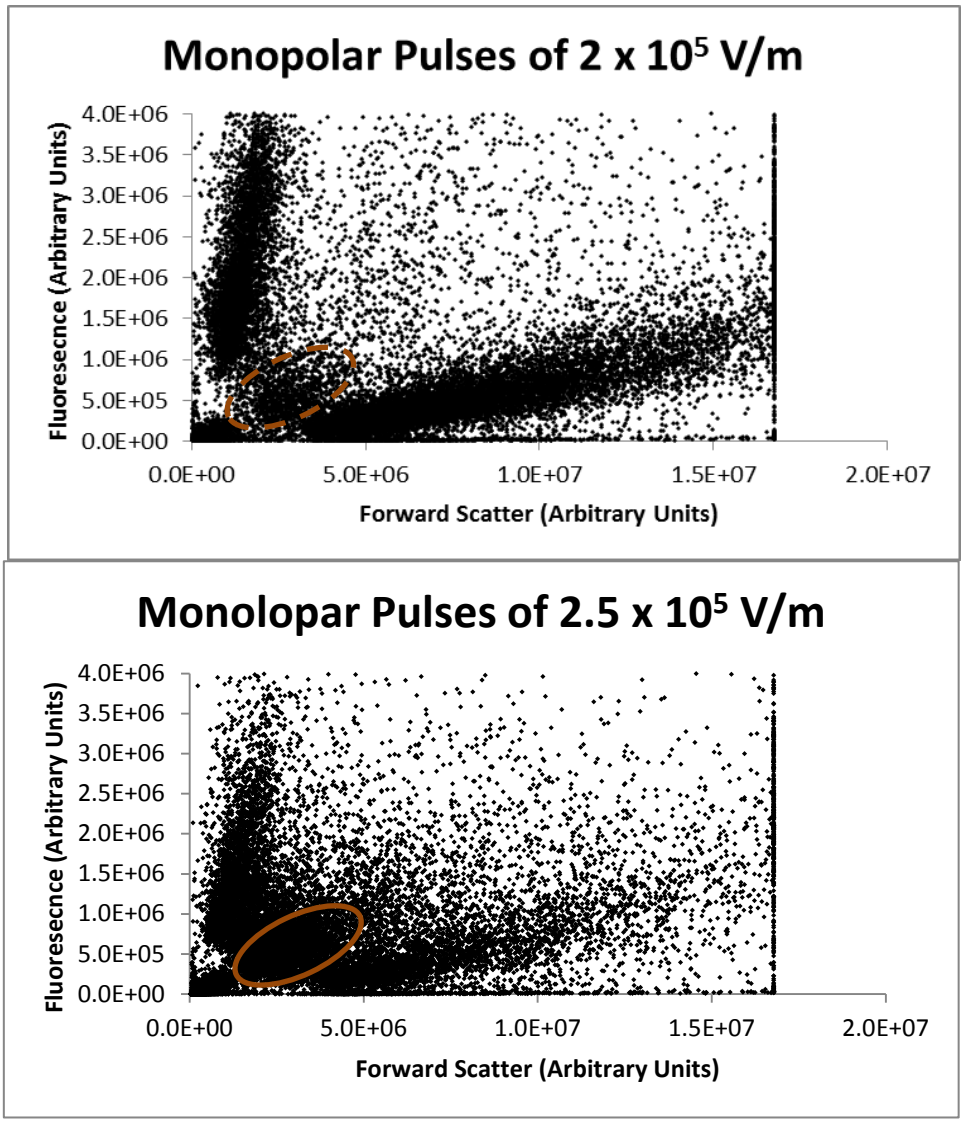

Figure 4.29. Raw dot plots comparing monopolar pulses at 2.0 x 10^5 V/m and 2.5 x 10^5 V/m. The number of transitional non-viable small to sub-normal size cells (mainly in the area circled in brown) have increased.

4.3.2.2.2 Bipolar 10 kHz pulse study

The first bipolar study analysed cells at 10 kHz, and results are presented in figure 4.30.

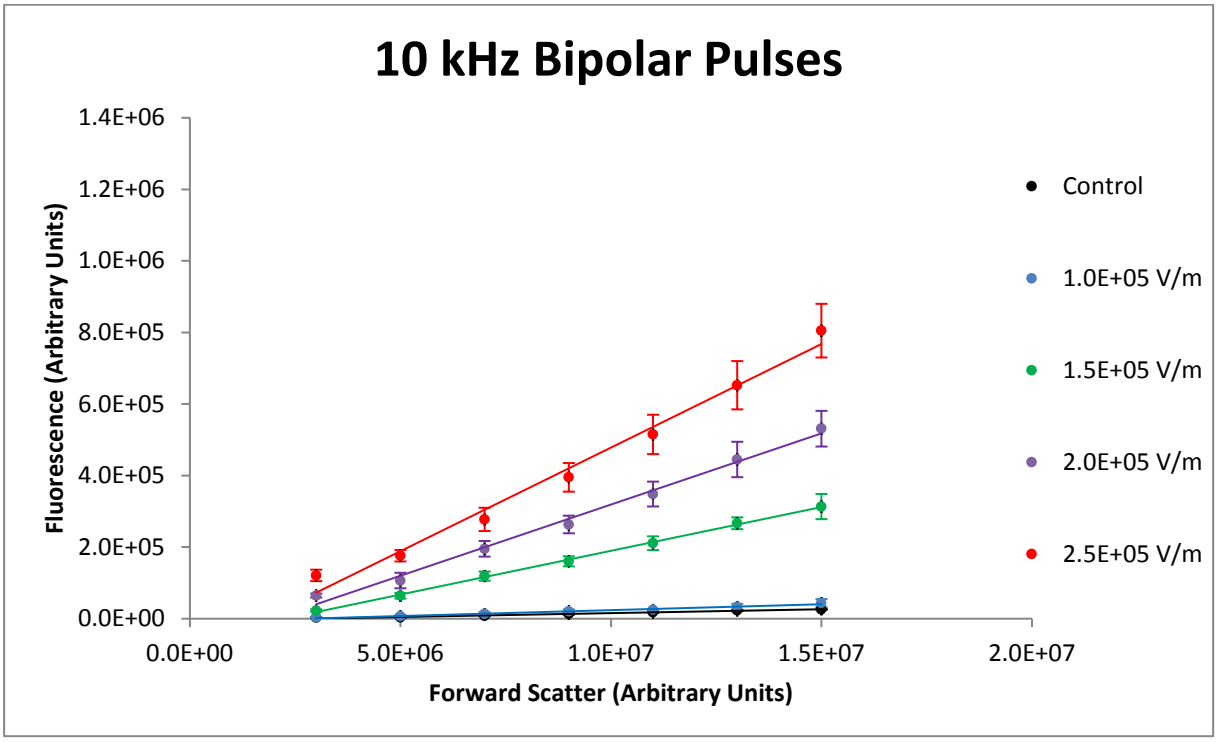

Figure 4.30. Maximum cell density plots of two bipolar pulses at a frequency of 10 kHz of 500 µs duration separated by 1 second, exposed to peak electric fields of 1.0 x 10^5 V/m to 2.5 x 10^5 V/m, including a Control. Error bars are shown for ±1 standard deviation.

As observed from figure 4.30 there is the usual increase in the slope from 0.00216 FOFS (Control), to 0.00330 FOFS (1.0 x 10^5 V/m), to 0.0245 FOFS (1.5 x 10^5 V/m), to 0.0398 FOFS (2.0 x 10^5 V/m), to 0.0579 FOFS (2.5 x 10^5 V/m), as the electric field strength is increased. The 1 x 10^5 V/m sample shows a very similar slope as for the Control sample, suggesting nearly no electroporation effect. At 1.5 x 10^5 V/m, the slope has increased nearly an order of magnitude, after which it practically increases by 50 % with every increment of 0.5 x 10^5 V/m. Compared with the monopolar pulse study, this data does not appear to have reached saturation values yet.

As seen in figure 4.31, unlike the monopolar pulses, the Viability only changed from 78 % to a minimum of 73 %, trending like the monopolar pulses, but by much smaller steps. Cell Recovery started at 100 % (Control), dropped to 92 % (2.0 x 10^5 V/m), then finally dropped to 88 % (2.5 x 10^5 V/m). Unlike the monopolar pulses, there appears to be only a small reduction in the number of viable cells.

These plots suggest using an electric field value of between 2.0 x 10^5 V/m and 2.5 x 10^5 V/m peak (or perhaps above) may maximise the number of observably electroporated cells remaining viable. From the 2.0 x 10^5 V/m sample, the densest point of the viable cells was located at a forward scatter of 5 x 10^6 arbitrary units and a fluorescence of 1.2 x 10^5 arbitrary units. This level of fluorescence is about half that for monopolar pulses at the same forward scatter level.

Also observed in figure 4.30 is the spread of values for each data point. Data spread is quite similar for bipolar as for monopolar pulses and is in the order of a standard deviation of up to ±5 %.

For comparative purposes (with the monopolar plot shown in Figure 4.29), a linearised dot plot is provided in figure 4.31. There is a substantially lower level of transitional small to non-viable sub-normal size cells compared to the monopolar pulse case.

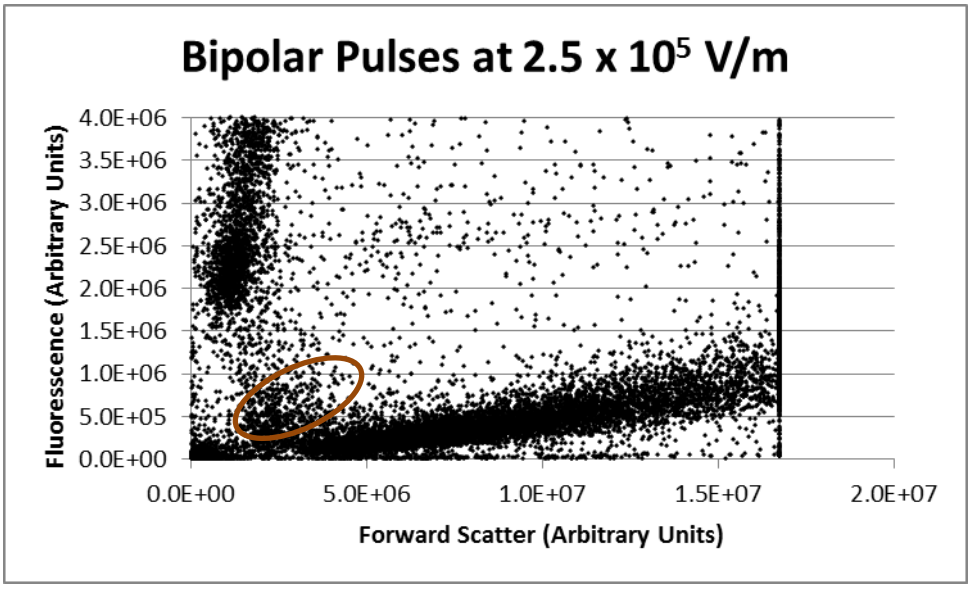

Figure 4.31. Raw linear axes dot plot for two bipolar pulses at a frequency of 10 kHz of 500 µs duration separated by 1 second, exposed to a peak electric field of 2.5 x 10^5 V/m. The number of transitional non-viable small to sub-normal size cells (mainly in the area circled in brown) have now reduced.

A bar graph in figure 4.32 shows the majority of the relative fractions of fluorescent particulate matter, Viability and Recovery rates.

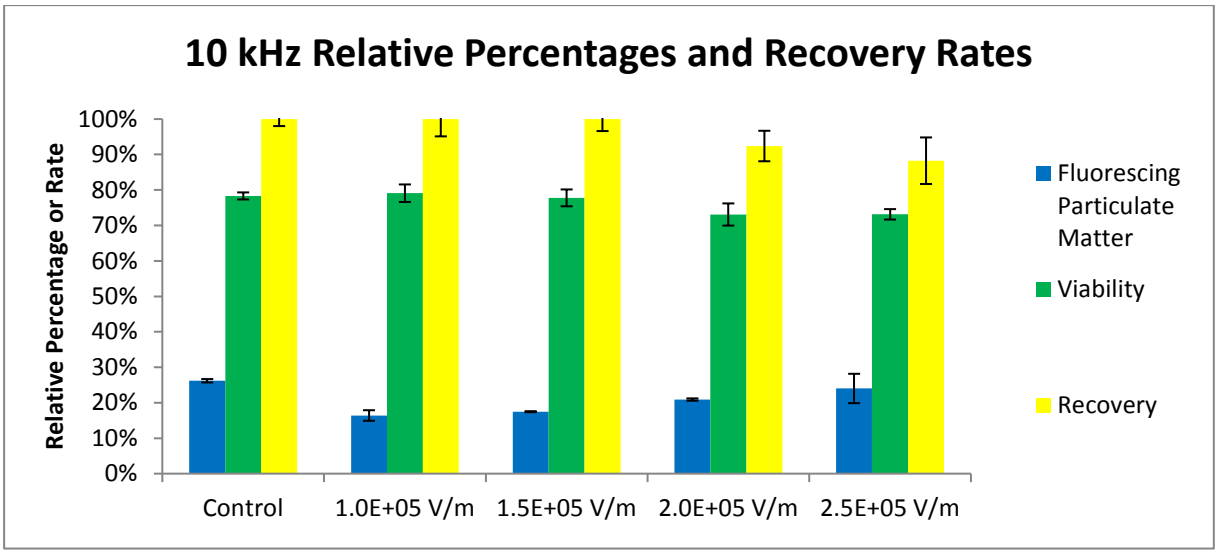

Figure 4.32. Bipolar 10 kHz electric field pulsed electroporation fractions and rates corresponding with results from figure 4.30. The left group represents the Control sample set, and the other groups represent the sample sets where the cells were exposed to bipolar pulses (1.0×10^5 V/m to 2.5×10^5 V/m). Error bars are shown for ±1 standard deviation.

Observed in figure 4.32 is a relatively static situation with not much change as the electrical treatment regime is intensified. This is consistent with observations noted in the maximum density analysis above, that there was practically no reduction in Viability of treated cells for the parameters investigated, contrasting with monopolar pulses.

4.3.2.2.3 Bipolar 20 kHz pulse study

The second bipolar study analysed cells at 20 kHz, and results are presented in figure 4.33.

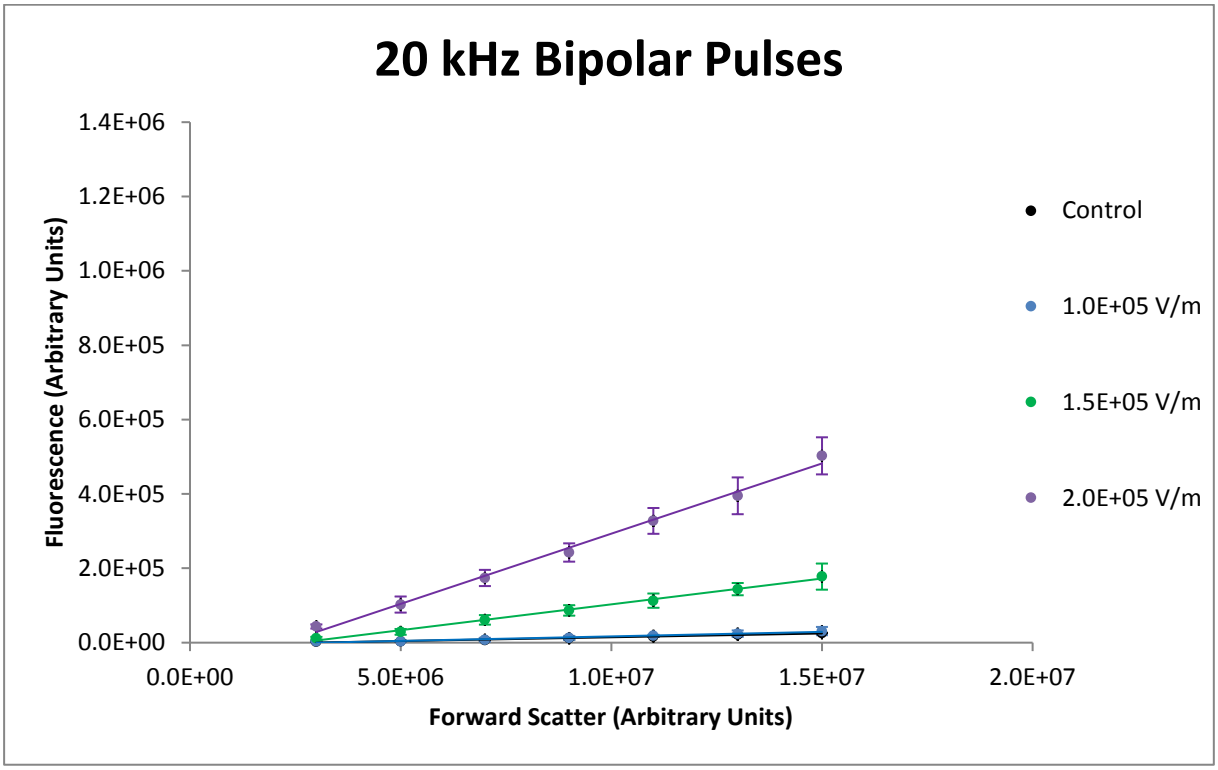

Figure 4.33. Maximum cell density plots of two bipolar pulses at a frequency of 20 kHz of 500 µs duration separated by 1 second, exposed to peak electric fields of 1.0 x 10^5 V/m to 2.0 x 10^5 V/m, including a Control. Error bars are shown for ±1 standard deviation.

Maximum cell density plots observed in figure 4.33 generally show similar trends to the 10 kHz study. The maximum density slopes ranged from 0.00204 FOFS (Control), to 0.00244 FOFS (1.0 x 10^5 V/m), to 0.0139 FOFS (1.5 x 10^5 V/m), to 0.0378 FOFS (2.0 x 10^5 V/m), coinciding with minimal effect at 1 x 10^5 V/m, then significantly increasing 6-fold at 1.5 x 10^5 V/m, then increasing again by a factor of 3 at 2 x 10^5 V/m. There is no maximum density slope for 2.5 x 10^5 V/m, since an accidental repeat experiment was performed at 2 x 10^5 V/m. The slopes here are generally quite similar to the slopes at 10 kHz. Once again, these results confirm a reasonable electroporation effect and minimal cell destruction at a level of 2 x 10^5 V/m. Also, cell percentages showed similar behaviour to those exposed to 10 kHz bipolar fields. See also figure 4.34, where fractions are presented in a bar graph.

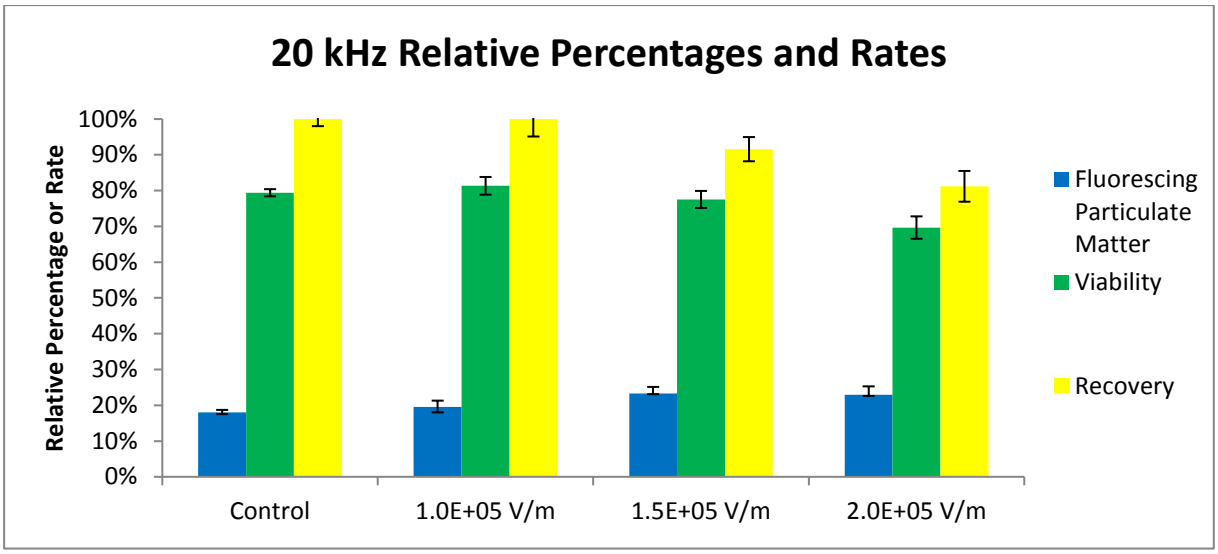

Figure 4.34. Bipolar 20 kHz electric field pulsed electroporation fractions and rates corresponding with results from figure 4.33. The left group represents the Control sample set, and the other groups represent the sample sets where the cells were exposed to bipolar pulses (1.0 x 10^5 V/m to 2.0 x 10^5 V/m). Error bars are shown for ±1 standard deviation.

Observed in figure 4.34 is a slight drop in Viability (79 % for Control down to 70 % for 2.0 x 10^5 V/m pulsing) and Recovery (100 % down to 81 %) which is slightly more pronounced than for the 10 kHz pulsed field study. Fluorescing particulate matter increased slightly, commensurate with the afore-mentioned changes. As for the 10 kHz pulsed field study, fields had not yet been intensified to the point where cells suffered high levels of destruction, so saturation levels were not reached yet.

4.3.2.2.4 Bipolar 100 kHz pulse study

Altogether 4 experiments were conducted for this study, since it was one of the earlier studies, and it was the intention to check consistency among experiments. Three of these experiments were identical, whilst the fourth used mid-step electrical field values. The latter was conducted in an attempt to find a finer resolution in values in the region of transition. Results are presented in figure 4.35.

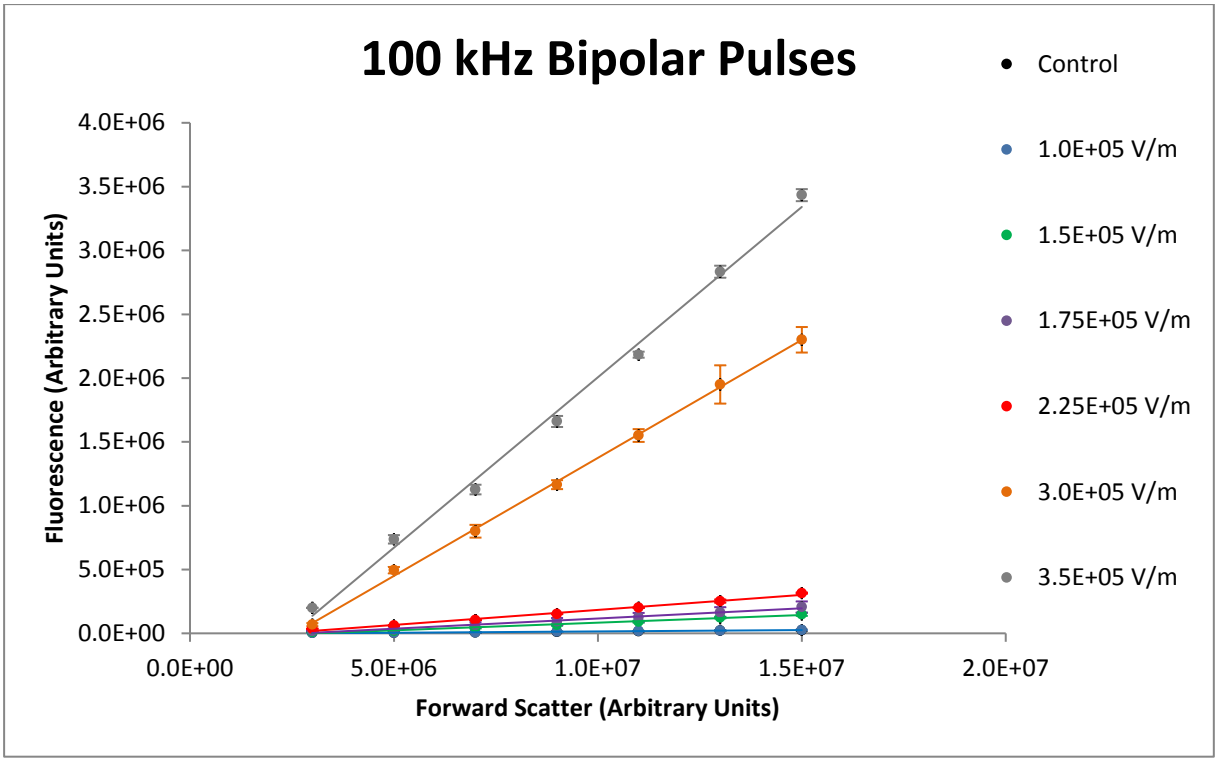

Figure 4.35. Maximum cell density plots of two bipolar pulses at a frequency of 100 kHz of 500 µs duration separated by 1 second, exposed to peak electric fields of 1.0 x 10^5 V/m to 3.5 x 10^5 V/m, including a Control. These data have been collected from four different experiments. Error bars are shown for ±1 standard deviation. Least mean squares linear trend lines have been included.

The maximum cell density plots from figure 4.35 at 100 kHz once again show a general increase in fluorescence as a function of the electrical regime. The Control and 0.5 x 10^5 V/m plots are very similar, suggesting no electroporation effect at this low level. Even up to 1.5 x 10^5 V/m the effect appears to be relatively insignificant. For data up to 2.25 x 10^5 V/m, however, the slopes are not consistent with the data observed at higher electric field strength (3.0 x 10^5 V/m and higher). When comparing the 100 kHz study data with similar electric field strength data in the 20 kHz, 10 kHz and monopolar studies, the results appear consistent. All these lower electric field strength data (including those for the 200 kHz, 400 kHz, and 800 kHz studies) had been generated within

several weeks where it is believed the PI dye efficacy had been reduced due to accidental continuous exposure to light during storage. PI should be stored, diluted in sterile PBS, in a tube wrapped with foil to keep it in the dark, and it should also be refrigerated at 4 ^{0}C. It is likely the foil wrap was compromised allowing light into the dye. Fresh dye had been made up afterwards, explaining higher dye efficacy, specifically for the experiments using the 3.0 x 10^5 V/m and 3.5 x 10^5 V/m pulse field settings. It has also been verified that the instrument had not been adjusted during the entire period used for these studies. The PI efficacy change affects interpretation of data for the 100 kHz to 800 kHz bipolar pulsed field studies, in that the 3 x 10^5 V/m and higher levels appear to have a greater fluorescence. However, while FOFS slopes are affected, proportions or fractions of the sub-populations of each full sample investigated are not affected by this change as sub-population specific gating and scaling has been applied and negative controls are used in every set of experiments, which normalises against any variation of PI efficacy.

Analysis of the slopes produced values of 0.00197 FOFS (Control), 0.00212 FOFS (1.0 x 10^5 V/m), 0.0120 FOFS (1.5 x 10^5 V/m), 0.0160 FOFS (1.75 x 10^5 V/m), 0.0235 FOFS (2.25 x 10^5 V/m), 0.185 FOFS (3 x 10^5 V/m), and 0.267 FOFS (3.5 x 10^5 V/m). This shows slight increases of slope up to 2.25 x 10^5 V/m, followed by an abrupt order of magnitude increase to 3 x 10^5 V/m which appears to be out of step for reasons identified above.

The bar graph in figure 4.36 shows the majority of proportions of the sub-populations. The Viability, highly fluorescing non-viable sub-normal size cells sub-population (not shown), fluorescing particulate matter and Recovery only started changing significantly from 3.0 x 10^5 V/m. Viability started at 83 % (Control), remained reasonably constant, then substantially dropped to 55 % (3.0 x 10^5 V/m), and finally dropped to 22 % (3.5 x 10^5 V/m). Simultaneously, percentages of the fluorescing particulate matter increased from 16 % (Control), to 32 % (3.5 x 10^5 V/m). Cell Recovery started at 100 % (Control), dropped significantly to 88 % (1.5 x 10^5 V/m), remained reasonably constant until 2.25 x 10^5 V/m, then dropped to 62 % (3.0 x 10^5 V/m), and finally reduced to 22 % (2.5 x 10^5 V/m). These numbers signal a rapid transition through the theoretical optimum point, where the ratio of electroporated cells to lysed cells is a maximum. This concept is discussed in detail later in this chapter, in section 4.3.2.3.5.

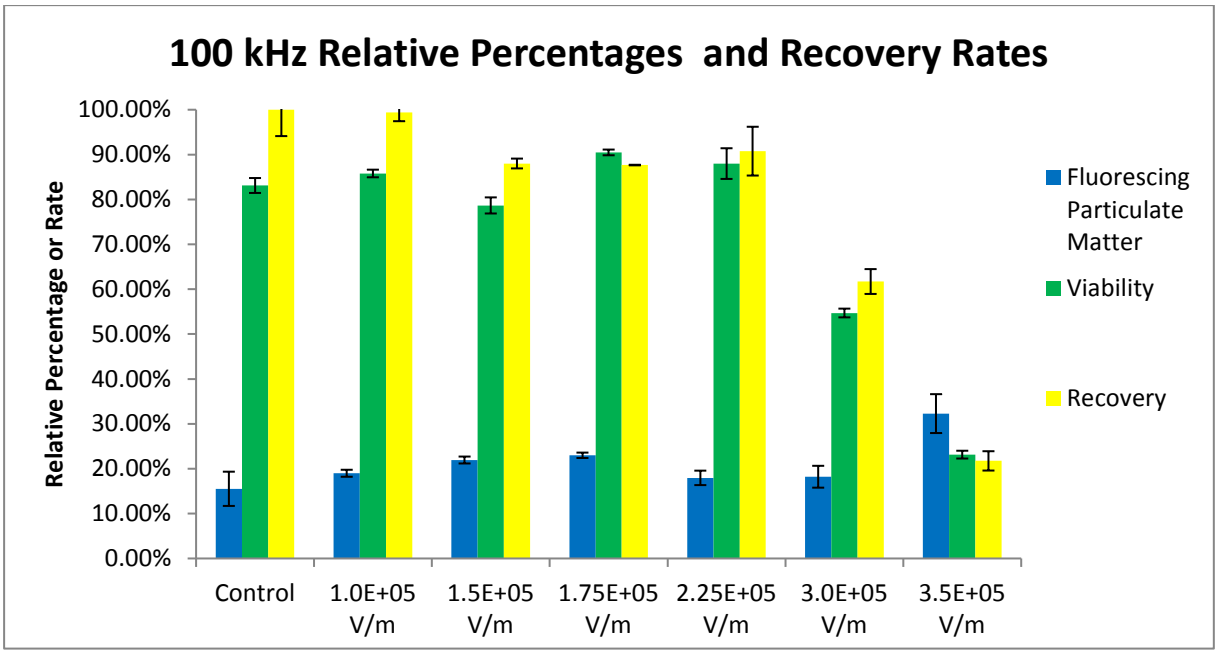

Figure 4.36. Bipolar 100 kHz electric field pulsed electroporation fractions and rates corresponding with results from figure 4.35. The left group represents the Control sample set, and the other groups represent the sample sets where the cells were exposed to bipolar pulses (1.0 x 10^5 V/m to 3.5 x 10^5 V/m). Error bars are shown for ±1 standard deviation.

The fluorescence microscopy experiments used electric field pulse levels up to 3 x 10^5 V/m at a frequency of 100 kHz with two sets of 500 µs duration pulses separated by 1 s, which are the same as one set of electric parameters used here. The data shown in figure 4.36 with the same electric field parameters corroborate those microscopy findings, with a similar high Yield and low lysis.

The major differences observed between the 100 kHz and 10 kHz studies is a marked drop in electroporation effect at the same electric field amplitude levels, thus requiring a higher electric field level before a grouping of similarly fluorescing viable cells is achieved. A likely explanation for this is that due to the high rate of electric field transitions through zero the percentage of time the membrane spends above a threshold is reduced at the higher frequency due to a lower overall duty ratio and the time constant associated with charging the membrane capacitance. Otherwise the characteristics appear quite similar.

4.3.2.2.5 Bipolar 200 kHz pulse study

The next bipolar study analysed cells at 200 kHz, and results are presented in figure 4.37.

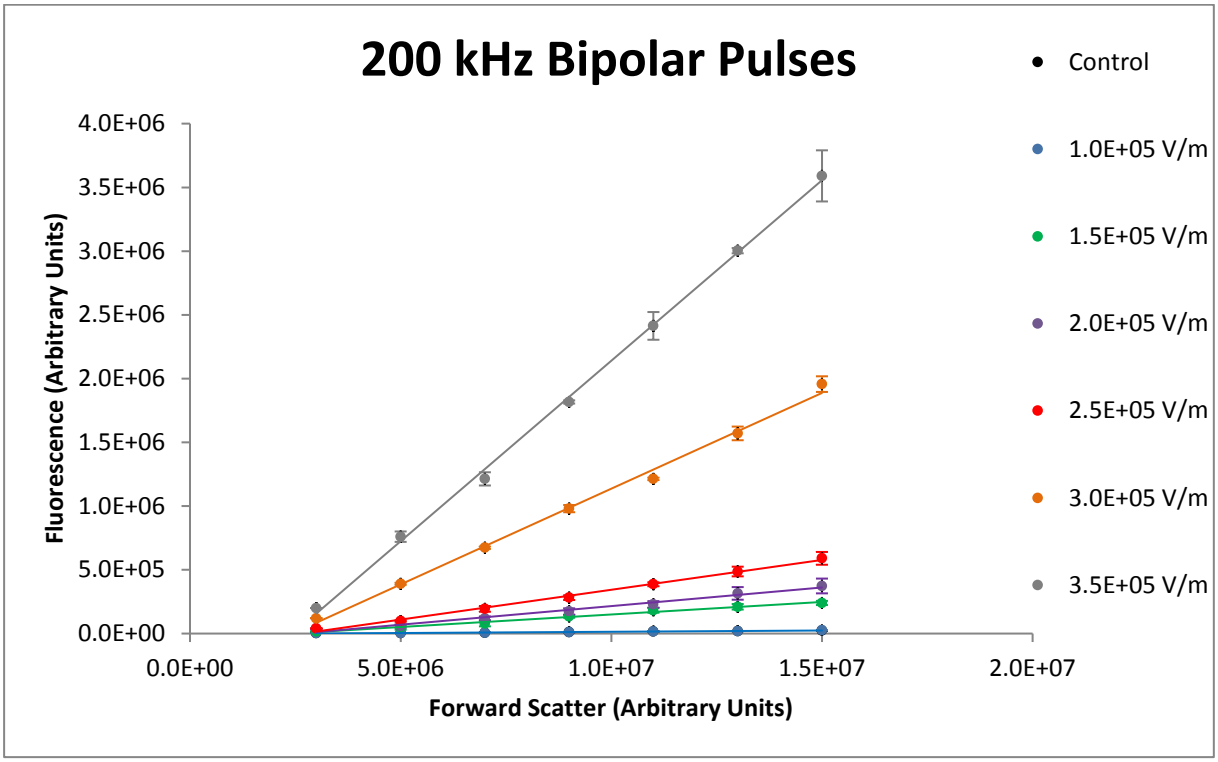

Figure 4.37. Maximum cell density plots of two bipolar pulses at a frequency of 200 kHz of 500 µs duration separated by 1 second, exposed to peak electric fields of 1.0 x 10^5 V/m to 3.5 x 10^5 V/m, including a Control. These data have been collected from three different experiments. Error bars are shown for ±1 standard deviation. Error bars are shown for ±1 standard deviation.

Quite similar to the 100 kHz study, similar trends and behaviours are observed in figure 4.37. The increase in fluorescence increases with the applied electric field intensity, although only starting to have an observable effect from 1.5 x 10^5 V/m. Once again the inconsistency between the set of samples up to 2.5 x 10^5 V/m and the samples above this field strength is noted.

Analysis of the slopes produced values of 0.00186 FOFS (Control), 0.00196 FOFS (1.0 x 10^5 V/m and 1.5 x 10^5 V/m), 0.0292 FOFS (2.0 x 10^5 V/m), 0.0468 FOFS (2.5 x 10^5 V/m), 0.150 FOFS (3.0 x 10^5 V/m), and 0.283 FOFS (3.5 x 10^5 V/m).

The bar graph shown in figure 4.38 identifies the majority of proportions of the sub-populations. Further analysis of the percentages of the features produced a Viability figure of 84 % (Control), which dropped to 60 % (3.0 x 10^5 V/m), and finally reduced to 21 % (3.5 x 10^5 V/m). Simultaneously, the fluorescing particulate matter figure was 9 % (Control), rising substantially

to 20 % (3.0 x 10^5 V/m), and then to 37 % (3.5 x 10^5 V/m). Recovery started at 100 % (Control), then dropped significantly to 61 % (3.0 x 10^5 V/m), and finally dropped to 17 % (3.5 x 10^5 V/m). These changes again suggest reaching a point beyond which Viability drops rapidly.

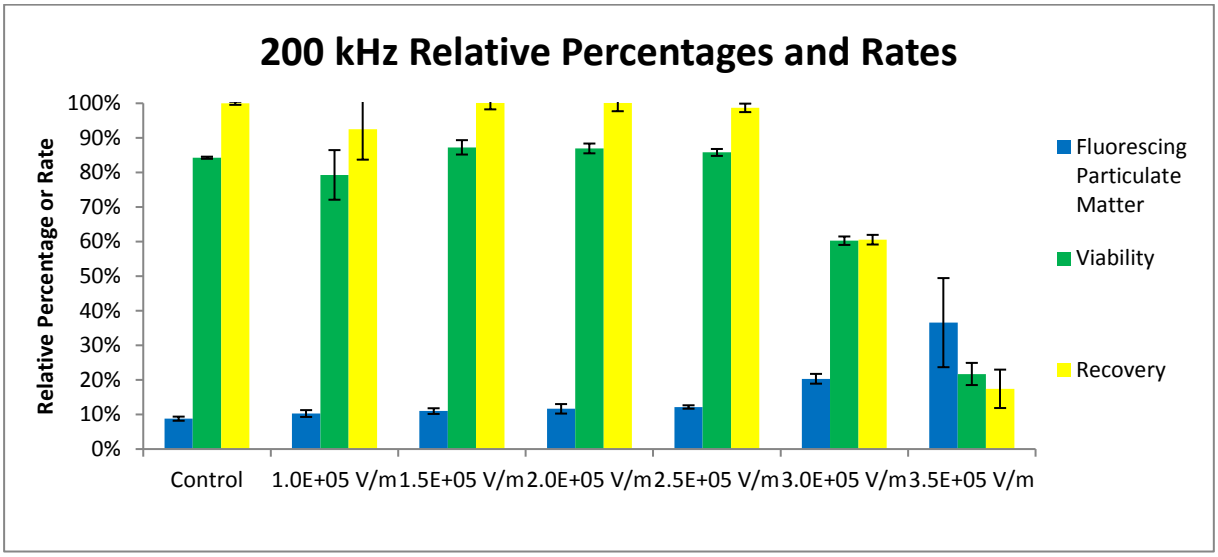

Figure 4.38. Bipolar 200 kHz electric field pulsed electroporation fractions and rates corresponding with results from figure 4.37. The left group represents the Control sample set, and the other groups represent the sample sets where the cells were exposed to bipolar pulses (1.0 x 10^5 V/m to 3.5 x 10^5 V/m). Error bars are shown for ±1 standard deviation.

4.3.2.2.6 Bipolar 400 kHz pulse study

Figure 4.39 illustrates a study at 400 kHz.

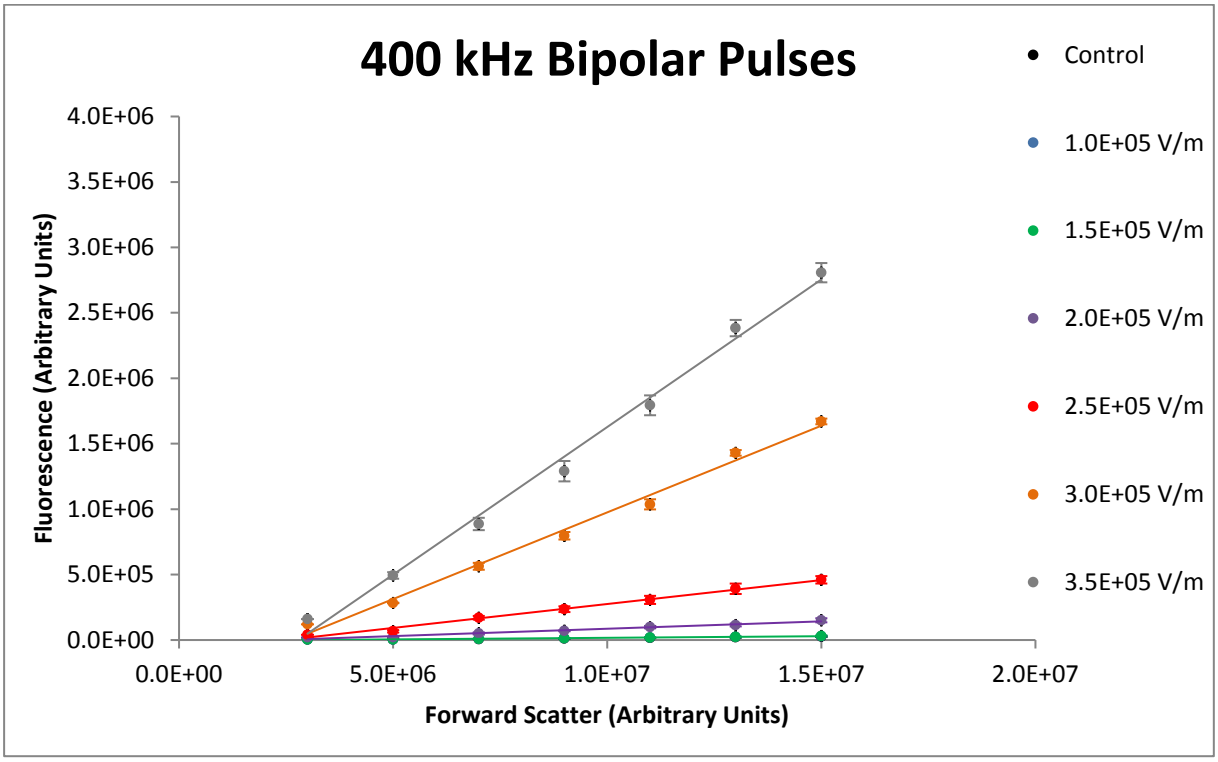

Figure 4.39. Maximum cell density plots of two bipolar pulses at a frequency of 400 kHz of 500 µs duration separated by 1 second, exposed to peak electric fields of 1.0 x 10^5 V/m to 3.5 x 10^5 V/m, including a Control. These data have been collected from three different experiments. Error bars are shown for ±1 standard deviation. Error bars are shown for ±1 standard deviation.

Again, seen in figure 4.39, the general expected characteristics are observed, with a general increase of fluorescence against electric levels, a near zero response at 1 x 10^5 V/m and 1.5 x 10^5 V/m, a very slight response at 2.0 x 10^5 V/m, and an increased response at 2.5 x 10^5 V/m and beyond.

Analysis of the slopes produced values of 0.00193 FOFS (Control), 0.00220 FOFS (1.0 x 10^5 V/m and 1.5 x 10^5 V/m), 0.0121 FOFS (2.0 x 10^5 V/m), 0.0389 FOFS (2.5 x 10^5 V/m), 0.129 FOFS (3.0 x 10^5 V/m), and 0.2168 FOFS (3.5 x 10^5 V/m). The slope for 3.5 x 10^5 V/m has dropped by 17 %, compared to the 200 kHz study.

Further analysis presented in figure 4.40 of the percentages of the features, produced a Viability figure of 81 % (Control), which then dropped to 69 % (3.0 x 10^5 V/m), and finally reduced to 42 % (3.5 x 10^5 V/m). Simultaneously, the fluorescing particulate matter figure was 11 % (Control),

which rose to 15 % (up to 2.5 x 10^5 V/m), then to 19 % (3.0 x 10^5 V/m), and finally to 23 % (3.5 x 10^5 V/m). Recovery started at 100 % (Control), then dropped to 77 % (3.0 x 10^5 V/m), and finally reduced to 45 % (3.5 x 10^5 V/m). These changes again suggest reaching a point beyond which Viability drops rapidly.

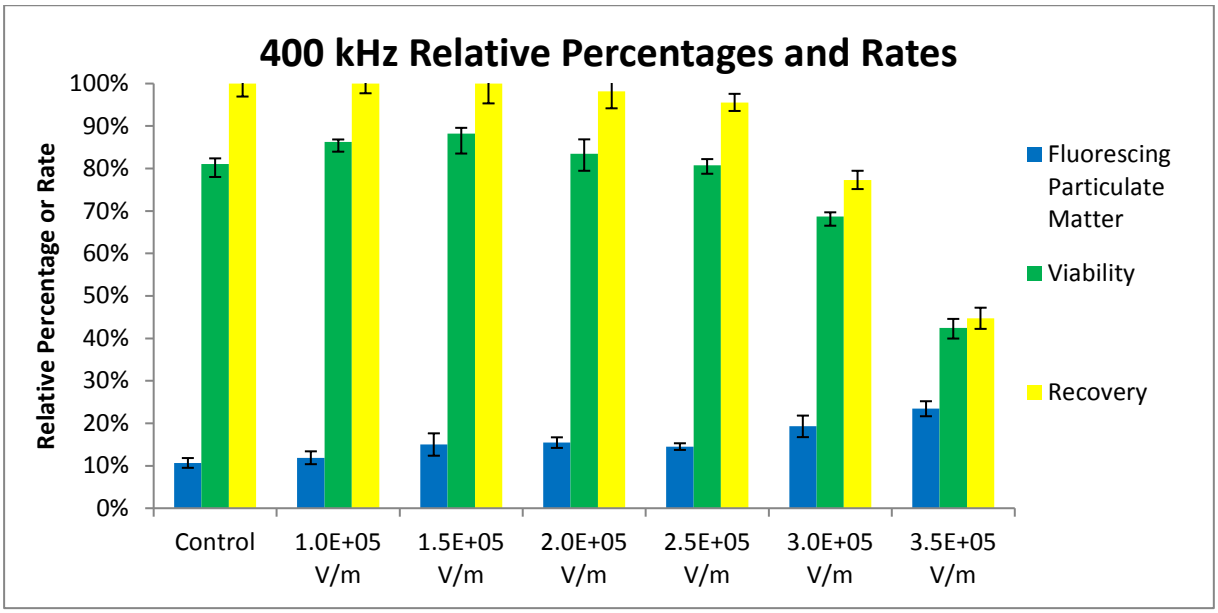

Figure 4.40. Bipolar 400 kHz electric field pulsed electroporation fractions and rates corresponding with results from figure 4.39. The left group represents the Control sample set, and the other groups represent the sample sets where the cells were exposed to bipolar pulses (1.0 x 10^5 V/m to 3.5 x 10^5 V/m). Error bars are shown for ±1 standard deviation.

4.3.2.2.7 Bipolar 800 kHz pulse study

The final frequency-magnitude study applied a frequency of 800 kHz, as is identified in figure 4.41.

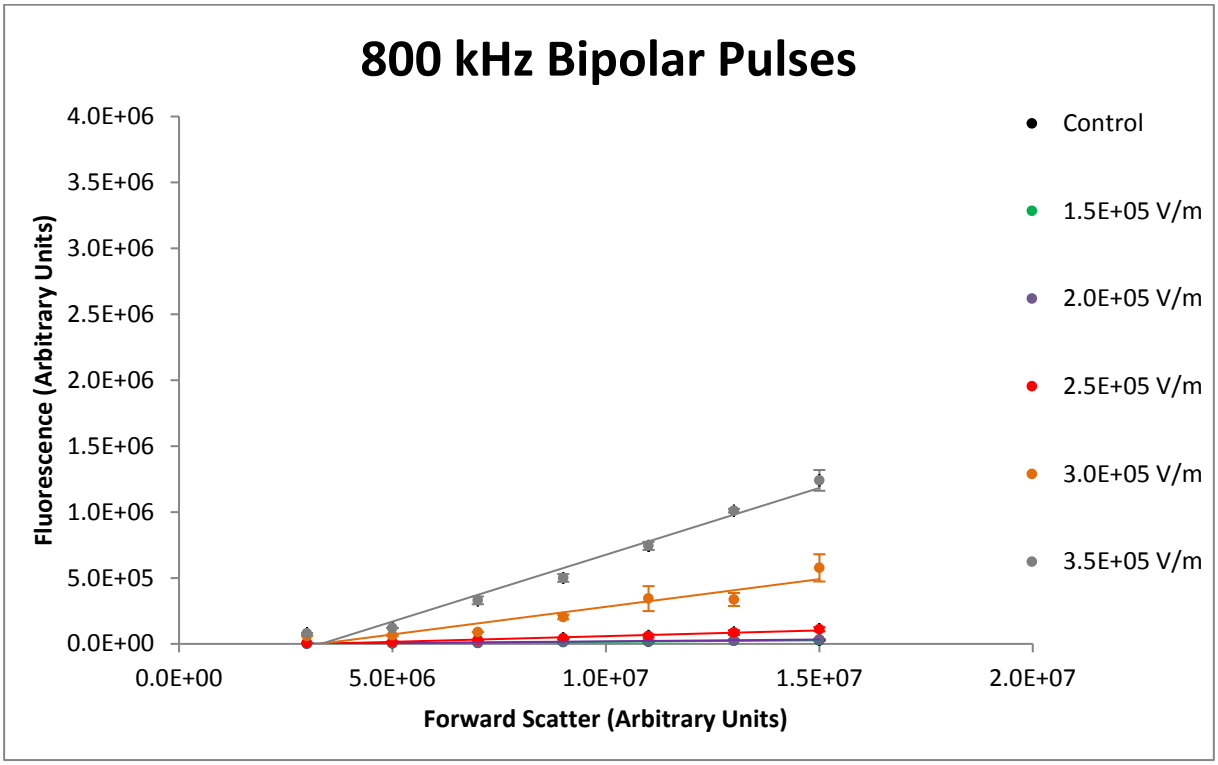

Figure 4.41. Maximum cell density plots of two bipolar pulses at a frequency of 800 kHz of 500 µs duration separated by 1 second, exposed to peak electric fields of 1.5 x 10^5 V/m to 3.5 x 10^5 V/m (excluding 3.0 x 10^5 V/m), including a Control. Data for 3.0 x 10^5 V/m have been ignored as they are inconsistent with the rest. These data have been collected from 2 different experiments. Error bars are shown for ±1 standard deviation. Error bars are shown for ±1 standard deviation.

As seen in figure 4.41, the 800 kHz plots once again are consistent with previous studies at lower frequencies including the typical increase in fluorescence as the electric levels increase, although it produced a near zero response up to 2.5 x 10^5 V/m.

Analysis of the slopes produced values of 0.00208 FOFS (Control), 0.00220 FOFS (1.5 x 10^5 V/m), 0.00289 FOFS (2.0 x 10^5 V/m), 0.00789 FOFS (2.5 x 10^5 V/m), and 0.0935 FOFS (3.5 x 10^5 V/m). The slope for 3.5 x 10^5 V/m has dropped by 57 %, compared to the 400 kHz study, signalling a rapid drop in electroporation level with frequency.

Further analysis, presented in figure 4.42, of the percentages of the features produced a Viability figure of 86 % (Control), which then dropped to 82 % (3.0 x 10^5 V/m) and finally reduced to 70 % (3.5 x 10^5 V/m). Simultaneously, the fluorescing particulate matter was 16 % (Control), which

rose to 17 % (up to 2.5 x 10^5 V/m), then finally reached 21 % (3.5 x 10^5 V/m). Recovery started at 100 % (Control), then dropped substantially to 77 % (3.5 x 10^5 V/m). These relatively minor changes in this case do not suggest reaching a point beyond which Viability drops rapidly.

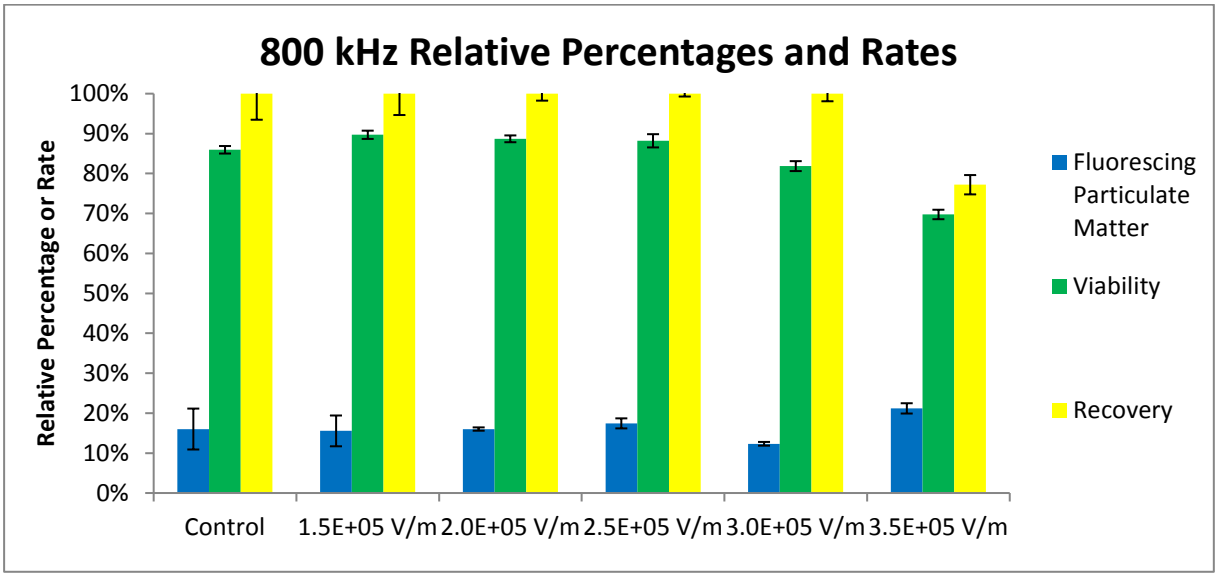

Figure 4.42. Bipolar 800 kHz electric field pulsed electroporation fractions and rates corresponding with results from figure 4.41. The left group represents the Control sample set, and the other groups represent the sample sets where the cells were exposed to bipolar pulses (1.0 x 10^5 V/m to 3.5 x 10^5 V/m). Error bars are shown for ±1 standard deviation.

This suggests that maximal electroporation has not yet been achieved for the 800 kHz pulses and higher electric field strength levels may need to be examined to identify a maximal level. An electric field strength of about 4 x 10^5 V/m will likely be required to achieve maximal combined poration and viability at 800 kHz, or, an alternative strategy may be to use 3 (or more) pulse bursts instead of the 2 used throughout these studies.

As a group the frequency-magnitude studies have demonstrated that:

- The effect of a set of monopolar pulses has a greater effect with regards to loss of cell viability than its bipolar counterpart for any given peak density slope (identifying a certain level of electroporation). As such, monopolar pulses may be more suitable for use in irreversible electroporation, due to its effective cell killing at relatively low pulse fields, in opposition to achieving the highest loading of cells without killing them.

- A peak fluorescence density curve of the nominal viable cells sub-population can be modelled reliably with a first order (linear) model. The slope of this line increases with pulse intensity.

- The electroporation effect diminishes with frequency if the same peak electric field values are used. This effect is well supported in the literature [51-54]. This is mainly due to two physical reasons. Firstly, due to transmembrane capacitance – the pulses go through more zero-crossing transitions as the frequency increases, reducing the mean time that the cell transmembrane potential is above a threshold required for electroporation initiation. Also associated with membrane capacitance, higher frequency signals do not induce as high transmembrane potentials as the membrane capacitance provides a lower impedance at these higher frequencies. Secondly, the finite slew rate of the electrical system makes the electric field waveform less square at higher frequencies resulting in a lower duty ratio and hence a lower time above a threshold transmembrane potential required for progression of electroporation.

- Generally, bipolar pulses are less likely to increase cell death and disintegration than monopolar pulses. Very high bipolar field values may cause this effect but this has not been studied.

- For the cells used in this study, a threshold value for electroporation appears to be below 1×10^5 V/m but above 0.5×10^5 V/m, for monopolar pulses, but above 1×10^5 V/m for bipolar pulses.

4.3.2.3 Cross study examination of all frequencies and applied electric fields studied

When considering all the previous analysis data as a whole, useful information emerges. Several aspects are now examined, including Viability, Recovery, electroporation Yield, comparison of Recovery and Yield, figure of merit, normalisation of electroporation across cell size range for increased pulsing frequencies: maximum density slopes and normalised fluorescence widths.

4.3.2.3.1 Viability

Firstly, it is common to monitor viability of cells during electroporation studies. It is normal to expect this figure to drop against increasing applied electric field magnitude, although not linearly. The process here involved gathering the percentages of the individual characteristic sub-populations, derived as the actual number of viable cells and non-viable cells, at the electric field levels tested, and then finding the ratio of viable cells to all cells (viable and non-viable). Viable cells include the nominally viable cells sub-population and any increase in the number of cells in the highly fluorescing non-viable normal size cells sub-population. The addition of these additional highly fluorescing normal size cells to the viable population is justified as they have shown a substantial increase in fluorescence, not being the result of originally dead (non-viable) cells typically seen in the negative control samples (untreated electrically). These cells are presumed to have survived, as they did not follow the characteristic process observed in these studies of shrinking. The non-viable cells included the highly fluorescing non-viable sub-normal size cells, the increase in the transitional non-viable small to sub-normal size cells and the highly fluorescing non-viable normal size cells from the Control samples. For definitions of the characteristic sub-populations, refer back to section 4.3.2.

4.3.2.3.2 Recovery of cells

Another metric analysed was “Recovery”, defined as the number of electrically treated viable cells compared with the number of Control viable cells. The Recovery metric may be more useful than Viability as it does not rely on interpretation of a number of sub-populations as Viability does, but only of the viable cell sub-population of the Control. Figure 4.43 plots Recovery of cells at the various pulsing frequencies and electric field intensities.

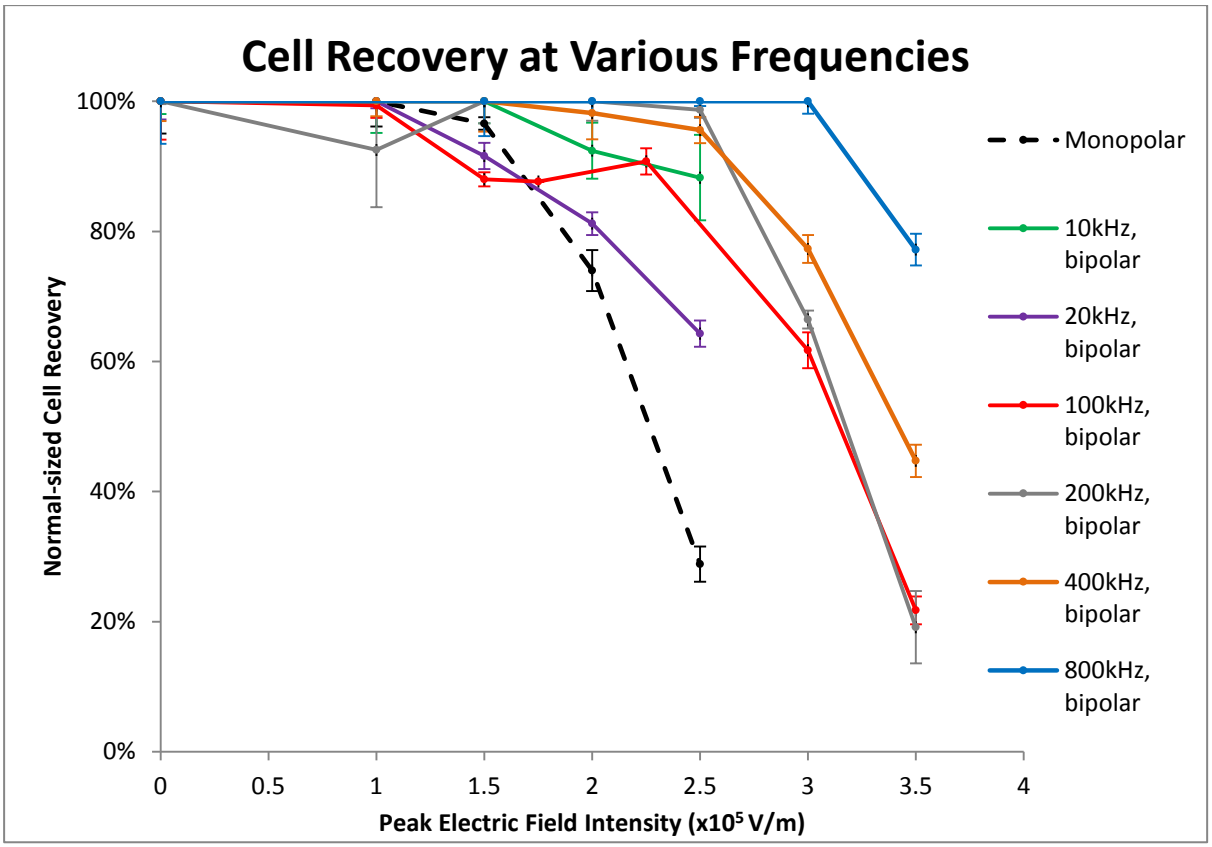

Figure 4.43. Graph showing normal-sized cell Recovery for all frequencies at the various applied field levels, with connecting lines between data points. Error bars are shown for ±1 standard deviation.

This result observed in figure 4.43 is consistent with the fluorescence microscope experiments showing Viability which is associated with Recovery, although not much data had been produced there. The results here represent a high Recovery and associated high Viability up to a very high electric field close to a very high electroporation level determined in this study, with a Yield-Recovery cross-over point at much higher than 50 %. This finding is contrary to the finding in [25], where monopolar field pulses were used, and where "optimal" electroporation is defined where there is a Yield-Viability cross-over at around 50 %.

4.3.2.3.3 Electroporation Yield

Electroporation Yield is examined next. This parameter is calculated as the proportion of the nominally viable cells sub-population that shows fluorescence above that for the Control viable cells, and is plotted against increasing electric field strength as presented in figure 4.44.

The number of Control viable cells is taken as a reference and tightly gated, thus falling in the low value fluorescence region of normal sized viable cells. The percentage of cells remaining in this

Control gated area (indicating immeasurably electroporated viable normal-sized cells) diminishes as the pulsed field is increased for non-control samples. Yield is expressed as

$$Yield = \left(1 - \frac{Number\ of\ viable\ cells\ in\ electroporated\ sample\ remaining\ in\ the\ Control\ gated\ area}{Number\ of\ viable\ cells\ in\ tightly\ gated\ Control\ sample}\right) \cdot 100\%. \quad (4.8)$$

The difference of close to 100 % Yield here compared to the 80 % in the microscopy analysis (see figure 4.7) is due to the slightly different definition of Yield. The 20 % difference is ascribed to the fact that this time the dead cells from the Control were not included as this sub-population of cells is not expected to change between Control and electroporated samples (obtained from the same stock of cells at the same time).

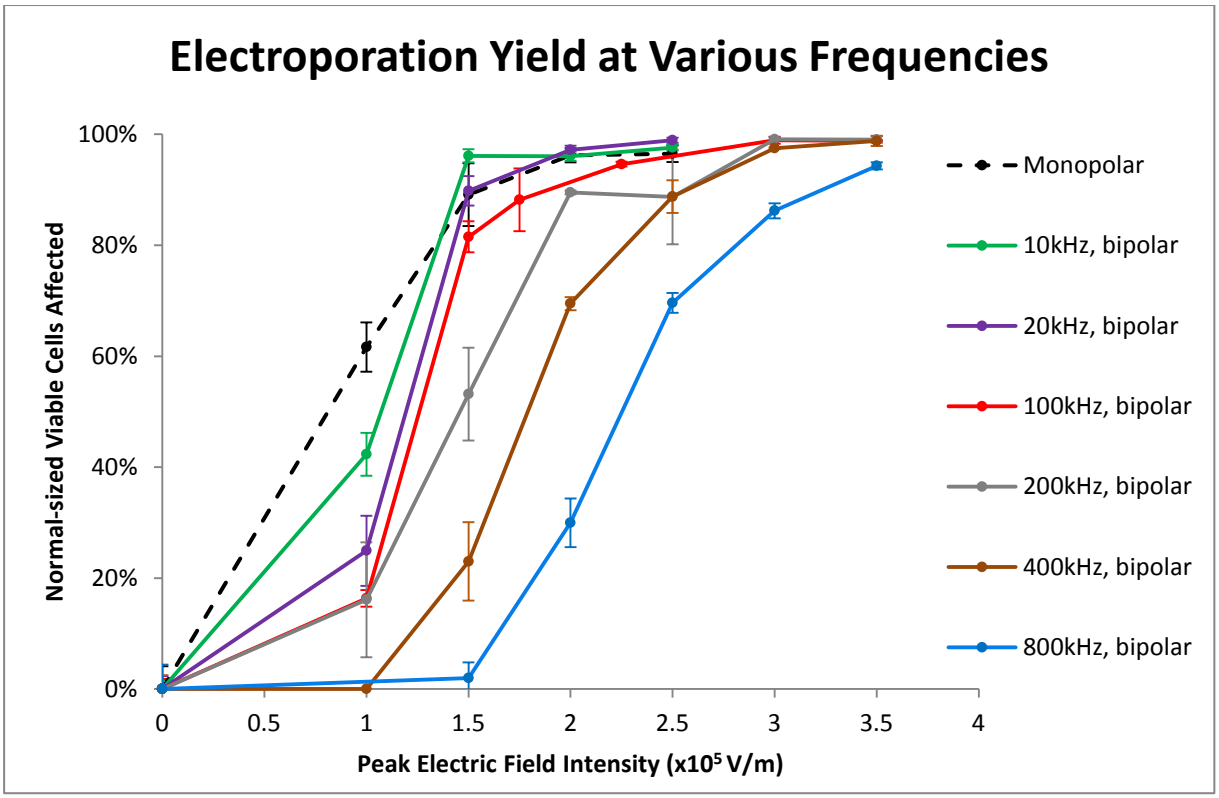

Figure 4.44. Graph showing electroporation Yield for all frequencies at the various applied field levels, with connecting lines between data points. Error bars are shown for ±1 standard deviation.

Observed in figure 4.44 is the typical widely reported sigmoidal curve [25, 55, 56]. Of note here is the general rightwards shift of the curve as a function of frequency, ranging from the monopolar pulses on the far left to bipolar pulses shifting more right as the pulsing frequency is increased.

4.3.2.3.4 Comparison of Recovery and Yield

Recovery and Yield are now compared, in a similar manner to that shown in figure 4.7 from the fluorescence microscope work. Figure 4.45 presents the Recovery and Yield graphs for both monopolar and 200 kHz bipolar pulses.

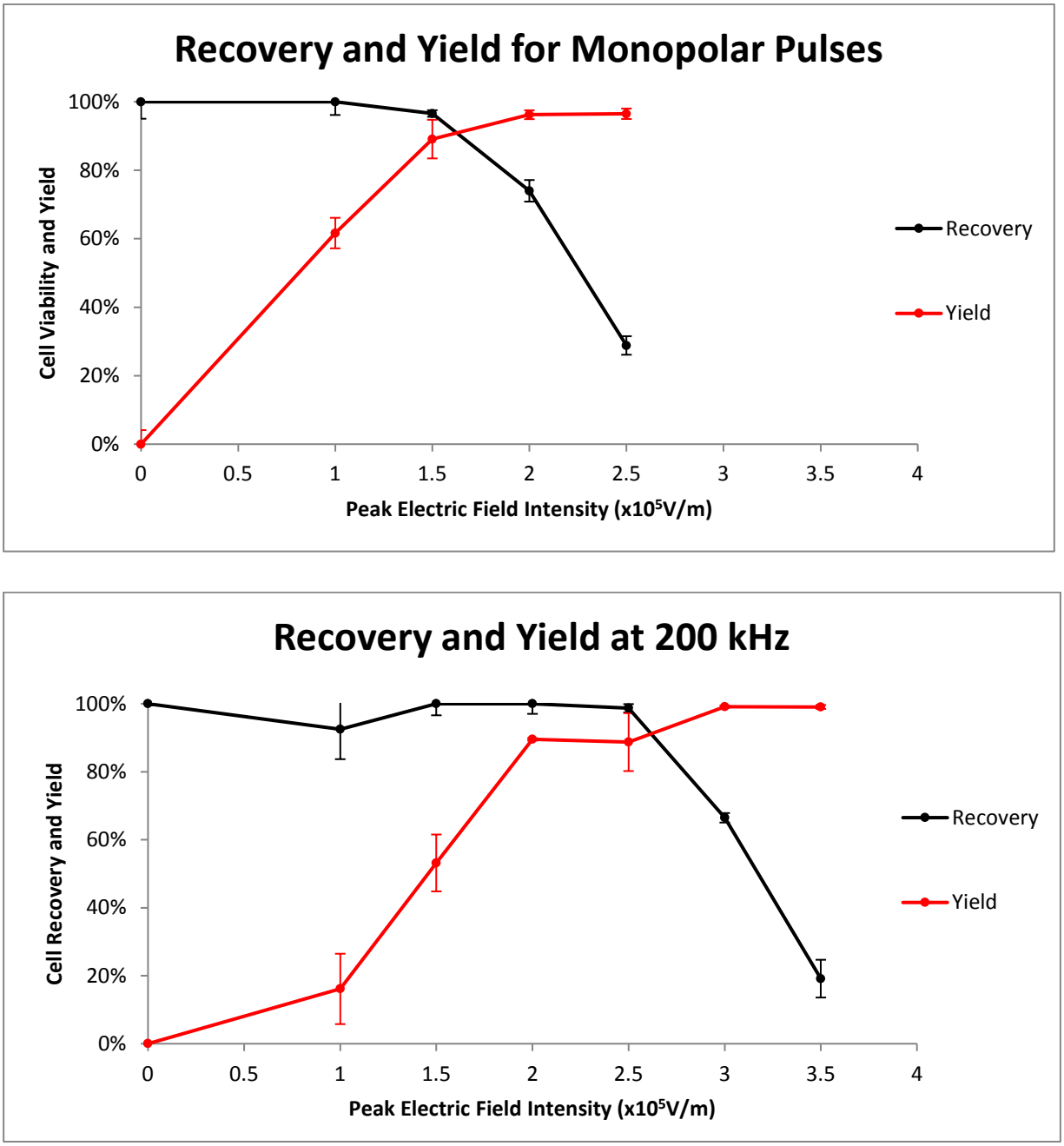

Figure 4.45. Graphs of cell Viability and electroporation Yield when applying monopolar field pulses (top), and bipolar electric field pulses at 200 kHz (bottom), with connecting lines between data points. Error bars are shown for ±1 standard deviation.

Figure 4.45 also shows connecting lines which have near sigmoidal behaviours. The top graph compares well with figure 4.7, in terms of shape, except for the lack of a curve between 0 and 1 x 10^5 V/m for Yield, likely due to the lack of data at 0.5 x 10^5 V/m.

4.3.2.3.5 Figure of Merit

Next, a Figure of Merit (FOM) is first defined and then derived, as is presented in figure 4.46. This FOM is calculated as the product of the two parameters, cell Recovery and electroporation Yield, expressed as

$$FOM = Recovery \cdot Yield \tag{4.9}$$

This definition of merit where the weightings are the same, e.g. 1.0 for Yield and 1.0 for Recovery, favours applications where it is desirable to maintain viability as much as possible but equally combined with loading the highest number of cells, such as for gene therapy and genome editing. Other applications such as electrochemotherapy and irreversible electroporation may benefit from a shift in emphasis, e.g. 1.0 weighting on Yield with a 3.0 weighting on Recovery (shifting the intersect point between Recovery and Yield to a higher electric field strength), where Recovery is less important. Taking the product of the weighted Recovery and Yield for the various pulsing frequencies produces a single peak value within the electric field intensity range, forming an application adjusted trade-off between Recovery and Yield.

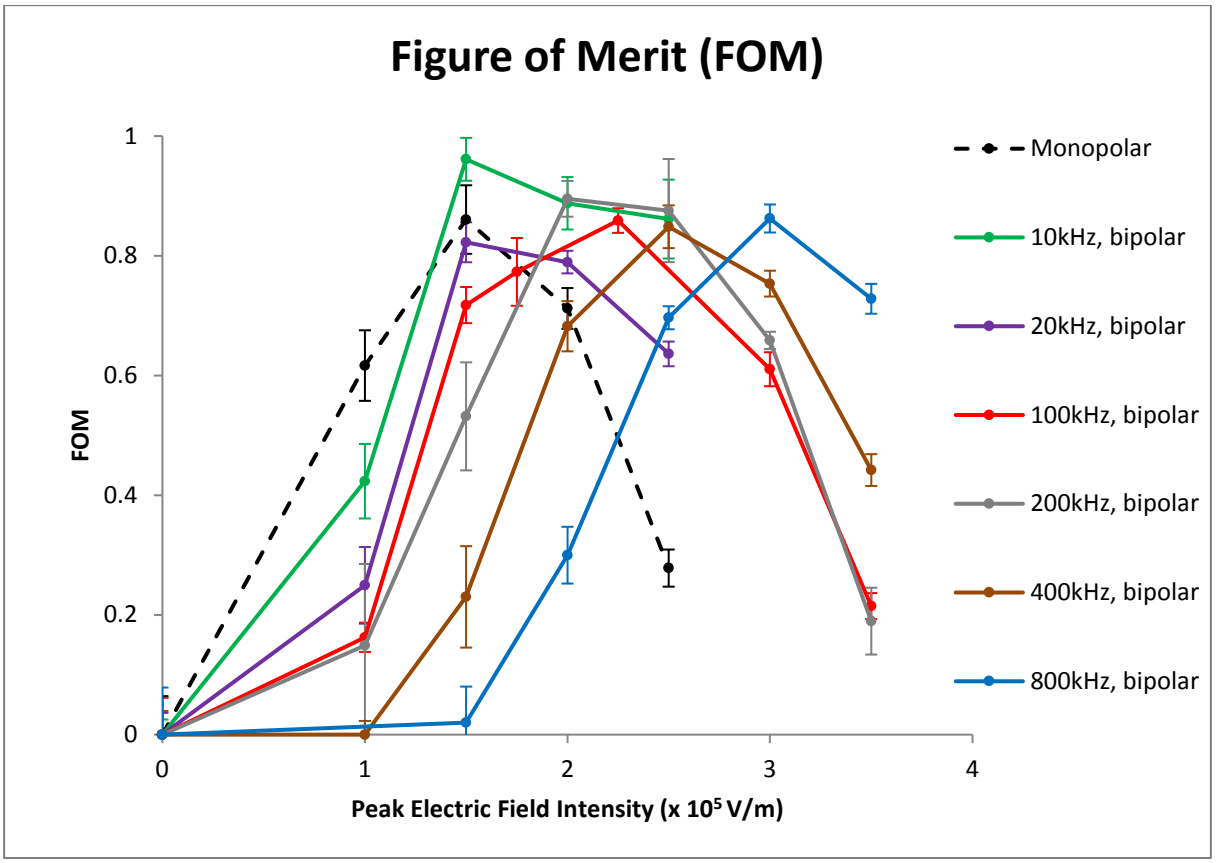

Figure 4.46. FOM graph with connecting lines between data points. Error bars are shown for ±1 standard deviation.

Observed in figure 4.46 are data points that typically rise to a peak and then fall again, as a function of the applied electric field. Of special note here is the general tendency for this peak to shift to the right as a function of pulsing frequency.

Figure 4.46 demonstrates that the FOM for low frequency (10 kHz and 20 kHz) bipolar pulses is similar for monopolar pulses, with their maxima located on a pulsing field strength of 1.5 x 10^5 V/m. A limitation in this graph is the lack of data points around the apparent peaks and also at lower values of pulsing field intensity. A generally apparent tendency is that the location of this maximum shifts towards the right requiring higher field strength pulses as the frequency is increased above 20 kHz. These results show that most pulsing frequencies share a common FOM (as defined) of approximately 0.86 with the exception of 10 kHz pulses at 0.96. This means the ratio of loading of cells with external molecules and simultaneously less cell lysis remains constant unless for 10 kHz which shows a slight improvement over all other pulsing frequencies.

Also observed in figure 4.46 is the consistent general rise in electric pulsed field intensity required as a function of frequency to obtain a maximum FOM (with the exception of the 200 kHz pulses where the peak FOM electric field strength is not very accurately defined owing to the larger data

deviation at this frequency in the vicinity of the peak at 2.5 x 10^5 V/cm). This implies a need to increase the intensity of the pulsing electric fields with pulsing frequency to achieve the desirable combination of maximal loading and minimal cell lysis.

4.3.2.3.6 Normalisation of electroporation relative to cell size range: comparison of maximum density slopes

Another cross study analysis has been performed to probe the speculation that there could be more normalised electroporation over a range of cell sizes when higher frequency electric field pulses are used (as suggested by some studies [29, 54, 57-60]). Normalisation in this instance is used to describe the instance where cells over the normal size range would experience a more consistent level of electroporation effect than they would as described by low frequency analysis. Such low frequency analysis indicates that the level of electroporation is proportional to cell diameter [54, 61]. This cross study analysis has been performed by first choosing a fixed maximum density point of fluorescence (1.0 x 10^5 arbitrary fluorescence units) at a forward scatter of 5 x 10^6 arbitrary units (small viable cell size) representing a mid-range degree of electroporation (high Yield and high Recovery) of the most populous cell size. The electrical parameters required at selected frequencies (including monopolar) that achieved a result closest to this chosen fluorescence and forward scatter were then determined. For the determined electrical parameters, the corresponding maximum density fluorescence points at maximum FOM were found at each frequency. The pulsing frequencies ranged across several orders of magnitude to cover the wide range, and included monopolar pulses (0 Hz), and bipolar pulses (10 kHz, 20 kHz, 100 kHz, 200 kHz and 400 kHz). The 800 kHz bipolar pulses were not included since these pulses were conducted at 3 x 10^5 V/m which occurred with higher efficacy PI assay work and would skew these values in favour of a higher slope. The results are shown in figure 4.47.

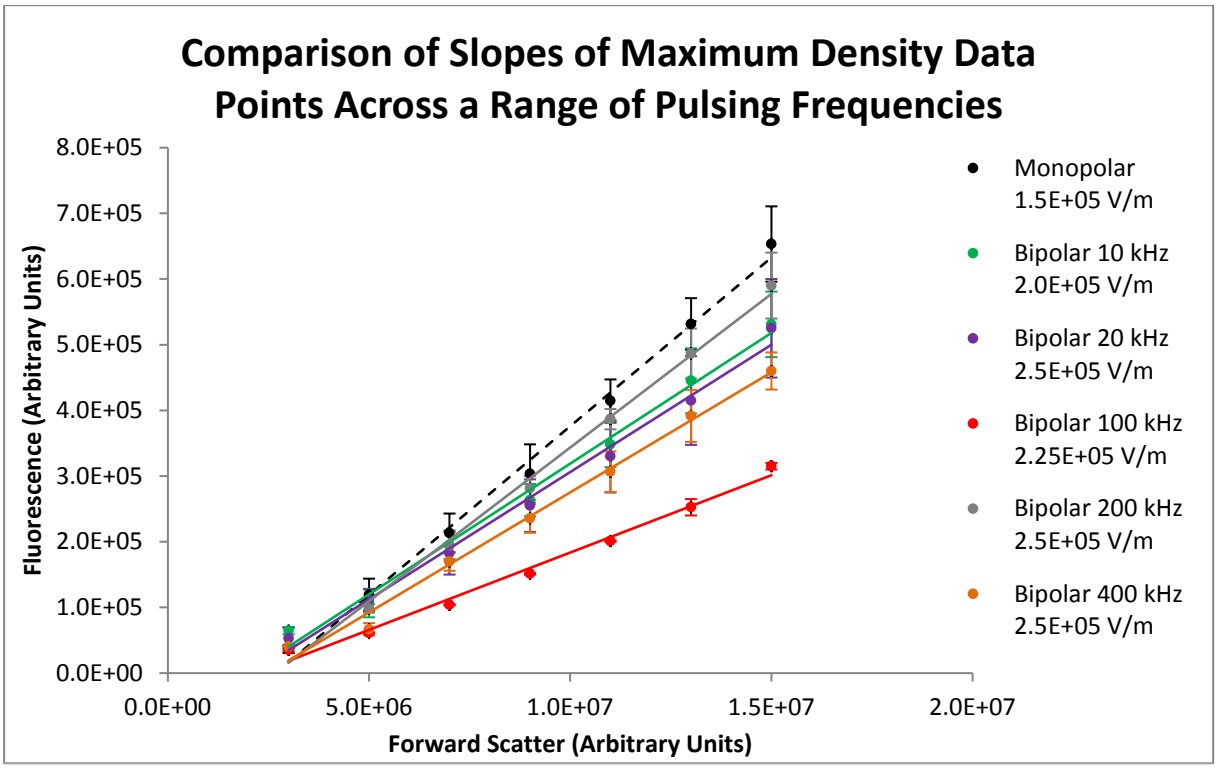

Figure 4.47. Graph showing slopes of maximum density points across the range of pulsing frequencies with a closest available comparable starting point at 1 x 10^5 fluorescence units for a forward scatter value of 5.0 x 10^6. Error bars are shown for ±1 standard deviation.

From figure 4.47 while it is observed that there is a reduction in the fluorescence slopes from monopolar (dashed black) to lower frequency bipolar pulses (10 kHz, 20 kHz, and 100 kHz, green, purple, and red lines respectively), the slopes for 200 kHz (grey) and 400 kHz (orange) do not follow this trend. Furthermore, with the large standard deviations experienced, the differences in slopes over the full frequency range are not significant due to large overlaps of data point spreads (table 4.4 lists these data points and their slopes). The implication here is that there is no observable consistent normalisation of electroporation effect over the range of normal cell sizes, over the frequency range tested.

Table 4.4. Average data points representing the graph in figure 4.47.

Pulsing Frequency (kHz)	Pulsing Field (x 10^5 V/m)	Maximum Density Curve Slope (x 10^{-2} FOFS)
0	1.5	5.14
10	2	3.98
20	2.5	3.88
100	2.25	2.35
200	2.5	4.68
400	2.5	3.65

4.3.2.3.7 Normalisation of electroporation relative to cells of a given size: comparison of normalised fluorescence widths

Another final metric of the dot plots is the relative or normalised width of the viable electroporated cell sub-population at the densest point, representing the greater majority of viable cells that have undergone measureable electroporation. This metric identifies the relative spread of fluorescence, where a relative narrowing of this width suggests a more consistent treatment or consistent poration of cells at any given cell size. This is an advantage over a wider spread of fluorescence suggesting a less consistent treatment. Data were derived from the histograms which were used to derive the data points on the maximum density plots and were then used to fit Gaussian curves using a least mean squares method. This process was repeated for each of the 3 samples in each experiment to provide a statistical mean and standard deviation and is identified in the associated graph. The Gaussian curves provide the standard deviation and mean for each set, as a function of electric field intensity and pulsing frequency. The normalised fluorescence width of viable electroporated cells is calculated as

$$Normalised\ Width = \frac{Fluorescence\ Gaussian\ Standard\ Deviation}{Fluorescence\ Gaussian\ Mean}. \qquad (4.9)$$

A graph of these normalised widths is presented in figure 4.48.

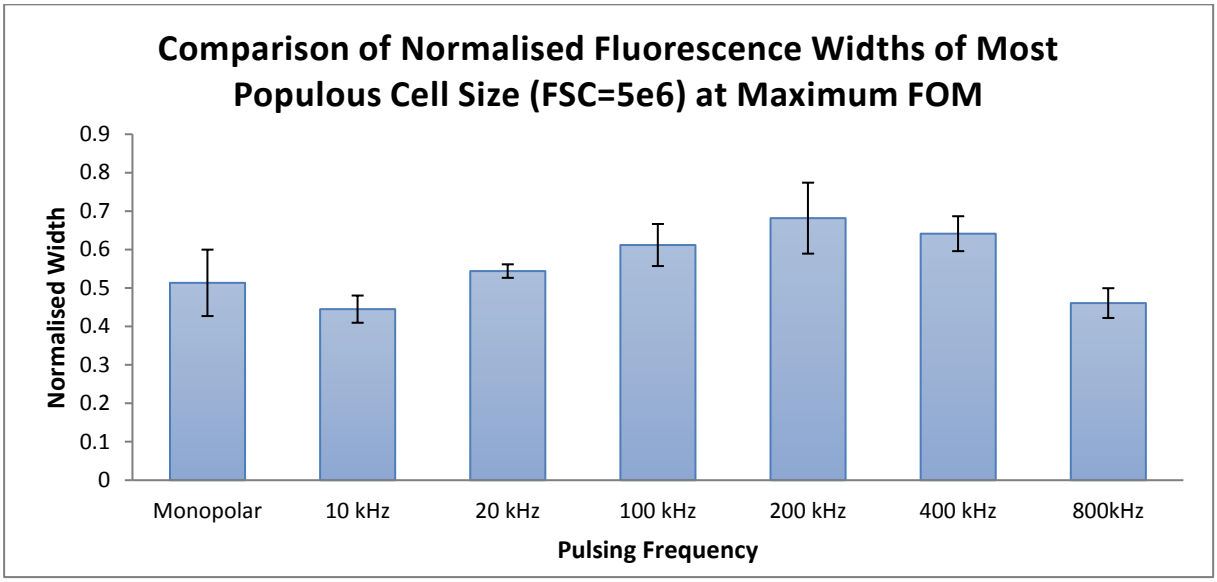

Figure 4.48. Normalised fluorescence width for the maximum FOM settings at the various pulsing frequencies for cells of average size 5 x 10^6 forward scatter units.

Observed from figure 4.48, where normalised widths were obtained for the most populous cell size of 5 x 10^6 (ranging between 4 x 10^6 and 6 x 10^6) fluorescence units of the respective electric field intensities for maximum FOM at the pulsing frequency, the monopolar width is 15 % greater

than that for 10 kHz. However, between 20 kHz to 400 kHz, the normalised width is higher than the monopolar case. At 800 kHz, the normalised width is again less than that for monopolar pulses. Given the limited number of experimental repeats, and the inconsistent trend with increasing frequency, no clear conclusions can be drawn about whether bipolar pulses can improve normalisation of electroporation at any given cell size.

4.3.2.4 General Observations in Flow Cytometric Analysis of Electroporation

The following general observations have been made about the experimental results throughout all the studies using the flow cytometer:

1. Negative and positive controls have been established, to discriminate between cells that are not affected, cells that are partially affected, cells that are moderately affected, cells that are overtly affected and cells that are dead/destroyed (non-viable).

2. The Ishikawa cell line used throughout these studies has been analysed by flow cytometry. Characteristics include its sub-populations (4 for Control samples and up to 6 for electrically treated samples), relative numbers of cells within each sub-population, relative position and shape within the "size-fluorescence" flow cytometry dot plots, and cell sub-population dynamics shortly after being treated electrically, across a range of pulsing frequencies and electric field intensities.

3. Electroporation is a threshold effect – for the cells used in this study the threshold lies between 0.5 and 1.0 x 10^5 V/m, for monopolar pulses and above 1 x 10^5 V/m for bipolar pulses depending on frequency.

4. Fluorescence increases with increasing PI dye concentration.

5. Fluorescence increases with magnitude of applied electric fields. This suggests that more dye molecules have entered the cells, thus a more pronounced effect of electroporation was the result.

6. Fluorescence increases with number of pulses applied, and hence total duration of pulses, suggesting an increase of electroporation.

7. The maximum density curve of viable cells exhibits a linear characteristic in the fluorescence intensity *vs* cell area region and the slope increases with increased magnitude of applied electric fields and increased number of pulses applied.

8. Monopolar pulses have a greater effect on cells than any equivalent bipolar pulses. Relatively high monopolar field pulses cannot sustain a reasonable number of well-electroporated but viable cells, while bipolar pulses can.

9. Bipolar pulses tend to produce less non-viable cells and fluorescing particulate matter than monopolar pulses at an equivalent viable cell sub-population peak density slope.

10. Bipolar pulses require a higher electric field strength for the same degree of electroporation at higher frequencies. It is likely that this occurs due to an inherent time constant associated with electric charge separation for a cell membrane, thus exceeding the threshold transmembrane potential required for electroporation for less time at higher frequencies than at lower frequencies. It is also due to the non-ideal pulse waveform at higher frequencies that the time above a threshold is further reduced.

11. The normal increase of electroporation effect as a function of cell diameter when applying a limited time static (monopolar) electric field pulse is a disadvantage within a population of a range of cell sizes, since it favours large cells over small cells. Thus longer duration monopolar electroporation pulses are less suitable for consistent treatment of tissue with a range of cell sizes. There is no conclusive evidence from the experiments carried out showing bipolar pulses up to 400 kHz help make electroporation more consistent over the normal cell size range. However, in chapter 2, section 2.1.1, it was indicated that with an electroporation buffer conductivity of 0.13 S/m such normalisation may not be observable until close to or over 1 MHz bipolar pulses are used.

12. There is no clear evidence that electroporation fluorescence is normalised or equalised for a given cell size for bipolar pulses up to 800 kHz. This means that there is still a relatively wide spread in fluorescence in a population of similar sized cells, despite raising the frequency of electroporation pulsing.

13. Finally, the high field value monopolar pulses produced an early (small forward scatter) plateau or even a slight peak in the maximum density curve, which did not appear with all the bipolar pulses. Careful re-analysis (see also figure 4.18, where special gating was performed to separate the viable cell sub-population into two groups) of this maximum density curve reveals the close proximity of an increased number of cells in the transitional non-viable small to sub-normal cell size sub-population that effectively skew this curve, suggesting an early migration of cells becoming non-viable under the prevailing electric parameters that are associated with severe conditions (that is, the rapid increase in number of cells becoming non-viable at 2.5×10^5 V/m monopolar pulses).

4.4 Considerations of Electroporation of Tissue

In this thesis experimental electroporation work focused on cancer cells in suspension. How would tissue respond to such treatment? As had been identified in section 4.2, a cell line was selected with the hope of doing some preliminary work on large clumps of cells or spheroids, thus it was required to be an adherent cell line, which is a characteristic of the Ishikawa cell line. Spheroids were successfully cultured over a sustained period of 1 month yielding 4 spheroids from a 12 compartment culture plate. These spheroids were not electroporated as the electroporation protocols and cuvette had not been developed sufficiently for assay work at the time.

Bipolar electroporation pulses may be beneficial in treatment of tissue for several reasons. First, since nett charge delivered is zero, bipolar pulses do not produce electrolytic by-products as may originate from the metals of electrodes which are generally toxic [62]. Secondly, high frequency bipolar pulses are likely to couple better through poorly conductive tissues allowing better penetration and thus less invasive placement of electrodes [63]. Thirdly, use of high enough bipolar frequencies are less likely to create muscle contractions than monopolar pulses, eliminating the need for muscle relaxants and pain management [64]. Fourth, malignant tumours have a large variety of cell sizes and morphologies [65], and any form of normalisation of the affect across these differences would be beneficial.

4.5 Conclusion

A successful cuvette has been developed for the experiments where electric field pulses have been applied to human cancer cells in suspension. This cuvette has been used for more than 60 experiments without any problems or failure, so has proved to be very robust and highly reliable. Modelling confirmed a uniform distribution of electric field, for static applied potentials, and likely confirms a uniform dynamic distribution.

Efficient cell culture and electroporation protocols have been developed and improved for the experiments undertaken.

A fluorescence microscopy protocol has successfully been developed and improved but has proved inefficient and showed low resolution of fluorescence, rendering this technique impractical. Nevertheless, a typical S-shaped curve was observed of percentage fluorescing cells against electric field strength as is typical in the literature. However, it was only possible to discern cells fluorescing brightly, dimly, or not at all.

A flow cytometry protocol has also successfully been developed and improved, and, in contrast with fluorescence microscopy, has proved to be a productive technique in analysing large populations of cells. Analysis was performed in terms of cell size and fluorescence, in fine detail, in a much shorter experimental time. This has enabled a detailed investigation into the differences inherent in different electric field strengths and different frequencies, and also comparison between square monopolar and bipolar electric field pulses applied to a particular human cancer cell line. Monopolar pulses appear to have more detrimental effects on cells compared to bipolar pulses for an equivalent mean fluorescence. Thus bipolar fields show an advantage over monopolar fields if the aim is to not kill cells directly but to maximally load cells with a specific molecule. Higher frequencies tend to demand higher electric field strength to produce the same degree of electroporation than at lower frequencies. There appears to be less cell lysis at higher frequencies. There is little evidence showing that bipolar electric field pulses up to 800 kHz tend to create a narrower spread of loading of cells with external molecules for any given cell size, or that electroporation is more consistent over the normal cell size range, compared to monopolar pulses.

Ishikawa cell line characteristics have been observed and categorised during these studies. These include the full range of sub-populations, and how they are affected as a result of electroporation, showing dynamics, across the range of pulsing frequencies and electric field intensities studied.

It has been demonstrated that the developed electroporator system is capable of successfully and reliably electroporating Ishikawa human cancer cells in suspension. Two widely different techniques have been developed to produce electroporation consistent with the literature, at a range of square wave pulses between monopolar and bipolar (10 kHz to 800 kHz) bursts. Differences between bipolar and monopolar pulses were examined and characterised, as well as differences with frequency and with electric field levels. These differences have been summarised in section 4.3.2.4.

4.6 References

[1] D. Baksh, L. Song and R. S. Tuan, "Adult mesenchymal stem cells: characterization, differentiation, and application in cell and gene therapy", *J Cell Mol Med*, Vol. 8, No. 3, pp. 301-316, 2004.

[2] J. A. Impellizeri, G. Ciliberto and L. Aurisicchio, "Electro-gene-transfer as a new tool for cancer immunotherapy in animals", *Vet Comp Oncol*, Vol. 12, No. 4, pp. 310-318, 2014.

[3] C. Y. Kim, et al., "Increased in vivo immunological potency of HB-110, a novel therapeutic HBV DNA vaccine, by electroporation", *Exp Mol Med*, Vol. 40, No. 6, pp. 669-676, 2008.

[4] B. Al-Sakere, et al., "A Study of the Immunological Response to Tumor Ablation with Irreversible Electroporation", *TCRT*, Vol. 6, No. 4, pp. 301-305, 2007.

[5] M. Hashimoto and T. Takemoto, "Electroporation enables the efficient mRNA delivery into the mouse zygotes and facilitates CRISPR/Cas9-based genome editing", *Scientific Reports*, Vol. 5, No. 11315, pp. 1-7, 2015.

[6] C. Jiang, R. V. Davalos and J. C. Bischof, "A Review of Basic to Clinical Studies of Irreversible Electroporation Therapy", *IEEE T Bio-med Eng*, Vol. 62, No. 1, 2015.

[7] The Online Oxford Dictionary, *Definition for "cuvette"*, Oxford University Press, 2015, [Online].
Available: http://www.oxforddictionaries.com/definition/american_english/cuvette

[8] Biorad, Gene Pulser/MicroPulser Electroporation Cuvettes, [Online]. Available: http://www.bio-rad.com/en-nz/product/gene-pulser-micropulser-electroporation-cuvettes

[9] Eppendorf, Vis Cuvettes, [Online]. Available: https://online-shop.eppendorf.com/OC-en/Detection-44540/Accessories-44542/Eppendorf-Vis-Cuvettes-PF-46666.html

[10] BTX, Electroporation Cuvettes Plus, [Online]. Available: https://www.btxonline.com/btx-electroporation-cuvettes-plus/

[11] USA Scientific, Electroporation Cuvette 0.4 cm Gap, [Online]. Available: http://www.usascientific.com/electroporation-cuvette-0.4cm.aspx

[12] T. Kotnik, D. Miklavcic and L. M. Mir, "Cell membrane electropermeabilization by symmetrical bipolar rectangular pulses: Part II. Reduced electrolytic contamination", *Bioelectroch*, Vol. 54, No. 1, pp. 91-95, 2001.

[13] Dow Corning, Sylgard 184 Silicon Elastomer Kit, [Online]. Available: http://www.dowcorning.com/applications/search/products/Details.aspx?prod=01064291

[14] Dow Corning, Sylgard 184: Material Safety Data Sheet, Ver. 1.1, 2014, [Online]. Available: http://www.dowcorning.com/DataFiles/0902770181dbef0a.pdf

[15] S. Tay, et al., "Single-cell NF-kB dynamics reveal digital activation and analogue information processing", *Nature*, Vol. 466, pp. 267-271, 2010.

[16] T. Kotnik, D. Miklavcic and T. Slivnik, "Time course of transmembrane voltage induced by time-varying electric fields: a method for theoretical analysis and its application", *Bioelectroch Bioener*, Vol. 45, No. 1, pp. 3-16, 1998.

[17] T. Kotnik and D. Miklavcic, "Theoretical evaluation of the distributed power dissipation in biological cells exposed to electric fields", *Bioelectromagnetics*, Vol. 21, No. pp. 385-394, 2000.

[18] J. M. Naciff, et al., "The Genomic Response of a Human Uterine Endometrial Adenocarcinoma Cell Line to 17a-Ethynyl Estradiol", *Toxicol Sci*, Vol. 107, No. 1, pp. 40-55, 2009.

[19] N. J. Hannan, et al., "Models for Study of Human Embryo Implantation: Choice of Cell Lines?", *Biol Reprod*, Vol. 82, pp. 235-245, 2010.

[20] M. Nishida, "The Ishikawa cells from birth to the present", *Human Cell*, Vol. 15, No. 3, pp. 104-117, 2002.

[21] R. Edmondson, et al., "Three-Dimensional Cell Culture Systems and Their Applications in Drug Discovery and Cell-Based Biosensors", *Assay Drug Dev Technol*, Vol. 12, No. 4, pp. 207-218, 2014.

[22] S. A. Altman, L. Randers and G. Rao, "Comparison of Trypan Blue Dye Exclusion and Fluorometric Assays for Mammalian Cell Viability Determinations", *Biotechnol Progr*, Vol. 9, No. 6, pp. 671-674, 1999.

[23] E. D. Mackowiac, Chapter 64, Diagnostic Drugs and Reagents, in *Remington: The Science and Practice of Pharmacy*, 21st ed., Ed. D. B. Troy and P. Berringer, Lippincot, Williams and Wilkins Publishers, Philadelphia, p. 1262, 2006.

[24] M. Pavlin, et al., "Effect of Cell Electroporation on the Conductivity of a Cell Suspension", *Biophys J*, Vol. 88, No. 6, pp. 4378-4390, 2005.

[25] J. Michie, et al., "Assessment of Electroporation by flow cytometry", *Flow Cytometry*, Vol. 41, No. 2, pp. 96-101, 2000.

[26] C. Riccardi and I. Nicoletti, "Analysis of apoptosis by propidium iodide staining and flow cytometry", *Nature Protocols*, Vol. 1, pp. 1458-1461, 2006.

[27] W. A. Dengler, et al., "Development of a propidium iodide fluorescence assay for proliferation and cytotoxicity assays", *Anticancer Drugs*, Vol. 6, No. 4, pp. 522-532, 1995.

[28] Chemspider, *Online chemical structure database*, 2015, [Online]. Available: http://www.chemspider.com/

[29] T. Kotnik, et al., "Cell membrane electropermeabilization by symmetrical bipolar rectangular pulses: Part I. Increased efficiency of permeabilisation", *Bioelectroch*, Vol. 54, No. 1, pp. 83-90, 2001.

[30] B. Valic, et al., "Effect of electric field induced transmembrane potential on spheroidal cells: theory and experiment", *Eur Biophys J*, Vol. 32, No. 6, pp. 519-528, 2003.

[31] H. M. Shapiro, *Practical flow cytometry*, 4th ed., John Wiley and Sons, 2003.

[32] M. G. Macey, "Principles of Flow Cytometry", in *Flow cytometry – Principles and applications*, M. G. Macey (ed.), Humana Press, Totawa, New Jersey, US, 2007.

[33] Becton Dickinson (BD Biosciences), *BD Accuri C6 Flow Cytometer Instrument Manual*, 7820018-01 Rev-2, 2012, [Online]. Available: https://www.bdbiosciences.com/documents/BD_Bipolarcuri_C6Flow_Cyto_Instrument_Manual.pdf

[34] Becton Dickinson (BD Biosciences), *BD Accuri C6 Software User Guide – Manual*, 7820095-01 Rev-0, 2012, [Online]. Available: http://www.bdbiosciences.com/documents/BD_Accuri_C6_Software_User_Guide.pdf

[35] C. Lu, et al., "Electroporative Flow Cytometry for Single-Cell Analysis", in *Chemical Cytometry: Ultrasensitive Analysis of Single Cells*, Ed. C. Lu, Wiley-VCH Verlag GmbH & Co. KGaA, Weinheim, Germany, 2010.

[36] G. Sersa, et al., "Electrochemotherapy of Small Tumors; The Experience from the ESOPE (European Standard Operating Procedures for Electrochemotherapy) Group", in *Clinical Aspects of Electroporation*, Ed. S. T. Kee, J. Gehl, and E. W. Lee, pp. 93-102, Springer, New York, 2011.

[37] A. Silve and L. M. Mir, "Cell Electropermeabilization and Cellular Uptake of Small Molecules: The Electrochemotherapy Concept", in *Clinical Aspects of Electroporation*, Ed. S. T. Kee, J. Gehl, and E. W. Lee, pp. 69-82, Springer, New York, 2011.

[38] J. R. Albani, *Principles and Applications of Fluorescence Spectroscopy*, p.139, Blackwell Publishing, Oxford University Press, 2007.

[39] Z. Gryczynski, I. Gryczynski and J. R. Lakowicz, Chapter 2, Basics of Fluorescence and FRET, in *Molecular Imaging*, Ed. A. Periasami and R. N. Day, p. 30, Oxford University Press, 2005.

[40] Doyen T. Nguyen, Lawrence W. Diamond, and Raul C. Braylan, Flow Cytometry in *Hematopathology: A Visual Approach to Data Analysis and Interpretation*, 2nd ed., p. 50, Humana Press, Totowa, NJ, USA, 2008.

[41] Tzur, A., et al., "Optimizing optical flow cytometry for cell-volume-based sorting and analysis", *PLoS One*, Vol. 6, No. 1, pp. 1-9, 2011.

[42] K. Itahana, L. Campisi J and G. P. Dimri, "Methods to detect biomarkers of cellular senescence: the senescence-associated beta-galactosidase assay", *Methods Mol Biol*, Vol. 371, pp. 21-31, 2007.

[43] J. W. Tung, et al., "Modern Flow Cytometry: A Practical Approach", *Clin Lab Med*, Vol. 27, No. 3, pp. 453–v, 2007.

[44] C. Grosse and H. P. Schwan, "Cellular membrane potentials induced by alternating fields", *Biophys J*, Vol. 63, pp. 1632-1642, 1992.

[45] S. Elmore, "Apoptosis: A Review of Programmed Cell Death", *Toxicol Pathol*, Vol. 35, No. 4, pp. 495-516, 2007.

[46] J. C. Weaver, "Electroporation of biological membranes from multicellular to nano scales", *IEEE T Dielect El In*, Volume 10, No. 5, pp. 754-768, 2003.

[47] J. Teissié, et al., “Electropermeabilization of cell membranes”, *Adv Drug Deliver Rev*, Vol. 35, pp. 3-19, 1999.

[48] T. Y. Tsong, “Electroporation of cell membranes”, *Biophys J*, Vol. 60, No. 2, pp. 297-306, 1991.

[49] R. Benz, F. Beckers and U. Zimmermann, “Reversible electrical breakdown of lipid bilayer membranes: a charge-pulse relaxation study”, *J Membrane Biol*, Vol. 48, No. 2, pp. 181-204, 1979.

[50] R. A. Böckmann, et al., “Statistics, and Energetics of Lipid Membrane Electroporation Studied by Molecular Dynamics Simulations”, *Biophys J*, Vol. 95, No. 4, pp. 1837–1850, 2008.

[51] C. B. Arena, et al., “Theoretical Considerations of Tissue Electroporation With High-Frequency Bipolar Pulses”, *IEEE T Bio-Med Eng*, Vol. 58, No. 5, pp. 1474–1482, 2011.

[52] E. Tekle, R. D. Astumian and P. B. Chock, “Electroporation by using bipolar oscillating electric field: An improved method for DNA transfection of NIH 3T3 cells”, *P Natl Acad Sci USA*, Vol. 88, pp. 4230-4234, 1991.

[53] A. T. Esser, et al., “Mechanisms for the Intracellular Manipulation of Organelles by Conventional Electroporation”, *Biophys J*, Vol. 98, pp. 2506–2514, 2010.

[54] S. Talele, et al., “Modelling single cell electroporation with bipolar pulse parameters and dynamic pore radii”, *J Electrostat*, Vol. 68, No. 3, pp. 261-274, 2010.

[55] D. Miklavcic and T. Kotnik. "Electroporation for electrochemotherapy and gene therapy", in *Bioelectromagnetic Medicine*, Ed. P. J. Rosch and M. S. Markov, pp. 637–656, Taylor and Francis, 2004.

[56] M. M. Sadik, et al., “Scaling Relationship and Optimization of Double-Pulse Electroporation”, *Biophys J*, Vol. 106, No. 4, pp. 801–812, 2014.

[57] S. Talele and P. Gaynor, “Non-linear time domain model of electropermeabilization: Response of a single cell to an arbitrary applied electric field”, *J Electrostat*, Vol. 65, No. 12, pp. 775-784, 2007.

[58] S. Talele and P. Gaynor, “Non-linear time domain model of electropermeabilization: Effect of extracellular conductivity and applied electric field parameters”, *J Electrostat*, Vol. 66, No. 5-6, pp. 328-334, 2008.

[59] D. C. Chang, P. Gao and B. L. Maxwell, "High efficiency gene transfection by electroporation using a radio-frequency electric field", *BBA-Mol Cell Res*, Vol. 1092, No. 2, pp. 153-160, 1991.

[60] E. Tekle, R. D. Astumian and P. B. Chock, "Electroporation by using bipolar oscillating electric field: an improved method for DNA transfection of NIH 3T3 cells", *P Natl Acad Sci USA*, Vol. 88, No. 10, pp. 4230-4234, 1991.

[61] A. Agarwal, et al., "Effect of Cell Size and Shape on Single-Cell Electroporation", *Anal Chem*, Vol. 79, No. 10, pp. 3589-3596, 2007.

[62] T. Kotnik, D. Miklavcic and L. M. Mir, "Cell membrane electropermeabilization by symmetrical bipolar rectangular pulses: Part II. Reduced electrolytic contamination", *Bioelectroch*, Vol. 54, No. 1, pp. 91-95, 2001.

[63] C. B. Arena, et al., "Theoretical considerations of tissue electroporation with high-frequency bipolar pulses", *IEEE Trans Biomed Eng*, Vol. 58, No. 5, pp. 1474-1782, 2011.

[64] C. B. Arena, et al., "High-frequency irreversible electroporation (H-FIRE) for non-thermal ablation without muscle contraction", *Biomed Eng Online*, Vol. 10, No. 102, pp. 1-20, 2011.

[65] A. I. Baba and C. Câtoi C. "Chapter 3, Tumor Cell Morphology", in *Comparative Oncology*. Bucharest: The Publishing House of the Romanian Academy, Bucharest, 2007.

CHAPTER 5

RADIO FREQUENCY ABLATOR HARDWARE DESIGN AND ELECTRICAL TESTING

5.0 Introduction

In the operating theatre, radio frequency ablation (RFA) is another procedure a surgeon can use, together with excision using the scalpel, and electrocautery using an electrosurgical apparatus. RFA is the clinical process where undesirable tissue, such as a tumour in the liver, is ablated or destroyed by heat. A radio frequency ablator is an apparatus used to perform this function, and has become a commonly used surgical tool as it offers a minimally invasive method compared to radical surgery. RFA is commonly indicated for liver cancer patients who have been deemed to have unresectable cancer. These patients typically suffer from secondary liver cancer most commonly due to colon cancer metastases, and the patient is referred to palliative and not curative treatment [1]. RFA uses radio frequency alternating electrical currents, to create a high current density at a local site causing energy deposition by Joule heating, ultimately raising the temperature of that tissue above the denaturation point to destroy it [2]. The term "coagulation necrosis" is also used.

A feature of varying the ablating power electrical frequency is what differentiates this apparatus from standard commercial equipment. A study has shown improved or preferential performance at lower frequencies than compared with RFA frequencies at around 450 kHz [3]. The reason for this is that liver tumour tissue has higher conductivity at lower frequencies compared to healthy liver tissue. So an intention of the planned research was to extend the frequency range to lower frequencies. No studies at higher frequencies than the normal RFA upper frequency of about 500 kHz have been found, indicating a gap in knowledge. Higher frequency currents tend to couple better through cells due to the cell membrane capacitance appearing as a lower impedance [4], and may prove to be advantageous favouring more uniform power deposition at a specific applied voltage in non-homogeneous tissue. As such there is a justification for further investigation of RFA at higher frequencies.

This chapter presents the design of a radio frequency ablator and results showing its performance and capabilities. It starts off by stating the specifications, and then it presents the topology, the design approach and the design considerations. It finishes off by presenting the results with discussion.

5.1 Design Specifications

As the intention of this design was to replace an existing commercial radio frequency ablator, commercial equipment were reviewed to form the basis of the design specifications. A typical commercial radio frequency ablator from Angiodynamics (Model RITA 1500X generator) claims the following specifications [5]:

- 466 kHz
- 250 W into 50 Ω
- 135 V rms (sinusoidal) into 80 Ω
- 600 VA rated machine.

Having consulted several other commercial devices [6], the high performance design specifications for this apparatus are:

- Fully electrically isolated for safety of patient and surgeon (medical grade of 4 kV)
- Variable or multiple selectable frequencies, e.g. 125 kHz, 250 kHz, 500 kHz, 1 MHz, 2 MHz
- 200 V peak into 50 Ω
- Bipolar waveform output (stepped quasi-sine wave with control of step levels)
- Adjustable peak for lower power output
- Thermal endurance of up to 20 minutes continuous operation.

5.2 Topology

It is difficult or impractical to produce adjustable frequencies over a wide range using a resonant sinusoidal design as is the custom in commercial RFA machines which operate at a fixed (single) frequency. On the other hand it is practicable to achieve a wide range of output frequencies using a switching system of which the timing of switching control signals are fully controllable. This can be implemented using a digital controlling device that controls all switch gates, like a microcontroller or an FPGA. A PWM type control strategy of turning the devices on and off very rapidly at a varying duty cycle to obtain a sine wave as an average is not appropriate for this design due to the high switching frequency required, of at least 10 times the normal sine wave frequency,

which demands very high clock speeds (order of 500 MHz) for the controller and exceptionally fast power MOSFETs (order of 200 MHz capability such that the slew rate is sufficiently high to ensure predominantly rectangular pulses at up to 20 MHz). To avoid this situation and as useful experience had been gained in designing successful high voltage pulsing circuits using a twin-stage cascaded multilevel inverter with equal voltage isolated power supplies, it was decided to use this topology for the RFA device design. Each stage comprised an H-bridge that uses four fast switching devices such as MOSFETs. Each switching device required its own gate driver circuit with its own power supply. Full isolation between the pulsing board and the controller is provided using optocouplers.

Similar to the electroporation system, the general scheme of the RFA system can be depicted as shown in figure 5.1. Each pulser board uses an H-bridge with four main switches (MOSFETs) that are driven by a set of gate drivers, and isolated from the controller by optocouplers.

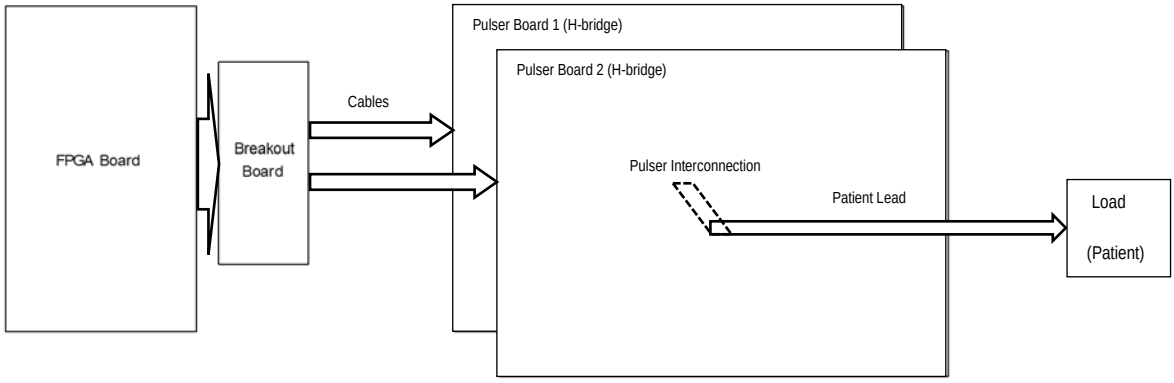

Figure 5.1. General scheme of the RFA system showing an FPGA pulse controller board with breakout board and cables for connecting to the 2 pulser boards, similar to the electroporator system.

5.3 Design Considerations

This section includes the power supply needs, switching device selection, heat sinking considerations, switching (gate) driver selection, gate driver external resistance design, bootstrap capacitance calculation, damping and general protection of the output circuit, interface between the digital controller and the gate driver chips, and general considerations for improved EMC operation.

5.3.1 Power Supply Needs

Power supply needs for the apparatus are quite diverse. They comprise altogether 5 supplies including two bus voltage supplies for each H-bridge, two gate driver supplies for the same H-bridges, and an FPGA board supply. These should ideally be supplied directly from mains at 230 VAC (50 Hz).

A potential of 200 V peak into 50 Ω translates to a peak current of 4 A. To make up for voltage drops required to provide adequate damping of the switched output, an additional 20 % of bus supply voltage for each H-bridge has been provided. This proportion has worked well in practice, providing adequate damping during hard switching into a load, thus mitigating significant ringing due to the resonant nature of the output circuit and load. This translates to a need for 120 VDC fully isolated (floating) power supplies. To meet the needs for adjustable output power, these supplies should have an adjustable or programmable output DC voltage. Figure 5.2 presents the general switching topology used.

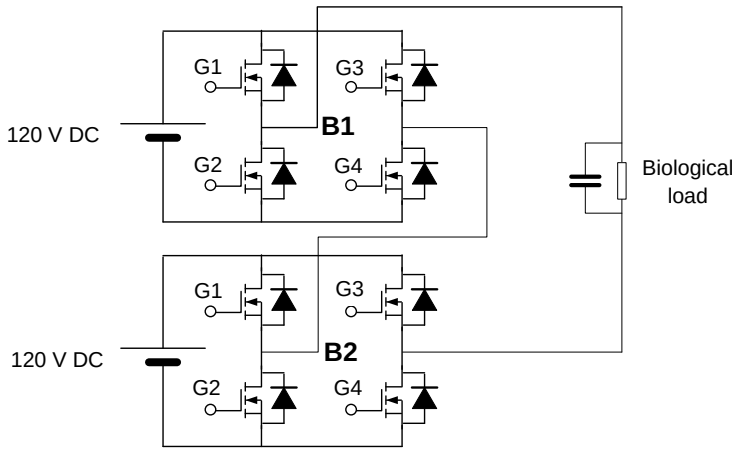

Figure 5.2. Basic topology of a 5-level cascaded MLI using two H-bridges and driving a typical biological load. B1 and B2 are the H-bridges, and G1 to G4 are the gates of the H-bridge switching devices (MOSFETs).

A pulsing scheme simplified for a dual bridge multilevel inverter of 10 out of 12 clock periods (or any multiples hereof) for the base voltage in the output waveform as contributed by B1 as shown in figure 5.2, and 6 out of 12 clock periods, for the upper part in the stepped quasi-sinusoidal waveform as contributed by the lower H-bridge B2 in figure 5.2, produces 4.7 % distortion and an effective power distribution of 57 % and 43 % for the respective power supplies. Figure 5.3 presents a diagram showing the switching scheme with switching comparative current *I* for a quasi-sine wave output of a dual stage multilevel inverter. This assumes perfectly square and symmetrical switching waveforms. This requires two power supplies at 120 VDC with DC power

needs of 320 W and 240 W respectively[1], totalling 560 W for the high voltage DC bus supplies only. Of special importance here is that these supplies have to be fully isolated (floating), and should ideally be of medical grade, thus providing in excess of 4 kV of isolation.

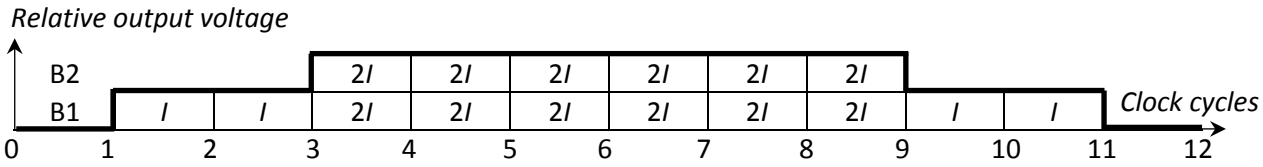

Figure 5.3. Timing-current schematic for the dual stage multilevel inverter to obtain a quasi-sine wave stepped output (thick outline), showing one half cycle. Twelve, or any multiple of 12, clock periods are used to obtain the contributions from bridge 1 (B1) and bridge 2 (B2). The values of each rectangle of either *I* or 2*I* are comparative current values switched by each bridge to assist in calculating power needs from the respective isolated power supplies. Refer to figure 5.2 for identifying B1 and B2.

For each level or stage a separate gate driver DC supply is needed. Medical grade fully isolated modular PCB mountable supplies are available, providing 15 VDC at 40 W from 230 VAC. These will provide up to 10 W per gate driver circuit as four are needed for each H-bridge.

Finally, another 5 VDC, 2.5 A supply is needed for the FPGA board. This does not need to be floating since it will be isolated from the switching board via 4 kV rated optocouplers.

So to summarise, power supply needs were (all units most likely switching type to reduce bulk):

1. 2 units of 230 VAC to 120 VDC adjustable (or programmable) regulated supplies, one with a 320 W output and the other 240 W output, both fully floating, with medical grade isolation.

2. 2 units of 230 VAC to 15 VDC fixed regulated supplies, 40 W output, both fully floating, with medical grade isolation.

3. 1 unit of 230 VAC to 5 VDC fixed regulated supply, 12.5 W output, medical grade isolation not required, since it will be provided by the optocouplers.

[1] It is possible to design a pulsing scheme that shares power equally between all switching devices in a cascaded multilevel inverter, but it needs a different switching scheme from one cycle to another to accomplish this. The simple single-cycle switching algorithm used in this design did not allow for this power equalisation. Further details are provided in Appendix B.

5.3.2 Switching Device Selection

The Power MOSFET devices to be used in the apparatus are required to switch efficiently up to frequencies in the order of 2 MHz. In fact, radio frequency (RF) type MOSFET devices work best as they offer very fast response times in the order of ns. This mitigates severe switching losses and allows for relatively high speed switching (order of 1 MHz) of moderately high voltages (order of 100 V to 200 V).

Such MOSFETs are produced by Microsemi Corporation and Ixys Corporation. Microsemi offer devices suitable at voltages of 500 V, 1000 V and 1200 V, but very few in the 200 V range, unfortunately only offering small devices with relatively high case thermal resistance or very bulky devices that are too slow or possess a gate capacitance that is too large (requiring very large peak currents from the gate drivers). In the range of interest, however, Ixys offered several devices classified as RF Power MOSFETs (switch-mode) and MOSFET drivers. These devices were available in their DE package range. These devices range from 100 V up to 1200 V breakdown voltage with current ratings from 8 to 55 A. For this application the most suitable device was determined to be the DE275-201N25A [7], rated at 200 V maximum drain-source breakdown voltage, 25 A maximum continuous drain current, 0.13 Ω maximum drain-source on-resistance, 5 ns typical rise time, 2500 pF typical gate capacitance and their special DE275 package offering very low maximum thermal resistance of 0.25 ^{0}C/W, and maximum ambient package power dissipation at 25 ^{0}C of 3 W for continuous operation.

5.3.3 Heat Sinking Considerations for the Power MOSFETs

Using an estimated[2] rise (and fall) time of 10 ns while switching at 2 MHz between 0 and 120 V and providing a current of 4 A, using

$$P_{sw} = V I f (t_{on} + t_{off})/2 \qquad (5.1)$$

yields P_{sw}, the estimated average switching power loss[3] of 9.6 W, given that V is the switched voltage peak, I the switched current peak, f the switching frequency, t_{on} the time for the MOSFET to turn on and t_{off} the time for the MOSFET to turn off. This rather high loss only occurs with the bridge contributing the upper part of the voltage waveform, as it has to switch 4 A while the other bridge only needs to switch 2 A at a time. Thus the first bridge MOSFET switching loss would be

[2] An estimate was needed at this stage to estimate heat. Rise and fall times can be controlled by altering a series gate resistor in the gate driver circuit. This has been estimated in the next section.

[3] This formula is based on a simple first order approximation of average power loss generated during a switching transition.

about half, at 4.8 W. However, subsequent modelling of this system using TINA simulation software [8] and the manufacturer SPICE model [7] for this MOSFET, produced total switching losses of approximately 12 W for the upper part and will consequently be used as a conservative measure.

Using first principles, conduction losses can be estimated using

$$P_{\text{cond}} = I_{\text{D}}^2 R_{\text{GS(on)}} D, \tag{5.2}$$

where P_{cond} is the average power loss of the MOSFET during the time it is turned on, I_{D} is the steady state current during a switching cycle, $R_{\text{GS(on)}}$ is the switching MOSFET channel resistance and D is the duty cycle.

As for the electroporator design, the pulsing regime identified by Rashid [9] was used – see chapter 3 and appendix B for more details. Using a duty cycle of 50 % for each switched device, each switching transistor shares energy loading. Also, using a timing system optimised for a close sinusoid approximation using a 20 ns resolution, each transistor conducts for 3 intervals in each cycle, being 2 intervals of $^1/_{12}$ cycle at unity current and 1 interval of ¼ cycle at double unity current, totalling $^2/_3$ equivalent (charge: $Q = I\,\Delta t$) units per cycle (see figure 5.2a and prior discussion on this topic).

This yields a conduction loss per transistor, P_{cond}, of

$$\begin{aligned} P_{\text{cond}} &= [2^2 \cdot 0.13 \cdot (1/6) + 4^2 \cdot 0.13 \cdot 0.25]\ \text{W} \\ &= (0.0867 + 0.520)\ \text{W} \\ &= 0.607\ \text{W}. \end{aligned} \tag{5.3}$$

This totals a conservative 12.6 W for each transistor, including both switching and conduction loss, and requires heat sinking since it is greater than 3 W.

Using the stated θ_{jc} (MOSFET thermal resistance from junction to case) of 0.25 ^{0}C/W will underestimate MOSFET rise in temperature as it does not include thermal paste (heat sink compound). Using Silfree 1020 paste of a uniform thickness of 0.1 mm and a heat sink contact area of 40 mm^2 produces a thermal resistance = 0.32 ^{0}C/W [10]. The practical total value of case-to-heatsink thermal resistance θ_{chs} is therefore 0.25 + 0.32 = 0.57 ^{0}C/W.

To calculate the heat sink specification, the following expression is used [11]

$$\theta_{\text{hs}} = \theta_{\text{total}} - \theta_{\text{case-to-heatsink}} \tag{5.4}$$

$$= (\Delta T/P) - \theta_{\text{case-to-heatsink}} \quad (5.5)$$

$$= [(T_j - T_a)/P] - \theta_{\text{case-to-heatsink}} \quad (5.6)$$

$$= \{ [(80 - 20)/12.6] - 0.57 \}\ ^0\text{C/W}$$

$$= 3.8\ ^0\text{C/W},$$

where θ_{hs} is the case-to-heatsink thermal resistance, θ_{total} is the total thermal resistance between the MOSFET junction and ambient air, $\theta_{\text{case-to-heatsink}}$ is the case-to-heatsink thermal resistance, ΔT is the differential temperature, P is the power that needs to be dissipated, T_j is the MOSFET junction temperature and T_a is the ambient temperature.

This was used to provide ample safety margin for a maximum junction temperature of 80 ^{0}C.

5.3.4 Gate Driver Selection

The gate driver was required to provide a high current peak to charge or discharge the gate capacitance rapidly – it serves purely to rapidly charge and discharge the gate capacitance. It may have needed heat sinking as well, so the choice also considered packaging. A TO-220 package or similar is suitable for this application. Not many manufacturers offer fast gate drivers with TO-220 packaging. One noteworthy exception is from Microchip Technology Incorporated – the TC4421A [12]. This device is a 9 A peak low-side gate drive IC. It offers typical values of R_{OH} = 1.6 Ω (gate drive IC output resistance when output is high) and R_{OL} = 1.2 Ω (gate drive IC output resistance when output is low). As the MOSFET has R_{G_MOSFET} = 0.3 Ω, this will have a minor effect on the value for external series resistance R_G needed for 10 ns switching times (on and off).

Using a specified Q_g = 125 nC for the MOSFET [7], the gate reactive driver power delivered to the MOSFET gate can be estimated as

$$P_{\text{gate-drive}} = (\textit{Energy stored in gate capacitance})/(\textit{Time interval or period}) \quad (5.7)$$

$$= E / \Delta T \quad (5.8)$$

$$= E f \quad (5.9)$$

$$= (\tfrac{1}{2}\, C\, V^2)\, f \quad (5.10)$$

$$= \tfrac{1}{2}\, (Q/V)\, V^2 f \quad (5.11)$$

$$= \tfrac{1}{2}\, Q\, V f \quad (5.12)$$

$$= \tfrac{1}{2}\, Q_g\, V_{drv}\, f_{sw} \quad (5.13)$$

$= 1.875$ VAr,

where $P_{\text{gate-drive}}$ is the total required average gate driver reactive power delivered to the MOSFET, $V_{\text{drv}} = 15$ V is the peak gate-drive voltage, $f_{\text{sw}} = 2$ MHz is the switching frequency, and Q_{g} is the required gate charge.

Quiescent power requirements for this driver IC are negligible at a supply current of 5 mA or less.

Gate driver power loss depends on switching frequency, total gate charge of the MOSFET, drive voltage and gate driver internal resistance. This was estimated using a similar equation as above and divided ratiometrically for both on and off resistances. Both events of turn on and turn off dissipate power. A useful application note [13] was used as follows (using worst case values for R_{OH} and R_{OL} of 2 Ω and 1.6 Ω, respectively) to calculate total average gate driver power loss:

$$P_{\text{tot}} = P_{\text{drv(off)}} + P_{\text{drv(on)}} \quad (5.14)$$

$$= [R_{\text{OH}}/(R_{\text{OH}} + R_{\text{G\_MOSFET}})]\, P_{\text{gate-drive}} + [R_{\text{OL}}/(R_{\text{OL}} + R_{\text{G\_MOSFET}})]\, P_{\text{gate-drive}} \quad (5.15)$$

$$= [2/(2 + 0.3)]\ 1.875 + [1.6/(1.6 + 0.3)]\ 1.875$$

$= 3.21$ W,

where P_{tot} is the total required average gate driver power loss, $P_{\text{drv(off)}}$ is the power loss when the MOSFET gate is driven low and $P_{\text{drv(on)}}$ is the power loss when the MOSFET gate is driven high.

This exceeds the 1.6 W that the device is capable of dissipating without a heatsink in still air [12]. Using an external resistor R_{G} diminishes this amount. At this design stage an optimal value for R_{G} had not yet been determined.

Heat sinking estimation for this gate drive IC is quite simple. Considering that $\theta_{\text{jc}} = 10\ ^0$C/W for the gate drive IC [12], with provision for a mounting thermal resistance θ_{mounting} (an electrical insulating mica washer and a double layer of thermal paste) of 1.4 ^{0}C/W (comprising 0.8 ^{0}C/W for the washer [14] and 2 x 0.3 ^{0}C/W for the two paste layers [15]), the gate drive IC total thermal resistance was calculated to be

$$\theta_{\text{total}} = \theta_{\text{jc}} + \theta_{\text{mounting}} + \theta_{\text{heatsink}} \quad (5.16)$$

$$= 10 + 1.4 + \theta_{\text{heatsink}}$$

$$= \Delta T / P \quad (5.17)$$

$$= (80 - 20) / 3.21$$

$= 18.7\ ^0C/W,$

where θ_{total} is the total thermal resistance between the device junction and ambient air, θ_{jc} is the gate drive IC junction to case thermal resistance, $\theta_{mounting}$ is the mounting thermal resistance including thermal paste and any other thermal resistance such as a washer, and $\theta_{heatsink}$ is the heatsink thermal resistance from its mounting surface to ambient air.

Thus the heat sink rating $\theta_{heatsink}$ was calculated to be

$$\theta_{heatsink} = 18.7 - 11.4$$

$$= 7.3\ ^0C/W.$$

This provides a conservative safety margin for a maximum junction temperature of 80 ^{0}C.

Subsequently, because it is desirable to avoid the use of a heatsink (since it simplifies the design, makes assembly more economical, and saves space making it easy to probe voltages during prototyping), another more suitable gate drive device was identified, notably the IXD-630 [16], from Ixys. This device claimed a peak current capability of 30 A and very small values for series resistance at 0.6 Ω (R_{OH}) and 0.45 Ω (R_{OL}) at maximum operating temperature and typical values of 0.17 Ω and 0.16 Ω at 25 ^{0}C, respectively. Using equation 5.14 and equation 5.15,

$$P_{tot} = P_{drv(off)} + P_{drv(on)}$$

$$= [R_{OH}/(R_{OH} + R_{G\_MOSFET})]\ P_{gate\text{-}drive} + [R_{OL}/(R_{OL} + R_{G\_MOSFET})]\ P_{gate\text{-}drive}$$

$$= [0.6/(0.6+0.3)]\ 1.875 + [0.45/(0.45+0.3)]\ 1.875$$

$$= 2.38\ W.$$

With a claimed θ_{jc} of only 3 ^{0}C/W [16] (instead of the value of 10 ^{0}C/W before), heat sink calculations yield

$$\theta_{total} = \theta_{jc} + \theta_{mounting} + \theta_{heatsink} \quad (5.18)$$

$$= 3 + 1.4 + \theta_{heatsink}$$

$$= \Delta T/P \quad (5.19)$$

$$= [(80 - 20) / 2.38]\ ^0C/W$$

$$= 25.26\ ^0C/W.$$

Thus heat sink rating should be

θ_{heatsink} = [25.26 – 4.4] ^{0}C/W

= 20.9 ^{0}C/W.

This represents a heat sink bulk of about a third compared to using the previous gate drive IC.

Adding external resistance of R_G further mitigates this heat. Using an external R_G of 2 Ω will reduce switching gate drive power further to

$$P_{\text{tot}} = P_{\text{drv(off)}} + P_{\text{drv(on)}} \quad (5.20)$$

$$= [R_{OH}/(R_{OH} + R_{G\_MOSFET} + R_{G\_ext})] P_{\text{gate-drive}} + [R_{OL}/(R_{OL} + R_{G\_MOSFET} + R_{G\_ext})] P_{\text{gate-drive}} \quad (5.21)$$

= [0.6/(0.6 + 0.3 + 2)] 1.875 + [0.45/(0.45 + 0.3 +2)] 1.875 W

= 0.695 W.

Since gate drive IC junction to ambient thermal resistance θ_{ja} is specified as 36 ^{0}C/W [16], this means that junction temperature rise ΔT will only be 25 ^{0}C which is acceptable without the use of a heat sink. Doing a similar calculation with the previous mentioned devices will not ensure sufficient slew rate at the MOSFET thus the gains there would be minimal, and would most likely still require heat sinking.

5.3.5 Selection of Gate Driver External Resistor

Designing the correct or ideal value for R_G poses a challenge. It may be omitted outright for maximum switching speed as for the electroporator detailed in chapter 3, but its use will control MOSFET slew rate which in itself is useful since it will require less damping and snubbing. Another advantage for using an added gate resistance is that it acts to reduce heat in the gate driver device as it absorbs power ratiometrically. As noted before in chapter 3, section 3.4.4, there are important considerations of reliability and safety that govern choice of externally added gate resistance, thus requiring the value for R_G to be optimised. Typically a MOSFET tends to turn on quicker than turn off. For matching of turn on and turn off, it is common practice to use a smaller value for R_G during turn off, thus using two different values for R_G, or to simply shunt R_G via a fast diode during the turn off phase. This objective may also be achieved using gate drivers that offer smaller internal resistance during turn-off than during turn-on.

Resistance R_G limits maximum gate current. However, specifying a driver with larger current capability is ultimately needed, for peak current will generally mean that its internal resistances are lower, thus rendering it more capable of handling power throughput. Additionally, being a medical device, reliability ranks much higher as a design goal than cost or more bulk.

The interval between the gate voltage rising from $V_{GS(threshold)}$ to $V_{GS(plateau)}$ can be calculated as

$$\Delta t = t_{plateau} - t_{threshold}, \quad (5.22)$$

where $V_{GS(threshold)}$ is the MOSFET gate-source threshold voltage at the instant the drain current starts flowing, $V_{GS(plateau)}$ is the MOSFET gate-source Miller plateau voltage at the instant the gate-source voltage produces a plateau and also when the drain current peaks [13].

The datasheet for the MOSFET [7] suggests values for these voltages of 6 V and 3 V, respectively. Using the classical capacitor charge relationship of

$$v_c(t) = E\, e^{-t/RC}, \quad (5.23)$$

and rearranging for t,

$$t = - RC \ln[\, v_c(t)/E \,], \quad (5.24)$$

yields $t_{threshold} = - RC \ln(0.4) = 6.64$ ns, and $t_{plateau} = - RC \ln(0.2) = 11.67$ ns, thus an interval of 5.03 ns. This equates to a slope of 3 V per 5.03 ns or 6 x 10^8 V/s. Note that R is taken as $R_{drive} + R_{G\_ext} + r_g = 0.6 + 2 + 0.3 = 2.9\ \Omega$, and C is taken as $C_{iss} = 2.5$ nF, with the latter two having been extracted from the datasheet for the DE275-201N25A MOSFET [7]. This is at least an order of magnitude larger than the previously calculated value of 2 x 10^7 V/s.

If the load was a pure resistor, then the above would have held true and a smaller value of R_{G_ext} could be used to guarantee an output slew rate of 8 x 10^9 V/s. However, the great difference is probably due to the capacitive nature of the load resulting in a very non-linear relationship between current and voltage at the very beginning of the transient.

Estimating the power dissipation for the external gate resistor $R_{G\_ext} = 2\ \Omega$ can be performed as

$$P_{tot} = P_{drv(off)} + P_{drv(on)} \quad (5.25)$$

$$= [R_{G\_ext} / (\, R_{OH} + R_{G\_MOSFET} + R_{G\_ext})]\, P_{gate\text{-}drive} + [R_{G\_ext} / (\, R_{OL} + R_{G\_MOSFET} + R_{G\_ext})]\, P_{gate\text{-}drive} \quad (5.26)$$

$$= [2/(0.6 + 0.3 + 2)]\ 1.875 + [2/(0.45 + 0.3 + 2)]\ 1.875 \ \text{W}$$

= 2.66 W.

This is quite substantial and requires a resistor power rating of at least 5 W, using a double power rating philosophy to increase reliability for power resistors [17] taking into consideration that the resistors will be grouped (in parallel) and the PCB will be mounted in an enclosure.

5.3.6 Calculation of Bootstrap Capacitance

The bootstrap charge pumping circuit is possibly the most elegant solution in providing cheap and reliable power to a high-side gate driver circuit of a bridge. It comprises a simple diode and capacitor series combination attached between the low-side gate drive power supply and the source of the high-side MOSFET, providing an output voltage slightly below the source voltage (one diode drop less) and is capable of floating up to a high voltage as is needed for the high-side supply. It operates by charging the capacitor up to the supply value (minus a single diode drop voltage) during the interval when the high-side is off and the low-side is on. The diode clamps the voltage across the capacitor when the low-side MOSFET is off. This technique is handicapped by its reliance on regular switching of the low-side MOSFET of that half-bridge while the high-side is turned off, so that the bootstrap capacitor can be charged. If low-side on time is insufficient for topping up charge then high-side gate drive voltage may suffer from voltage droops. Moreover, overestimation of capacitor value will cause the system to suffer a similar failing.

At start up, the capacitor is charged by maintaining continuity of the charge circuit by keeping the low-side MOSFETs turned on for sufficient time while the high-side MOSFETs are turned off. Once the switching sequence starts, sufficient charge must already be in the capacitor and sufficient charge must be shuttled to the capacitor between cycles to guarantee sufficient gate drive voltage at the high-side.

The bootstrap diode should be fast, have small reverse recovery charge, have sufficient reverse blocking voltage such as the bridge supply voltage, and have a very high peak current. A suitable device is the ultrafast silicon surface mount rectifier BYG22D [18] with 200 V maximum repetitive peak reverse voltage and 2 A maximum average forward current, 25 ns maximum reverse recovery time, and 35 A peak forward surge current ratings.

To calculate capacitance, we can start with the fundamental equation of $Q = C\,\Delta V$, or $C = Q / \Delta V$. Using ΔV of 1.0 V as droop allowed, and a charge of total gate charge (125 nC) plus an allowance (≈ 10 %) for leakage or supply current to the gate driver chip, produces

$$C = (125\ \text{nC} * 110\ \%) / 1\ \text{V} \tag{5.27}$$

= 138 nF.

A suggested value of 20 % higher to account for general tolerance of capacitors is 165 nF. This value is still relatively small, as this capacitor must also provide power to the output stage of the optocoupler, which typically draws 18 mA continuously and also approximately 1 mA into the safety pull-up or down resistor during a full cycle – this is based on the HCPL-2400 optocoupler – see section 5.3.8. This requires an additional 20 mA for a full cycle of lowest frequency of use, say 100 kHz. Thus a period of 10 µs, or additional charge of 200 nC is required. This will require additional capacitance of 200 nF, totalling 338 nF. Selecting 1 µF will guarantee a voltage drop of around 338 nC / 1 µF = 0.338 V.

To verify sufficient charging during a short interval of say 250 ns (a 50 % duty cycle at 2 MHz) means taking 5 time constants, RC = 50 ns, thus R = 50 ns / 1 µF = 0.05 Ω. This may be unachievable since parasitic values are rarely this small. The suggested capacitance value of 1 µF can be evaluated experimentally, and no series bootstrap resistance is to be added (often used for EMC mitigation).

5.3.7 Damping and General Protection in the Output Circuit

Since circuit parasitics always exist no matter how well the layout has been designed, resistor-inductor-capacitor (RLC)-type characteristics will exist causing unwanted ringing and overshoot. Damping was used successfully in the electroporation pulser circuit as a simple solution. However, for that circuit with very low duty cycle, substantial losses were tolerated – up to 25 % of the load resistance value was added in the form of damping resistors. Such losses cannot be tolerated in this particular circuit due to the high duty cycle used in practice. For example, using an equivalent 20 Ω total damping resistance for both H-bridges into a 50 Ω load, or 4 times 5 Ω in series will generate average power of approximately

$$P_{\text{damp}} = \{ R_{\text{damp}} / [\, 2\, (R_{\text{load}} + R_{\text{damp}}) \,] \} \, P_{\text{load}} \tag{5.28}$$

$$= \{ R_{\text{damp}} / [\, 2\, (R_{\text{load}} + R_{\text{damp}}) \,] \} \, [\, (V_{\text{Lpeak}}/\sqrt{2})^2 / R_{\text{L}} \,] \tag{5.29}$$

$$= \{ 20 / [\, 2\, (50 + 20) \,] \} \, [\, (240^2/2)/ 50 \,] \text{ W}$$

$$= 0.143 \cdot 576 \text{ W}$$

$$= 82 \text{ W}.$$

This means power dissipation of 10 W per resistor for eight resistors (both sets of alternate switches for both bridges). Ideally they should be rated for pulse applications, thus specifying

pulse withstanding chip resistors would be the best choice, such as the Welwyn-TT Electronics PWC [19] series. This takes into consideration that there are two diagonal pairs that share the load equally.

Using instead a value of 4 Ω per combination resistor (instead of 5 Ω) allows for better matching of available resistor values and ratings. Each combination resistor now comprises 8 physical resistors of 1.5 W each. This means a 12 W rating for each combination should be adequate. Recalculating yields

$$P_{\text{damp}} = \{ R_{\text{damp}} / [\, 2\, (R_{\text{load}} + R_{\text{damp}}) \,] \} P_{\text{load}} \tag{5.30}$$

$$= \{ R_{\text{damp}} / [\, 2\, (R_{\text{load}} + R_{\text{damp}}) \,] \} [\, (V_{\text{Lpeak}}/\sqrt{2})^2 / R_{\text{L}} \,] \tag{5.31}$$

$$= \{ 16.5 / [\, 2\, (50 + 16.5) \,] \} [\, (240^2/2)/ 50 \,] \text{ W}$$

$$= 0.124 \cdot 576 \text{ W}$$

$$= 71 \text{ W}.$$

This means power dissipation of 8.9 W per resistor for eight resistors. Thus the 12 W rating of each combination of 8 resistors in parallel may just be adequate.

Generally, power is proportional to resistance, assuming current is held constant (achieved by small relative changes of the total resistance), so halving the damping resistors resistance would halve the power dissipated by those resistors. On the other hand, halving the resistance would halve the effect of damping, so it is important to consider the ringing/overshoot occurring to verify whether there is adequate damping.

Modelling using TINA has shown ringing and overshoot due to parasitic components added (see fig. 5.4), based on approximate values (the origin of these provided below). The topology used was a single MOSFET as part of the H-bridge, and since the focus was on the turning on event rather than turning off, a single device was considered sufficient. Values for stray inductance were added amounting to 60 nH per H-bridge current path. This was based on the general approximation for track inductance of about 1 nH per mm of track, erring on the high-side [20]. Simulating a range of values (30 nH to 120 nH) for this inductance has shown (see figure 5.4) that more inductance tends to limit di/dt and thus also limits dv/dt (slew rate) for a mostly resistive load and produces a much lower instantaneous power peak, but causes a much higher ringing amplitude at the MOSFET output terminals. However, this ringing is not necessarily a disadvantage since it does not exceed overshoot limits. This knowledge is useful for purposes of the layout, as the system seems to be quite tolerant of a range of values.

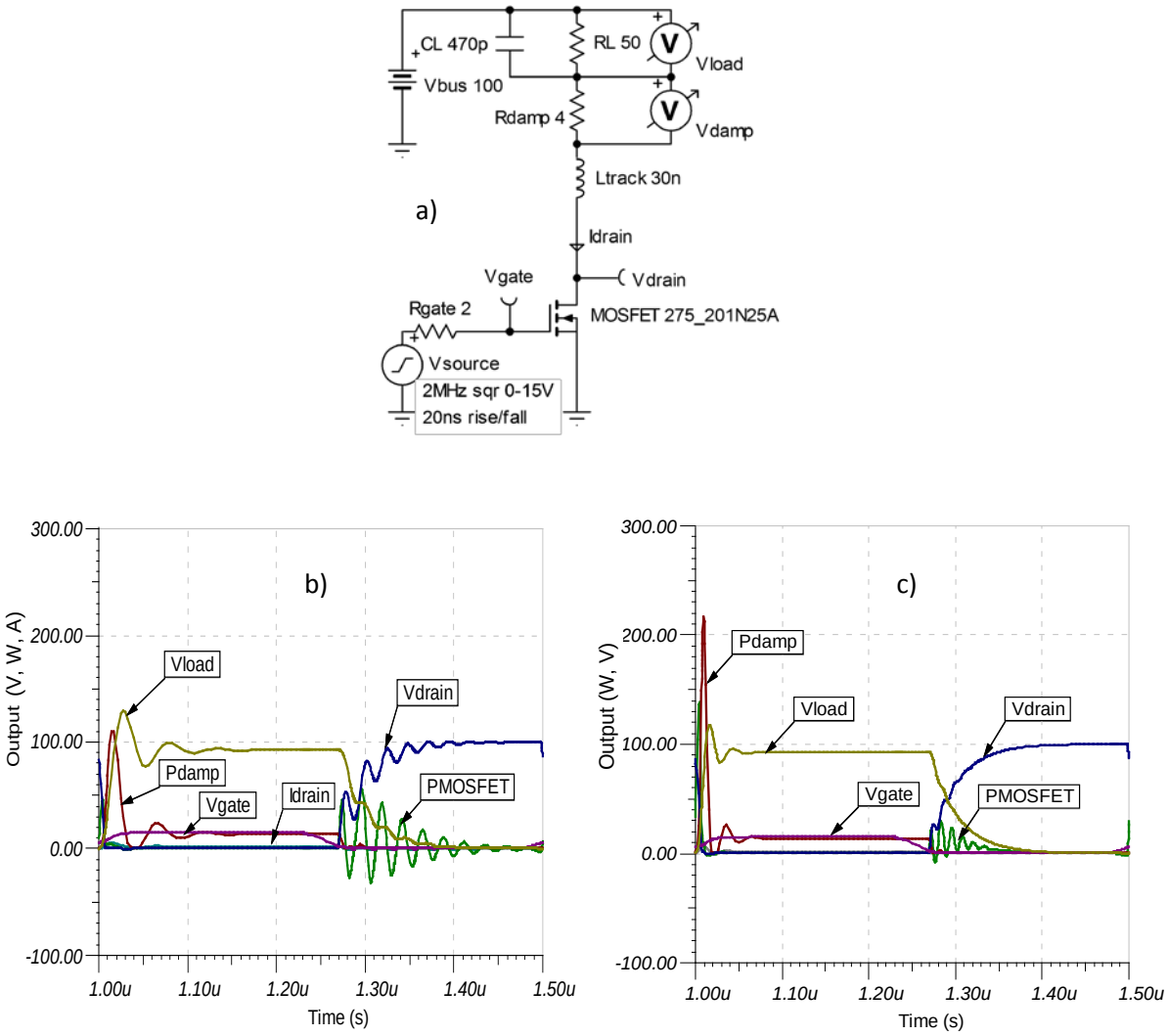

Figure 5.4. Modelling of a single switching cycle of only one MOSFET showing a) schematic and outputs for b) 120 nH and c) 30 nH parasitic track inductance. Variables measured are indicated on the plots. The variables are: the voltage across the load Vload, the voltage across the damping resistor Vdamp, the drain current Idrain, the drain-source output voltage Vdrain, and the gate-source voltage Vgate. The parameters are load resistance RL, load capacitance CL, damping resistance Rdamp, track parasitic inductance Ltrack, external gate resistance Rgate and supply voltage Vbus.

The inherent body diodes in MOSFETs are vulnerable to high input dv/dt and high reverse currents. To solve this problem, the MOSFETs are complemented with external diodes that essentially shunt current away from the body diodes. External diodes must be fast and possess low forward voltage drops. Each MOSFET is only turned on for half a cycle and takes a peak driving current of 4 A, which is 2 A on average. Since this external diode does not carry all this current, and generally is rated at the working current of the MOSFET, it should be sufficient if it is rated at

2 A. The smallest possible current rating is desirable since other parameters like junction capacitance, reverse recovery time and avalanche energy are lower. A small profile is also desirable, so ultra-fast surface-mount silicon rectifier diodes were selected – the BYG22D [18], with 200 V maximum repetitive peak reverse voltage and 2 A maximum average forward current, 25 ns maximum reverse recovery time, and 35 A peak forward surge current ratings. These diodes can be soldered directly across the pins of the MOSFET if needed. This is the technique used for the aforementioned electroporation pulser that had been designed and successfully operated.

The circuit board was to be manufactured with provision for resistor-capacitor-diode (RCD) snubbers as shown in figure 5.5, but was trialled without them while starting at light loads. The load and supply voltage were then ramped up while carefully monitoring ringing across MOSFET drain to source terminals. Eventually the snubber circuits were included. The snubber circuits used the same diode as was specified for the anti-parallel diodes. Design of the RCD snubber circuit also followed the example used in the electroporator design, thus R was set to a tenth of the load resistance (≈ 4.7 Ω), and C to double the output capacitance of the MOSFET, at 1 nF. D1 is the external body diode protection diode, while D2, R and C are the components of the RCD snubber – see figure 5.5.

Traditional snubber design [21] suggests values for C and R (and power in R) as follows:

$$\begin{aligned} \text{Let } C_S &= 5 \text{ x } C_{oss} \\ &= 5 \text{ x } 265 \text{ pF} \\ &= 1.33 \text{ nF}, \end{aligned} \tag{5.32}$$

where C_S is the snubber capacitance and C_{oss} is the output equivalent capacitance of the MOSFET. Let

$$\begin{aligned} R_S &= 0.5 \text{ sqrt}(L_{para}/C_{para}) \\ &= 0.5 \text{ sqrt}(20 \text{ nH}/265 \text{ pF}) \\ &= 4.3 \text{ Ω}, \end{aligned} \tag{5.33}$$

where R_S is the snubber resistance, L_{para} is the equivalent circuit parasitic inductance parallel to the capacitance, and C_{para} is the equivalent circuit parasitic capacitance.

These original but arbitrarily estimated values were close to the traditionally estimated values, so were ultimately used.

To estimate the power dissipation of the snubber resistor, the amount of charge shuttled through it in a certain time duration determines the quantity, thus let

$$P_{\mathrm{Rs}} = C_{\mathrm{S}}\, V_{\mathrm{overshoot}}{}^2\, f \qquad (5.34)$$

$$= 1 \text{ nF x } (20 \text{ V})^2 \text{ x } 2 \text{ MHz}$$

$$= 0.8 \text{ W},$$

where P_{Rs} is the power dissipated in the snubber resistor, $V_{\mathrm{overshoot}}$ is the overshoot voltage taken at 20 % of 100 V and f is the maximum switching frequency. This value is tolerable and 2 W rated resistors were used. The MOSFET output is shown in figure 5.5.

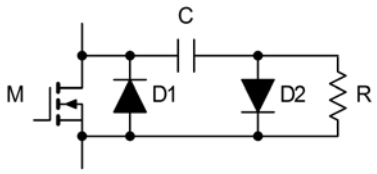

Figure 5.5. MOSFET showing an external anti-parallel diode, D1, and an RCD snubber, C-D2-R.

Being a lossy snubber, during turn off, the resistor dissipates power, so also needs a high power rating. A reason for avoiding the use of such a snubber would be its tendency to limit the output slew rate of the MOSFET (the very purpose of a snubber), which may in turn cause more heat to be produced in the snubber and thus in total, which is counterproductive. Nevertheless, the snubbers were used to protect the MOSFETs.

5.3.8 Interface Between the Digital Controller and the Gate Drive ICs

An interface is needed between the digital controller and the gate drive ICs. It must meet the same requirements as for the electroporator – see chapter 3, section 3.4.7.

The gate controller pulses are derived from an FPGA board using the Spartan 3E Starter Kit Board [22] manufactured by Digilent, as used successfully for the electroporator system. A breakout board has also been designed, and provides RJ45 sockets for standard CAT 5E patch cords as was designed and proven for the electroporator system – see again chapter 3, section 3.4.7.

The Avago HCPL-2400 [23] single optocoupler IC was selected, as for the electroporator system.

Similarly, current limiting resistors and a blocking diode have been selected, as previously for the electroporator system, and are again shown in the schematic diagram in figure 5.6.

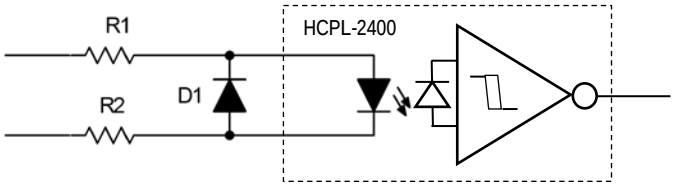

Figure 5.6. Optocoupler with preceding balanced series resistors and clamping diode.

As before, as a safety precaution, a pull-down resistor (for the high sides of the H-bridge to assure that the high side MOSFETs remain turned off if the gate drive IC fails as open) or pull-up resistor (for the low sides of the H-bridge to assure that the low side MOSFETs remain turned on, thus grounding the load, if the gate drive IC fails as open) has been used between the optocoupler output and the gate driver input. Values for these resistors should be carefully chosen to avoid overheating of the preceding devices. A value of 2.2 kΩ had been selected, drawing an average 1 mA for a continuous 50 % duty cycle from the output of the optocoupler, and is negligible.

Figure 5.7 gives a general overview of the main devices that form part of a single channel on the pulsing board.

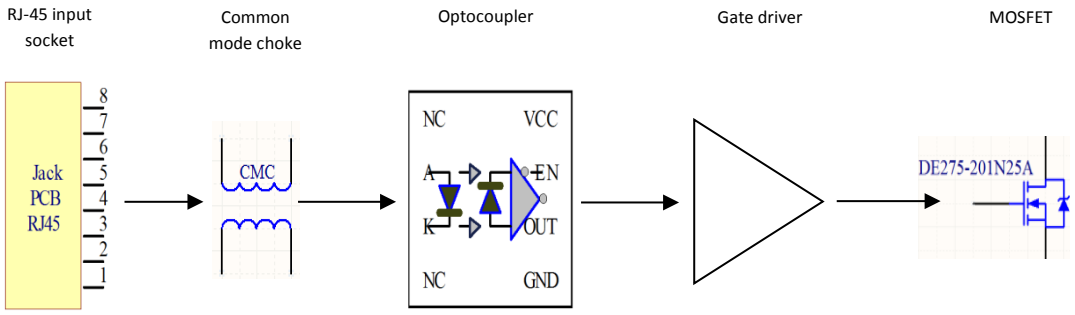

Figure 5.7. Basic block diagram showing the main devices in the path of a single channel, from jack to MOSFET. All components are not shown. For each pulser board there are four of these channels that make up the full H-bridge. Again, this is similar to the scheme of the electroporator system.

5.3.9 General Considerations for Improved EMC Operation

As for the electroporation system detailed in chapter 3, EMC is a major consideration determining the success or not of the system, although voltage pulses here are one order of magnitude lower into a similar load. Where the electroporation system used potentials of around 6 to 10 times that of this design requiring greater clearances and consequently greater parasitic components and problems with ringing, this system is now laboured with a severe heat problem due to the greater

average duty cycle. Similar design practices have been followed. Improved strategies and combinations including important design aspects are as listed in chapter 3, section 3.4.8.

5.4 Thermal and Electrical Test Results and Discussion

Figure 5.8 shows a photograph of the RFA system, using only a single H-bridge. It was considered adequate using only a single bridge as it is capable of producing more than 100 W into 50 Ω, and should be adequate to apply to low to medium power applications. For more power a second bridge could be cascaded in a multilevel inverter arrangement as for the electroporator system.

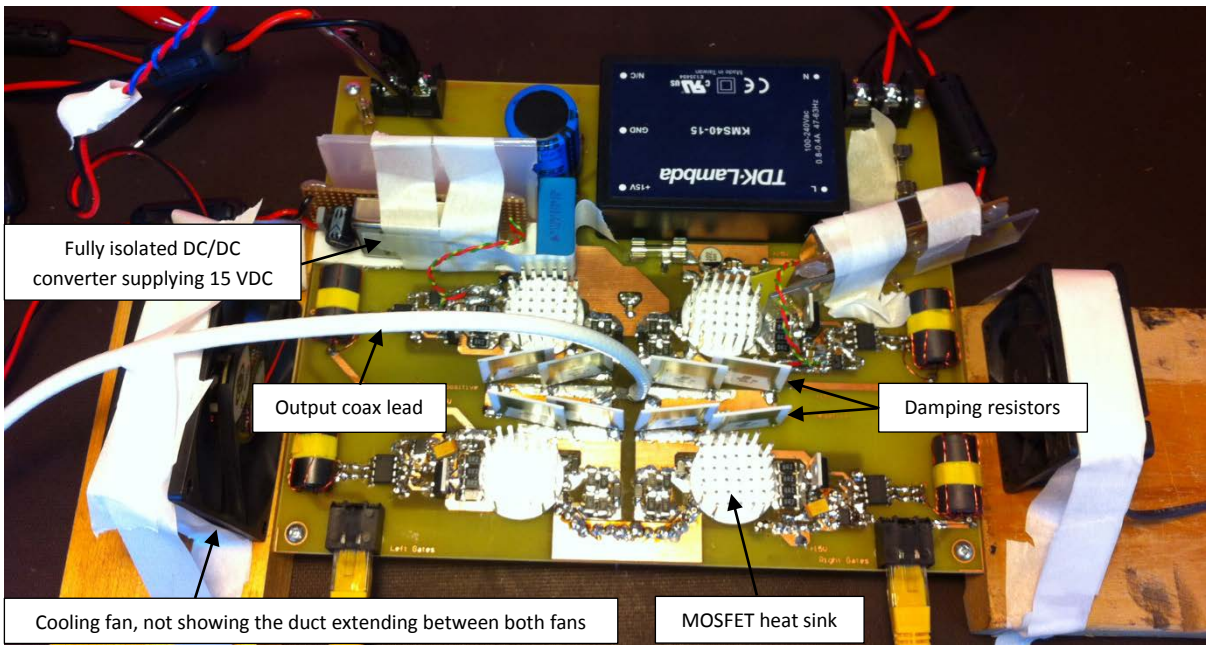

Figure 5.8. Single-stage RFA system using only one H-bridge. The 4 circular aluminium heat sinks sit atop the switching MOSFETs. Damping resistors are located around the connection of the white coaxial lead appearing as vertical white and black ceramic rectangular plates. On the left and right sides are the push pull fans that provide convective cooling. A partial duct (not shown) was placed longitudinally over the fans, assisting in removal of heat. A complete duct would further improve the design. For more details, refer to figure 3.7 in chapter 3, which uses a very similar layout.

Initially the output voltage waveforms appeared to be as expected. However, when probing for a long period of time (hundreds of cycles) it was discovered that the output intermittently became asymmetrical rather than continuously symmetrical (producing only positive pulses and not negative pulses) – it would run for many cycles without any problems, then it would turn off one half of the output for a certain number of cycles after which it would recover, and repeat this

process. It was postulated that the cause for this was the large damping resistance in the charging path of the bootstrap capacitors, and was confirmed by reduction of two damping resistors of one half bridge causing that side to operate without turning off. Of course the required damping was compromised as a result. This was a rather difficult problem as the damping feature was essential to avoid excessive ringing and overshoot. This problem and its solution are shown in figure 5.9. A Tektronix TDS2033B was used to measure these waveforms, with a stated vertical DC accuracy of ±3 % [24].

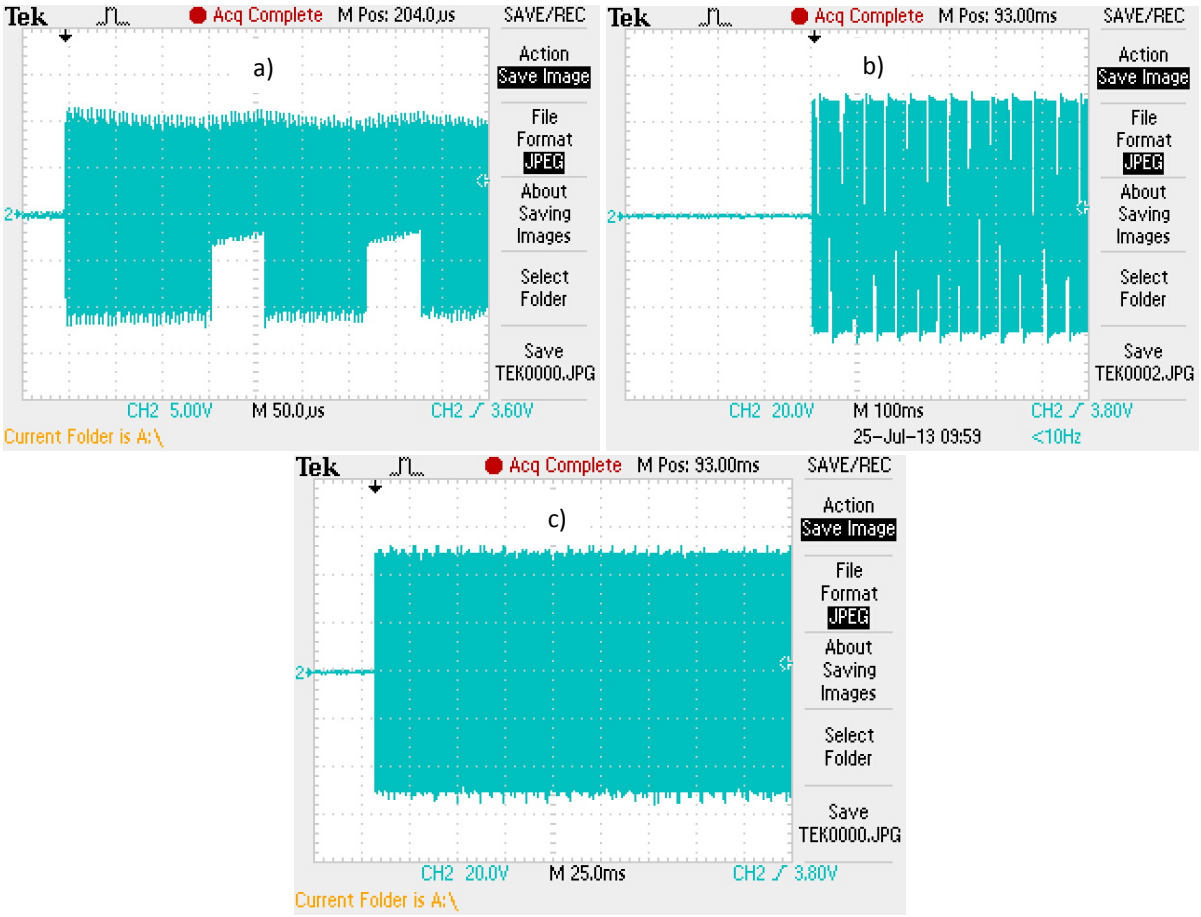

Figure 5.9. Output waveforms over a large number of switching cycles revealing the problem mentioned previously. a) Waveform across 0.5 ms total interval, b) waveform across 1 s total interval, and c) the solved problem shown for an interval of 250 ms.

Several approaches were considered to solve this problem including increasing the external gate resistors, and reducing the damping resistance and/or reducing the bootstrap capacitance. The first approach seemed to have the best potential but this led to poor switching of the MOSFETs due to a greatly emphasised "Miller-plateau" switching action as seen when probing the gate voltage. This poor switching caused the MOSFET to have a heavily reduced output slew rate and thus caused excessive heating of the MOSFET. This effect was extremely sensitive to small

increases of external gate drive resistance, and was observed to start having an effect with increasing this resistance by just 1 Ω. The second approach of reducing bootstrap capacitance was eliminated because insufficient capacitance could not provide sufficient charge to power the gate drivers sustainably at high output duty cycles.

Having abandoned the first two approaches, the only remaining option was to provide the high-sides with independent floating power supplies. This increased the power supply requirement quite substantially from 2 to 4 units (per bridge). At first, consideration was given to using the normal gate driver supply as a source together with a hybrid DC-DC isolated power converter for each high-side. However, these units had capacitance of 1 nF between input and output. This meant that large current "spikes" would be transmitted across to the high-sides when charging and discharging this interconnecting capacitance, up to several amps due to the high dv/dt, so this idea was abandoned. Instead, fully isolated sources were built and incorporated into the design. This solved the problem entirely, although at the cost of additional expense and bulk. Sealed lead acid batteries of 7 Ah were used, coupled via DC-DC converters to each high-side driver to guarantee isolated 15 VDC supplies for each high-side. These changes are shown in figure 5.10.

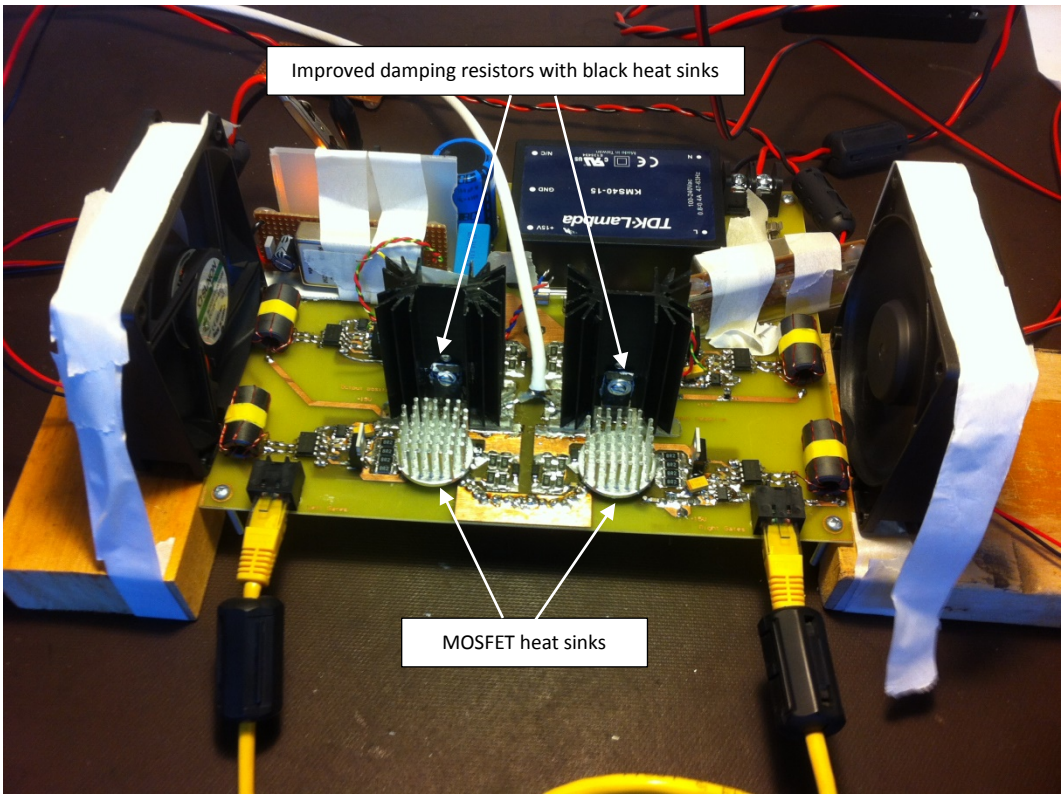

Figure 5.10. Photograph of improved RFA apparatus showing improved damping resistors and their heatsinks and additional DC-DC converters (also shown before in figure 5.8) for the high-sides (in white).

The next challenge was to verify the RFA system output capability while monitoring temperatures to avoid potential damage. The system was capable of driving the standard load at the maximum supply voltage, duty cycle and frequency for a short duration, but the damping resistors rapidly heated up. A Fluke Ti20 thermal imaging camera (with stated accuracy of ±2 ^{0}C [25]) was used to identify hotspots and their temperatures on the PCB. Several potential hotspots were monitored, including the MOSFETs (the heatsinks on top of them), the MOSFET driver ICs, the external MOSFET gate resistors, the snubber resistors and the damping resistors. An image of a thermal camera screen is shown in figure 5.11. The damping resistors suffered from the greatest increase in temperature, as they were at higher temperatures than all the other mentioned components, rendering the others negligible in comparison. An instance was observed where one of the snubber circuit resistors had a raised temperature, but this was corrected after it had been identified as having an incorrect value resistance. Using different supply voltages, frequencies and duty cycles, the RFA system was operated and examined to determine its limits.

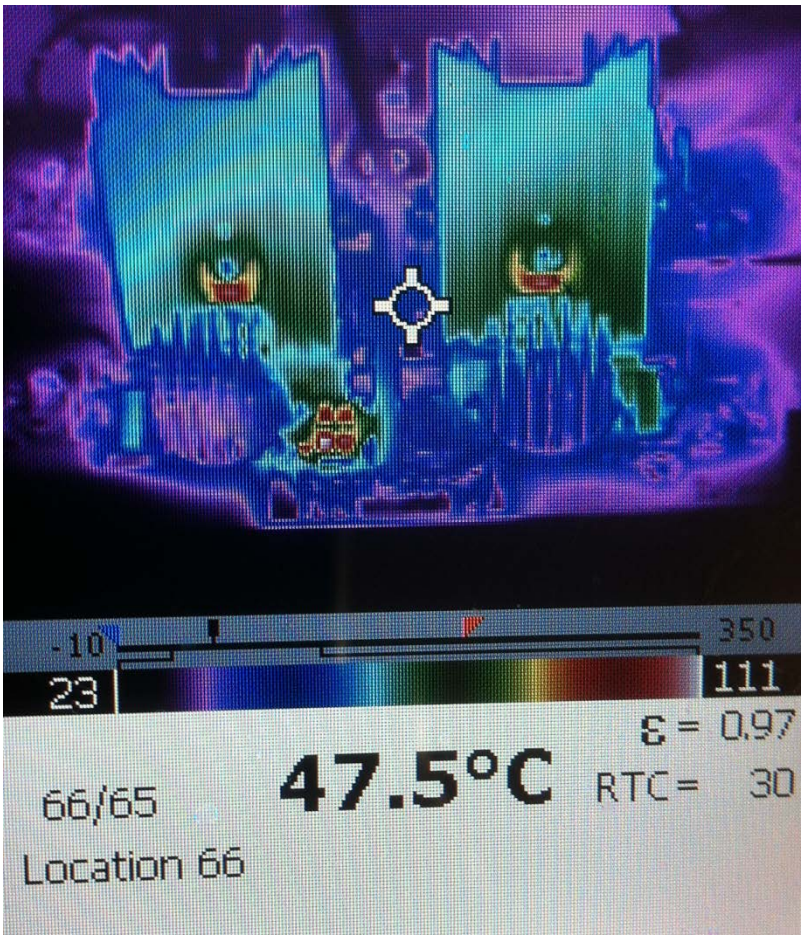

Figure 5.11. Image of the thermal imaging camera focused on the damping resistor heatsinks above (behind) the two low-side MOSFET heatsinks. The focal site is at 47.5 ^{0}C while the maximum temperature in this image (white) is at 111 ^{0}C. The ambient temperature was 23 ^{0}C. There are 3 hotspots, including the two similar sites at the damping resistors connected to the heatsinks, and also a third where one of the snubber circuit resistors is located. This high snubber resistor temperature was corrected afterwards by replacing these resistors with correct (larger valued) resistors, for which there is no image.

Several thermal studies were conducted. They started off with the original designed damping resistors, which were upgraded twice, and which also saw introduction of forced convective cooling. Initially, large surface mount thick film damping resistors (8 in parallel rated at a total of 12 W) were used in conjunction with a single unducted fan and proved insufficient as resistor surface temperature rose rapidly without any detectable stabilisation at a temperature exceeding 160 ^{0}C. This was followed by use of large vertical ceramic substrate thick film resistors rated at 20 W in total using again the single unducted fan. Higher output power settings were used but the maximum temperature continued rising beyond the 180 ^{0}C maximum manufacturer temperature rating. Another convective fan was added and the system was ducted with the fans arranged for

maximal one-direction through flow. Although this improved heat removal substantially, this strategy still proved insufficient at maximal output settings of 100 V peak from a supply voltage of 120 VDC into the 50 Ω load at a 1 MHz switching frequency and 90 % duty cycle.

For the final design iteration TO-220 package thick film resistors were used, attached to heat sinks. With similar loading as before, extensive tests were conducted at a range of frequencies, supply voltages and duty cycles. Figure 5.12 shows the result at worst case conditions.

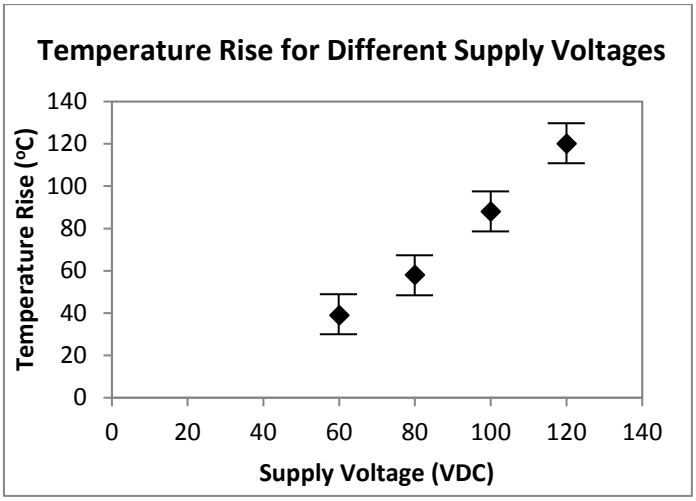

Figure 5.12. Temperature rise at 920 kHz switching frequency of heat sink surface at various supply voltages into a 50 Ω RF load at a 90 % duty cycle. Note that the highest point is slightly underestimated as the partially ducted push-pull fan supply was increased just a little to accommodate heating of the damping resistor, from 370 mA to 400 mA. Indicative error bars of ±5 ^{0}C are shown.

The curve in figure 5.12 is quite consistent with a square law, as expected for an increasing applied voltage to a constant load, from $P = V^2/R$, and indicates adequate heat sinking of the radio frequency ablator at the most stressful conditions tested since the highest temperature is tolerated.

Having solved the intermittent problem with the additional power supplies, electrical waveforms were probed under all conditions, and a selection are presented in figure 5.13 covering the switching frequency and duty cycle ranges. Voltages and currents were probed to provide instantaneous output power, from which average (cycle) power was computed by the oscilloscope. Several general aspects are evident, including slew rates, slight non-symmetry of waveforms, and a general increase of output power. An Agilent DSO3034, with a stated vertical DC accuracy of ± 2 % [26], was used to measure these signals.

Figure 5.13. Four Oscillographic images showing output waveforms of the voltage (yellow), current (green) and instantaneous power (pink), using a 50 Ω RF load and a supply of 80 VDC. Current was monitored using a current probe and amplifier [27], and the oscilloscope was adjusted to correct for skew (delay) caused by the current amplifier, as specified in the datasheet. Indicated in the results panel on the bottom right of each image is the switching frequency of a) 229.4 kHz, b) 463.1 kHz, c) 694.7 kHz and d) 925.9 kHz. Cycle RMS values are also shown for voltage and current. Finally, average cycle power is also shown for each image. The duty cycles are a) 30 %, b) 50 %, c) 70 % and d) 90 %.

Slew rate clearly has a significant impact on pulses, being especially visible at the highest switching frequency of 920 kHz. When examining the average output power, this aspect impacts on output power which is less than may have been expected at higher frequency at the high duty cycle of 90 %, despite an even increase in the duty cycle of 20 % between each image (25 W, 38 W, 49 W, 58 W, for a 30 %, 50 %, 70 % and 90 % duty cycle, respectively, as derived from figure 5.13). Power increased non-linearly with the duty cycle, as shown in the data in table 5.1.

Table 5.1*. Cross-sectional power values corresponding with the different duty cycles, but also to the range of frequencies.

Frequency (kHz)	Duty cycle (%)	Average output power (W)
229	30	24.8 ±5
463	50	37.6 ±5
694	70	49.0 ±5
925	90	57.8 ±5

** It is not the intention for this table to be used by clinicians. It is shown purely from the point of view of demonstrating technically that the system produces increased output power with increased duty cycle (see waveforms in figure 5.14), and that this relationship is not linear, especially with the power output at 925 kHz showing a smaller increase than every other step in duty cycle. It also demonstrates output power performance across a range of pulsing frequencies.*

When considering the output power waveforms in figure 5.13, a non-symmetry (between the positive and negative pulses) is noticeable. The power corresponding with the negative voltage portion of the waveform is a slightly larger magnitude compared to the positive voltage portion of the waveform and shows more ringing than the positive portion. The reason for this has not been investigated, although this effect may be due to a slight imbalance in the resistance in the current path when comparing one H-bridge diagonal to the other.

The single H-bridge that was used for this circuit can be scaled up to 2 bridges, as was originally considered (to produce an output of 250 W into 50 Ω at a peak voltage of 200 V), with the current switching MOSFETs being capable of approximately double the current peaks experienced in this circuit. The only required change would be an increase in the power handling capabilities of the damping resistors, which would have to be doubled.

5.5 Conclusion

In this chapter the design and results for the RFA system have been discussed in detail, and show successful operation.

In particular, it is capable of operating at a supply of up to 120 VDC for low and high frequencies and duty cycles, without thermal overload. It was capable of delivering 100 W into a 50 Ω load, although this data is not shown above – during this high power testing attention was focused on

thermal survival of the circuit and no oscilloscope traces were recorded. This was ensured by extensive adaptation of the electroporator design from a high voltage very low duty cycle capability to a low voltage high duty cycle, but otherwise using a practically identical layout. Scaling this circuit up to two H-bridges would be a simple task, with minor changes mainly involving doubling the power dissipation capabilities of the damping resistors, and the system would then be capable of delivering 2 times the output power equal to 200 W or higher.

The only limitation of the RFA system is its power output at the highest switching frequency (920 kHz), which is restricted due to the inherent slew rate of the design.

5.6 References

[1] K. Sato, et al., "Treatment of Unresectable Primary and Metastatic Liver Cancer with Yttrium-90 Microspheres (TheraSphere): Assessment of Hepatic Arterial Embolization", *CardioVasc Inter Rad*, Vol. 29, No. 4, pp. 522-529, 2006.

[2] Y. Ni, S. Mulier, et al., "A review of the general aspects of radiofrequency ablation", *Abdom Imaging*, Vol. 30, No. 4, pp.381-400, 2005.

[3] D. Haemmerich and B. J. Wood, "Hepatic radiofrequency ablation at low frequencies preferentially heats tumour tissue", *Int J Hyperthermia*, Vol. 22, No. 7, pp. 563-574, 2006.

[4] C. B. Arena, et al., "Theoretical considerations of tissue electroporation with high-frequency bipolar pulses", *IEEE Trans Biomed Eng*, Vol. 58, No. 5, pp. 1474-1782, 2011.

[5] Angiodynamics, *Rita 1500x: User's Guide And Service Manual*, Rev. 3, [Online]. Available: http://www.angiodynamics.com/uploads/pdf/102210-114840_Model%201500X%20IFU.pdf

[6] P. L. Pereira, et al., "Radiofrequency Ablation: In Vivo Comparison of Four Commercially Available Devices in Pig Livers", *Radiology*, Vol. 232, No. 2, pp. 482-490, 2004.

[7] Ixys, *Data sheet for DE275-201N25A RF Power MOSFET*, Rev. 4, [Online]. Available: http://ixapps.ixys.com/DataSheet/de275_201n25a.pdf

[8] DesignSoft, *TINA Pro Circuit Simulator for Analog, RF, Digital, MCU, HDL, Symbolic & Mixed Circuit Simulation with Integrated PCB Design*, 2016, [Online]. Available: http://www.tina.com

[9] M. H. Rashid, *Power electronics: circuits, devices, and applications*, 3rd ed., Upper Saddle River, NJ, Pearson/Prentice Hall, 2004, pp. 417-422.

[10] Aavid-Thermaloy, *Thermal greases with thermal resistance calculator*, 2015, [Online]. Available: http://www.aavid.com/product-group/interface/greases

[11] P. Horrowitz and W. Hill, *The art of electronics*, 2nd ed., Cambridge University Press, 1995, pp. 312-316.

[12] Microchip, *TC4421A/4422A 9A: High-speed MOSFET Drivers datasheet*, Rev. B, 2013, [Online]. Available: http://ww1.microchip.com/downloads/en/DeviceDoc/21946B.pdf

[13] L. Balogh, *Design and Application Guide for High Speed MOSFET Gate Drive Circuits*, 2016, [Online]. Available: http://www.radio-sensors.se/download/gate-driver2.pdf

[14] Alutronic, *Mica Washer Products*, 2016, [Online]. Available: http://alutronic.com/products/accessories-thermal-interface-material/mica-washers

[15] Aavid Thermaloy, Thermal Greases, 2016, [Online]. Available: http://www.aavid.com/product-group/interface/greases

[16] Ixys, *IXD-630: 30A Low-Side Ultrafast MOSFET Drivers Data sheet*, Rev. 3, 2012, [Online]. Available: http://www.clare.com/home/pdfs.nsf/www/IXD_630.pdf/$file/IXD_630.pdf

[17] Ohmite, *Resistor Selection Application Notes*, 2016, [Online]. Available: http://www.ohmite.com/techdata/res_select.pdf

[18] Vishay, *BYG22D: Ultra-Fast Silicon Mesa SMD Rectifier Datasheet*, Rev. 5, 2000, [Online]. Available: http://www.datasheetcatalog.org/datasheet/vishay/86011.pdf

[19] TT Electronics, *PWC series pulse withstanding chip resistors datasheet*, 2014, [Online]. Available: http://www.ttelectronicsresistors.com/datasheets/pwc.pdf

[20] Texas Instruments, *Chapter 17: Circuit Board Layout Techniques*, SLOA089, 2008, [Online]. Available: http://www.ti.com/lit/ml/sloa089/sloa089.pdf

[21] Philip C. Todd, *Snubber Circuits: Theory, Design, and Application*, Application Note, Unitrode Corporation, 1993.

[22] Digilent, *Spartan-3E FPGA Starter Kit Board User Guide*, UG230 (v1.2), 2011, [Online]. Available: http://www.xilinx.com/support/documentation/boards_and_kits/ug230.pdf

[23] Avago, *HCPL-2400, 20 MBd High CMR Logic Gate Optocoupler Datasheet*, 2008, [Online]. Available: http://www.avagotech.com/docs/AV02-0962EN

[24] Tektronix, *Data sheet for Tektronix TDS1000B or TDS2000B Series*, 2010, [Online]. Available: http://www2.tek.com/cmsreplive/psrep/13295/3GM_19558_2_2011.02.10.07.25.34_13295_ES-MX.pdf

[25] Fluke, *User manual for Fluke Ti20 Thermal Imager*, 2006, [Online]. Available: http://media.fluke.com/documents/Ti20___umeng0000.pdf

[26] Keysight, *Datasheet for Keysight InniiVision 3000 X-Series Oscilloscopes*, 2014, [Online]. Available: http://cp.literature.agilent.com/litweb/pdf/5990-6619EN.pdf

[27] Tektronix, *AC/DC Current Measurement Systems Datasheet*, TCPA300, TCPA400, 2016, [Online]. Available: http://www.tek.com/sites/tek.com/files/media/media/resources/TCPA-Amplifiers-and-TCP300-400-Probes-Datasheet-60W1645810_2016.02.01.11.29.29_13540_EN.pdf

CHAPTER 6

RADIO FREQUENCY ABLATOR APPLICATION TO ANIMAL LIVER

6.0 Introduction

The previous chapter detailed the design, development and electrical testing of the radio frequency ablator. This chapter follows through by detailing experimental work carried out on animal liver to test and characterise the ablator with an application-specific load. Animal liver was chosen for this study because its intended application included ablating animal or human liver tumours. Although fresh and healthy animal liver was used instead of cancerous liver tissue, it still served as a useful model for proof of principle testing. The chapter starts off by discussing the design of the probe followed by the experimental protocol, results, discussion and conclusion.

6.1 Probe Design

Delivering radio frequency currents to animal tissue requires an electrode system. Electrodes in use in a clinical setting can be classified into monopolar and bipolar types. Monopolar electrodes[1] in clinical terms means a single probe where high current density is created at the site where ablation is required, producing Joule heating to destroy live tissue, working in concert with a return electrode, such as a large plate(s) or pad(s) typically located in close contact with the thighs of a patient. Bipolar electrodes are usually a pair of identical conductive rods or surfaces both applied at the site where ablation is required providing its own electrical circuit. It was decided

[1] The terms monopolar and bipolar have a different meaning in clinical practice opposed to electrical engineering. The clinical terms relate to the number of active electrodes used, thus a monopolar electrode is normally a single active electrode at the site where heat is applied, working in concert with a passive return electrode normally of very large relative area. Consequently a bipolar electrode set uses two similar electrodes both at the site of ablation, with no separate return electrode. In electrical engineering these terms relate to the applied voltage or current waveform, with monopolar meaning a voltage waveform of a single polarity, and bipolar meaning a voltage of alternating polarities, both positive and negative.

to use a monopolar type electrode, mainly due to its simplicity, and also based on a published study [1] as basis for comparison.

A wide range of "state-of-the-art" electrodes are available commercially including rod probes, multiple tine probes, and bipolar probes. Examples are presented in figure 6.1.

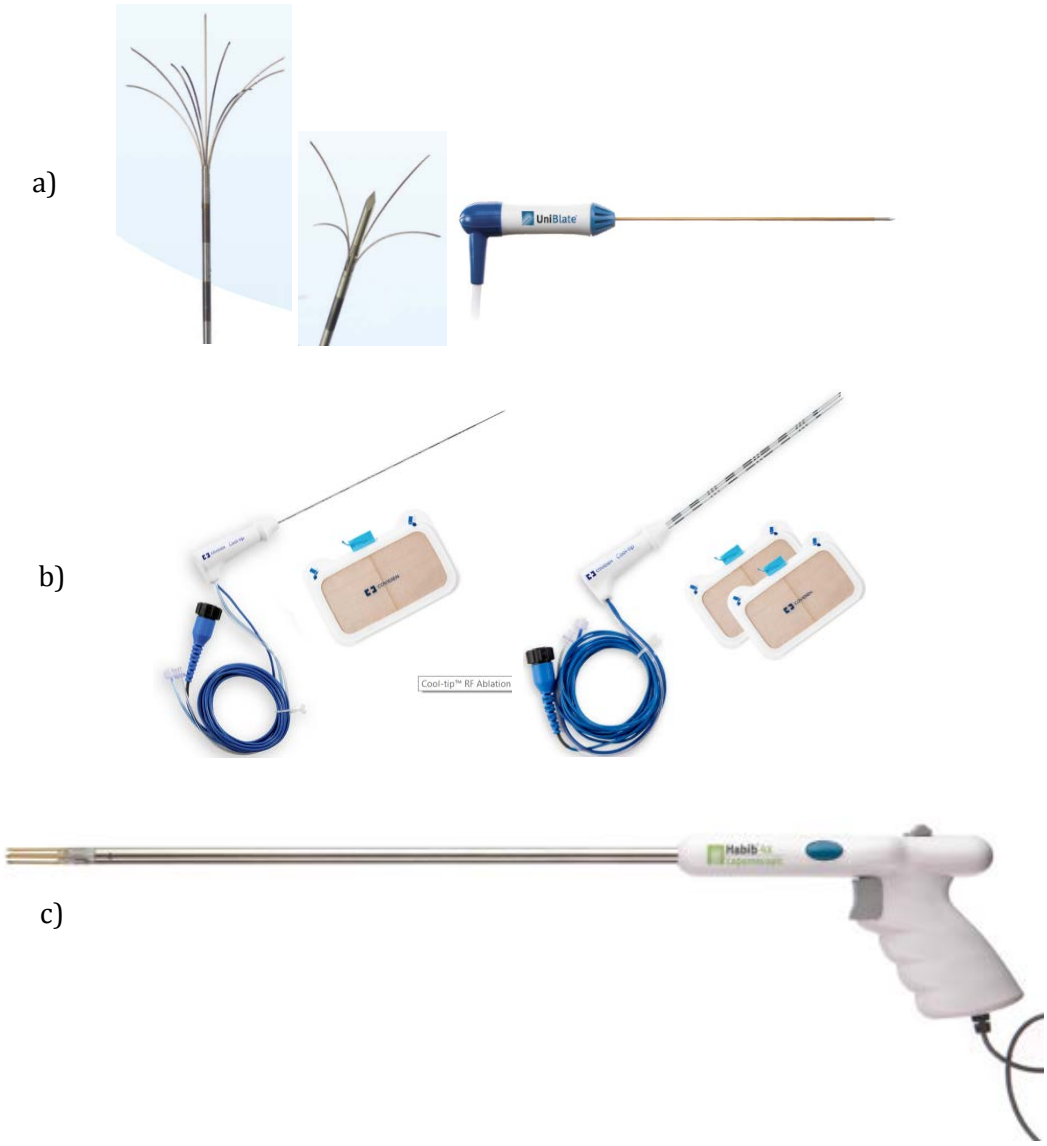

Figure 6.1. Several examples of modern RFA electrodes covering a good range of designs. The top two rows are all monopolar electrodes, including a) the Starburst XL, Talon, and Uniblate from Angiodynamics [2], and b) the Covidien Cool-tip E-series showing single and cluster electrodes with separate return pad electrodes [3]. c) The Angiodynamics Habib 4X bipolar probe [4] is a bipolar type electrode that uses 4 tips, although 2 tips would also suffice to perform the function.

A photograph of the custom designed probe used in the experimental work described here is shown in figure 6.2.

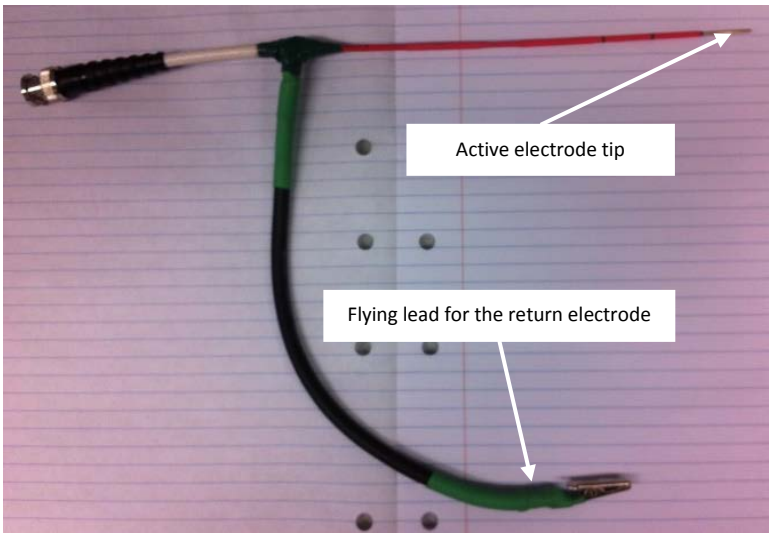

Figure 6.2. Custom designed radio frequency ablator probe.

The probe in figure 6.2 comprises a brass rod of 1.5 mm diameter, of total length of 160 mm. The material has been chosen due to solderability and availability. Although brass contains copper, the prototype was never intended to be used on live animals. It was coated with polyurethane lacquer with the last 20 mm of the tip exposed, and was combined with a heat shrink sleeve which was marked every 20 mm as a depth guide. It is terminated with a BNC socket for connecting to an interface printed circuit board (PCB) used for current and voltage monitoring. The interface PCB was subsequently attached to the ablator lead.

The return electrode was constructed from a stainless steel plate of which the main area is immersed in a saline solution in which the liver specimen is located. The plate is connected to the flying lead of the probe.

Figure 6.3 shows the setup of the radio frequency ablation experiment.

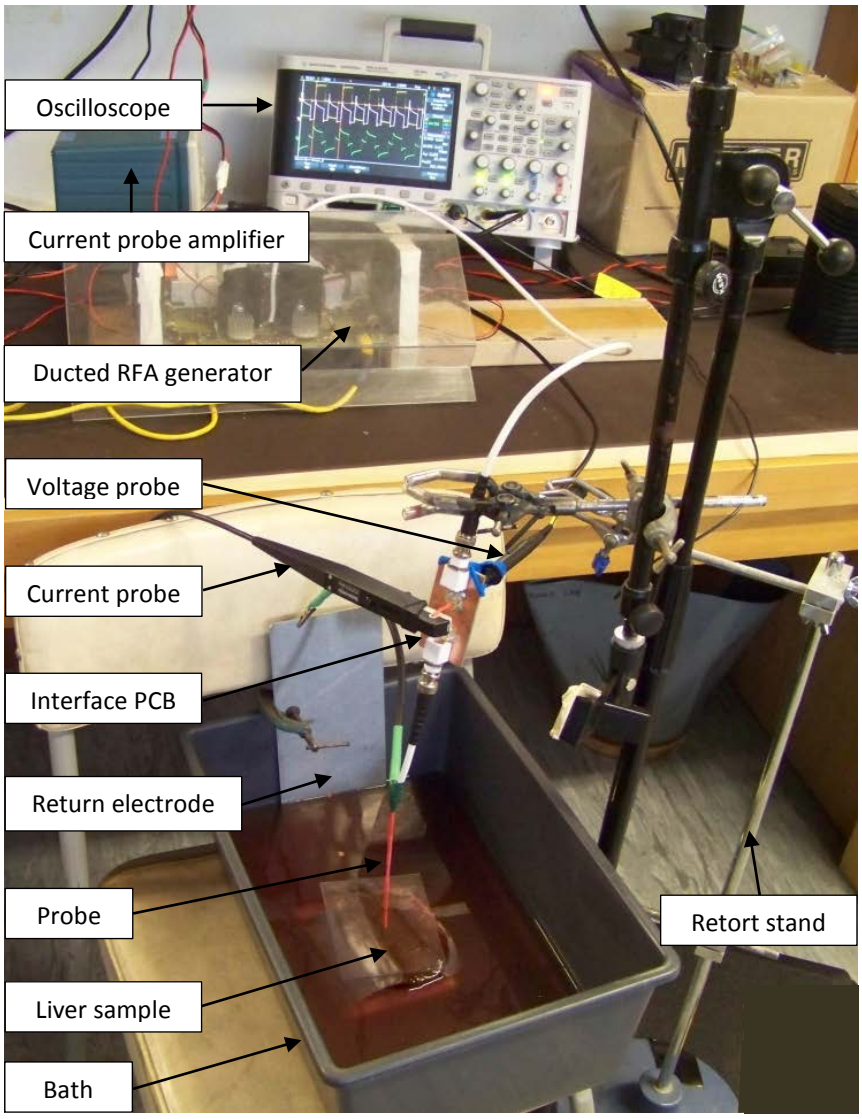

Figure 6.3. Set up showing saline bath, probe, return electrode, and other associated equipment for monitoring ablation power.

As seen in figure 6.3, the experimental work was carried out using a grey rectangular Acrylonitrile Butadiene Styrene (ABS) plastic container (bath) holding saline solution, into which the liver specimen was placed. The saline liquid level was adjusted to be just under the level of the upper surface of the specimen. The bath was located close to the ablator and the instruments, including a voltmeter (not shown), a current amplifier, an oscilloscope and a timer (not shown). This method was extensively based on the comparable study mentioned [1], and follows in the next section.

6.2 Experimental Protocol

6.2.1 Materials

Fresh beef or lamb liver was obtained and cut into specimen blocks of approximately 8 cm cubed. A saline solution was made up using a concentration of 0.9 % of NaCl in 3 L of distilled water.

6.2.2 Equipment

The designed radio frequency ablator, with selectable frequencies (230 kHz to 920 kHz, adjustable in steps of 230 kHz) and adjustable bus power supply voltage, nominally running at 50 W, with possibility of controlling the power manually (ramping it up, then maintaining a constant level), was used.

The custom designed liver probe with active electrode and flying lead shown in figure 6.2 was also used. The return (dispersive) electrode was a stainless steel plate of area 23 cm x 15 cm (approximately 1 mm thick), attached to the middle side inside surface of the saline bath container.

A 100 MHz specified two-channel oscilloscope (Agilent Infinivision DSO3014A [5]), with capability of a math function of the product between channel values, was used. It required a programmable skew to account for the current amplifier delay. It also required the capability to calculate and display a real time average power in W, averaged over several cycles. A 100 MHz specified current probe (Tektronix TCP312) and its current probe amplifier (Tektronix TCPA300) was used [6]. A custom voltage-current (V-I)-probe interface PCB, was also required and constructed.

The bath container was of ABS material with approximate dimensions of 40 cm x 25 cm x 15 cm (l x w x h). A G-clamp was used for attaching the return electrode to the inside of the bath. A retort stand and clamp was used to hold the ablator probe in place. A timer was also used.

6.2.3 Method

The method has been based on published work in [1]. Fresh liver at room temperature (at approximately 20 ^{0}C) was used. The prepared saline solution (see above), was at room temperature.

Two oscilloscope probes were connected to the interface PCB to determine V and I (the latter is determined using a current amplifier). The oscilloscope was set up to show both traces: V (10 x, 10 V/div) and I (1 V/A, 1 A/div), and it was further set to show several cycles across the screen at the frequency of interest.

The dispersive electrode clip of the probe flying lead was clipped to the stainless steel plate. A safe working area was ensured by checking for leaks and ensuring that the electronics are properly shielded from splashing water. Safety goggles were worn. All accessible points were fully isolated (floating), including the power supplies and the oscilloscope.

Next, a liver specimen was placed in the centre of the empty bath, on top of the aluminium base plate (with short protrusions to avoid specimen slipping away). Then the bath was filled up to a level that allows the liver to sit on the bottom centre area so that it just does not float (about 3 L of saline). Solution thermal equalisation with the liver specimen was achieved after about 10 minutes. Other specimens were inserted into the bath at that time to aid in their equalisation.

The active electrode of the probe was inserted vertically from the top into the centre of the liver specimen, to a depth of at least 3 cm deeper than the exposed tip, using the marks on the probe, followed by its BNC connection to the probe interface PCB. The probe was supported by a retort stand and clamp.

Power was applied gradually while continuously pressing the pulse fire button, with the other hand controlling the variac to adjust ablation power using the power protocol detailed in section 6.2.4. Once completed, all power was shut down and the system was carefully isolated from all power sources.

The liver was left to stand for 5 minutes, after which the probe and sample were removed from the bath. The liver was carefully sliced open along the line of the probe hole. Where more than one ablation was needed per specimen, a thin wooden stick was inserted into the previous hole, acting as a guide for later slicing. Lesions were inspected and photographed with a reference dimension

alongside e.g. a short ruler. The process was repeated on new liver specimens at frequencies of 230 kHz, 460 kHz, 690 kHz and 920 kHz, all being at a 70 % duty cycle, to best emulate a sinusoidal waveform. This process should be repeated 3 times and a critical comparison of lesion sizes/volumes should be performed. However, experimental data of only one single process is presented in this chapter due to time limitations.

6.2.4 Power Application Protocol

Figure 6.4 shows the power profile. The protocol is started by ramping up power to 10 W in 10 s. This power level is then maintained for 30 s. Then power is ramped up further to 15 W in 10 s and maintained for 30 s. This is followed by ramping power up to 20 W in 10 s. Power is maintained for 30 s, if possible. If power starts rolling off, the operator should maintain a constant voltage supply until 2 minutes total time has elapsed, rapidly turning supply down to zero at that time. Pause for 1 minute. Repeat this process once.

The phenomenon of a sudden rolling off of power is quite common in clinical RFA. It is characterised by a popping sound, followed by a rapid ramping down of power despite continuous application of voltage. It is apparently caused by a localised substantial rapid water vapour pressure increase in the close vicinity of the tip. A study found that a change of the probe impedance, sometimes a slight drop or a ramping up depending on the type of liver tumour, is often an indicator or predictor of the onset of rapid pressure change, and should be used to avoid this event, which is a risk factor for complications such as bleeding and physical damage to abdominal structures [7].

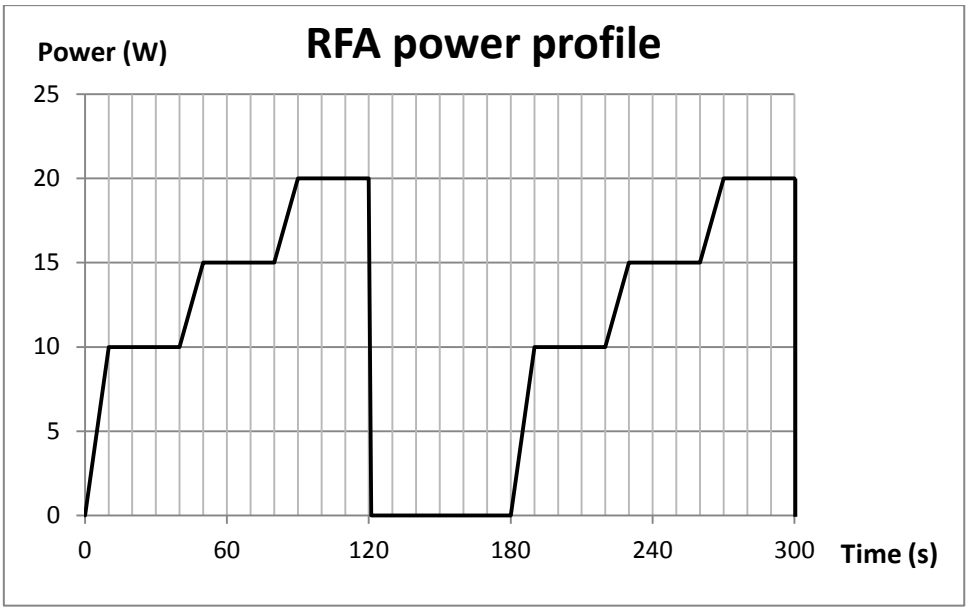

Figure 6.4. Power profile used for RFA experiments.

The power protocol shown in figure 6.4 represents an accumulated energy of 1.7 kJ per cycle or 3.4 kJ for the entire protocol (2 cycle, 20 W, 5 minute), assuming the power does not drop off before ending one of the cycles. This protocol of gradually increasing the power then pausing could be considered typical, although the peak power levels were lower than in clinical practice [8].

6.3 Results and Discussion

A trial run was conducted using lamb liver, to become familiar with the method and all aspects of the experiment. This trial identified several problems, including specimen slippage, operator problems, power drop-off (rapid water vapour pressure change) and other less significant aspects.

The specimen tended to slip around making it hard to stabilise the probe set up at the start of the experiment – this was solved by fabricating an aluminium base plate with jagged corners pointing down (to stabilise the plate on the bottom surface) and an array of jagged edges pointing up (to stabilise the specimen). Operation required two persons initially but with rearrangement of the equipment only one person was required to operate the system. Another problem associated with the rapid water vapour pressure increase was that the power rapidly dropped off after 30 s to 40 s, although the applied voltage was held constant for a total duration of 5 minutes. The experiment applied approximately 50 W at the start (operator controlled – no electronic feedback system was

employed). Literature identified that this is a normal effect [8]. The power drop off can likely be explained by an increase in impedance once a volume of tissue (surrounding the exposed probe tip) has been sufficiently ablated due to denaturation and desiccation [1, 8].

Only one satisfactory lesion was produced in this trial (it was difficult to find the lesions after removing the probe – this was solved by using thin wooden sticks which were immediately inserted into the nearly invisible hole where the probe was removed). A photograph of a bisected lesion is shown in figure 6.5. The lesion plug as shown in figure 6.5 was created during the ablation procedure, representing a cylindrical volume of tissue that is denatured or destroyed to such an extent that it detaches from the surrounding tissue. This type of detached lesion plug was only ever encountered with the lamb liver where the probe was not inserted deep enough into the tissue due to the small size of the liver.

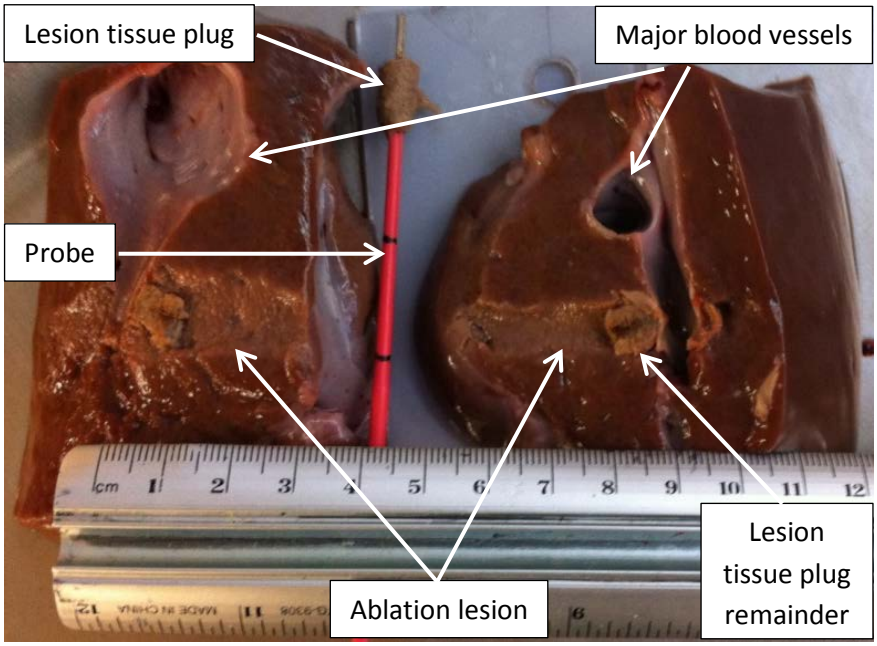

Figure 6.5. Lamb liver sectioned showing the RFA lesion – folded open from the centre. The red rod in the centre is the probe – note its exposed tip at the top with one half of the exposed tip holding a partial plug of lesion tissue, and further below sleeved with red electrical insulation with its depth markers. Major blood vessels are also visible on the sectioned specimen, as well as the ablation lesion (that includes the remainder of the lesion tissue plug).

The lesion was estimated at a length of 35 mm and a diameter of 12 mm. The volume was calculated assuming a prolate spheroid using

$$V = (4/3)\pi(L/2)(D/2)^2, \quad (6.1)$$

with V = volume in cubic centimetre, L = length, and D = diameter, using centimetres, resulting in a volume of approximately 2.6 cm^3.

The second experiment involved a bovine (beef) liver[2] which is approximately 5 kg for a fully grown steer. It was cut up into several blocks of approximately 100 mm x 100 mm x 50 mm. Table 6.1 shows the results.

Table 6.1. Tabulated results of 8 ablation lesions created in a bovine liver, at an ambient temperature of 20 ^{0}C. Estimated experimental error of measurements is ±0.1 cm, translating to a volume error of approximately ±0.5 cm^3.

Length(cm)	Diameter(cm)	Volume(cm^3)
3	1.4	3.079
3	1.4	3.079
3	1.4	3.079
2.8	1.2	2.111
3	1.1	1.901
3.2	1.4	3.284
3	1.2	2.262
3.2	1.3	2.832

Although this was a relatively small sample set (8), and only applied to one beef liver, it produced an average lesion volume of 2.7 cm^3, with a standard deviation of 0.5 cm^3 and a median of 3.0 cm^3. Figure 6.6 shows the sectioned beef liver with several lesions.

[2] This liver was kindly donated by Ashburton Meat Works.

Figure 6.6. Sectioned beef liver samples with lesions in prolate spheroid shapes. The image on the right shows the centre right lesion set in more detail. White arrows indicate measurement dimensions.

These lesions appear to be consistent with those produced in another study [8] where larger lesions (3 cm and 5 cm diameters) were created in a similar set up but with solution and specimen controlled at 37 ^{0}C. Experiments in that study created 3 cm diameter lesions producing an ablated volume ranging from 17 cm^3 to 29 cm^3, in a duration ranging from 5 minutes to 21 minutes, depending on the equipment (and power protocol) used. This was far in excess of the power protocol used here, time-wise and power-wise. That study represents a volume increase of 6-fold to 10-fold compared to this study. It is not possible to accurately compare these volumes as the power protocols for the tested equipment in the other study are not clearly stated. However, taking an estimate of an example (Boston Scientific RF3000) used an accumulated energy of 11.7 kJ per cycle (3 minutes), but was restarted adding more energy per experiment to accumulate around 13.5 kJ. This represents a factor of 4, which may be realistic considering that this experiment was conducted at 20 ^{0}C, needing an additional raise of temperature of 17 ^{0}C in the tissue before being able to be compared with tissue at 37 ^{0}C.

It should also be noted that, in several instances in this experiment, the power dropped off shortly before reaching the end of a cycle settling in the region of only 5 W to 10 W each time, diminishing the energy transferred to the tissue. This timing has not been recorded, thus no energy calculation correction can be made.

A third experiment was conducted where the objective was to compare equivalent energy/power protocols between two different pulsing frequencies. Ablations were performed on a fresh beef liver. It was expected that higher frequencies may result in more consistent ablation for highly vascularised liver tumour tissues since such tissues may be morphologically and dielectrically

more variable than healthy tissue. Since higher frequencies tend to couple current better through cell membrane capacitance [9], this may prove to be an advantage when ablating variable/non-homogeneous tissue, favouring more uniform power deposition at a specific applied voltage. Initially 8 ablations were performed at each frequency (230 kHz and 920 kHz), but only 4 useful samples could be gathered at the lower frequency of 230 kHz. Figure 6.7 shows the liver samples used for the data.

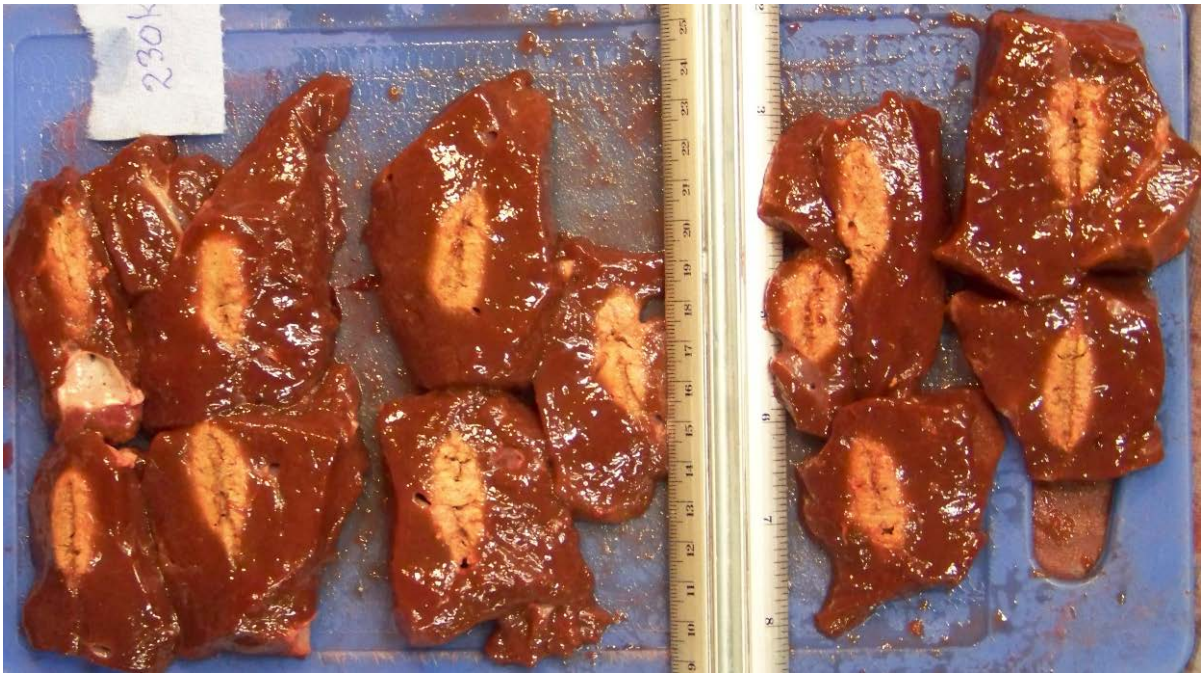

Figure 6.7. Photograph showing 12 beef liver specimens, sectioned to reveal the ablation lesions. The left-most group (of four) were pulsed at 230 kHz and the rest at 920 kHz. In this instance, samples were ablated at room temperature of 18 ^{0}C.

From the image in figure 6.7, no apparent distinction is noted between the two frequencies in terms of morphology, colouration, or any other aspect. Ablation lesion volume results are given in table 6.2. Volumes were calculated using a prolate spheroid, as before. It may be noted that the method does tend to underestimate dimensions as it is nearly impossible to section the lesions exactly along its longitudinal centre line, and when it is not exactly in the centre, dimensions will be smaller, so data can be regarded as conservative.

Table 6.2. Ablation lesion volume data and statistics, at the two switching frequencies. These ablations were performed on beef liver using the same 2 - cycle - 20 W - 5 minute power protocol as before. The second table shows the accumulated statistics. Estimated experimental volume error is approximately ±0.5 cm^3, based on a ±1 mm measurement error.

Switching frequency (kHz)	Lesion length (mm)	Lesion diameter (mm)	Ablated volume(cm^3)
230	33.33	13.33	3.10
230	32.00	13.33	2.98
230	30.00	12.00	2.26
230	33.33	14.67	3.75
920	31.25	13.75	3.09
920	34.38	15.00	4.05
920	31.25	13.75	3.09
920	35.00	13.00	3.10
920	25.00	13.00	2.21
920	30.00	13.00	2.65
920	32.00	15.00	3.77
920	32.00	12.00	2.41

Switching or pulsing frequency (kHz)	Average ablated volume(cm^3)	Standard deviation (cm^3)	Number of samples
230	3.02	0.53	4
920	3.05	0.59	8

From the results shown in table 6.2 no lesion volume distinction based on frequency is clear. The averages and standard deviations are very similar. This may be as a result of the small sample, but, even if the 230 kHz results were taken together with experiment 2, a distinction does not yet appear to arise, and the experimentally obtained data can still be regarded as a small sample.

The supposition that better ablation might be achieved at either lower or higher frequency is clearly not answered here. However, since the protocol is controlled to transfer approximately the same amount of power into the specimen, it would naturally not show any difference. What would have helped is if the applied voltage and system total power was monitored at the time, to provide system efficiency for comparison. Also, healthy liver tissue tends to be relatively homogenous, which reduces any effects associated with tissue structure/type variation – especially when supplied with a significant vascular blood flow.

As a further point of note, when calculating latent heat of water (4.2 kJ per kg of water per ^{0}C rise in temperature), and applying a similar heating protocol of 0.34 MJ to a perfectly insulated 3 cm^3 bolus of water, the bolus will experience an average theoretical rise in temperature of 270 ^{0}C. This is approximately 10 times the rise in temperature that actually occurs in the liver tissue during RFA, and consequently the direct application of heat to *ex-vivo* liver is only 10% efficient (at room temperature) owing to the heat conduction properties of the surrounding tissue. This may be compounded with the heat sinking effect of vascular blood flow rendering the effect even less efficient [10].

6.4 Conclusion

A test probe has been developed for the sake of low power experimental work on *ex-vivo* animal liver at room temperature. Also, a low power ablation protocol has been established, based partly on protocols found in other studies. The radio frequency ablator has created comparatively sized (to other studies) lesions for the low power used. The lesions were created using a low power protocol of two cycles of a ramped up 20 W each in 5 minutes producing an average lesion volume of 2.7 cm^3, which appears to be consistent with another study where several commercial RFA apparatus were compared.

A distinction in size of lesion between the two frequencies when power is partially controlled is not apparent, and the system is less electrically efficient at higher frequencies due to the slew rate and corresponding switching power at the switching devices. As such there appears to be no evidence, for the small set of results obtained, to indicate any direct advantage gained by using higher frequencies when ablating normal tissue, noting also that other studies including especially [11] have indicated that a lower frequency may be beneficial in some instances. Future work of ablation at higher frequencies than the normal RFA frequency of 450 kHz of malignant liver tumour tissue that is highly inhomogeneous and vascularised may provide more comprehensive results.

6.5 References

[1] J. M. Lee, et al., "A Comparative Experimental Study of the In-Vitro Efficiency of Hypertonic Saline-Enhanced Hepatic Bipolar and Monopolar Radiofrequency Ablation", *Korean J Radiol*, Vol. 4, No. 3, pp. 163-169, 2003.

[2] AngioDynamics, *RFA products*, 2015, [Online]. Available: http://www.angiodynamics.com/products/rfa-in-service

[3] Covidien, *Cool-tip RF Ablation System E Series Electrodes & Accessories*, 2015, [Online]. Available: http://surgical.covidien.com/products/ablation-systems/radiofrequency-ablation/cool-tip-rf-ablation-system-e-series-electrodes#products

[4] AngioDynamics, *Surgical products*, 2015, [Online]. Available: http://www.angiodynamics.com/uploads/pdf/052014-083843_160-104029_Rev_04_Artwork.pdf

[5] Keysight, *Datasheet for Keysight InniiVision 3000 X-Series Oscilloscopes*, 2014, [Online]. Available: http://cp.literature.agilent.com/litweb/pdf/5990-6619EN.pdf

[6] Tektronix, *AC/DC Current Measurement Systems Datasheet*, TCPA300, TCPA400, 2016, [Online]. Available: http://www.tek.com/sites/tek.com/files/media/media/resources/TCPA-Amplifiers-and-TCP300-400-Probes-Datasheet-60W1645810_2016.02.01.11.29.29_13540_EN.pdf

[7] H. Iida, et al., "Effectiveness of impedance monitoring during radiofrequency ablation for predicting popping", *World J Gastroenterol*, Vol. 18, No. 41, pp. 5870-5878, 2012.

[8] H. Rathke, et al., "Comparison of four radiofrequency ablation systems at two target volumes in an *ex vivo* bovine liver model", *Diagn Interv Radiol*, Vol. 20, No. 3, pp. 251-258, 2014.

[9] C. B. Arena, et al., "Theoretical considerations of tissue electroporation with high-frequency bipolar pulses", *IEEE Trans Biomed Eng*, Vol. 58, No. 5, pp. 1474-1782, 2011.

[10] A. J. Aschoff, et al., "How does alteration of hepatic blood flow affect liver perfusion and radiofrequency-induced thermal lesion size in rabbit liver?", *Journal of Magnetic Resonance Imaging*, Vol. 13, No. 1, pp. 57-63, 2001

[11] D. Haemmerich and B. J. Wood, "Hepatic radiofrequency ablation at low frequencies preferentially heats tumour tissue", *Int J Hyperthermia*, Vol. 22, No. 7, pp. 563-574, 2006.

CHAPTER 7

CONCLUSIONS AND FUTURE WORK

7.0 Introduction

This chapter identifies the thesis conclusions, offers recommendations for future work, presents the novel intellectual contributions made, and lists the publications arising from this research.

7.1 Conclusions

Incidence of cancer is growing in modern society, motivating development and research into new therapies. The ultimate goal of the work in this thesis is to offer novel methods for use in cancer therapy.

Literature suggests that there are certain physical means of producing more consistent electroporation among a variety of different cells in a tumour, and these means need to be further explored. The goal of this thesis was to design an apparatus that can be used to test or validate these new physical means of improving electroporation.

A novel electroporator apparatus that uses a dual stage cascaded multilevel inverter topology with high voltage RF MOSFETs has been designed and used successfully for the majority of experiments in this study. It meets the broad initial specifications, being adjustable or programmable in terms of voltage, frequency, and pulse burst regime. It offers a variety of output waveforms and it is also capable of producing bipolar or monopolar pulses. To the author's knowledge, there is no other example such a fast high voltage pulser with all these capabilities identified in literature associated with electroporation research, which in itself is a contributing factor why combined high frequency high voltage electroporation studies have not been carried out yet. The developed apparatus has demonstrated operational performance up to 1 MHz pulses into a load of 80 Ω in parallel with 235 pF from a dual isolated supply of 1,600 VDC total. This was despite substantial coupled noise in the circuit. However, the circuit was tolerant of this noise and produced useful output waveforms.

A successful cuvette has been developed for the experiments in this study where electric field pulses have been applied to human cancer cells in suspension. The electroporation chamber in the cuvette fabricated for the experiments in this study has a uniform electric field distribution, as is supported by numerical modelling. This cuvette has been used for more than 60 experiments without any problems or failure, so has proved to be robust and reliable. Efficient cell culture and electroporation protocols have been developed for the experiments undertaken.

The body of work completed involved pulsed electric field electroporation of Ishikawa human cancer cells in suspension. Two separate experimental methods were employed, fluorescence microscopy and flow cytometry. Microscopic analysis proved less efficient than flow cytometric analysis and also lacked fluorescence resolution.

It has been demonstrated that the developed electroporator system is capable of successfully and reliably electroporating cancer cells in suspension. Differences between bipolar and monopolar pulses were examined and characterised in detail, and is summarised at the end of chapter 4. DC (monopolar) pulses appear to have more detrimental effects on cells compared to AC (bipolar) pulses for an equivalent mean fluorescence. Thus bipolar electric fields show a clear advantage over monopolar fields if the aim is not to kill cells directly. Higher frequencies tend to demand higher electric fields to produce the same degree of electroporation compared to lower frequencies. It has not been absolutely established whether higher frequency pulses produce a more even or normalised degree of electroporation on different sized cells. To the knowledge of the author, the set of experimental results involving high frequency pulses up to 800 kHz and up to 3.5 kV/cm, and the use of the flow cytometer in this particular way, are unique.

A radio frequency ablator using the above-mentioned general topology was successfully developed with selectable pulse frequency, voltage and waveform. Also, a radio frequency ablation probe has been developed for the sake of low power experimental work on ex-vivo animal liver at room temperature. Furthermore, a low power ablation protocol has been established, based partly on protocols found in other studies. The radio frequency ablator system was used to successfully and reliably ablate fresh animal liver with very similar characteristics to standard commercial radio frequency ablation systems. The system performed less electrically efficiently at high frequencies. Electrical efficiency is essentially irrelevant in medical treatment applications. The heat can always be handled with appropriate heat removing methods. It could not be established whether higher frequencies are capable of producing better ablation performance as could be expected when considering that tissues tend to be more conductive at higher frequencies due to inherent tissue capacitance causing the impedance to drop.

7.2 Recommendations for future work

Further cytometric assessment of human cancer cells in suspension is needed to span the full electroporation range at a frequency of 800 kHz, requiring a pulse field strength in the order of 4 or 4.5 kV/cm. Viability studies across the frequency and electric field strength ranges also needs to be done. More work is still needed to show whether higher frequency pulses produce a more normalised electroporation effect compared to monopolar pulses with respect to cell size/radius/morphology, for cells in a tissue structure. The first stage of this work will be well represented by electroporation of cell cluster spheroids – a quasi-tissue structure that can be readily produced with the same Ishikawa cancer cells used in the cell suspension experiments detailed in chapter 4. Work of this nature may be performed with slight modifications to the hardware design identified in this thesis.

Radio frequency ablation at higher field frequencies remains to be further investigated, to identify whether it might offer better results at higher frequencies than 450 kHz. Overcoming the electronic circuit heat problem (possibly through the use of active electronic cooling systems) will enable this further work.

Finally, an integrated cancer therapy apparatus, as may be used for liver cancer therapy by an interventional radiologist, has been proposed in appendix H. This apparatus is intended to utilise a combination of electrochemotherapy, irreversible electroporation and radio frequency ablation, for a multimodality therapy procedure on deep tissue malignant tumours (such as in primary or secondary liver cancer). Some specifications for the system have been described, including physical and electrical aspects. This proposed apparatus would assist further work in other applications such as electrofusion, gene therapy and genome editing.

7.3 Contributions

A novel electroporator apparatus that uses a dual stage cascaded multilevel topology with high voltage RF MOSFETs has been successfully developed. This design is useful for a multitude of applications, and particularly where a combination of high frequency and high voltage pulses of substantial instantaneous power capability is required. The electroporator is fully scalable for even higher voltages due to the use of the multilevel inverter topology.

A successful cuvette has been developed for the experiments where electric field pulses have been applied to human cancer cells in suspension. This cuvette has been used for more than 60 experiments without any problems or failure, so has proved to be robust and reliable.

Efficient cell culture and electroporation protocols have been developed and improved for the experiments undertaken.

A new body of detailed experimental work has been presented identifying clear and substantial differences between monopolar (DC) and bipolar (AC) electric field pulses. This work used the well-established flow cytometry analysis method which has not been applied to electroporation experimental work as detailed in this thesis. Flow cytometry provided raw data from human cancer cells (Ishikawa cell line) that have been exposed to electroporative treatments while suspended in a medium with propidium iodide fluorescence dye. It was possible to discern different sub-populations of cells within the samples.

A novel radio frequency ablator system, including the electrical circuit and the ablation probe, has been designed and tested, using pulsed potentials instead of commonly used sinusoidal potentials.

A novel multimodality cancer therapy system, offering a combination of electrochemotherapy, irreversible electroporation therapy and radio frequency ablation therapy for application in deep tissue cancer tumours, has been proposed and described.

7.4 Publications to Date Arising from the Research

T. Cronje and P. Gaynor, "High voltage and frequency bipolar pulse generator design for electroporation-based cancer therapy", in *Proceedings of the Power Engineering Conference (AUPEC), 2013 Australasian Universities*, Hobart, Australia, on IEEExplore, pp. 1-7, 2013.

T. F. Cronje and P. T. Gaynor, “Cancer Zapper: Cascaded Pulser”, in *Canterbury Health Research Poster Expo*, Christchurch, New Zealand, 2013.

T. F. Cronje, P. T. Gaynor and G. Lau, “A new multipurpose cancer zapper”, Abstract, *New Zeal Med J*, Vol. 123, No. 1324, p. 96, 2010.

T. Cronje, P. Gaynor and G. Lau, “Electricity vs Cancer: Punching holes into cells”, in *Canterbury Health Research Poster Expo*, Christchurch, New Zealand, 2009.

T. Cronje and P. Gaynor, “A new multipurpose cancer zapper: The way forward”, in *Proceedings of the Fourteenth Electronics New Zealand Conference* (ENZCon 2007), Wellington, New Zealand, pp. 89-94, 2007.

APPENDIX A

ELECTRIC FIELD DISTRIBUTION MODELLING WITH RESPECT TO BIOLOGICAL CELLS

A.0 Introduction

This appendix provides a graphic two-dimensional understanding of the basic concepts involved with electric field distribution characteristics leading to electroporation by presenting modelling of the biophysical effect of an applied electric field with the model based on dielectric materials structures. It starts with modelling from the literature as background then moves on to brief numerical modelling of electric field distribution, as it relates to cells in suspension and in a packed formation. This modelling work is not intended to be considered as being quantitatively complete, rather as providing indicative general characteristics of electric field concentration prior to onset of electroporation.

A.1 Modelling From the Literature

Modelling has been performed by several groups, including noteworthy examples from Slovenia, New Zealand and the USA. Studies were carried out to establish the effect of bipolar against monopolar applied fields for several waveforms, and also the effect of frequency on a population of varied cell sizes in suspension [1-3]. This group found that higher frequency bipolar (AC) waves produced better normalisation of the electroporation effect on a range of different cell sizes with respect to lower AC frequencies. The high frequency nature of the electric field counteracts the well documented basic theory that exposure of suspended cells to a static field creates a larger transmembrane potential for larger cells over smaller cells (see chapter 2). What this group also noted was that using lower extracellular medium conductivity aids the process of electroporation, and particularly for a range of cell sizes, over a bias towards larger cells. Lower extracellular medium conductivity, however, produces more potential drop across the medium relative to the

cell membrane, thus requiring higher applied fields for the same electroporation effect, than for higher conductivity media. Thus there is a lower limit on the conductivity of the extracellular medium for effective electroporation to occur.

Another group has also modelled electroporation of a single cell [4, 5]. The general theme was to evaluate the transmembrane potential as a function of time as the cell is exposed to a time variant electric field, and also to study the dynamic behaviour of the electropores, the latter of which also received considerable attention in [1, 2].

Modelling of cells in a tissue-like structure has been demonstrated in several papers [6-9]. A study [6] considering irregularly shaped cells in tissue has presented a new approach and found that electroporation occurred mostly at invaginations and at tight junctions of cells. Another study [7] has studied and recommended the use of high frequency bipolar pulsed electric fields for a heterogeneous skinfold model, particularly at frequencies between 500 kHz and 1 MHz. Another study worthy of mention determined potential difference distribution on a cell membrane and how it interacted with the transmembrane potential, using different arrangements of cell lattices [8]. The findings were that induced transmembrane potential depended on the cell volume fraction (or how tightly they were packed), and that, inside a cluster of cells, the transmembrane potential is not dependent on the cell radius. Yet another study [9] modelled cell assemblies connected with gap junctions, to probe the effect of exposure of cells to weak electromagnetic fields. They found that a typical cell behaves like a low pass filter with an additional band stop filter added just before the cut-off point (due to the presence of a gap junction) and that there is a need for more complex models to properly assess the behaviour of cells with gap-junctions.

Parameters used for modelling have been based on the above-mentioned studies and others [10, 11], and are listed in the table A.1. In these latter papers this group modelled the temporal nature of transmembrane potential as a function of various applied field waveforms, and also the distribution of dissipated power in cells exposed to electroporation regimes.

Table A.1. Parameters used for the models.

PARAMETER DESCRIPTION	PARAMETER
Cell diameter	10 μm
Membrane thickness	5 nm
Intracellular medium conductivity	0.3 S/m
Extracellular medium conductivity	0.3 S/m*
Membrane conductivity	0.3 μS/m
Intracellular relative permittivity	80
Extracellular relative permittivity	80
Membrane relative permittivity	5

** As opposed to physiological mammalian conductivity of around 1.6 S/m*

This set of parameter values given in table A.1 provide a reasonable starting point, although they are considered constant across frequencies and under constant external applied conditions — this is not true in real cells, but nevertheless assist in providing an understanding of effects.

A.2 Modelling of Cells in Suspension

When cells are in a suspension and well separated, like in biotechnology applications, they can easily be modelled using a finite element analysis (FEA) tool such as COMSOL Multiphysics version 4.2.

The modelling tool solves the differential form of Maxwell's equations, expressed in the time-variant version [12],

$$\nabla \times \mathbf{H} = \mathbf{J} + \frac{\partial \mathbf{D}}{\partial t} \quad \text{(A.1)}$$

$$\nabla \times \mathbf{E} = -\frac{\partial \mathbf{B}}{\partial t} \quad \text{(A.2)}$$

$$\nabla \cdot \mathbf{D} = \rho \quad \text{(A.3)}$$

$$\nabla \cdot \mathbf{B} = 0 \tag{A.4}$$

where equation A.1 is Maxwell-Ampère's law, A.2 is Faraday's law, A.3 Gauss' electric law and A.4 is Gauss' magnetic law. The equation of continuity is required to solve these equations, thus

$$\nabla \cdot \mathbf{J} = -\frac{\partial \rho}{\partial t} \tag{A.5}$$

with **H** the magnetic field intensity, **D** the electric displacement field intensity, **J** the current density, **E** the electric field intensity, **B** the magnetic flux density and ρ the electric charge density.

The relationship between **D** and **E** is

$$\mathbf{D} = \varepsilon_0 \varepsilon_\mathrm{r} \mathbf{E} \tag{A.6}$$

where ε_0 is the permittivity of vacuum and ε_r the relative permittivity of any specific dielectric material.

The generalised version of current density is

$$\mathbf{J} = \sigma \mathbf{E} + \mathbf{J}_\mathrm{e} \tag{A.7}$$

with σ the electrical conductivity and $\mathbf{J}_\mathrm{e}$ the external generated current density.

Using the "electric currents interface", the general problem is solved by the following equations

$$\nabla \cdot \mathbf{J} = Q_j \tag{A.8}$$

$$\mathbf{J} = \left(\sigma + \varepsilon_o \varepsilon_r \frac{\partial}{\partial t} \right) \mathbf{E} + \mathbf{J}_e \tag{A.9}$$

$$\mathbf{E} = -\nabla V \tag{A.10}$$

$$\mathbf{D} = \varepsilon_0 \varepsilon_\mathrm{r} \mathbf{E} \tag{A.11}$$

where **J** is current density, Q is charge, **E** is the electric field vector, **D** is electric flux density vector, σ is conductivity, ε_o is permittivity of a vacuum, ε_r is relative permittivity, Q_j is line charge, and $\mathbf{J}_e$ is externally generated current density. Equation A.9 is a form of Ohm's law.

The two-dimensional model of a single cell in a suspension is constructed as a representative central cross-sectional square (20 μm x 20 μm), with the two outside boundaries vertical boundaries treated as highly conductive copper surfaces (electrodes), the top boundary as an air interface, and the bottom boundary as a glass interface, partially mimicking the electroporator chamber – see chapter 4. The model is then meshed as shown in figure A.1.

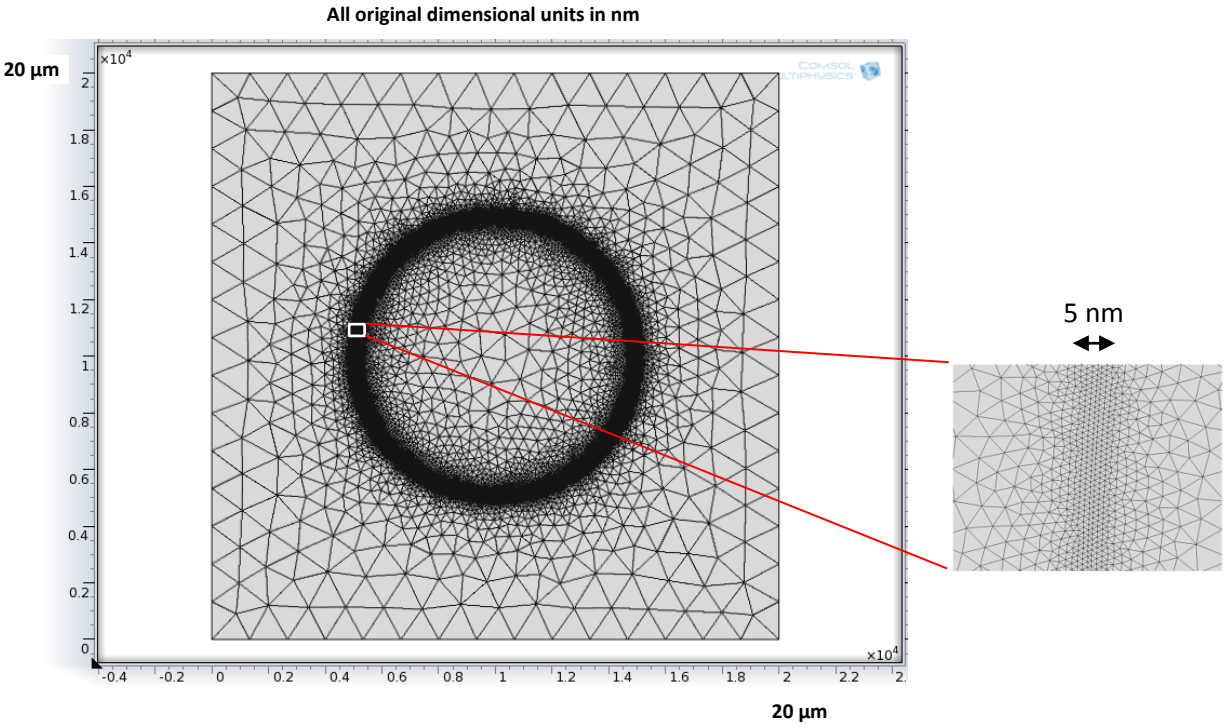

Figure A.1. A plot of a two-dimensional model showing meshing of a central cross section of a single spherical cell suspended in a medium. The vertical side boundaries are a highly conductive set of electrodes (effectively parallel plates). The image on the right is a zoomed in area indicated on the left membrane (white rectangle). Note the unit multipliers given in the corners are in nm. The cell has a diameter of 10 µm and a membrane thickness of 5 nm.

A surface FEA plot is presented in figure A.2 after a short interval, having applied a stepped ramp.

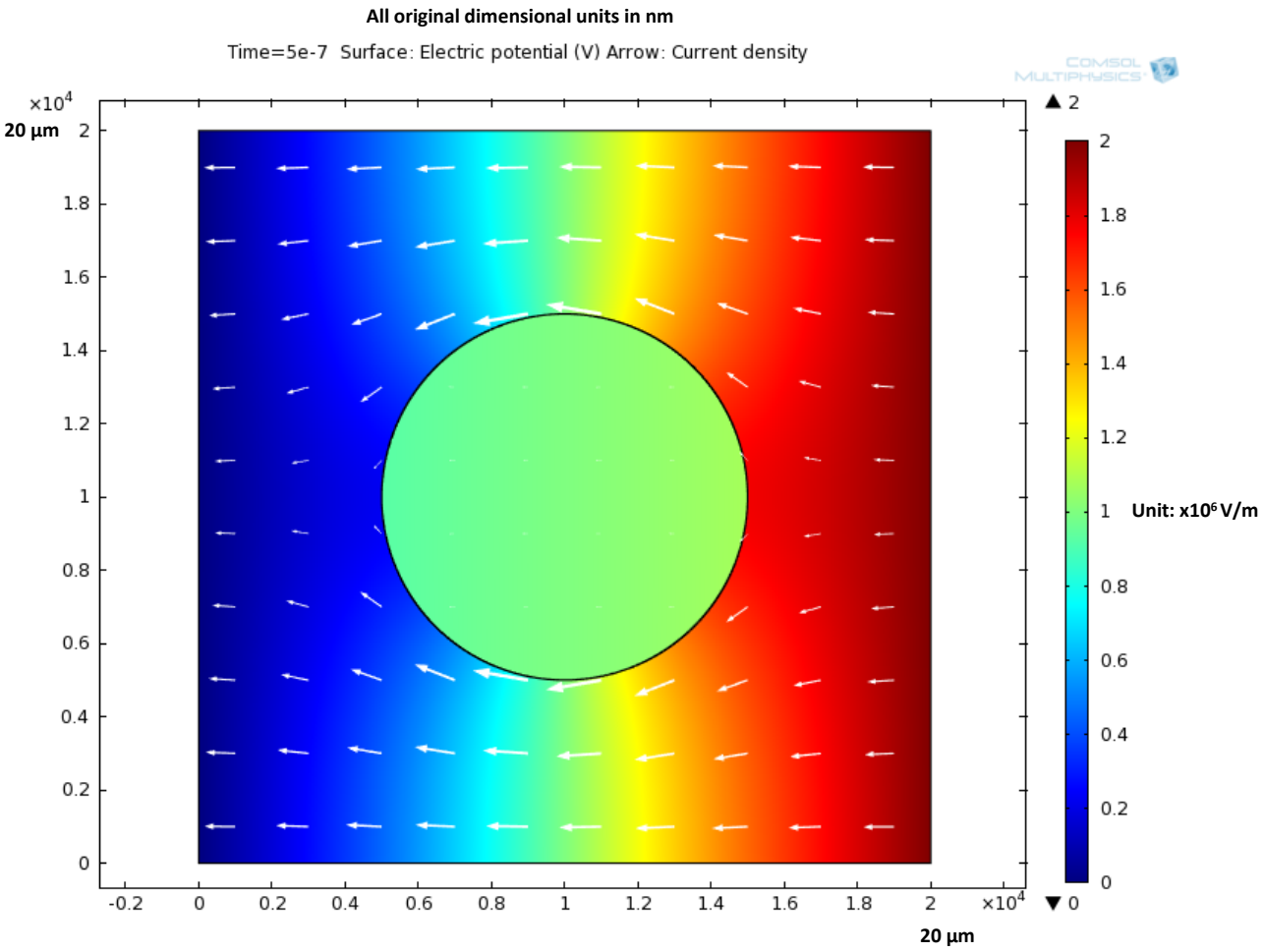

Figure A.2. A two-dimensional COMSOL finite element analysis (FEA) model of a central cross section of a single spherical cell in low conductivity medium after 500 ns, having been exposed to a stepped ramp potential difference across the electrodes. The ramp potential can be expressed as $u(t) = at$, is clamped at 2 V, and is applied on the right side while the left side is maintained at zero. The ramp slope, a, is 50 x 10^6 V/s, essentially reaching 2 V in 40 ns then maintained at 2 V, and represents the proportional potential difference pulses applied to the electroporator chamber when set to 1 x 10^5 V/m. The arrows represent proportional current density and direction. This image is after the point where the electric field and current density have become static.

Figures A.1 and A.2 show the model, its meshing, and electrical behaviour of a central cross section of a spherical cell in a low conductivity medium. A sequence of images is offered in figure A.3, showing the transient response. Figure A.1 shows meshing forming very small triangular elements in the region of the membrane. Figure A.2 shows several interesting aspects. The red on the far right is a potential of 2 V and the dark blue on the far left is a potential of 0 V. In-between there is a gradual transition of potentials, but this pattern is distorted by the presence of the cell. Clearly seen here is the very consistent potential inside the cell (same colour throughout equal to

1 V) – this can be explained by the relatively high conductivity inside the cell, and this explains the "warping" of the potential field occurring outside the cell since the potential drop across its width is negligible. In terms of the proportional and directional current density arrows it is also clear that there is little or negligible current flowing inside the cell at this point in time.

However, this is quite different from the rapid changes seen at the onset of the ramped potential applied as seen in figure A.3. Also, the current is diverted around the cell, with an almost imperceptible amount still penetrating the cell. The sequence in figure A.3 demonstrates an initial capacitive coupling right through the cell (behaves like an extension of the external media) with an apparent parallel field, but as time progresses this field becomes increasingly warped due to the DC blocking nature of the non-conducting capacitive membrane, and when the current is diverted around the cell.

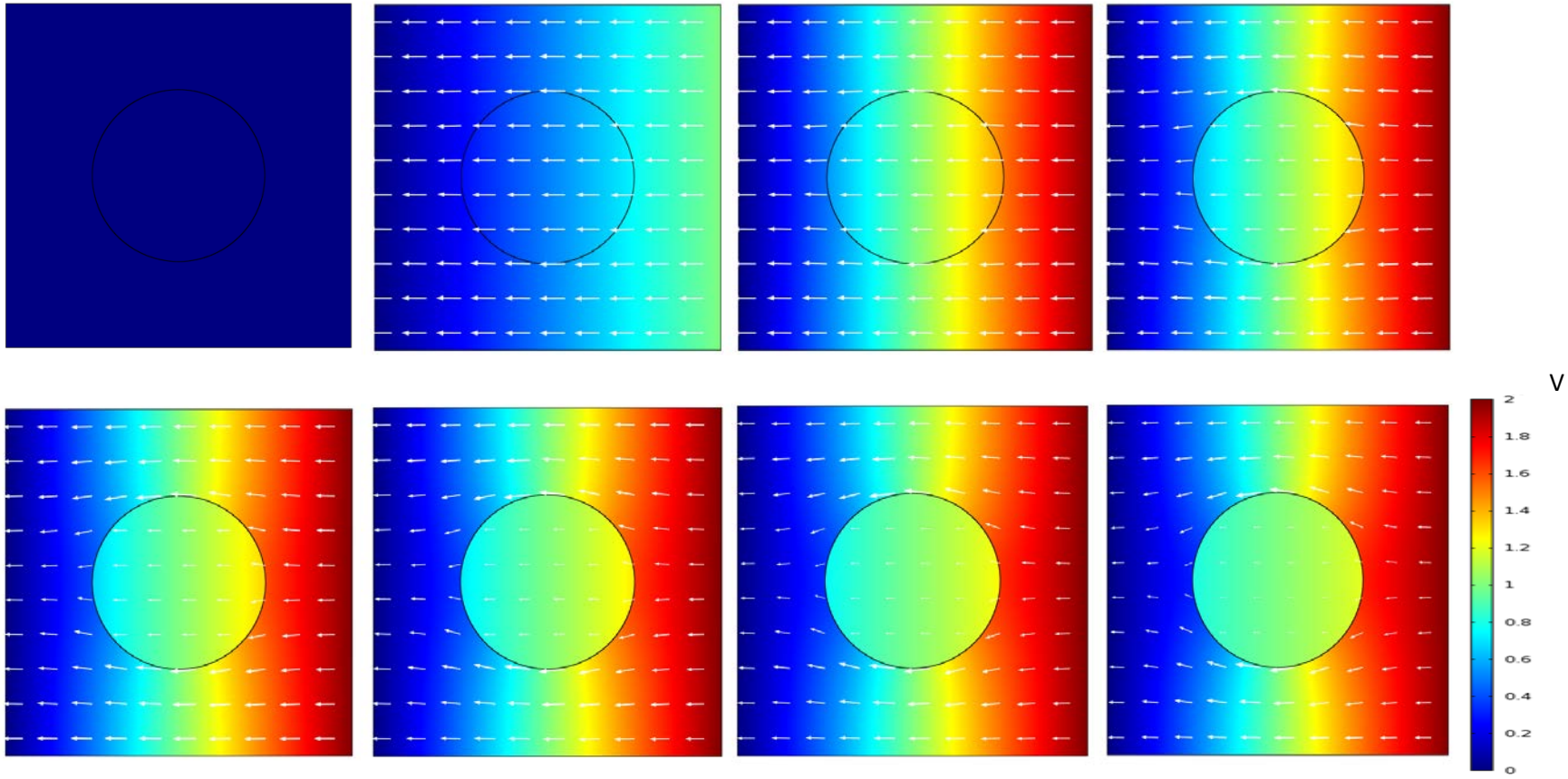

Figure A.3. Sequence of 8 plots showing time evolution of electric potential and current density in and around a cell model when applying a ramped step voltage ($v(t) = at$, with slope a = 2V/40ns, peaking at 2 V) and analysing it at instants t = 0, 20, 40, 80, 120, 160, 200, 250 ns, from top left to right followed by bottom left to right, respectively. This set of plots has been provided to show the rapid initial transition. The plot colour represents electric potential (voltage) – see the colour scale on the right. Arrows represent current density J, with arrow size and direction indicative of current magnitude and direction.

It is not worth showing the electric field colour map for the typical geometries used above as the ratio of membrane thickness to cell diameter of 1:4000 for the model renders large fields existing inside the membrane unobservable from an overall point of view. A much larger ratio of 1:20 was chosen for maximised elucidation. Although this is not to scale, it helps in qualitative assessment.

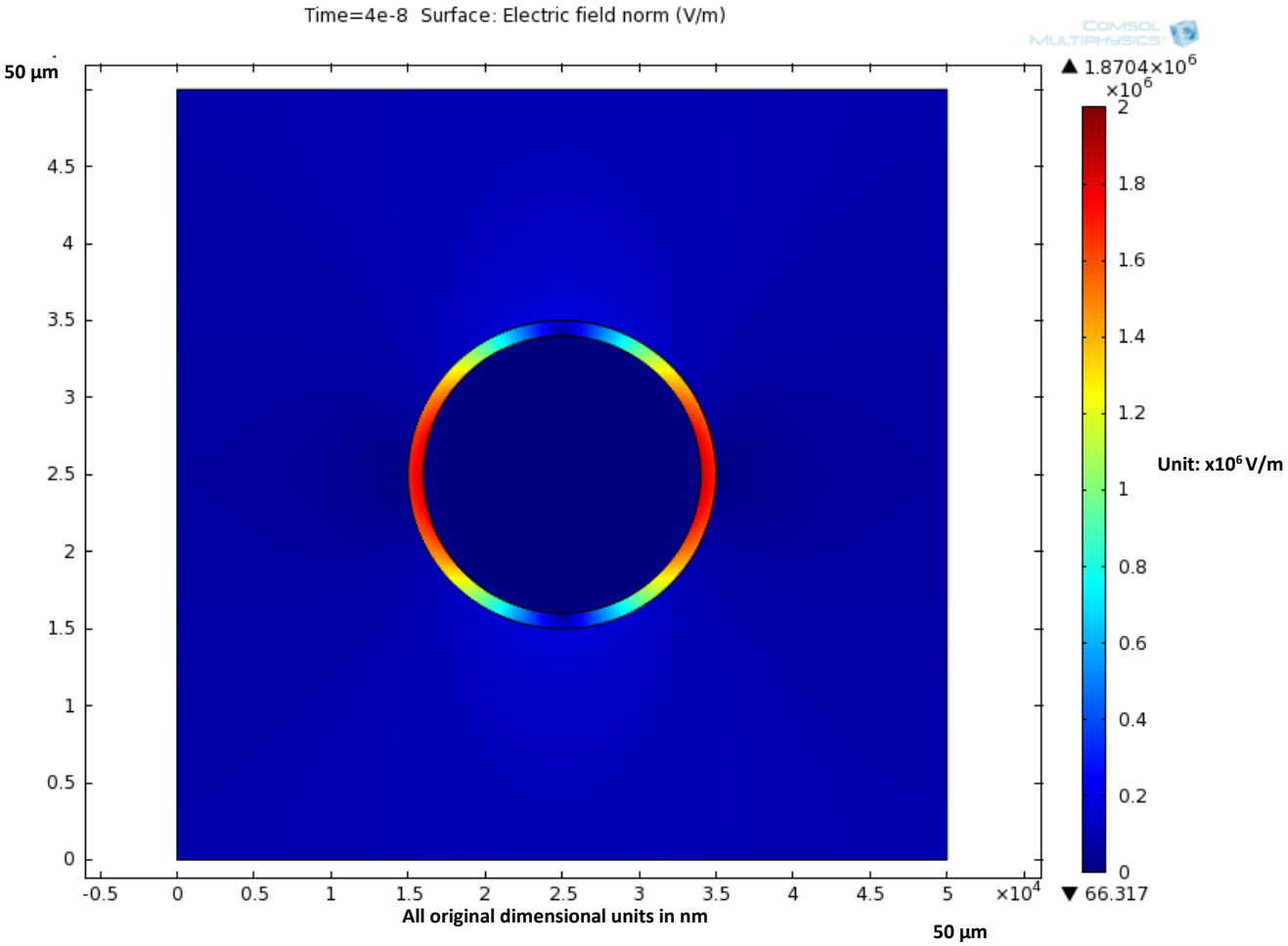

Figure A.4. A two-dimensional static COMSOL finite element analysis (FEA) image of a central cross section of a single cell in an aqueous suspension. The electrodes are parallel plates that extend on the lateral vertical sides of the blue "block". The cell has a diameter of 20 µm and has a membrane thickness of 1 µm. Parameters of the membrane and inner and outer solutions are stated in table A.1.

In figure A.4 a DC potential difference of 5 V was applied across the electrodes on the left and right sides for a typical 1 x 10^5 V/m applied field. Despite the ratio reduction the model still demonstrates the relative quantitative effects that convey a good qualitative understanding of the electric fields and potentials in and around the cell. Clearly the lateral poles of the cell facing the electrodes are greatly stressed by a strong electric field inside the membrane of about 1.8 x 10^6 V/m or 1.8 V across the thickness of the membrane. This effect diminishes towards the "equatorial" regions (top and bottom), becoming zero on top and on the bottom. This is consistent

with the theory described in chapter 2, which suggests a cosine effect as a function of angle with respect to the central horizontal cross section of the cell. The media in and outside the cell are reasonably conductive explaining the low field value throughout their bulk. Note the strong symmetry — this is not normally the case for a monopolar applied potential difference, due to the resting potential of approximately -70 mV of the inside with respect to the outside of the cell [13]. This natural resting potential will skew the fields inside the membrane aiding the side facing the positive electrode (anode) and diminishing the field by the same amount on the cathode side.

A.3 Modelling of Packed Cells

An attempt was made to emulate tissue by placing "spherical cells" in close proximity, without using interconnecting channels such as gap junctions. Gap junctions are special tube-like channels that promote communication between neighbour cells as they allow cytoplasm of the two cells to be in direct contact [14]. This can be advantageous or disadvantageous — these channels aid cell-to-cell communication which assists in more rapid signalling for normal growth and repair [15], but also allow neighbouring cells to suffer disease in the so-called *bystander effect* [16]. It has been shown that cancer cells often have compromised or reduced gap junctions [17]. A lack of gap junctions in cancer cells may be argued to protect them in the event of neighbour cancer cells being loaded with toxins like chemotherapeutic drugs, acting in a way as a buffer or isolator. However, less gap junctions might favour electroporation as each cell remains more isolated from its neighbours thus developing higher transmembrane potentials that ultimately lead to poration.

Clusters of cells are modelled in close proximity and the effect of applied DC potentials across the lateral electrodes can be seen. They have all been exposed to a static field of 1×10^5 V/m with the exception of figure A.8 that has been ramped up to 1×10^5 V/m. Using the same parameters as for figure A.4, results are presented in figures A.5 to A.8.

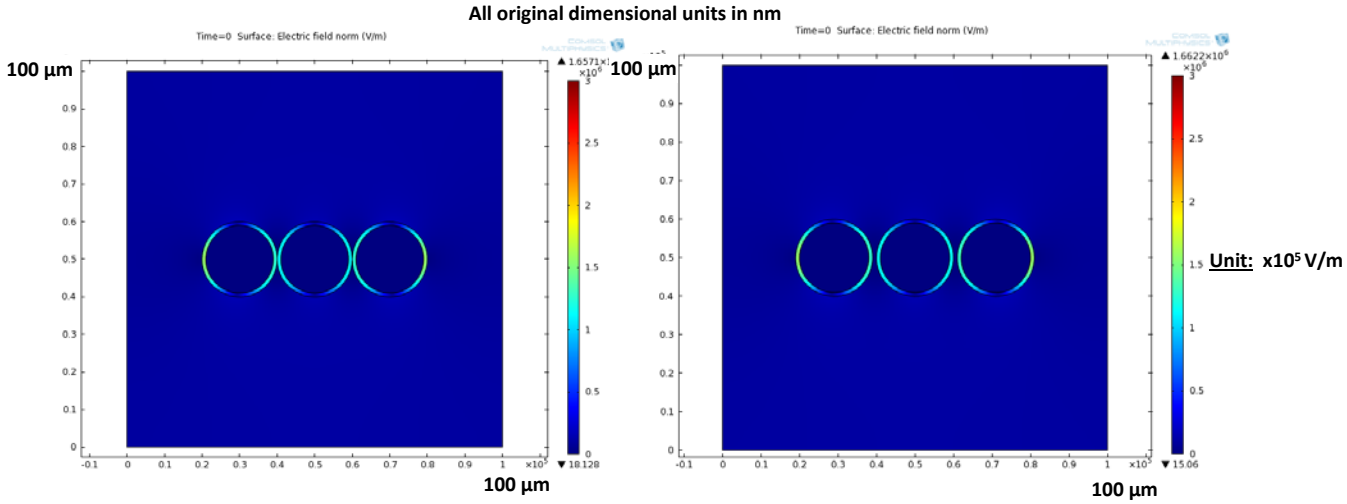

Figure A.5. Linear array of 3 touching cells (left) and lightly packed (right).

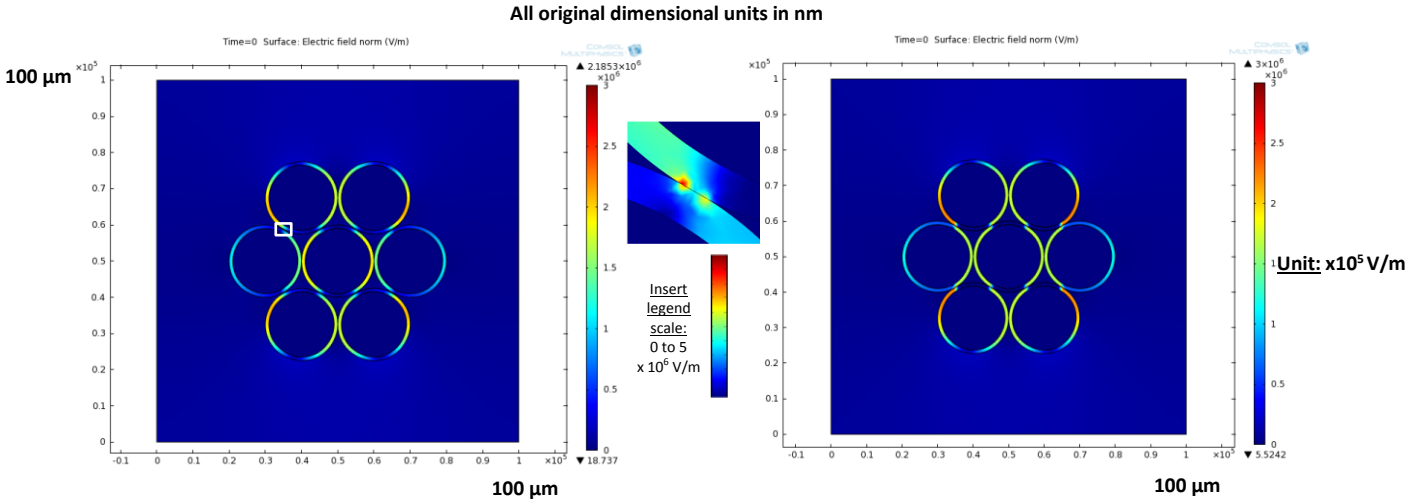

Figure A.6. Cluster of 7 cells tightly packed (left), showing a zoomed area (white rectangle) of interest in the centre. The right shows a slightly less tight formation.

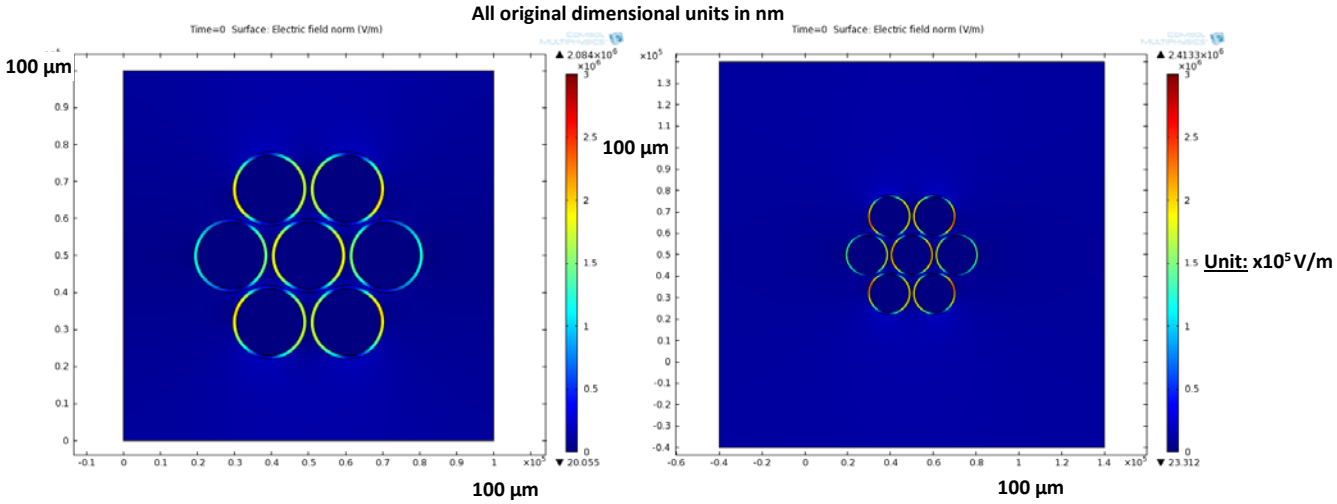

Figure A.7. Cluster of 7 cells lightly packed (left) and for a larger spacing of electrodes (right).

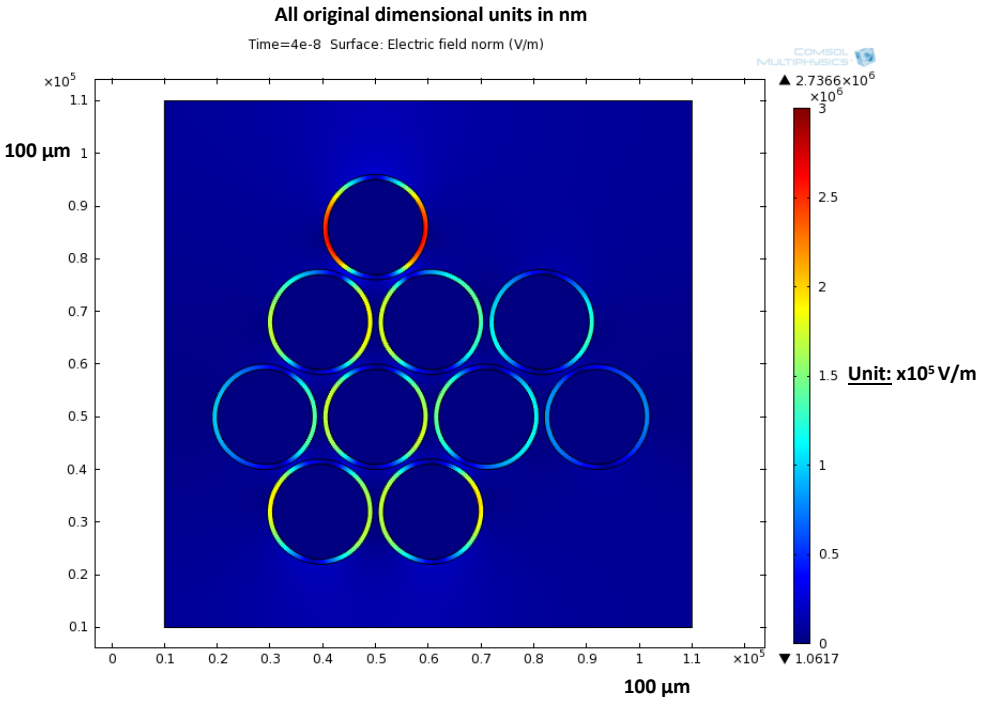

Figure A.8. Odd-shaped cluster of 10 lightly-packed cells – this latter simulation applied a step of 10 Vdc, slew-rate limited at 0.25 V/ns.

In figure A.5 it is evident that with three cells in a row the impact is the greatest on the edge cells facing the electrodes. The behaviour of lightly packed three cells on the right is not substantially different from the tightly packed cells. Between figure A.5 and A.6 there is a clear increase of electric field values, in particular where there is cell contact and where there are more than one row of cells. In figure A.6 the tightly packed cluster of 7 cells is in close agreement with the less tight packed one on the right. Shown in the middle is a zoomed section where there are very small but intense fields generated at the contact points between the neighbouring cells, noting the increased legend scale. The slightly less tightly packed cluster on the right shows more typical behaviour with the top and bottom rows consistent with behaviour in figure A.5, but contrary behaviour is exhibited in the middle row with the central cell being affected the greatest (largest length of membrane at high levels) in the cluster. Also of note is the slight distortion of the effect towards the middle, with the upper and lower rows showing the highest levels slightly "pulled in" towards the centre. In figure A.7 this latter behaviour is continued even though the cells are packed even lighter. The right image shows an increased geometry for the model with very slight differences, validating the smaller set of overall dimensions used (cell dimensions unchanged). In figure A.8 an odd-shaped cluster is shown with behaviour consistent to the shape. As observed also in figure A.7, A.8 exhibits focusing for centrally located cells. Of particular interest in the odd-shaped cluster is the high field exposure of the upper alone-standing cell, which may be explained due to the lack of potential drops along a horizontal line sectioning the top cell.

A study [18] performed numeric modelling of electric field distribution in and around a subcutaneous tumour model. A comparison was made with the tumour modelled as linear (constant tissue conductivity) and non-linear (tissue conductivity dependent on the electric field) and these were compared with *in vivo* measurements. The non-linear model was found to be more consistent with experimental data, suggesting a dependence on the electric field.

Taken together, these aspects demonstrate just how complex the fields become as they are perturbed in complex ways in and around clusters of cells.

A.4 Conclusion

Modelling of a single cell in a suspension has been carried out by several groups internationally where several themes were explored including bipolar *vs* monopolar applied potentials, various waveforms, increased pulsing frequencies, reduced extracellular medium conductivities and pore (area) behaviours. These have shown that bipolar higher frequency pulses, lower extracellular media conductivity and certain waveforms favour electroporation over others, thus improving the outcome.

Modelling of multicellular structures by others all agree that the resultant fields are extremely complex and should be modelled more intensively to better understand how electric fields and potentials are distributed in and around it and what factors may affect them and how. This will become even more complex if the dynamics of electroporation is included.

Numerical modelling in this appendix has demonstrated the general electric field distribution behaviour of suspended cells in a low conductivity medium as being consistent with analytical modelling by others in almost all respects. A sequence of images in time should also provide understanding of the transient nature of a cell being exposed to a ramped input similar to the slew rate from the hardware developed in chapter 3.

It has also been demonstrated here that clusters of cells show very complex behaviours and warrant further exploration and study.

Although modelling generally suffers from large limitations, it can be used to demonstrate several behavioural effects in cells.

A.6 References

[1] S. Talele, et al., "Modelling single cell electroporation with bipolar pulse parameters and dynamic pore radii", *J Electrostat*, Vol. 68, No. 3, pp. 261-174, 2010.

[2] S. Talele, et al., "Modelling single cell electroporation with bipolar pulse: Simulating dependance of electroporated fractional pore area on the bipolar field frequency", in M. Iskander, et al., Eds., *Technological developments in education and automation*, Springer, 2010, pp. 355-359.

[3] S. Talele and P. Gaynor, "Non-linear time domain model of electropermeabilization: Effect of extracellular conductivity and applied electric field parameters". *J Electrostat*, Vol. 66, No. 5-6, pp. 328-334, 2008.

[4] K. A. DeBruin and W. Krassowska, "Modeling Electroporation in a Single Cell. I. Effects of Field Strength and Rest Potential", *Biophys J*, Volume 77, No. 3, pp. 1213-1224, 1999.

[5] W. Krassowska and P. D. Filev, "Modeling Electroporation in a Single Cell*", Biophys J*, Vol. 92, No. 2, pp. 404-417, 2007.

[6] T. R. Gowrishankar and J. C. Weaver, "An approach to electrical modeling of single and multiple cells", *P Natl Acad Sci USA*, Vol. 100, No. 6, pp. 3203-3208, 2003.

[7] C. B. Arena, et al., "Theoretical Considerations of Tissue Electroporation With High-Frequency Bipolar Pulses", *IEEE Trans Biomed Eng*, Vol. 58, No. 5, pp. 1474-1482, 2011.

[8] M. Pavlin, N. Pavselj and D. Miklavcic , "Dependence of Induced Transmembrane Potential on Cell Density, Arrangement, and Cell Position Inside a Cell System", *IEEE Trans Biomed Eng*, Vol. 49, No. 6, pp. 605-612, 2002.

[9] E. C. Fear and M. A. Stuchly, "Modeling assemblies of biological cells exposed to electric fields", *IEEE Trans Biomed Eng*, Vol. 45, No. 10, pp. 1259-1271, 1998.

[10] T. Kotnik, D. Miklavcic and T. Slivnik, "Time course of transmembrane voltage induced by time-varying electric fields: a method for theoretical analysis and its application", *Bioelectroch Bioener*, Vol. 45, No. 1, pp. 3-16, 1998.

[11] T. Kotnik and D. Miklavcic, "Theoretical evaluation of the distributed power dissipation in biological cells exposed to electric fields", *Bioelectromagnetics*, Vol. 21, No. pp. 385-394, 2000.

[12] COMSOL, “Chapter 4 – The electric field interfaces”, in *AC/DC Module User’s Guide*, COMSOL 4.2, pp. 97-162, 2001, OnLine. Available: http://www.mht.bme.hu/~bilicz/oktatas/mezoszim/ACDCModuleUsersGuide.pdf

[13] T. Kotnik, et al., “Cell membrane electropermeabilization by symmetrical bipolar rectangular pulses - Part I. Increased efficiency of permeabilisation”, *Bioelectrochemistry*, Vol. 54, No. 1, pp. 83–90, 2001.

[14] K. Willecke, et al., “Structural and Functional Diversity of Connexin Genes in the Mouse and Human Genome”, *Biol Chem*, Vol. 383, No.5, pp. 725-737, 2005.

[15] W. L. Bi, et al., "In vitro evidence that metabolic cooperation is responsible for the bystander effect observed with HSV tk retroviral gene therapy", *Hum Gene Ther*, Vol. 4, No. 6, pp. 725-731, 1993.

[16] H. P. Ehrlich and T. Diez, "Role for gap junctional intercellular communications in wound repair". *Wound Repair Regen*, Vol. 11, No. 6, pp. 481-9, 2003.

[17] C. M. Corsaro and B. R. Migeon, “Comparison of Contact-Mediated Communication in Normal and Transformed Human Cells in Culture”, *P Natl Acad Sci USA*, Vol. 74, No.10, pp. 4476-4480, 1977.

[18] S. Corovic, et al., “Modeling of electric field distribution in tissues during electroporation”, *BioMedical Engineering OnLine*, Vol. 12, No. 16, pp. 1-26, 2013, http://www.biomedical-engineering-online.com/content/12/1/16

APPENDIX B

BASIC INTRODUCTION TO MULTILEVEL INVERTERS (MLIs) INCLUDING CLASSIFICATION

B.0 Introduction

A good introduction to multilevel inverters (MLIs) is available from [1], in particular from its Chapter 9. This summary below draws liberally from that text.

Where a direct current (DC) voltage needs to be converted to an alternating current (AC) voltage – a process known as inversion – such as in converting renewable DC sources like photovoltaic (solar) or fuel cells to AC for connection to an AC grid, or such as in motor drives where a DC (or even an AC but then rectified to DC) source is used to drive an AC motor, a "two-level" inverter would only just serve the purpose, as it provides a very crude AC consisting of maximally 3 levels (0 V and $\pm V_{\mathrm{dc}}$). This results in substantial ripple or harmonic content which may cause electromagnetic compatibility (EMC) and other problems. MLIs can substantially improve on this situation by adding more levels, thus providing a closer approximation to a sinusoidal wave, thus reducing harmonic content significantly. Another advantage is that the switching devices used, such as metal-oxide silicon field effect transistors (MOSFETs) or insulated gate bipolar transistors (IGBTs), may be configured so that they share voltage stresses as they would then be effectively connected in cascade, resulting in handling only a fraction of the output voltage each. This allows the use of such switching devices for the generation of outputs of substantially above a thousand volts, not possible otherwise using solid state devices. If required, current handling capacity of these switches can be increased by connecting these switches in parallel.

In simple terms, an MLI is configured in such a way that it adds (then subtracts) separate voltages sequentially to build up a "staircase-like" output voltage that approaches a sine wave.

MLIs can be classified into three main types [2]:

- Diode-clamped MLIs;
- Flying-capacitor MLIs; and
- Cascaded MLIs.

B.1 The diode-clamped MLI

A diode-clamped MLI uses an ingenious arrangement of a string of series-connected voltage "storage" capacitors across a DC bus, connected via an arrangement of clamping or "directing" diodes to a string of series-connected switching devices such as silicon controlled rectifiers (SCRs).

Disadvantages of the diode-clamped MLI include:

- Very high number of diodes required for high number of levels; and
- Difficulty of controlling the flow of real power of individual converters in multi-converter systems (this may not be apparent in the brief description above, but it is associated with the unbalance of capacitor voltages).

B.2 The flying-capacitor MLI

A flying-capacitor MLI uses an arrangement where, instead of a multitude of diodes as in the clamped-diode MLI, a multitude of capacitors is used. It is also a slightly simpler circuit than the diode-clamped MLI.

Disadvantages of the flying capacitor MLI include:

- Requires excessive number of capacitors at high levels – becomes bulky and expensive;
- Inverter control may be quite complex; and
- Switching losses may be high.

B.3 The cascaded MLI and its basic operation

Although there are several subtypes of cascaded MLIs (see appendix C) this section will focus on the basic type. Two full H-bridges (comprising four N-channel MOSFETs) are configured as shown below in figure 3. The bridges are denoted as B1 and B2. In the example below, each bridge is separately supplied by a 1000 V DC supply, and is connected to another bridge in such a way that the voltages are superposed on each other to produce a quasi-sine wave. This is common practice for designs of inverters that produce AC from DC and also for motor drives. A smoother quasi-sine wave can be generated using more stages of H-bridges in cascade thus making a longer chain.

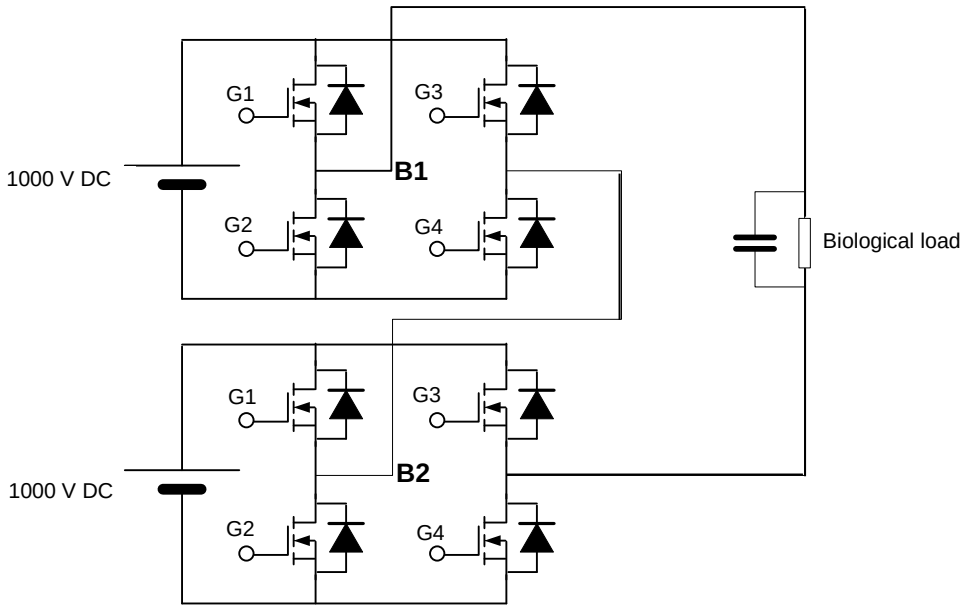

Figure B.1. Basic topology of a 5-level cascaded MLI using two H-bridges and driving a typical biological load.

The gates must be driven by a special sequence of pulses, all of length of 180^{o} (π radians) of the full cycle [1]. The timing diagram for the gate pulses together with the effective outputs of each bridge and the ultimate output voltage is shown below. Each device in the vertical pairs of the bridges is operated at the logic inverse, thus the gates are driven in logic opposition. For example, when G1 is driven high, G2 will be driven low, and *vice versa*. For the sake of simplicity only the upper devices will be mentioned. Gates are denoted as "Gx" where x defines its position.

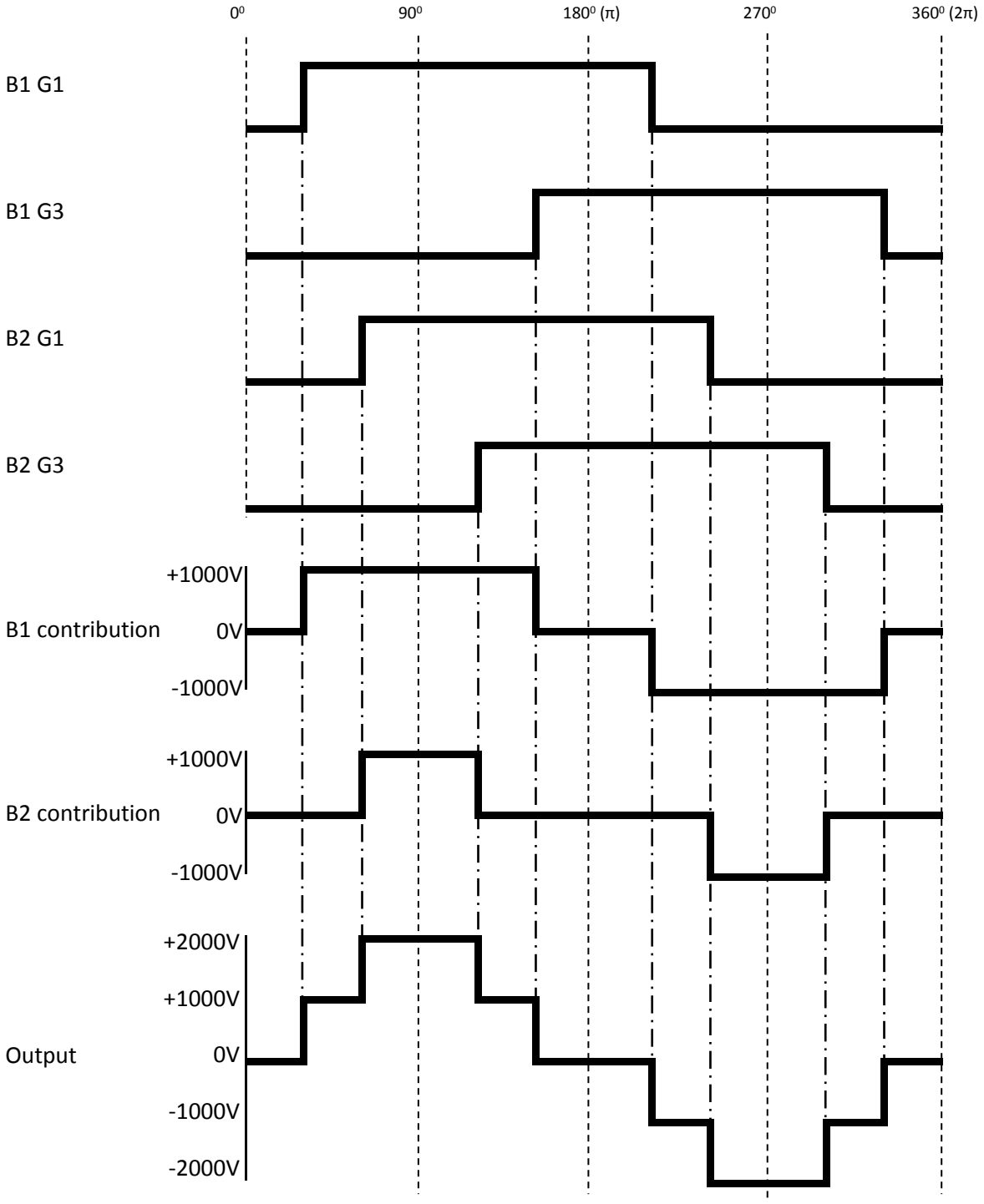

Figure B.2. Timing diagram for the basic 5-level cascaded MLI.

For the sake of demonstrating the basic sequence, the illustration in figure B.2 above uses uniform spacing throughout. Note that the lower switching MOSFETs of each vertical half bridge in each H-bridge is not shown in the timing diagram, and that they are all switched in the logic inverse of the upper (shown) switches.

Operation of this cascaded MLI is as follows (M# is associated with the relevant MOSFET taking the same number as its gate)(ideally the timing and schematic diagrams should be viewed side by side):

Step 1: When B1 M1 turns on, B1 M2 is turned off. Current from the upper bridge source is shunted through B1 M1 to the upper load lead, through the load, through B2 M4 (turned on), up through B2 M2, through the bridge interconnection, down through B1 M4, and finally returned to the upper bridge source. All other paths are disabled during this interval. It generates 1000 V across the load.

Step 2: The next event is signalled by B2 M1, which, when turned on, B2 M2 is turned off, so alters the current path at the bottom bridge to pass instead through its source and return along the upper MOSFET B2 M1 via the interconnection, to B1's source as before, effectively switching the two sources in series, thus producing 2000 V across the load.

Step 3: The next event is signalled by B2 M3, shunting current in B2 through both upper MOSFETs, effectively bypassing B2's source, thus output voltage will drop back to 1000 V, and so on.

In short, the upper bridge, B1, contributes by providing the first 1000 V, bipolarly switched, thus providing +1000 V and -1000 V pulses. During these pulses, B2 contributes the shorter pulses of an additional 1000 V either way. These contributions are summed to provide the total output voltage.

Finally, note that the timing diagrams also cannot show the dead time — a short interval that allows the lower MOSFET to be turned off before the upper one is turned on — to avoid the possibility of simultaneous conduction of the upper and lower MOSFET known as shoot-through.

The maximum voltage that each single device in each bridge must tolerate is the applied voltage across that bridge, in this example 1000 V.

A notable difference between this MLI and the previous two is that it is the only one shown using transistors as the switching devices. (This does however not preclude these previous two types from the use of transistors instead of silicon controlled rectifiers (SCRs)). This type of MLI can

produce a bipolar range of m levels using zero capacitors, $2(m - 1)$ switching devices and zero diodes. Clearly this topology has an advantage in the sheer economy of components needed.

Features of the cascaded MLI include [1]:

- Separate DC sources are required, particularly if real power is to be generated. This lends itself very well to renewable energy sources;
- For back-to-back converters it is not recommended to switch the two dc sources in series as this may result in a short-circuit if the synchronisation is not perfect.

Advantages of the cascaded MLI include:

- It requires the smallest number of components for the same number of output levels, compared to the diode-clamped and the flying-capacitor MLIs;
- It lends itself very well to packaging optimisation in terms of modular design (due to its "daisy-chaining" ability) and also due to the lack of clamping diodes and capacitors;
- As it uses IGBTs or MOSFETs it is possible to use soft-switching techniques for reduction in device stress and enhancement of sinusoidal waves (reduction of harmonics); and
- All MOSFETs (or whatever switching devices are used) equally share the burden of carrying current for equal intervals due to the square wave nature (approximately 50 % duty cycle) of their operation [1].

The major disadvantage is:

- For the conversion of real power it needs separate isolated DC sources – this limits its range of applications.

B.4 References

[1] M. H. Rashid, *Power electronics: circuits, devices, and applications*, 3rd ed., Upper Saddle River, NJ, Pearson/Prentice Hall, 2004, pp. 417-422.

[2] J.-S. Lai and F. Z. Peng, "Multilevel converters - a new breed of power converters," *IEEE Transactions on Industry Applications*, vol. 32, pp. 509-517, 1996.

APPENDIX C

SCHEMATIC DIAGRAMS OF THE ELECTROPORATOR AND THE RADIO FREQUENCY ABLATOR CIRCUITS

ELECTROPORATOR SIGNALS SCHEMATICS SHEET

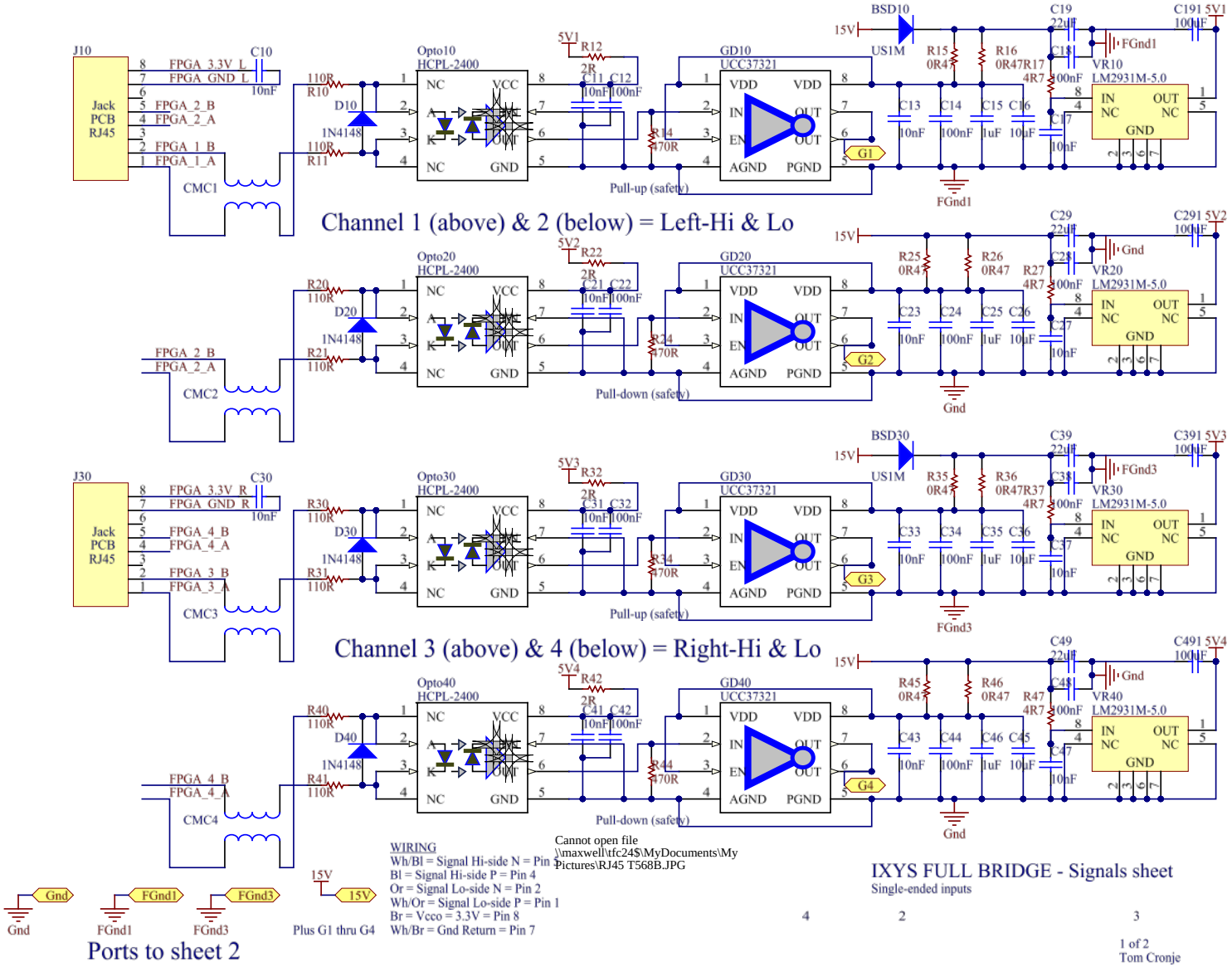

ELECTROPORATOR POWER SCHEMATICS SHEET

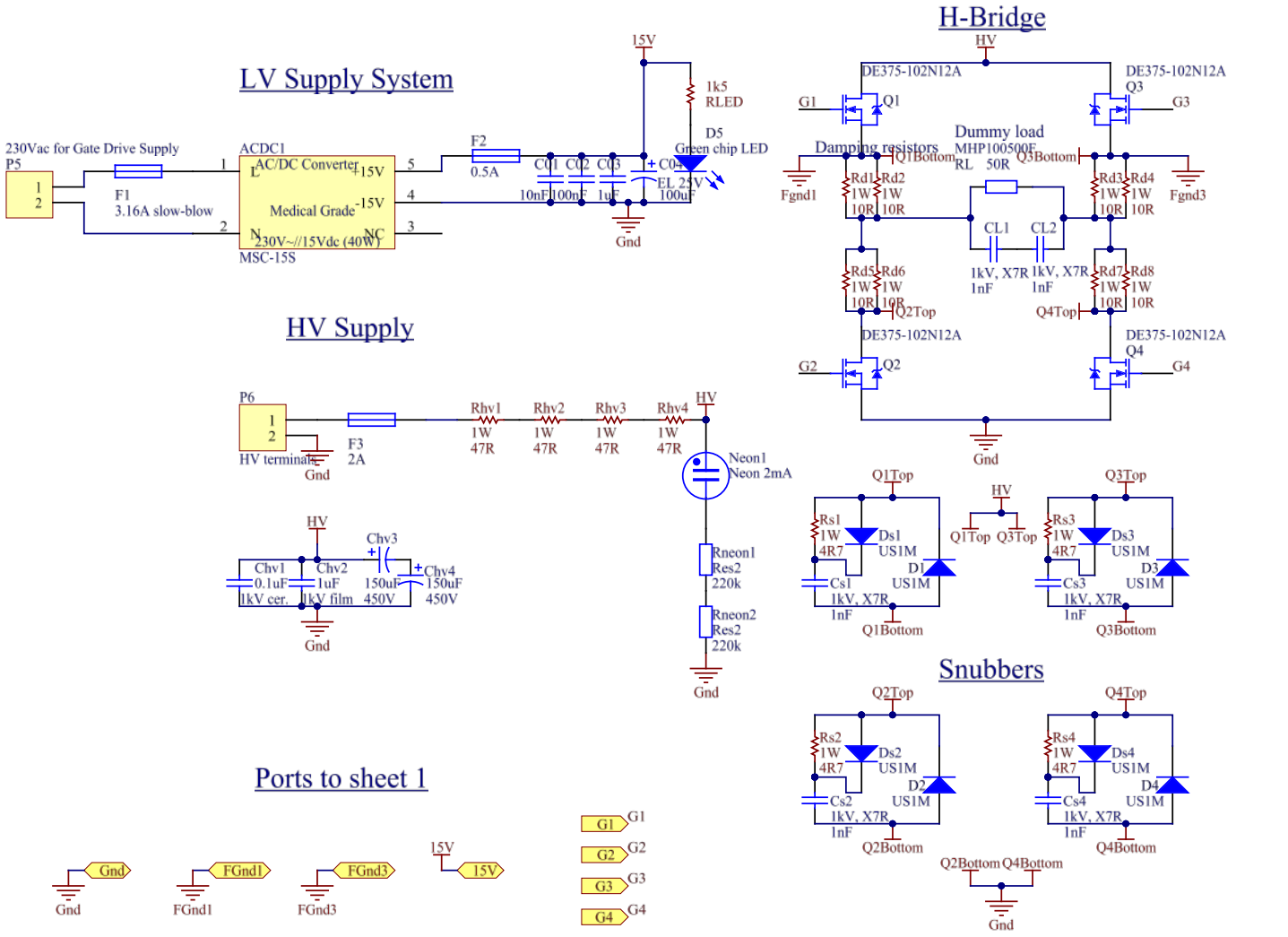

RADIO FREQUENCY ABLATOR (RFA) SCHEMATICS

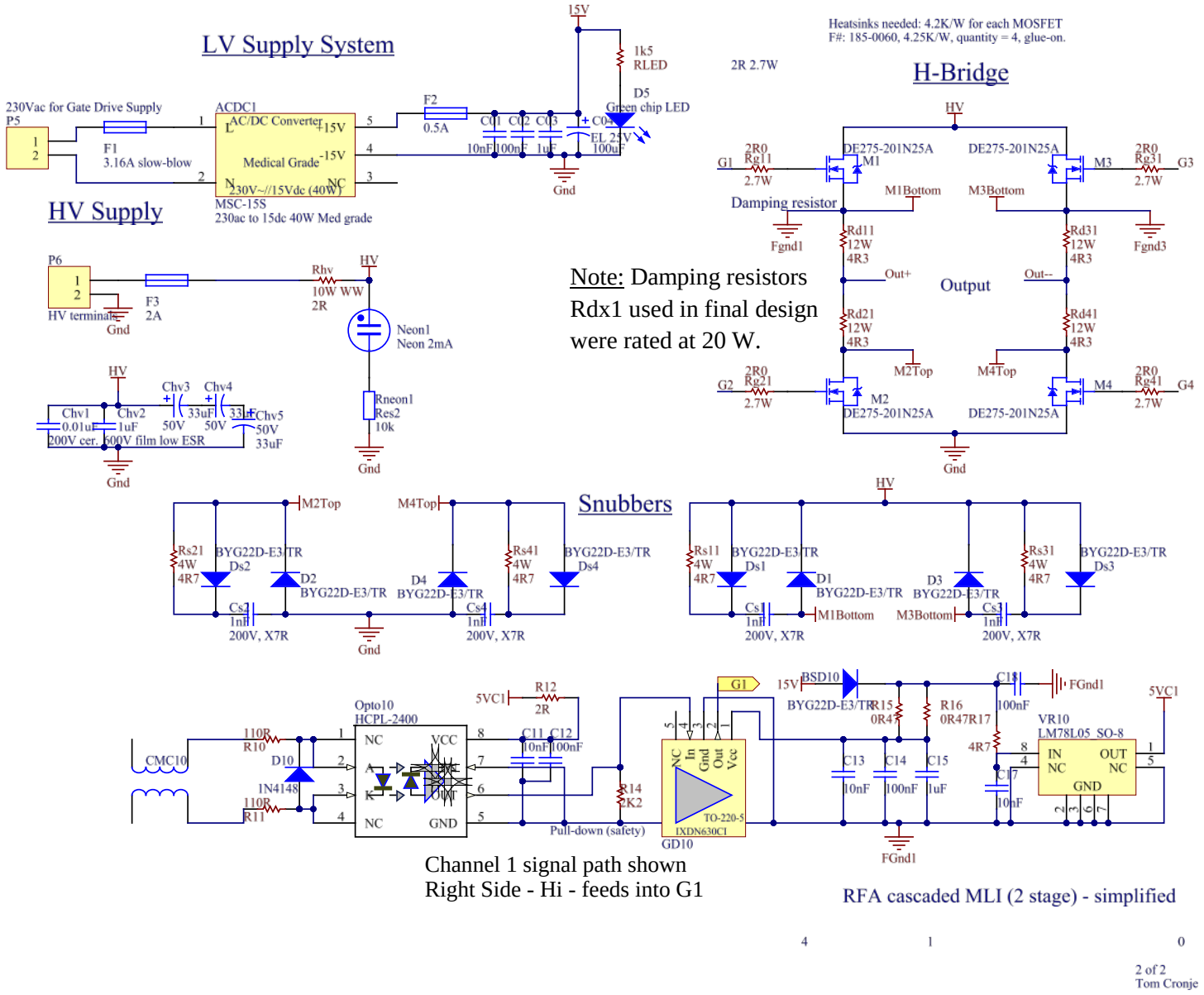

APPENDIX D

PROLIFERATION OF MULTILEVEL INVERTER TOPOLOGIES IN THE EARLY 2000'S

D.0 Introduction

Since the early 1980's, publications on solid-state multilevel inverters have seen the light [1, 2]. However, it has only been since the late 90's that there appears to have been a renewed (perhaps more academic) interest in this useful type of inverter. These were mainly attempts at improving the topology by bringing about advantage(s) such as reduction in components per output level to reduce cost and increase reliability, or improvement in reduction of output harmonics. As noted before – see the basic introduction to MLIs – multilevel inverters (MLIs) essentially share the high voltage between several switching devices enabling the generation of high alternating current (AC) voltages using lower voltage rated switching devices. This practice becomes essential for output voltages above 1000V as this voltage represents a practical limit.

From a range of publications reviewed, it appears that the field of MLIs has enjoyed a *renaissance* in the early 2000's starting in 2002 [3]. This "renewal" has continued until at least 2006 and includes at least 10 significant papers. These papers can be classified into five subtypes, mainly falling within the cascaded MLI types.

D.1 Cascaded MLI types

The first group of papers [3-5] have treated and analysed a topology using trinary sources, e.g. 1V, 3V and 9V. These devices are also referred to as hybrid cascade MLIs. The sources have then been ingeniously added or subtracted to give a large number of discrete output voltages utilising the different combinations and using few sources in an attempt to minimise harmonics – as the intention is to generate a quasi-sine wave. This group appears to be the first "attempt" at "breaking away" from the idea of using similar valued sources. A more refined approach [6] of the trinary group followed 2 years later where a high-speed bridge had been employed together with other normal bridges bringing about significant improvement in general performance. This subtype may not be useful in applications of renewable energy such as photovoltaic or fuel cells or any collection of sources/cells that produce a similar direct current (DC) voltage. An example is shown in figure D.1. Note that the DC sources follow a trinary sequence of values.

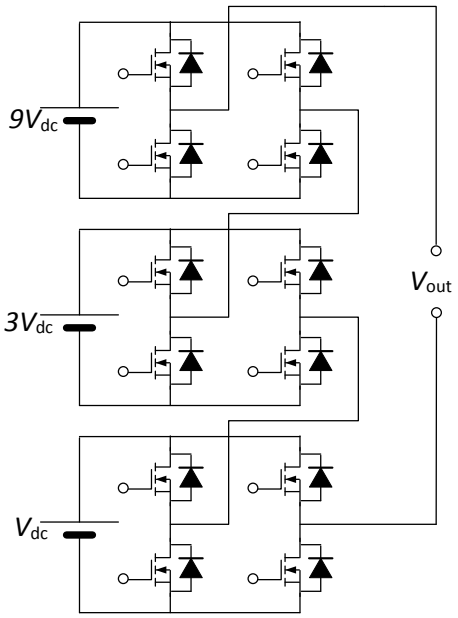

Figure D.1. The trinary sourced cascaded MLI topology [6].

The second subtype appears to originate from a single paper with an application into induction heating [7]. This is an interesting deviation from the norm in that it treated a solid-state version of a Marx generator. The original Marx generator was developed in 1924 by Erwin Marx and works by charging a bank of capacitors in parallel, then by switching them in series to provide a higher voltage. This basic idea is also used quite commonly in switched capacitor or "charge-pump" power supplies. The original generator used spark gaps or Avalanche devices which were not controllable such as solid-state switches (or for that matter evacuated tube triodes, which only became available later). The "attraction" of this "Marx inverter" – coined in the paper [7] – is mainly its economy in the use of switching devices. An example of this topology is shown in figure D.2 below. The "standard" cascaded MLI uses roughly 2 devices per voltage level whereas the Marx inverter uses approximately 1½ devices per voltage level – that is when the output stage comprising the right-most two MOSFETs is replaced by a full bridge of four MOSFETs, then providing seven levels from 10 devices, with every couple of additional levels requiring an additional three devices and a capacitor.

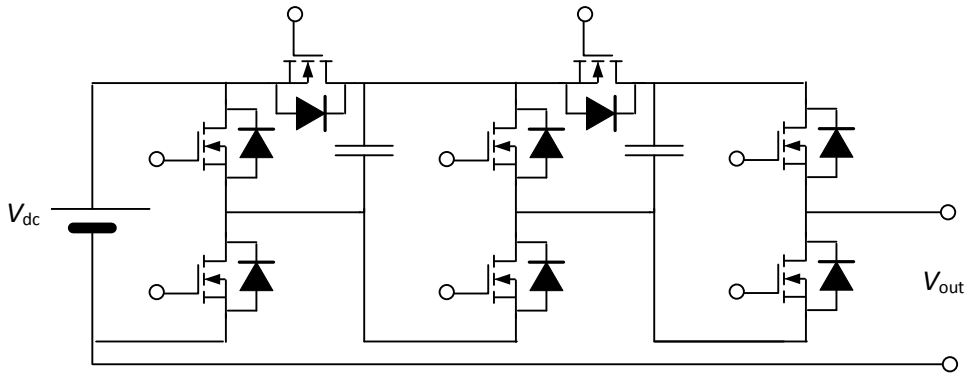

Figure D.2. The Marx inverter MLI topology [7].

The third subtype of cascaded MLI is not a cascaded MLI in the true sense. Three papers [8-10] treated a special arrangement of an H-bridge with an additional bidirectional switch inserted between one of its outputs and connected on the other side to the mid-point "suspended" between two series capacitors that are connected across the power supply rails. See figure D.3 below for the topology. In addition, this MLI includes the use of modulation within the period of switch-on of each switching device, effectively extending its range (number) of in-between values or levels. The first paper here proposed this new topology and validated it through simulation and physical testing. It concluded by proposing a further extension of this circuit to provide any number of output levels by merely adding more capacitors and bidirectional switches. The next paper [9] treated an application using a transformer in a high-frequency link. The last paper [10] again established the position of this subtype of MLI in terms of its low component count, claimed as the lowest.

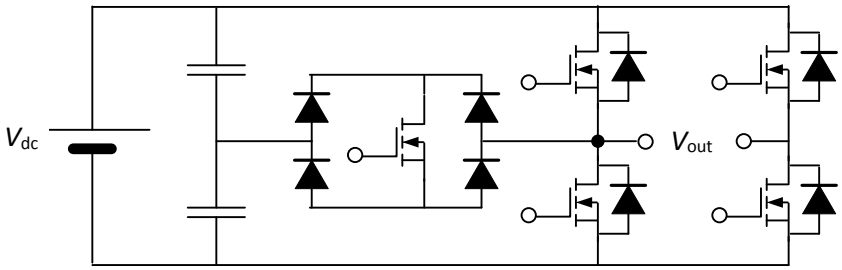

Figure D.3. The bridge and bidirectional switch type MLI topology [8-10].

The fourth subtype of MLI is a variation of the cascaded H-bridge MLI that instead uses additional capacitors (and not power sources) to increase its number of levels [11]. This technique is interesting in that it can generate a voltage of nearly up to twice the power source voltage, but the author considers this as not a significant gain (in reducing components) as the added capacitor(s) need to be charged by additional circuitry not shown, essentially making each an independent power supply with adequate smoothing capacitance. An example is shown in figure D.4 below.

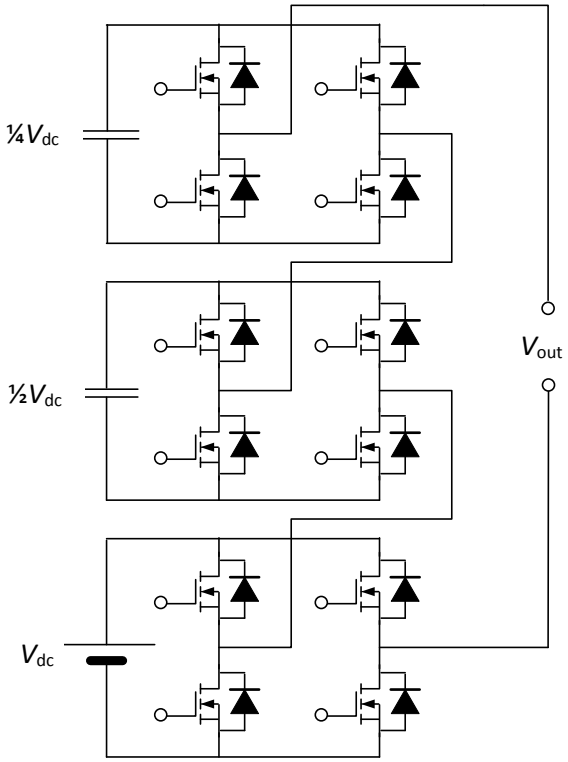

Figure D.4. The "doubler" cascaded MLI topology [11].

The final subtype in this discussion comprises a general cascaded MLI using only one single power source and several capacitors – that is one capacitor with each additional H-bridge [12]. This new topology has been shown to self-balance the capacitors and can be used in single directional mode (for a normal passive load) or in bidirectional mode where the load could become either passive or regenerative. The particular "attraction" of this latest topology is that it acts successfully as a voltage multiplier and can produce an output AC voltage of several times the input DC supply voltage. An example is shown in figure D.5 below.

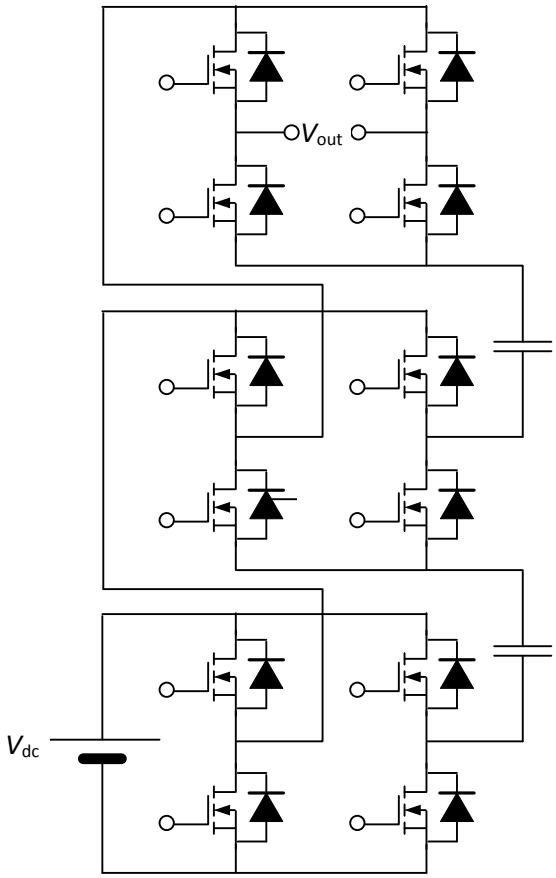

Figure D.5. The single-source capacitor self-balancing cascaded MLI topology [12].

D.2 References

[1] A. Nabae, I. Takahashi and H. Akagi, "New Neutral-Point-Clamped PWM Inverter," *Conference Record - IAS Annual Meeting (IEEE Industry Applications Society)*, pp. 761-766, 1980.

[2] P. M. Bhagwat and V. R. Stefanovic, "Generalized Structure of a Multilevel PWM Inverter," *IEEE Transactions on Industry Applications*, Vol. IA-19, pp. 1057-1069, 1983.

[3] Y. S. Lai and F. S. Shyu, "New topology for hybrid multilevel inverter," in *Proceedings from Power Electronics, Machines and Drives International Conference,* No. 487, Bath, United Kingdom, 2002.

[4] Z. M. Zhao, et al., "Comparisons of PWM and one-cycle control for power amplifier with multilevel converter," *IEEE Transactions on Industrial Electronics*, Vol. 49, pp. 1342-1344, 2002.

[5] S. Joo, et al., "A novel hybrid multilevel inverter using DC-Link voltage combination," in Proceedings from *IEEE Electron Devices and Solid-State Circuits Conference*, pp. 159-162, 2003.

[6] S. M. Ayob, et al., "A New Hybrid Multilevel Inverter Topology with Harmonics profile improvement," in Proceedings from *International Conference Power Electronics and Drives Systems (PEDS),* Phuket, Thailand, Vol. 2, pp. 999-1002, 2005.

[7] J. I. Rodriguez and S. B. Leeb, "A multilevel inverter topology for inductively-coupled power transfer," *IEEE Transactions on Power Electronics*, Vol. 21 ,No. 6, pp. 1607-1617, 2006.

[8] G. Ceglia, et al., "A new multilevel inverter topology," in *Proceedings of the Fifth IEEE International Caracas Conference on Devices, Circuits and Systems,* Vol. 1, pp. 212-218, 2004.

[9] J. Beristain, et al., "A New Single-Phase HF-Link Multilevel Inverter," in *Proceedings from Power Electronics Specialists Conference, PESC '05, IEEE 36th*, Recife, Brazil, pp. 237-243, 2005.

[10] G. Ceglia, et al., "A New Simplified Multilevel Inverter Topology for DC & AC Conversion," *IEEE Transactions on Power Electronics,* Vol. 21, pp. 1311-1319, 2006.

[11] D. Zhong, et al., "A cascade multilevel inverter using a single DC source," in Proceedings of *Twenty-First Annual IEEE Applied Power Electronics Conference and Exposition, APEC '06,* 2006.

[12] Y. Liu and F. L. Luo, "Multilevel inverter with the ability of self-voltage balancing," *Electric Power Applications, IEE Proceedings*, vol. 153, pp. 105-115, 2006.

APPENDIX E

ELECTROPORATION ASSAY

(APPLICABLE TO FLUORESCENCE MICROSCOPE STUDIES)

1. Harvest cells during late log-phase from monolayer culture in 25 cm^2 flask, re-suspending them in warm growth medium (DMEM/F12 + 10 % foetal bovine serum (FBS) + 1 % penicillin-streptomycin (PenStrep) + 1 % Glutamax. Appendix D describes the protocol for sub-culturing (or "splitting" of) the Ishikawa cell line, whence cells may be harvested.

2. Set up electroporator for correct electrical regime. Verify using oscilloscope. Note that high conductivity medium (e.g. culture medium or standard phosphate buffered saline (PBS), both around 1.6 S/m) may cause voltage droop due to charge depletion of storage capacitor. This does not happen though when using low conductivity “electroporation buffer” (EPB) – dilute 100% PBS to 1/16.5 conc. then add 1 g sucrose to make up 10.7 mL 1x EPB. When using EPB, ensure that osmolarity is at physiological value of around 290 mOs – this is to avoid undesirable cell shrinkage or swelling that may lyse/kill cells.

3. Double rinse electroporator chambers with double distilled water (d2H_2O). Dry out using compressed N_2 gas. If dirty, use enzyme (trypsin-PBS) or detergent to clean electroporator (particularly electrode) surfaces. Then use alcohol and dry as above.

4. Warm up microscope mercury light source.

5. Make up several numbered test samples of 100 µL in 1.5 mL Eppendorf tubes, of suspended cells (3 x 10^6 cells/mL with viability above 95 % - verify in haemocytometer (H)) in culture medium. Incubate them at 37 ^oC.

6. Centrifuge a sample for 1 minute at 1000 RPM.

7. Discard supernatant, resuspend cells in residual supernatant by vigorous tapping, then add 90 µL of EPB at room temperature (RT). Gently pipette up and down several times to guarantee cells are not in clumps.

8. Add 4 µL propidium iodide fluorescent dye (PI) and disperse/mix thoroughly (using 250 µg/mL conc. for 10 µg/mL final conc.) and agitate gently with pipette to break up any clumps.

9. Incubate at room temperature (RT) for about 2 minutes.

10. Pipette 45 µL aliquot of dyed sample into electroporator chamber as experiment – E.

11. Immediately afterwards pipette another 45 µL aliquot of dyed sample into a dummy chamber as control – C.

12. Immediately electroporate (EP) the E sample while checking oscilloscope to verify correct electrical parameters by capturing the single sequence.

13. As soon as possible, transfer the 45 µL samples from each chamber to marked and pre-warmed Eppendorf tubes.

14. Centrifuge both samples for 1 minute at 1000 RPM. This is to wash dye from around cells for better survival, and to avoid having too much background fluorescence.

15. Pipette off the supernatant and add 45 µL pre-warmed culture medium.

16. Incubate both samples for 5 minutes at 37 ^{o}C.

17. If necessary, clean H and EP chambers during this period.

18. Load 10 µL into H, for both E and C – opposite sides of slide – mark E and C on a label stuck onto the H.

19. Put onto microscope (non-inverted with high pressure mercury vapour lamp source and appropriate filters).

20. Set on normal light source (from beneath).

21. Do microscopy as follows (turn brightness of both bright light and mercury source down to minimum between images):
    a. Set excitation source to green (540 nm) and read emission at red (615 nm) – filter #3
    b. For each side of H, save 5 cross squares of 1 mm^2 at 10x (obj) 10x (eye) = 100x magnification, C and E.
    c. For each of C and E, first view and save bright light images (also using green light thus also showing orange cells), then turn off normal source and save fluorescing dark images.

22. For both C and E, calculate fractions as follows:
    a. Count total number of cells in view
    b. Count number of red fluorescing cells (for C-sample: dead cells, and for E-sample: dead (bright fluorescence) and electroporated cells (dim fluorescence))
    c. Calculate fractions for each image and calculate average fraction and standard deviation (latter provides variation of values)
    d. Subtract C fraction from E fraction, to provide EP yield
    e. To calculate dead cells from EP, deduct bright red fraction from E-sample from all red fraction (bright and dim) – alternatively use trypan blue stain to show dead fraction.

23. This provides one single point on a graph, and this entire experiment will need repeats – at least another 2 repeats, to provide a point with "error bars".

APPENDIX F

SUB-CULTURING (PASSAGING) OF ISHIKAWA CELL LINE

1. Before starting, check flask under microscope to verify log-phase growth, and ensure a confluence of between 70 and 90 % confluence.

2. Pre-warm fresh media (DMEM/F12 + 10 % foetal bovine serum (FBS) + 1 % PenStrep + 1 % Glutamax) and phosphate buffered solution (PBS) solution, 20 to 30 minutes in incubator at 37 ^{o}C.

3. Prepare laminar flow hood (LFH), and place trypsin (0.5 %)(to bring to room temp) in there for 5 to 10 minutes. Fill spare 15 mL conical tube with 5 mL water and place in centrifuge as counterbalance.

4. Place new, sterile 25 cm^2 vented and surface treated culture flask and new 15 mL conical tube in LFH and label them plus put flask with cells in LFH.

5. Using a 10 mL serum pipette, discard old media from flask.

6. Rinse by adding 2 mL PBS, swirling and discard using same 10 mL pipette. Repeat.

7. Pipette 0.5 mL trypsin into flask, swirl quickly, then add 1.5 mL PBS and swirl again.

8. Immediately incubate for 5 minutes at 37 ^{o}C.

9. to Remove from incubator, swirl and tap flask and view under microscope (10x10x=100x) verify all cells are loose.

10. Immediately add 3 mL warm fresh media (to neutralise the enzyme) then gently up and down pipette then transfer to 15 mL tube. Discard old flask.

11. Centrifuge tube at 1000 RPM* for 5 minutes (Heraeus Labofuge 300).

12. Immediately place in LFH and suck off supernatant. Vigorously tap to resuspend cells in residual fluid.

13. Add 3 mL warm fresh media.

14. Immediately withdraw 0.38 mL aliquot of cell mix and place into new flask (1:8 split[#]).

15. Utilise remaining 2.4 mL of cell mix or discard by adding bleach first then waiting before rinsing.

16. Add another 6 mL media to flask, gently swirl without wetting the vent filter and place into incubator at 37 ^{o}C and 5 % CO_2.

17. Check flask under microscope after several hours to verify settling and even dispersion of cells.

18. Cells should be 80 to 90 % confluent after 3 days.

19.[#] For different periods use the following splits (these were determined based on experience):

    1 day: 1:2

    2 days: 1:4

    3 days: 1:8

    4 days: 1:15

    5 days: 1:25

Centrifugal Gravitational Acceleration Force = 11.18(n/1000)2*r = 11.18*(1000/1000)2*13 = 145 g.

(with n = RPM, r = spinning arm radius)

APPENDIX G

FLOW CYTOMETRY

G.0 Introduction

This appendix is a brief introduction to flow cytometry.

G.1 Basics

Flow cytometry is an advanced technique used in a research or clinical laboratory to study characteristics of particles, or more specifically cells. As the name suggests, it is the process of measuring cells while in flow. In its simplest form, a flow cytometer comprises a microfluidics system, a system of lasers and optics, a system of electronics and finally a computer for data processing [1].

Flow cytometers have the ability to measure several parameters simultaneously and very rapidly. They are extremely powerful because they can distinguish between subpopulations in a heterogeneous population of cells [2]. Figure G.1 depicts a typical flow cytometer.

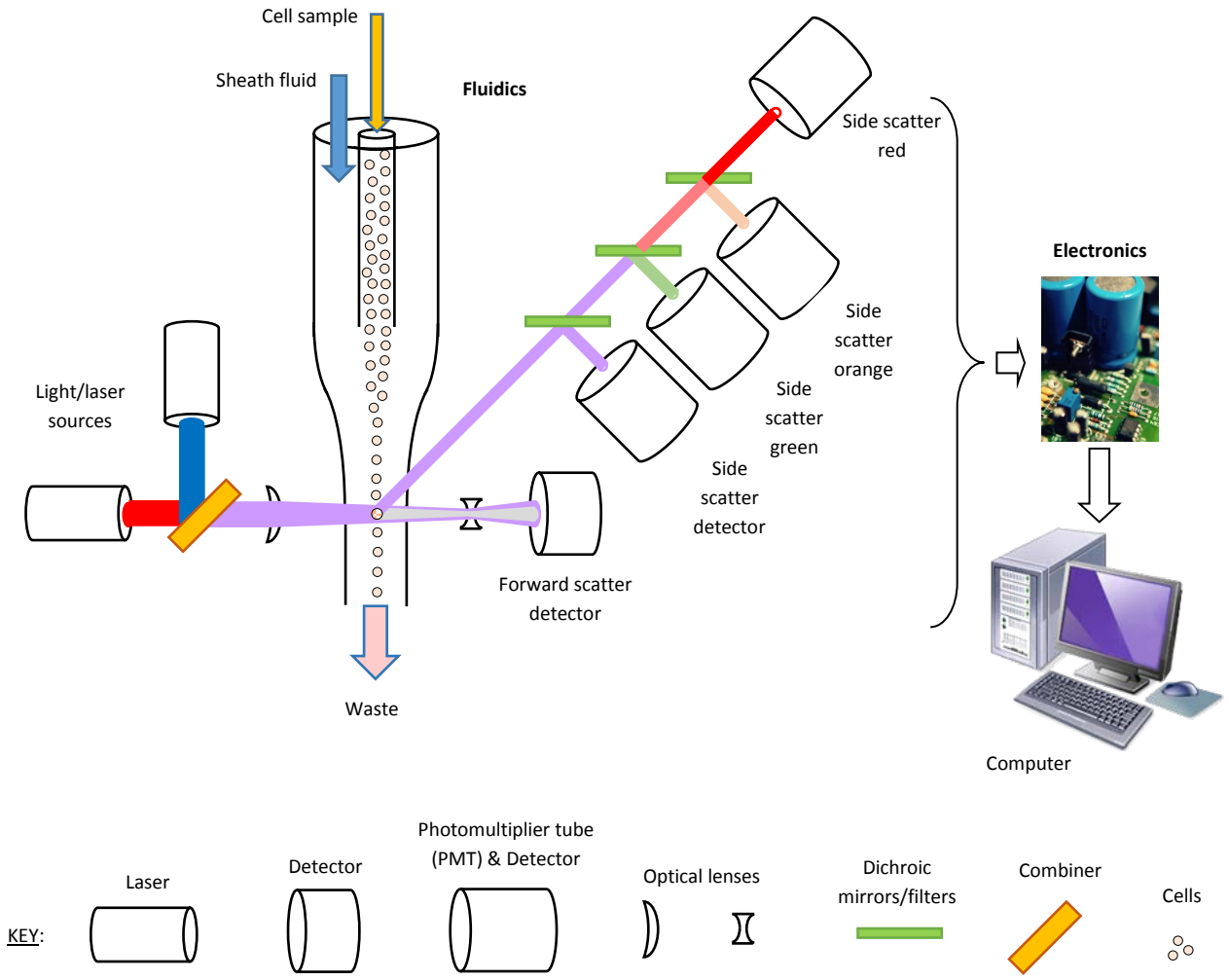

Figure G1. Schematic of a basic flow cytometer (redrawn and adapted from [3]).

A sample of cells or particles in suspension is injected into the microfluidics system which ultimately produces a single stream of cells in a narrow tube. This is achieved by adding a fluid as a "sheath" to the injected stream and hydro-dynamically focusing it, after which the effect of laminar flow is utilised to ultimately produce a carefully focused jet of cells in their original fluid.

A system of lasers is used to excite fluorescent dyes in the cells that are passing through the beams one by one. Several standard lasers are used, such as the Argon laser that produces a source of light at a wavelength of around 350nm (ultra violet) or exactly at 488nm (blue-green), or the Helium Neon laser at 633nm (red). Optics are used to shape and point laser beams towards the narrow tube, and to split up the various emitted wavelengths using dichroic mirrors to steer them towards specific colour assigned photo detectors. An excited fluorescent dye molecule sheds off energy in the form of heat then also in the form of a photon at a longer wavelength (or a lower frequency), known as the Stokes shift.

Once the photo detector receives emitted photons the electronics amplifies the signal and quantifies it. This output signal is then digitised and processed digitally then fed into a standard computer for further data processing and graphing using specialised software.

Normally, flow cytometers separately detect forward scattered and side scattered photons from the cells as they pass through. Forward scattered beams produce outputs that are closely related to the size of each particle or cell, while side scattered beams produce outputs that are related to the granularity of the cells and general fluorescence at various wavelengths, as split up using dichroic mirrors/filters. All this information is gathered in real time while the cells pass through the laser beams.

Ultimately the user can obtain numbers of cells counted, split up into the sizes of these cells, and their granularities in a graphical format such as histograms of two dimensional dot plots. To this can be added different emissions if using more than one fluorescent dye. Using special features in the software allows the user to “gate” or set borders around high density “spots” of cells in dot plots in an effort to distinguish them into their different populations like dead cells, debris, and different sized or types of cells. More advanced features such as mapping can also be found in modern software.

Another popular feature that can be added onto a flow cytometer is the sorter, also known as the fluorescence-activated cell sorting (FACS) machine. This system detects whether a cell fluoresces at a desired wavelength or not and then sorts those cells accordingly by electrostatically charging droplets carrying each cell, and steering those droplets into their specific streams or bins. This allows further assaying or processing of the separated populations of cells.

The major manufacturers of flow cytometers are BD Biosciences, Beckman Coulter, Dako (now owned by Agilent Technologies), and Sysmex-Partec [2]. University of Canterbury School of Biological Sciences, Free Radicals Group, owns a flow cytometer, namely a BD Accuri C6.

Flow cytometry would enable rapid data collection (analysing cells in the order of 10,000 per second) in electroporation experiments on suspended cells compared to using fluorescence microscopy (order of 1 cell per second, considering that analysis was done afterwards), and would in particular allow discrimination between different cell sizes and effect on these cells in terms of fluorescence intensity.

G.2 References

[1] H. M. Shapiro, *Practical flow cytometry*, 4th ed., John Wiley and Sons, 2003.

[2] Marion G. Macey, "Principles of Flow Cytometry", in *Flow cytometry – Principles and applications*, M. G. Macey (ed.), Humana Press, Totawa, New Jersey, US, 2007.

[3] M. G. Ormerod, *Flow Cytometry – A Basic Introduction*, 2008. [Online]: Accessed http://www.denovosoftware.com/site/introtoflowormerod.shtml,

G.3 Further reading

Flow cytometry – Educational guide, 2nd edition, Dako, 2006.

Introduction to Flow Cytometry: A Learning Guide, BD Biosciences, 2000.

Purdue University Cytometry Laboratories (PUCL), http://www.cyto.purdue.edu, updated 2014.

APPENDIX H

INTEGRATION OF SYSTEM

H.0 Introduction

This appendix considers both the electroporator and the radio frequency ablator, as they might be integrated into a single practical clinical apparatus. This is to fulfil the original desire for developing a new cancer therapy treatment and the equipment necessary to achieve this. This chapter is intended to form a basis for development of such an apparatus. One of the target users of this system is likely to be an interventional radiologist, who treats liver tumours in patients where surgery is not viable.

A poster was presented where such a solution to cancer therapy was proposed [1]. It suggested the use of a triple modality, instead of simply using radio frequency ablation (RFA) as a single modality procedure as is currently the practice. The idea was to have a system that utilises the benefits of all three modalities, effectively in the same time (or slightly longer) that a radio frequency ablation procedure is performed. It would use a similar electrode system, but otherwise add electrochemotherapy and irreversible electroporation just before tissue ablation for each tumour to be treated. Figure H.1 shows the proposed system.

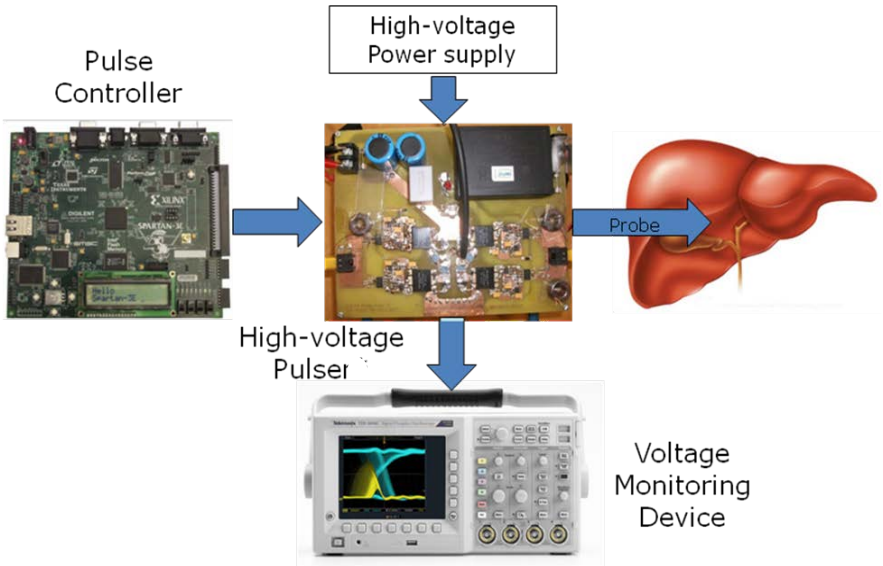

Figure H.1. The proposed main system components for the liver cancer therapy system [1].

The system shown in figure H.1 would only be capable of performing electroporation, including both electrochemotherapy (ECT) and irreversible electroporation (IRE). To achieve ablation requires a different circuit due to the lower voltage but continuous operation which tends to create a lot of heat in the circuit — this requires an entirely different approach to heat sinking and forced fan ventilation — see chapter 5. This implies that the proposed system needs at least two separate circuits, one for high voltage and very short duty cycle pulsing, and the other for continuous lower voltage, continuous high power application.

H.1 Commercially Available Equipment

Radio frequency ablators are manufactured and supplied by many original equipment manufacturers (OEMs), including major brands like Angiodynamics, Rita Medical, Boston Scientific, Covidien, and Stryker [2, 3]. They are normally supplied with a foot pedal for the radiologist.

Electroporators are manufactured and supplied also by many OEMs, including major brands like Genetronics, Biorad, Eppendorf and BTX [4]. These are mostly used for laboratory work, in particular for treating cells in suspension. Another very prominent design developed by a large group in Europe is the Cliniporator [5, 6], which was developed for electroporating human tissue directly, for example skin cancer. It is manufactured by IGEA in Italy. This is arguably the most modern design in existence. It is also supplied with a foot pedal and offers a selection of advanced electrode systems [7]. It complies with EN60601-1 and meets the European directives, in particular medical devices 93/42/CEE and 2007/47/CEE, and it is marked CE0051 under the control of the Notification Body IMQ. Operating procedures have also been published and have been peer reviewed [5]. See figure H.2 for the Cliniporator.

Figure H.2. The Cliniporator [7].

The Cliniporator offers electrochemotherapy (ECT) or electro gene therapy (EGT) modes and requires the use of IGEA electrodes. It offers electrical parameter settings as shown in figure H.3.

FEATURES	HIGH VOLTAGE	LOW VOLTAGE
Pulses number	1 ÷ 10	1 ÷ 10
Pulses amplitude	[100 ÷ 1000] Volt	[20 ÷ 200] Volt
Pulses length	[50 ÷ 1000] µs	[1 ÷ 200] ms
Rise up time	< 2 µs a 1000 Volt	
Pause between pulses		[1 ÷ 2000] ms
Pulses repetition frequency	[1 ÷ 5000] Hz	
Maximum supplied current	20 Ampere	5 Ampere
Pulse amplitude precision	±5%	±5%
Pulse length precision	±2 µs	±1%
Pause between high and low voltage pulses	1 – 2000 ms	

Figure H.3. Cliniporator electrical pulse specifications [7].

For the purposes of the intended system, the Cliniporator is limited to a peak output voltage of 1 kV, where the intention is to generate pulses of an amplitude of several kV. The Cliniporator pulse widths are not short enough, where the intended system should be capable of producing pulses with a width of less than 1 µs. It is also not capable of producing an ablation mode such as in RFA. Finally, and very importantly, the Cliniporator does not offer bipolar (alternating polarity) pulses.

H.2 Proposed System

Physically the cancer therapy system will comprise a trolley-based system with lockable castors, a complete electrode system and a foot pedal. It will have the following features:

- The trolley-based system will be a stand-alone unit that generates all electrical signals with its own simple touch screen user interface. It will be encased in a durable and robust polymer that can be cleaned easily using detergents and alcohol, and be resistant to UV radiation for added sterilisation. It will be connected to electrical mains, and may be offered with an optional rechargeable battery system which makes it completely mobile.

- The electrode system will include shorter and longer plug-in leads with a variety of different plug-in electrode heads. The electrodes shall be of two types, namely monopolar (two separate leads, for an active and a return electrode) and bipolar (single lead for a dual closely spaced electrode system). These systems are likely to be disposable, so must be as economical as possible.

- The foot pedal will have a single lead for plugging into the apparatus. The pedal and lead shall be hermetically sealed, so that its operation cannot be compromised by fluids. It will be disposable as it is unlikely to survive autoclaving, and must thus be as economical as possible.

Electrically the system will comprise a number of components as depicted in figure H.4.

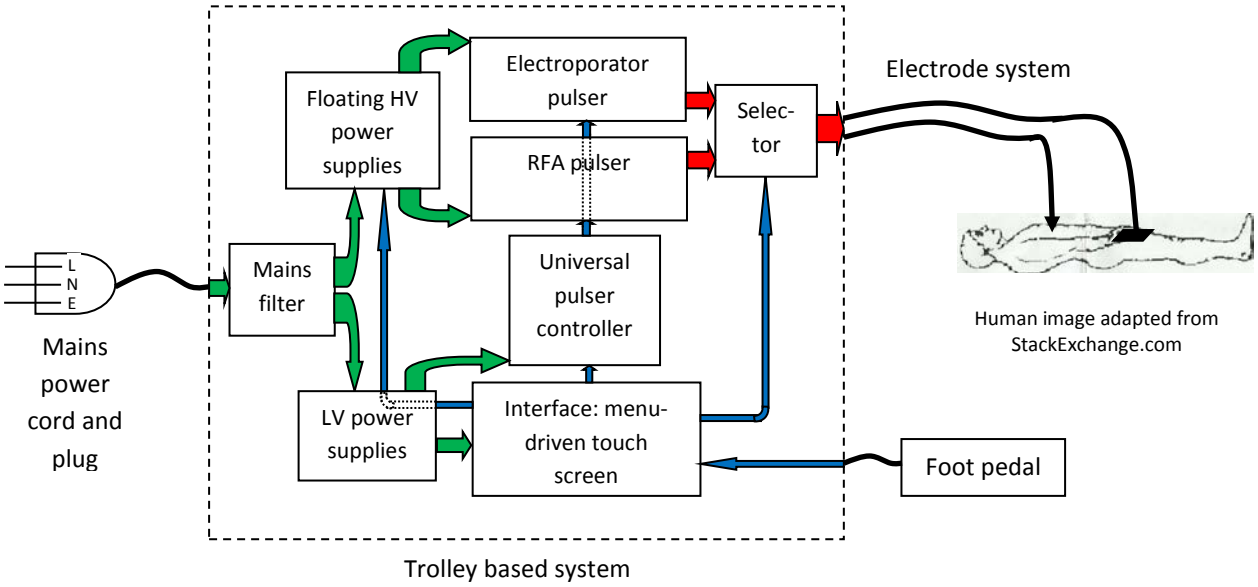

Figure H.4. Functional block diagram of the proposed cancer therapy system. The green arrows represent power, blue represents data or signalling and red represents output pulses.

External connections to the system are the mains power cord and plug, the electrode system and the foot pedal. The radiologist will interact with the system using the interface and the foot pedal, after carefully placing the electrodes on the patient, who should be laying on an isolated operating theatre table. The most common electrode arrangement is the monopolar electrodes as shown, using an active probe inserted into the organ, e.g. the liver, and a return pad on the patient thigh.

Internally there are several blocks as shown in figure H.4. These are:

- Mains filter: This is required to meet the relevant EMC standards as the system is capable of producing substantial electromagnetic interference (EMI). It is likely to be an LC filter including one or two common-mode chokes.

- Low voltage (LV) power supplies: These are required to feed the interface and the universal pulse controller. These would typically be switched and isolated ac to dc converters and would likely supply 5 VDC at several watts for the universal pulse controller and other required low voltage supplies for the menu-driven touch screen interface. They should cater for universal 90 VAC to 250 VAC mains at 50 Hz or 60 Hz.

- Floating high voltage (HV) power supplies: Each pulser system requires several floating HV supplies, typically 2 to 3 for each. These supplies shall be fully isolated and shall possess very low inter-supply capacitance, in the order of only several pF. This is to avoid coupling and leakage currents at the high frequencies and particularly at the edges of pulses due to the high slew rates of switching. The output voltages of these supplies shall all be controllable from the interface. A typical range of voltages for the RFA pulser may be from 10 VDC to 100 VDC and be capable of continuously providing up to 200 W of power each, for a procedure of up to 15 minutes per tumour, and for several tumours in one full procedure. The electroporator pulsers require much higher voltages, ranging between 100 VDC to 750 VDC (or higher ranges depending on the switching devices used and their break down voltages), but are not required to provide continuous power like the RFA supplies. It is anticipated that 100 W would be sufficient to allow for satisfactory charging of on-board capacitors. All HV supplies will be switch mode and isolated. Also, they should cater for universal 90 VAC to 250 VAC mains at 50 Hz or 60 Hz.

- Menu-driven touch screen interface: This interface will likely be a dedicated microprocessor system with a dedicated operating system, with the following features:

    1. A menu system that should allow the user to set:

        * modality between RFA, ECT and IRE

        * choice between screen or foot pedal activation

        * choice of monopolar (DC) or bipolar (AC) mode

        * pulser output voltage

        * pulser frequency

        * pulser waveform

        * pulser number of pulses per burst

        * pulser number of bursts

        * pulser interval between bursts

    2. A 22-inch in-built touch screen LED backlight LCD monitor.

    3. A full diagnostics system that regularly checks the system, starting at power up and continuously thereafter.

4. A means for providing the radiologist with feedback of elapsed or remaining time (typically for an RFA event), for monitoring the average pulse peak voltages and also to confirm satisfactory electrode impedance.

5. A data storage system with capability of transferring data to other media for recording purposes and later retrieval.

- Universal pulser controller: This controller controls the pulser circuits, and contains all firmware on-board in ROM. It may be an FPGA or microcontroller based system. The clock speed should be of the order of 50 MHz to 100 MHz and it should provide a differential output for every MOSFET device of the pulser circuits thus requiring a large number of input-output pins (i/o).

- Electroporation pulser: All inputs to this pulser shall be isolated to medical grade (4 kV). This pulser will be capable of generating pulses up to several kV with very fast rise and fall times (order of 20 ns to 40 ns) but will only run for very short duty cycles, in the order of 0.1 % or less, when operating. It should be capable of producing pulses up to 1 MHz or 2 MHz, and also be capable of producing monopolar (DC) and bipolar (AC) shaped pulses. It will likely use H-bridges in its basic switchers, cascaded together as a multilevel inverter (MLI). It will also be supplied by filtered mains power and have its own on-board medical grade low voltage power supplies to power the gate drivers, being one LV supply per H-bridge. It will be designed to be fail-safe, and hence will cease operating in the event of any foreseeable failure.

- RFA pulser: This pulser will be similar in architecture, layout and almost all technical specifications to the electroporation pulser, but with slight differences, as mentioned before. It will require three LV isolated (4 kV) supplies for its gate drivers per H-bridge. It shall be provided with sufficient internal cooling capability due to the continuous nature of its operation. It shall also be provided with its own thermal cut-out that will shut its operation down in the event of overheating.

- Selector: This solid-state switch will allow the radiologist to select a particular output and shall be extremely reliable. Its default mode will be an open-circuit.

- Optional rechargeable battery-pack: This optional energy source can provide superior mobility and also superior safety, and have a sufficient capacity to operate the system at maximum workload for an hour. This implies a need for a spare drop-in battery pack or alternatively a very fast charge system capable of charging it fully in 15 minutes.

Safety is paramount to avoid electrocution of the patient and of the radiologist. It shall comply with IEC (or EN) 60601-1 and other relevant standards referred to within this general electromedical equipment safety standard. This implies, among many others, fail-safe design throughout, and at least 4 kV isolation between mains power and any accessible points or outputs. Additionally it shall meet the CISPR standards as required in Europe and also in the US, and all European directives for Europe, and FDA approval for the US.

H.3 Conclusion

This chapter presented a brief overview of an integrated cancer therapy apparatus, as may be used for liver cancer therapy by an interventional radiologist. Specifications for the system have been described, including physical and electrical aspects. The proposed system offers a triple modality procedure, instead of only radio frequency ablation.

H.4 References

[1] T. Cronje and P. Gaynor, *Cancer Zapper: Cascaded Pulser*. Canterbury Health Research Poster Expo, Christchurch, New Zealand, 2012.

[2] Y. Ni, et al., "A review of the general aspects of radiofrequency ablation", *Abdom Imaging*, Vol. 30, No. 4, pp. 381-400, 2005.

[3] P. L. Pereira, et al., "Radiofrequency Ablation: In Vivo Comparison of Four Commercially Available Devices in Pig Livers", *Radiology*; Vol. 232, No. 2, pp. 482-490, 2004.

[4] M. Rebersek and D. Miklavcic, "Concepts of Electroporation Pulse Generation and Overview of Electric Pulse Generators for Cell and Tissue Electroporation", from Chapter 16 in *Advanced Electroporation Techniques in Biology and Medicine*, A. G. Pakhamov, D. Miclavcic and M. S. Markov, (Eds.), CRC Press, FL, Taylor and Francis, 2010, pp. 323-339.

[5] L. Mir, et al., "Standard operating procedures of the electrochemotherapy: Instructions for the use of bleomycin or cisplatin administered either systemically or locally and electric pulses delivered by the Cliniporator by means of invasive or non-invasive electrodes", *E J C Supplements*, Vol. 4, No. 11, pp. 14-25, 2006.

[6] Mir, L., et al., "Successful conclusion of Cliniporator project", *ESOPE Newsletter*, No. 3, 2003.

[7] IGEA, *Cliniporator Technical Sheet*, 2013, [Online]. Available: http://www.igeamedical.co.uk/skyblucms/resources/cliniporatortechnicalsheet-1-1.pdf